

Ph.D. Dissertation



**International Doctoral School in Information
and Communication Technology**

DISI - University of Trento

INNOVATIVE TECHNIQUES FOR ANTENNA SYNTHESIS
IN MODERN WIRELESS COMMUNICATION SYSTEMS

Leonardo Lizzi

Advisor:
Andrea Massa, Professor
Università degli Studi di Trento

March 2011

Acknowledgements

I would like to thank Prof. Andrea Massa because he never doubted my capabilities and he always pushed me to get the best of me, becoming a friend as well as a professor.

Thanks to the Eledia group's people for their help and friendship. I will always be one of them.

I would like to thank also Prof. Douglas H. Werner and Prof. Takashi Takenaka because working with them has been invaluable from both the scientific and the human point of view.

A special thanks to Fede who shared this experience with me because he taught me the power of the strength of will and because I can always count on him.

I want to thank all my friends because my achievements would lose their value if I could not share with them. I feel lucky when I think about them.

A special thanks goes to my parents, my sister and my brother because they taught me and always remind me that nothing is unreachable. They made who I am.

Finally, I will never thank enough Silvia for the precious and unconditional support she always gives me, helping me in making my dreams come true.

Abstract

This thesis deals with the study and development of innovative techniques for the synthesis of antennas able to fulfill the tight requirements of modern wireless communication systems. By exploiting the advantages given by the use of geometries based on spline and fractal shapes, the aim of the proposed synthesis techniques is the design of small Ultra-Wideband (UWB) and multi-band antennas. The synthesis of UWB antennas is carried out by means of two different approaches which consider the antenna characterization in the frequency and in the time domain, respectively. The antenna structure is based on a spline representation which allows the description of complex contour by means of a limited set of control parameters. Regarding the synthesis of multi-band antennas, an approach based on the perturbation of fractal geometries is proposed. The perturbation breaks the fixed relationships among resonances typical of standard fractal geometries, allowing the use of fractal antennas for practical applications. By exploiting the knowledge acquired during the synthesis of UWB spline-shaped antennas, a preliminary assessment of an approach for the design of multi-band antennas with spline-based geometries is also reported. Finally, the integration of UWB antennas in array layouts is addressed. Towards this end, first a methodology for the design of aperiodic UWB linear arrays populated by spline-shaped radiating elements is proposed. Successively, the design of an array of UWB elements for imaging applications is described. In order to assess the effectiveness as well as the reliability of the proposed antenna synthesis approaches, both numerical and experimental results are reported.

Keywords

Antenna synthesis, ultra-wideband (UWB) antennas, multi-band antennas, fractal geometries, spline curves, UWB arrays, aperiodic arrays.

Published Journal Papers

- [R1] L. Lizzi, F. Viani, R. Azaro, and A. Massa, "Optimization of a spline-shaped UWB antenna by PSO," *IEEE Antennas and Wireless Propagation Letters*, vol. 6, pp. 182-185, 2007.
- [R2] F. Viani, L. Lizzi, R. Azaro, and A. Massa, "Spline-shaped ultra-wideband antenna operating in the ECC released frequency spectrum," *Electronic Letters*, vol. 44, no. 1, pp. 7-8, January 2008.
- [R3] L. Lizzi, F. Viani, R. Azaro, and A. Massa, "Design of a miniaturized planar antenna for FCC-UWB communication systems," *Microwave and Optical Technology Letters*, vol. 50, no. 7, pp. 1975-1978, July 2008.
- [R4] M. D. Migliore, D. Pinchera, A. Massa, R. Azaro, F. Schettino, and L. Lizzi, "An investigation on UWB-MIMO communication systems based on an experimental channel characterization," *IEEE Transactions on Antennas and Propagation*, vol. 56, no. 9, pp. 3081-3083, September 2008.
- [R5] L. Lizzi, F. Viani, R. Azaro, and A. Massa, "A PSO-driven spline-based shaping approach for ultra-wideband (UWB) antenna synthesis," *IEEE Transactions on Antennas and Propagation*, vol. 56, no. 8, pp. 2613-2621, August 2008.
- [R6] R. Azaro, F. Viani, L. Lizzi, E. Zeni, and A. Massa, "A monopolar quad-band antenna based on a Hilbert self-affine pre-fractal geometry," *IEEE Antennas and Wireless Propagation Letters*, vol 8, pp. 177-180, 2009.
- [R7] F. Viani, R. Azaro, L. Lizzi, and A. Massa, "A miniaturized UWB antenna for wireless dongle devices," *IEEE Antennas and Wireless Propagation Letters*, vol. 7, pp. 714-717, 2008.
- [R8] L. Lizzi, F. Viani, and A. Massa, "Dual-band spline-shaped PCB antenna for Wi-Fi applications," *IEEE Antennas and Wireless Propagation Letters*, vol. 8, pp. 616-619, 2009.

-
- [R9] L. Lizzi, F. Viani, E. Zeni, and A. Massa, "A DVBH/GSM/UMTS planar antenna for multimode wireless devices," *IEEE Antennas and Wireless Propagation Letters*, vol. 8, pp. 568-571, 2009.
- [R10] L. Lizzi and G. Oliveri, "Hybrid design of a fractal-shaped GSM/UMTS antenna," *Journal of Electromagnetic Waves and Applications*, vol. 24, pp. 707-719, 2010.
- [R11] L. Lizzi, G. Oliveri, P. Rocca, and A. Massa, "Planar monopole UWB antenna with UNII1/UNII2 WLAN-band notched characteristics," *Progress in Electromagnetics Research B*, vol. 25, pp. 277-292, 2010.

Published Conference Papers

- [C1] L. Lizzi, F. Viani, R. Azaro, P. Rocca, A. Massa, “An innovative spline-based shaping approach for ultra-wideband antenna synthesis,” in *Proc. 2007 IEEE Antennas and Propagation Society International Symposium*, Honolulu, Hawaii USA, pp. 757-760, June 10-15, 2007.
- [C2] L. Lizzi, M. D. Migliore, D. Pinchera, F. Schettino, M. Benedetti, R. Azaro, and A. Massa, “Experimental channel characterization of a MIMO-UWB communication system,” in *Proc. 2008 IEEE Antennas and Propagation Society International Symposium*, San Diego, USA, pp. 1-4, July 5-11, 2008.
- [C3] M. Benedetti, L. Lizzi, F. Viani, R. Azaro, P. Rocca, and A. Massa, “A time-based approach for the synthesis of antennas for UWB communication systems,” in *Proc. 2008 IEEE Antennas and Propagation Society International Symposium*, San Diego, USA, pp. 1-4, July 5-11, 2008.
- [C4] L. Lizzi and A. Massa, “Analysis of perturbed fractals for antenna synthesis,” in *Proc. 2009 IEEE Antennas and Propagation Society International Symposium*, Charleston, SC, USA, pp. 1-4, June 1-5, 2009.
- [C5] L. Lizzi, F. Viani, P. Rocca, and A. Massa, “PSO-based time-domain antenna synthesis for enhanced UWB communication systems,” in *Proc. 2009 IEEE Antennas and Propagation Society International Symposium*, Charleston, SC, USA, pp. 1-4, June 1-5, 2009.
- [C6] L. Lizzi, L. Manica, and A. Massa, “Time domain analysis for UWB antenna synthesis,” in *Proc. 39th European Microwave Conference 2009 (EuMC2009)*, Rome, Italy, pp. 93-96, September 28 - October 2, 2009.
- [C7] L. Lizzi, G. Oliveri, M. D. Gregory, D. H. Werner, and A. Massa, “A novel design methodology for integration of optimized ultra-wideband elements with aperiodic array topologies,” in *Proc. 2010 IEEE Antennas and Propagation Society International Symposium*, Toronto, Ontario, Canada, pp. 1-4, June 11-17, 2010.

- [C8] L. Lizzi, G. Oliveri, M. D. Gregory, and D. H. Werner, "Synthesis of antenna elements for utilization in UWB arrays," in *Proc. 26th Annual Review of Progress In Applied Computational Electromagnetics (ACES2010)*, Tampere, Finland, pp. 1-4, April 26-29, 2010.
- [C9] L. Lizzi, G. Oliveri, P. Rocca, and A. Massa, "Synthesis of notched band UWB antennas with a hybrid PSO-Spline technique," in *Proc. 40th European Microwave Conference 2010 (EuMC2010)*, Paris, France, September 26 - October 1, 2010.

Contents

1	Introduction	1
2	The Antenna Synthesis Problem	5
3	Frequency Domain Synthesis of UWB Antennas	9
3.1	Spline-shaped Antenna Synthesis	11
3.2	Numerical and Experimental Validation	16
3.2.1	Optimization Process Analysis	19
3.2.2	UWB Antenna for Wireless Dongle Devices	21
3.2.3	FCC Compliant UWB Antenna	29
3.2.4	UWB Antenna with WLAN-band Notched Characteristics	33
3.2.4.1	Band Notched Antenna Design	34
3.2.4.2	Antenna Performances	36
3.3	Conclusion	46
4	Time Domain Synthesis of UWB Antennas	47
4.1	Time Domain Analysis	49
4.2	Antenna Synthesis	50
4.3	Numerical and Experimental Validation	54
4.4	Conclusion	69
5	Synthesis of Multiband Antennas	71
5.1	Fractal-shaped Antennas	74
5.1.1	Fractals	74
5.1.2	Fractal Perturbation	76
5.1.3	Antenna Synthesis	80
5.1.4	Numerical and Experimental Validation	82
5.1.5	Conclusion	90
5.2	Spline-shaped Antennas	90
5.2.1	Antenna Design	91
5.2.2	Numerical and Experimental Validation	92
5.2.3	Conclusion	98

6	Synthesis of UWB Aperiodic Linear Arrays	99
6.1	Design Approach	102
6.2	Optimized Antenna System	105
6.2.1	Element Geometry and Array Layout	105
6.2.2	Element Performances	106
6.2.3	Array Performances	107
6.3	Conclusion	111
7	Synthesis of an Array of UWB Antennas for Imaging Applications	115
7.1	Single Radiating Element	117
7.1.1	Element Design	117
7.1.2	Element Performances	119
7.2	Array Design and Performances	128
7.3	Conclusion	136
8	Conclusions and Future Developments	139

List of Tables

3.1	<i>UWB Dongle Antenna</i> - Geometric descriptors of the synthesized antenna.	23
3.2	<i>FCC Compliant Antenna</i> - Geometric descriptors of the synthesized antenna.	29
3.3	<i>Band Notched Antenna</i> - Values of the geometric descriptors of the antenna prototype.	36
4.1	<i>Test Case A</i> - Descriptive parameters of the synthesized antenna.	58
4.2	<i>Test Case B</i> - Descriptive parameters of the synthesized antenna.	64
5.1	Simulated performances.	85
6.1	Coordinates of the spline control points describing the patch geometry of the synthesized antenna element.	105

LIST OF TABLES

List of Figures

2.1	Main ideas of the antenna synthesis problem.	6
2.2	PSO-based automatic procedure for the synthesis of an antenna.	7
3.1	Descriptive parameters of the spline-based antenna representation.	12
3.2	<i>Optimization Process Analysis</i> - Evolution of the antenna shape: (a) $k = 0$, (b) $k = 10$, (c) $k = 19$, and (d) $k = k_{conv} = 28$	13
3.3	<i>Optimization Process Analysis</i> - Plot of (a) $ s_{11} $, (b) $ s_{21} $, (c) $\angle s_{21}$, and (d) τ versus the frequency at different iterations of the optimization process.	14
3.4	<i>Optimization Process Analysis - Parametric approach</i> - Descriptive parameters for the circular monopole reference geometry.	17
3.5	<i>Optimization Process Analysis - Parametric Approach</i> - Evolution of the antenna shape: (a) $k = 0$, (b) $k = 100$, (c) $k = 300$, and (d) $k = K = 400$	18
3.6	<i>Optimization Process Analysis - Parametric Approach</i> - Plot of (a) $ s_{11} $, (b) $ s_{21} $, (c) $\angle s_{21}$, and (d) τ versus the frequency at different iterations of the optimization process.	20
3.7	<i>Optimization Process Analysis</i> - Comparison between parametric approach and spline-based approach - Plot of the optimal value of the cost function Ω and corresponding terms versus the iteration number k	21
3.8	<i>Optimization Process Analysis</i> - Behavior of the quality indexes F_{11} , F_{21} , F_{GD} and of k_{conv} versus the number of control points N	22
3.9	<i>UWB Dongle Antenna</i> - (a) Front view and (b) back view of the antenna prototype.	23
3.10	<i>UWB Dongle Antenna</i> - Amplitude of s_{11} vs. frequency.	24
3.11	<i>UWB Dongle Antenna</i> - Amplitude of s_{21} vs. frequency.	25
3.12	<i>UWB Dongle Antenna</i> - Group delay τ_g vs. frequency.	25
3.13	<i>UWB Dongle Antenna</i> - Simulated H-plane radiation pattern.	26
3.14	<i>UWB Dongle Antenna</i> - Measured H-plane radiation pattern.	26
3.15	<i>UWB Dongle Antenna</i> - Simulated E-plane radiation pattern ($\phi = 0^\circ$).	27
3.16	<i>UWB Dongle Antenna</i> - Simulated E-plane radiation pattern ($\phi = 90^\circ$).	27

LIST OF FIGURES

3.17	<i>UWB Dongle Antenna</i> - Measured E-plane radiation pattern ($\phi = 0^\circ$).	28
3.18	<i>UWB Dongle Antenna</i> - Measured E-plane radiation pattern ($\phi = 90^\circ$).	28
3.19	<i>FCC Compliant Antenna</i> - Comparison between simulated and measured s_{11} amplitude values.	30
3.20	<i>FCC Compliant Antenna</i> - Comparison between simulated and measured s_{21} amplitude values.	30
3.21	<i>FCC Compliant Antenna</i> - Comparison between simulated and measured s_{21} amplitude values.	31
3.22	<i>FCC Compliant Antenna</i> - Radiation patterns in the horizontal plane.	31
3.23	<i>FCC Compliant Antenna</i> - Radiation patterns in the $\phi = 0^\circ$ vertical plane.	32
3.24	<i>FCC Compliant Antenna</i> - Radiation patterns in the $\phi = 90^\circ$ vertical plane.	32
3.25	<i>Band Notched Antenna</i> - Antenna prototype and descriptive parameters.	35
3.26	<i>Band Notched Antenna</i> - Behavior of the magnitude of s_{11} within the UWB frequency range.	37
3.27	<i>Band Notched Antenna</i> - Plots of the surface currents at $f_1 = 4\text{ GHz}$ [(a) Front side and (b) back side], $f_{notch} = 5.25\text{ GHz}$ [(c) Front side and (d) back side], and $f_2 = 8\text{ GHz}$ [(e) Front side and (f) back side].	39
3.28	<i>Band Notched Antenna</i> - Behavior of the magnitude of s_{11} varying the parameters (a) b_1 , (b) b_2 , and (c) b_3 describing the slot.	40
3.29	<i>Band Notched Antenna</i> - Three-dimensional representation of the absolute gain pattern at (a) $f_1 = 4\text{ GHz}$, (b) $f_{notch} = 5.25\text{ GHz}$, and (c) $f_2 = 8\text{ GHz}$.	41
3.30	<i>Band Notched Antenna</i> - Behavior of the absolute gain at (a)-(b) $f_1 = 4\text{ GHz}$, (c)-(d) $f_{notch} = 5.25\text{ GHz}$, and (e)-(f) $f_2 = 8\text{ GHz}$ along (a)(c)(e) the horizontal ($\theta = 90^\circ$) and (b)(d)(f) the vertical plane ($\phi = 90^\circ$).	43
3.31	<i>Band Notched Antenna</i> - Behavior of the (a)-(b) cross-polar and (c)-(d) co-polar gain components along (a)-(c) the horizontal ($\theta = 90^\circ$) and (b)-(d) the vertical plane ($\phi = 90^\circ$) at $f_1 = 4\text{ GHz}$, $f_{notch} = 5.25\text{ GHz}$, and $f_2 = 8\text{ GHz}$.	44
3.32	<i>Band Notched Antenna</i> - Transmitted (a)(c) and received (b)(d) pulses at the frequency bands (a)(b) $3 - 5\text{ GHz}$ and (c)(d) $6 - 10\text{ GHz}$ of the UWB system composed of two identical face-to-face copies of the proposed antenna.	45
4.1	UWB communication system composed by a pair of two identical antennas.	50

4.2	<i>Antenna Efficiency</i> - Examples of transmitted and reflected signals giving (a) $E = 0.9$ and (b) $E = 0.5$	51
4.3	<i>System Fidelity</i> - Examples of transmitted and received signals giving (a) $F = 0.9$ and (b) $F = 0.5$	51
4.4	<i>Similarity Factor</i> - Examples of radiated electric field towards different directions and the corresponding similarity factor values. (a) $0.9 < S(\theta, \phi) < 1$ and (b) $0.2 < S(\theta, \phi) < 0.6$	52
4.5	Antenna geometry.	53
4.6	<i>Test Case A</i> - Time domain behavior of the input signal $u(t)$. . .	54
4.7	<i>Test Case A</i> - Evolution of the geometric variables $\{\alpha_1, \dots, \alpha_4\}$ over the iterations.	55
4.8	<i>Test Case A</i> - Evolution of the coordinates of the control points of the splines modeling (a) the radiating part and (b) the ground plane of the antenna over the iterations.	56
4.9	<i>Test Case A</i> - Evolution of the antenna performance (antenna efficiency E , system fidelity F , and similarity factor S) over the iterations compared with the cost function ξ	57
4.10	<i>Test Case A</i> - Comparison between the input signal $u(t)$ and the reflected signal $w(t)$	59
4.11	<i>Test Case A</i> - Comparison between the energy-normalized input signal $\hat{u}(t)$ and the energy normalized received signal $\hat{v}(t)$	59
4.12	<i>Test Case A</i> - Radiated electric field towards different directions and corresponding similarity factor values.	60
4.13	<i>Test Case A</i> - Magnitude of (a) s_{11} and (b) s_{21} parameters.	60
4.14	<i>Test Case A</i> - Antenna prototype.	61
4.15	<i>Test Case A</i> - Simulated total gain radiation patterns at (a) 4 GHz , (b) 6.5 GHz , and (c) 9 GHz	62
4.16	<i>Test Case A</i> - Comparison between simulated and measured values of total gain at (a)-(b) 4 GHz , (c)-(d) 6.5 GHz , and (e)-(f) 9 GHz in the (a)-(c)-(e) horizontal ($\theta = 90^\circ$) and (b)-(d)-(f) vertical plane ($\phi = 90^\circ$).	63
4.17	<i>Test Case B</i> - Antenna prototype.	64
4.18	<i>Test Case B</i> - Comparison between the input signal $u(t)$ and the reflected signal $w(t)$	65
4.19	<i>Test Case B</i> - Comparison between the energy-normalized input signal $\hat{u}(t)$ and the energy normalized received signal $\hat{v}(t)$	65
4.20	<i>Test Case B</i> - Radiated electric field towards different directions and corresponding similarity factor values.	66
4.21	<i>Test Case B</i> - Magnitude of (a) s_{11} and (b) s_{21} parameters.	66
4.22	<i>Test Case B</i> - Simulated total gain radiation patterns at (a) 2.5 GHz , (b) 4 GHz , and (c) 5.5 GHz	67

4.23	<i>Test Case B</i> - Comparison between simulated and measured values of total gain at (a)-(b) 2.5 GHz, (c)-(d) 4 GHz, and (e)-(f) 5.5 GHz in the (a)-(c)-(e) horizontal ($\theta = 90^\circ$) and (b)-(d)-(f) vertical plane ($\phi = 90^\circ$).	68
5.1	Fractal antenna geometries considered in the perturbation analysis. (a) Sierpinski antenna and (b) Koch antenna.	75
5.2	<i>Perturbation analysis</i> . Behavior of the normalized resonant frequencies of the Sierpinski antenna varying the $m_{11}^{(1)}$ parameter.	77
5.3	<i>Perturbation analysis</i> . Behavior of the normalized resonant frequencies of the Sierpinski antenna varying the $m_{22}^{(1)}$ parameter.	78
5.4	<i>Perturbation analysis</i> . Behavior of the normalized resonant frequencies of the Koch antenna varying the $n_{11}^{(1)}$ parameter.	79
5.5	<i>Perturbation analysis</i> . Behavior of the normalized resonant frequencies of the Koch antenna varying the $n_{12}^{(1)}$ parameter.	80
5.6	<i>Perturbation analysis</i> . Behavior of the normalized resonant frequencies of the Koch antenna varying the $n_{11}^{(2)}$ parameter.	81
5.7	Geometry of the multimode three-band antenna.	83
5.8	Behaviors of the cost function statistics during the iterative <i>PSO</i> optimization.	84
5.9	Simulated VSWR values, at the center of each frequency band, for the trial solutions at the convergence.	84
5.10	Three-band Antenna Prototype.	85
5.11	Simulated and measured VSWR values.	86
5.12	Simulated 3D radiation patterns - (a) Total gain at $f_0^{DVBH} = 610 MHz$; (b) Total gain at $f_0^{GSM1800} = 1850 MHz$; (c) Total gain at $f_0^{UMTS} = 2100 MHz$	87
5.13	Simulated and measured radiation patterns - (a) Horizontal plane ($\theta = 90^\circ$) at $f_0^{DVBH} = 610 MHz$; (b) Vertical plane ($\phi = 90^\circ$) at $f_0^{DVBH} = 610 MHz$; (c) Horizontal plane ($\theta = 90^\circ$) at $f_0^{GSM1800} = 1850 MHz$; (d) Vertical plane ($\phi = 90^\circ$) at $f_0^{GSM1800} = 1850 MHz$; (e) Horizontal plane ($\theta = 90^\circ$) at $f_0^{UMTS} = 2100 MHz$; (f) Vertical plane ($\phi = 90^\circ$) at $f_0^{UMTS} = 2100 MHz$	88
5.14	Simulated surface currents at (a) $f_0^{DVBH} = 610 MHz$, (b) $f_0^{GSM1800} = 1850 MHz$, and (c) $f_0^{UMTS} = 2100 MHz$	89
5.15	Antenna geometry - (a) Front view and (b) back view.	92
5.16	Antenna Prototype - (a) Front view and (b) back view.	93
5.17	Simulated and measured VSWR values.	93
5.18	Simulated 3D radiation patterns - Total gain at (a) $f_1 = 2.448 GHz$ and (b) $f_2 = 5.512 GHz$. Co-polar component at (c) $f_1 = 2.448 GHz$ and (d) $f_2 = 5.512 GHz$. Cross-polar component at (e) $f_1 = 2.448 GHz$ and (f) $f_2 = 5.512 GHz$	95

5.19	Simulated and measured radiation patterns - Horizontal plane ($\theta = 90^\circ$) at (a) $f_1 = 2.448 GHz$ and (b) $f_2 = 5.512 GHz$. Vertical plane ($\phi = 0^\circ$) at (c) $f_1 = 2.448 GHz$ and (d) $f_2 = 5.512 GHz$. Vertical plane ($\phi = 90^\circ$) at (e) $f_1 = 2.448 GHz$ and (f) $f_2 = 5.512 GHz$	96
5.20	Simulated surface current - Front view at (a) $f_1 = 2.448 GHz$ and (b) $f_2 = 5.512 GHz$. Back view at (c) $f_1 = 2.448 GHz$ and (d) $f_2 = 5.512 GHz$	97
6.1	Array element geometry. (a) Front view and (b) back view.	103
6.2	Array parametrization.	104
6.3	Positions (in meters) in the elements of the optimized array layout.	106
6.4	Prototype of the synthesized array element. (a) Front view and (b) back view.	106
6.5	Simulated and measured s_{11} magnitude values exhibited by the synthesized array element.	107
6.6	Three-dimensional representation of the total gain pattern at (a) 2, (b) 4 and (c) 6 GHz.	108
6.7	Behavior of the co-polarized and cross-polarized gain components in the plane of $\theta = \frac{\pi}{2}$ at (a) 2, (b) 4 and (c) 6 GHz.	109
6.8	Peak sidelobe level performances over an extended bandwidth of the optimized array and of a periodic array populated by the same number of elements.	110
6.9	VSWR values for all the elements of the array at (a) 2, (b) 4 and (c) 6 GHz.	111
6.10	Comparison between the normalized power pattern and the array factor of the array at (a) 2, (b) 4 and (c) 6 GHz.	112
7.1	Geometry of the printed rectangular monopole antenna. (a) Front view, (b) back view and (c) side view.	118
7.2	Prototype of the synthesized antenna element. (a) Front view and (b) back view.	119
7.3	Simulated and measured $s_{1,1}$ magnitude values exhibited by the synthesized antenna element.	120
7.4	Surface currents flowing on the feedline and the patch of the synthesized antenna element. (a)(c)(e) Front and (b)(d)(f) back side at (a)(b) 2.5, (c)(d) 4.0, and (e)(f) 5.5 GHz.	122
7.5	Surface currents flowing on the groundplane of the synthesized antenna element. (a)(c)(e) Front and (b)(d)(f) back side at (a)(b) 2.5, (c)(d) 4.0, and (e)(f) 5.5 GHz.	123
7.6	Surface currents flowing on the feedline and the patch of the modified antenna element (without the slit). (a)(c)(e) Front and (b)(d)(f) back side at (a)(b) 2.5, (c)(d) 4.0, and (e)(f) 5.5 GHz.	124

LIST OF FIGURES

7.7	Surface currents flowing on the groundplane of the modified antenna element (without the slit). (a)(c)(e) Front and (b)(d)(f) back side at (a)(b) 2.5, (c)(d) 4.0, and (e)(f) 5.5 GHz.	125
7.8	Simulated and measured $s_{1,1}$ magnitude values exhibited by the modified antenna element (without the slit).	126
7.9	Simulated $s_{1,1}$ magnitude values exhibited by the antenna for different values of the slit width s_w	126
7.10	Electric near field radiated by the synthesized antenna. (a)(c)(e) Vertical and (b)(d)(f) horizontal plane passing by the center of the rectangular patch at (a)(b) 2.5, (c)(d) 4.0, and (e)(f) 5.5 GHz.	127
7.11	Layout of the 24-element array.	129
7.12	Prototype of the 24-element array.	130
7.13	Simulated and measured return loss values exhibited by the array elements. (a) $ s_{1,1} $, (b) $ s_{3,3} $, (c) $ s_{11,11} $, (d) $ s_{14,14} $, (e) $ s_{18,18} $, and (f) $ s_{22,22} $	131
7.14	Simulated and measured transmission coefficient values exhibited by the array elements. (a) $ s_{2,1} $, (b) $ s_{11,1} $, (c) $ s_{16,1} $, (d) $ s_{3,2} $, (e) $ s_{18,2} $, and (f) $ s_{6,3} $	132
7.15	Electric near field radiated by the array antenna #4 on the horizontal plane passing by the center of the rectangular patch at (a) 2.5, (b) 4.0, and (c) 5.5 GHz.	133
7.16	Electric near field radiated by the array antenna #4 on the vertical plane passing by the center of the rectangular patch at (a) 2.5, (b) 4.0, and (c) 5.5 GHz.	134
7.17	Electric near field radiated by the array antenna #4 on the vertical plane passing by the center of the antenna #21 rectangular patch at (a) 2.5, (b) 4.0, and (c) 5.5 GHz.	135

Structure of the Thesis

The thesis is structured in chapters according to the organization detailed in the following.

The first Chapter deals with an introduction to the thesis, focusing on the main motivations and on the subject of this work.

Chapter 2 presents the antenna synthesis problem which can be conveniently formulated as an optimization problem.

In Chapter 3, an approach for the synthesis of spline-shaped UWB antennas carried out in the frequency domain is proposed. The effectiveness of the approach is pointed out by the reported numerical and experimental results regarding the realization of different prototypes. The flexibility of the proposed approach in dealing with different project requirements is demonstrated through the synthesis of UWB antenna with frequency notched characteristics.

A time domain approach for the synthesis of UWB antennas whose geometry is based on the spline representation is described in Chapter 4. The reported design examples demonstrate the capability of the proposed approach to synthesize antennas fulfilling the time domain UWB requirements.

Chapter 5 deals with the synthesis of multi-band antennas. A approach based on the analysis of the perturbation of fractal geometries is reported and its effectiveness is validated by means of a representative result concerning the realization of a three-band Sierpinski antenna. A preliminary assessment of an approach for the synthesis of multi-band antennas with spline-based geometries is also reported.

A methodology for the design of UWB aperiodic linear array constituted by spline-shaped radiating elements is proposed in Chapter 6.

In Chapter 7, the realization of an array of UWB antennas suitable for imaging applications is described and discussed.

Conclusions and further developments are presented in Chapter 8.

Chapter 1

Introduction

Driven by the great expansion of telecommunication sectors such as mobile telephony or personal communications, much research has been recently invested in developing innovative antenna systems which must meet different requirements depending on the particular application. Among all the possible attributes an antenna should possess, the most highly desirable are the “ultra-wideband (UWB)” and the “multi-band” behavior, depending if the antenna is intended for the transmission of a large amount of data or for multi-services applications, respectively. In addition, small dimensions and good radiation properties are also usually required. In this sense, the antenna system turns out to be a key component that must be carefully designed in order not to compromise the performances of the whole communication system.

Dealing with many present communication applications that require the transmission of a huge amount of information, UWB antennas are able to provide high data rates by transmitting/receiving very short time pulses. However, this makes the synthesis as well as the analysis of UWB antennas very demanding tasks, since also the quality of the transmitted and the received signals must be taken into account [1]. Usually, the characterization of radiating systems is carried out in the frequency domain by analyzing some parameters such as efficiency, input impedance, gain, polarization properties and radiation patterns [2]. All these terms depend strongly on frequency [3]. Dealing with narrowband systems, such parameters can be analyzed at the center frequency, providing a comprehensive description of the system. When UWB systems are considered, antenna parameters can be expressed as a function of frequency, or they can be properly translated in the time domain.

Several antennas operating over ultra-wide frequency ranges have been proposed over the last years. Their designs are usually based on the optimization of the geometrical descriptors of reference shapes. These techniques allow the description of the geometrical characteristics of the antenna in a simple and effective way, however, they lack flexibility in generating different antenna configurations which is usually required for designing antennas that fulfill difficult requirements. An alternative and much more flexible approach is to represent

the antenna geometry with spline curves. The spline representation allows the definition of complex curvilinear shapes which are described by a small set of control points.

Concerning multi-band antennas, in the last years, several antenna designs have been proposed. Promising solutions are certainly represented by the so-called “fractal antennas”. Fractal antennas are radiating systems that employ fractal rather than Euclidean geometric concepts in their design. The term “fractal” was originally coined by Mandelbrot [4] to name a family of complex shapes that are self-similar, that is, they are composed by many copies of themselves at different scales. In other words, it can be said that fractals have no characteristic size [5]. Such a particular property allows fractal antennas to defy the strong relationship between the behavior of the antenna and its size relative to the operating frequency, which has represented for decades a tight constraint to the antenna designer. Moreover, the recursive methodologies usually involved in the generation of the fractal geometries result in the possibility to enclose an infinitely long curve in a finite area. By an engineering perspective, this means the possibility to add more electrical length in less volume. Thanks to such unique properties, fractal-shaped antennas have recently demonstrated to be good candidates for both miniaturization and multi-band purposes.

This thesis deals with the study and the development of innovative techniques for the synthesis of radiating systems able to fit the tight requirements needed by modern wireless communication applications. The underlying idea of these techniques is the exploitation of the advantages given by spline and fractal geometries to design small UWB and multi-band antennas.

Regarding UWB antennas, their synthesis is first carried out by means of an optimization strategy in which the description of the antenna geometry is based on the spline representation. As commonly adopted, the characterization of the antenna is carried out in the frequency domain. Nevertheless, the antenna is the result of a full approach aimed at matching all the UWB specifications including not only the impedance bandwidth but also the need to correctly receive the transmitted UWB pulse waveform. The effectiveness of the approach is demonstrated by the reported numerical and experimental results regarding the realization of different prototypes. Driven by the recent concern about the interference between UWB systems and other communication standards, the synthesis of a UWB antenna exhibiting a frequency notched behavior is also reported.

However, two main drawbacks affect an approach based on the antenna frequency domain characterization. First, even if the antenna electrical parameters can be expressed as a function of frequency, they would lose their usefulness as compact descriptions of the antenna’s behavior [6]. Secondly, a frequency-by-frequency analysis would be particular inefficient for very large bandwidths in terms of required time and computational resources. Therefore, it seems to be more natural to analyze UWB radiating systems in the time domain, where all the frequencies are treated together. Accordingly, the development of a fully time

domain approach for the synthesis of UWB radiating systems is then proposed. Towards this end, the requirements typical of an UWB communication system are conveniently translated in the time domain by defining a set of suitable time domain definitions of classical antenna parameters. More in detail, three main requirements are identified. The former is that the antenna should be able to radiate as much energy as possible. Such a constraint is more important in UWB systems than in narrowband ones because of the very low energy usually characterizing the UWB transmitted waveforms. Secondly, the whole UWB system, constituted by a pair of antennas, is considered in order to guarantee the non-distorted reception of the transmitted signal. In other words, the UWB system is required to be a distortionless system. Finally, as usually required in communication applications, the antennas should present omnidirectional radiation patterns over all the frequencies. On the basis of this time domain analysis, an automatic approach for the synthesis of spline-shaped antennas is proposed. Such an approach provides a high number of degrees of freedom in generating antenna shapes controlled by a limited number of geometric variables.

Regarding multi-band antennas, the first step is aimed at carefully analyzing the effects of geometrical perturbations on the performances of different fractal antennas. As first examples, the Koch and the Sierpinski antennas are considered. The Koch antenna can be generated from the Koch curve by iteratively applying the Hutchinson operator. Such antenna has been one of the first to be thought as a possible simple multi-band antenna and it is an effective example to illustrate that fractals can improve some features of common Euclidean shapes. The arising antenna geometry is characterized by a highly rough and uneven shape, thus suggesting it can become an efficient radiator. On the other hand, the Sierpinski antenna can be obtained by means of an iterative procedure starting from a main triangle shape. At the first iteration, a central inverted triangle is subtracted from the main triangle shape. This generates other three equal triangles, each one having one half of the size of the original one. The ideal fractal Sierpinski gasket is obtained by iteratively performing such a subtracting procedure an infinite number of times. The result is, as many other fractal shapes, a self-similar structure, i.e., an object composed by many scaled replicas of itself. The study of the variations of the geometric parameters of the different fractal antennas is devoted to define some a-priori rules for the synthesis process. Towards this end, a set of descriptive parameters which control the antenna structure at hand are defined and the achievable antenna performances are studied by means of numerical simulations. Such an analysis provides useful information for the definition of analytic relationships for the behavior of the resonant frequencies. However, since only an exhaustive search for all the possible combinations of the antenna descriptors would provide an analytic synthesis tool, the analysis is devoted to obtain a suitable initialization for global optimization procedures. This approach allows the identification of the best set of antenna geometric parameters without the need for excessive time and computational resources. The result

is an automatic procedure for the synthesis of multi-band antennas characterized by perturbed fractal geometries. By exploiting the knowledge acquired during the synthesis of UWB antennas, a preliminary assessment of an approach for the synthesis of spline-shaped multi-band antennas is also reported.

The underlying global optimization required for the synthesis of both fractal and spline-shaped antennas is faced by means of a PSO-based procedure. PSO is a stochastic evolutionary algorithm based on the movement and intelligence of the swarms, and it has widely demonstrated its effectiveness in optimizing difficult multidimensional problems even in the electromagnetic field.

Finally, the integration of UWB antennas into array layouts is discussed. More specifically, first a methodology for the design of aperiodic linear arrays constituted by spline-shaped radiating elements is proposed. A good impedance matching over an extended bandwidth is a necessary requirement for antennas that must be used as elements of a UWB array, however, maintaining low cross-polarized radiation over the operating bandwidth is also an important factor deserving for consideration. Indeed, it is not uncommon for UWB antennas to develop several lobes in the radiation pattern and possess increased cross-polarized radiation at their upper range of operating frequencies. Consequently, proper attention is paid during the synthesis process in order to minimize such undesirable behavior that would degrade the performances of the entire UWB array. Successively, the design of an array of UWB elements for imaging applications is proposed. The design process consists of two steps. First a UWB monopole antenna is synthesised to be employed as the element of the array. Consequently, specific constraints are imposed on the electrical and physical characteristics of the antenna. Successively, multiple copies of the synthesised element are properly arranged on the walls of a cubic dielectric chamber in order to obtain an array fulfilling the requirements needed by imaging applications.

Chapter 2

The Antenna Synthesis Problem

The antenna synthesis problem is based on three main ideas (Fig. 2.1). The first one is the use of a smart representation of the antenna geometry that allows the description of the antenna with a limited set of parameters, but that also must be very flexible in defining different antenna shapes. The second one is the utilization of an optimization procedure able to cleverly explore the solution space in order to identify the “best” antenna shape, i.e., an antenna fitting all the project requirements. The last one is the definition of a customized cost function taking into account all the project requirements and used by the optimization procedure as an index of the goodness of the solutions.

In this chapter, the focus is on the optimization procedure, while the other two blocks (the cost function and the geometry representation) will be deeply discussed for each one of the antenna synthesis approaches proposed in the next chapters.

In optimization problems, there exist different solutions which have different degrees of satisfaction with respect to the project requirement. The degree of satisfaction is measured through a function, usually called cost function, which is representative of the problem at hand. Mathematically speaking, the functional representing the problem has many local minima. The goal of optimization is the identification of the optimal solution, i.e. of the global minimum.

Optimization strategies can be classified in two big classes: the *Local Search Techniques* and the *Global Search Techniques*. In order to achieve the global minimum of the problem by means of a local search algorithm, it is mandatory to choose an initialization point belonging to the attraction basin of the global minimum. This means that, although effective in terms of convergence speed, these algorithms require a-priori information for the selection of the initialization point. Differently, global search algorithms are characterized by the so-called hill-climbing behavior, meaning that if they are trapped within the attraction basin of a local minimum, they are able to “climb the hill” and “jump” within the solution space to reach the global minimum.

Since the type and the number of unknowns to be determined can vary among the optimization problems, the selection of the proper optimization algorithm is

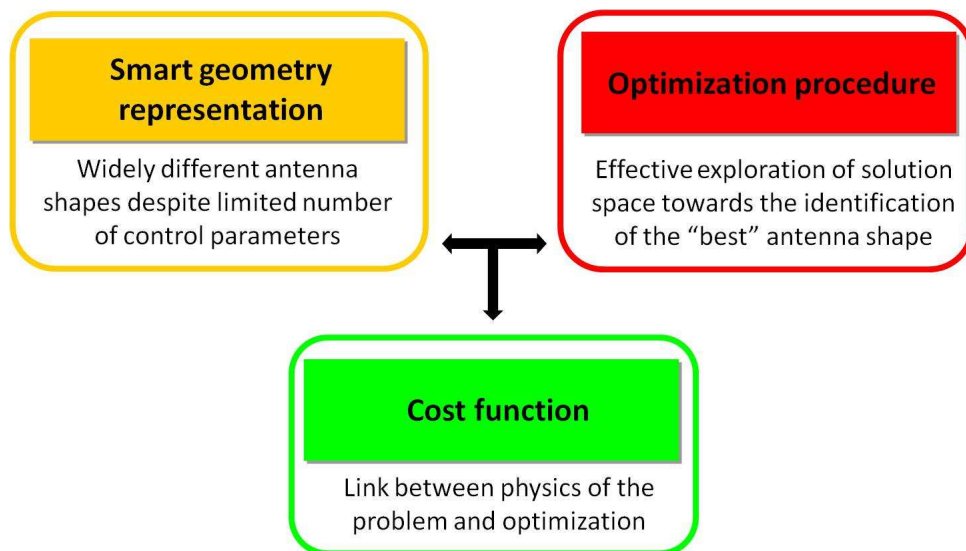


Figure 2.1: Main ideas of the antenna synthesis problem.

a key issue and a general rule for this choice does not exist. According to the “no free lunch” theorems [7], the average performance of any pair of algorithms across all possible problems is identical. This implies that if an algorithm performs better than random search on some class of problems, then it must perform worse than random search on the remaining problems. Roughly speaking, it means that the choice of the optimization algorithms depends on the problem at hand.

From a practical point of view, the main features necessary for an optimization algorithm are the ability to deal with complex functionals or cost functions, the simplicity of use, a limited number of control parameters, good convergence properties and the exploitation of the parallelism offered by modern PC clusters. In this sense, evolutionary algorithms (EAs) seem to be good candidates. They have been applied to a huge variety of problems in different and very heterogeneous fields ranging from engineering to economics, up to business and natural science.

In antenna synthesis problem, two evolutionary algorithms are the most commonly used: the Genetic Algorithm (GA) and the Particle Swarm Optimizer (PSO). Genetic algorithms have been proposed by John Holland in 1975. They basically imitate the concepts of natural selection and evolution, and therefore they are based on the competition among the agents to find the optimal solution. Differently from Gas, the PSO is based on the concept of social interaction and cooperation. As a matter of fact, it has been developed taking inspiration from the study of the behavior in the motion of swarms of bees, flocks of birds and schools of fishes.

When dealing with the synthesis of antennas the use of PSO demonstrated to

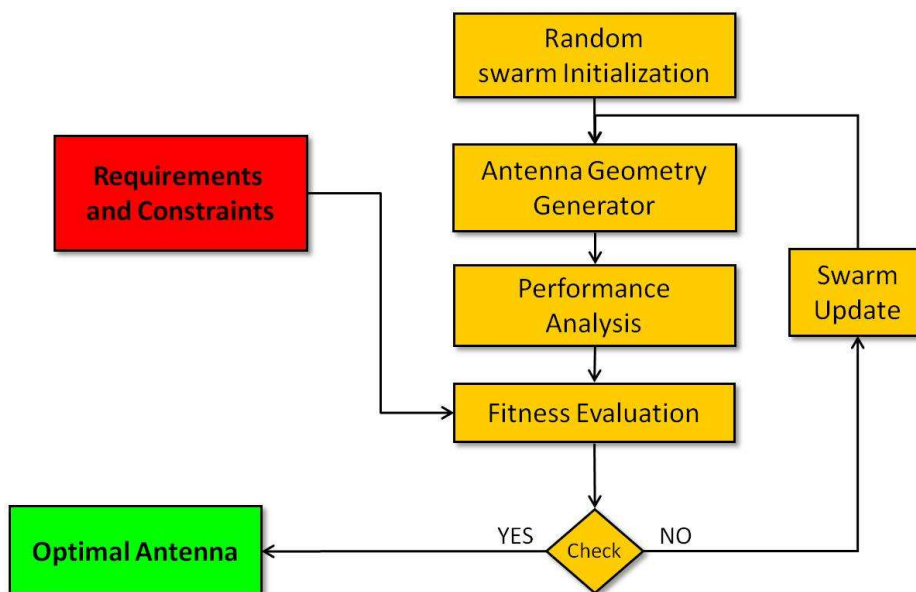


Figure 2.2: PSO-based automatic procedure for the synthesis of an antenna.

be more attractive than GA. As a matter of fact, PSO is easier to implement with respect to the GA, it is easier to calibrate since it has fewer control parameters, it is able to prevent the stagnation since it is based on cooperation instead of competition, and finally, it is particularly efficient in dealing with the optimization of continuous variables, as usually happens for the antenna optimization problem.

Without entering into the detail, PSO is based on the behavior of the swarms of bees. The bees explore the space surrounding the nest looking for the regions with more flowers to collect more pollen as possible. The movement of each bee is based on the combination of three factors: 1) the knowledge of the place with the largest amount of pollen encountered by the bee itself, the knowledge of the place with the largest amount of pollen encountered by the whole swarm and finally the curiosity of the bee to move towards unexplored places. Analogously, the exploration of the solution space by the PSO agents is based on the same three factors (for a more detailed explanation of PSO please refer to [8]).

In order to build an automatic process for the synthesis of an antenna (Fig. 2.2), the PSO optimization procedure is integrated with an antenna geometry generator (*AGG*) and a method to analyze the performances of the solutions. The *AGG* must be able to model a wide number of trial antenna structures A as a function of a small set of optimization variables ξ . Starting from the requirements and the constraints of the antenna that must be designed, the unknown representative descriptors are tuned through an iterative procedure aimed at minimizing a suitable cost function $\Omega(A)$ which acts as an index of the

goodness of the solution, i.e.,

$$\widehat{\xi} = \arg \min_{\xi} \{ \Omega (\xi) \}. \quad (2.1)$$

The final result is the identification of an optimal antenna geometry $\widehat{A} = AGG \{ \widehat{\xi} \}$, i.e., an antenna satisfying all the project requirements.

More in detail, a set of initial solutions $\xi_r^{\{k\}}$; $r = 1, \dots, R$; $k = 1, \dots, K$ (r and k being the trial index and the iteration index, respectively) is randomly generated. The electric parameters of each trial antenna are computed by means of an electromagnetic simulator in order to evaluate its fulfilling $\Omega_p^{(k)} = \Omega \left(\xi_p^{(k)} \right)$ with the project specifications. At each iteration k of the minimization process, each PSO particle moves closer to its own best position found so far

$$\zeta_r^{(k)} = \arg \min_{k=1, \dots, K} \{ \Omega (\xi_r^{\{k\}}) \} \quad (2.2)$$

(indicated as *personal best* position) as well as towards the best position encountered by the entire swarm,

$$\zeta^{(k)} = \arg \min_{r=1, \dots, R} \{ \Omega (\zeta_r^{(k)}) \} \quad (2.3)$$

(referred to as *global best* position) [8] according to the rules of evolution of the PSO [9]. The process stops whether $k = K$ or $k = k_{conv}$ when $\Omega [AGG (\zeta^{(k)})] \leq \eta_{conv}$, η_{conv} being a user-defined threshold. Then, $\widehat{\xi} = \zeta^{(k)}$ and $\widehat{A} = AGG (\zeta^{(k)})$.

Chapter 3

Frequency Domain Synthesis of UWB Antennas

Ultra-wideband (*UWB*) is a term commonly used to describe a wireless technology where very short low-power time pulses, which occupy a very large frequency bandwidth, are transmitted/received. Such a communication technique allows high transmission data-rates, multipath immunity, low probability of intercept, low power consumption, and good time domain resolution allowing for localization and tracking application [10]. Moreover, it enables the possibility for a single system to simultaneously operate in different ways (e.g., as a communication device, a locator or a radar) [11]. Since the US Federal Communication Commission (*FCC*) revision on *UWB* transmissions in 2002 [12] and the Electronic Communications Committee (*ECC*) decision in Europe about the use of *UWB* technologies [13], the design of *UWB* systems has drawn a considerable attention becoming a key topic in the framework of wireless communications.

As far as the radiating sub-system is concerned, unlike conventional narrow-band systems where modulated sinusoidal waveforms occupy small portions of the frequency spectrum, the assumption of a uniform behavior of the antenna is no longer reliable when dealing with *UWB* frequency bandwidths and the distortion of the transmitted time-domain pulses should be taken into account and carefully prevented. Consequently, *UWB* antennas turn out to be critical components of the whole system and their electrical parameters need an accurate optimization in a wide range of frequencies to minimize/reduce the signal distortions [?]. In order to properly address such an issue, suitable techniques are necessary since a standard synthesis process aimed at determining classical frequency-domain parameters of both the transmitting antenna and the receiving one (e.g., gain, radiation patterns, reflection coefficients, and polarization) is not enough to ensure the distortionless of the *UWB* system and the correct transmission/reception of time-domain pulses. More specifically, the design of an *UWB* antenna requires customized synthesis techniques to satisfy the *UWB* requirements [14] as well as proper analysis tools for an accurate description of

the antenna behaviors in the time domain [15].

Generally speaking, two main methodologies for the antenna design can be usually recognized. The former, indicated as *parametric approach*, considers a reference shape defined by a fixed number of geometric descriptors to be optimized to satisfy the project guidelines. In such a framework, different examples of *UWB* antennas have been studied starting from simple shapes as triangular [16], circular disc [17], annular ring [18], rectangular structure [19], diamond [20][21], and bow-tie [22]. On the other hand, the so-called *building-block approach* synthesizes the antenna geometry through a suitable combination of elementary building-blocks as shown in [23] and [24].

In this chapter, by exploiting the best features of both approaches, an innovative *UWB* antenna synthesis method is carefully described and analyzed. In order to design *UWB* antennas that meet the user needs, both the simplicity in describing some geometrical characteristics (e.g., the feedline extension, the groundplane, and substrate dimensions) of the parametric approach and the flexibility of a mother structure-based method are necessary to allow a fast and effective synthesis procedure. Moreover, there is the need to integrate the synthesis technique with an analysis method aimed at evaluating not only the impedance bandwidth and radiation properties but also taking into account the effects of the propagation channel on the *UWB* system. Towards this end, both the transmitting antenna and the receiving one are considered to simulate the whole system.

3.1 Spline-shaped Antenna Synthesis

The UWB antenna synthesis problem is formulated in terms of an optimization problem where a set of unknown representative descriptors are tuned through an iterative process aimed at fitting suitable requirements/constraints on the electrical behavior in the *UWB* bandwidth [12][13]. Towards this end, a spline-based [25] shape generator and a *PSO* procedure [8] are used to define the convergent succession of trial solutions. By using a set of “control points” and geometrical descriptors to code the antenna shape representation, a set of trial geometries is evaluated at each iteration and updated through the *PSO* strategy until a suitable matching between estimated and required specifications is obtained. As far as the electrical behavior of each trial shape is concerned, a *MoM*-based [26] electromagnetic simulator, developed at the *ELectromagnetic DIAgnostic* Laboratory (ELEDIA) of the University of Trento and implemented following the guidelines in [27] and [28], is used to simulate both the transmitting antenna and the receiving one (assumed of identical shapes) as well as the propagation channel.

The first issue, addressed in dealing with *UWB* antenna synthesis, is concerned with a suitable and flexible representation of the antenna shape. To this end, there is the need to provide an antenna geometry generator (*AGG*) able to model a wide set of planar patch structures as a function of a small number of optimization variables. Accordingly, a combination of “parametric” descriptors and spline curves [25] (assumed as “building blocks”) seems to be a good solution. In particular, some antenna features are expressed in terms of the values of geometrical parameters in fixed ranges. In particular, the feedline is assumed of rectangular shape as well as both the groundplane and the substrate (Fig. 3.1). Those parts are fully determined by fixing their extensions (i.e., their lengths and widths). The description of the antenna geometry is completed by a spline-based representation aimed at coding complex contours by means of a limited set of control points.

By assuming a symmetry with respect to the $y-z$ plane, only one half of the physical structure of the antenna has to be modeled. Let

$$\{\varphi_l; l = 1, \dots, L; L = 4\} \quad (3.1)$$

be the set of parametric descriptors. More specifically, φ_1 is the substrate length, φ_2 is one half of the substrate width, φ_3 is one half of the feed-line width, and φ_4 is the length of the groundplane. Moreover, $\varphi_l^{(min)} \leq \varphi_l \leq \varphi_l^{(max)}$, $\varphi_l^{(min)}$ and $\varphi_l^{(max)}$ being fixed constants that define the range of admissible variation of the l -th descriptor.

As for the remaining part of the antenna geometry, the spline curve used to model the patch contour is a cubic B-spline curve whose shape is determined by the positions of a set of N control points $P_n = (x_n, y_n)$, $n = 1, \dots, N$. Consequently, the patch perimeter turns out to be smooth since its second derivative is

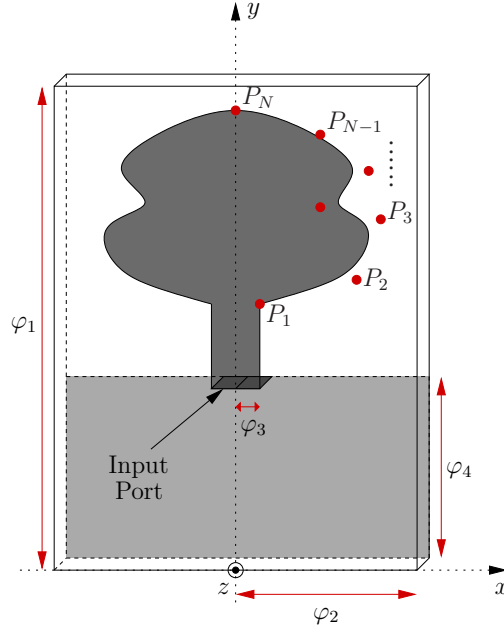


Figure 3.1: Descriptive parameters of the spline-based antenna representation.

continuous whereas its third derivative is piecewise continuous. Mathematically, such a curve can be described as a function $\Delta(t) = \{x(t), y(t)\}$ of the curvilinear coordinate t . More in detail, $\Delta(t)$ is constituted by N curve segments δ_n ; $n = 1, \dots, N$ such that

$$\Delta(t) = \sum_{n=1}^N \delta_n(t-n). \quad (3.2)$$

By definition, the curve segments have a compact support domain. In particular, the generic segment $\delta_n(t-n)$ is nonzero only for $(t-n) \in [0, 1]$, so that $\Delta(t) = \delta_n(t-n)$ when $n \leq t \leq n+1$. Moreover, by defining $\tau = t-n$, each curve segment $c_n(\tau)$ is a linear combination

$$c_n(\tau) = P_{n-1}Q_0(\tau) + P_nQ_1(\tau) + P_{n+1}Q_2(\tau) + P_{n+2}Q_3(\tau) \quad (3.3)$$

of four cubic polynomials $Q_0(\tau)$, $Q_1(\tau)$, $Q_2(\tau)$, and $Q_3(\tau)$ defined as

$$\begin{aligned} Q_0(\tau) &= \frac{1}{6}(1-\tau)^3 \\ Q_1(\tau) &= \frac{1}{2}\tau^3 - \tau^2 + \frac{2}{3} \\ Q_2(\tau) &= -\frac{1}{2}\tau^3 + \frac{1}{2}\tau^2 + \frac{1}{2}\tau + \frac{1}{6} \\ Q_3(\tau) &= \frac{1}{6}\tau^3 \end{aligned} \quad (3.4)$$

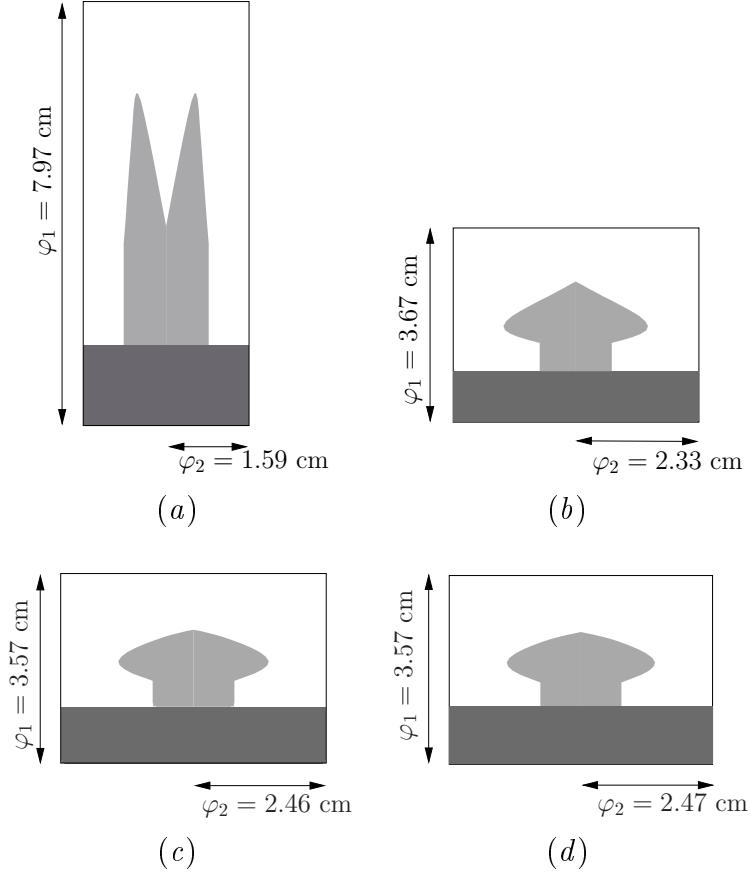


Figure 3.2: *Optimization Process Analysis* - Evolution of the antenna shape: (a) $k = 0$, (b) $k = 10$, (c) $k = 19$, and (d) $k = k_{conv} = 28$.

in the domain $\tau \in [0, 1]$. Moreover, the constraints $P_1 = P_2$ and $P_{N+2} = P_{N+1} = P_N$ are imposed. In order to avoid the generation of unrealistic structures, the following constraints are imposed, as well: $x_1 = \varphi_3$ and $x_N = 0$.

According to such a representation, a trial antenna shape A is the result of the application of the operator AGG

$$A = AGG(\underline{\xi}) \quad (3.5)$$

where

$$\begin{aligned} \underline{\xi} &= \{(x_n, y_n), n = 1, \dots, N; \varphi_l; l = 1, \dots, L\} \\ &= \{\xi_j, j = 1, \dots, J; J = 2 \times N + L\} \end{aligned} \quad (3.6)$$

codes the set of variables, to be optimized to fulfill the *UWB* project requirements, which unequivocally identifies the corresponding geometrical model of A .

3.1. SPLINE-SHAPED ANTENNA SYNTHESIS

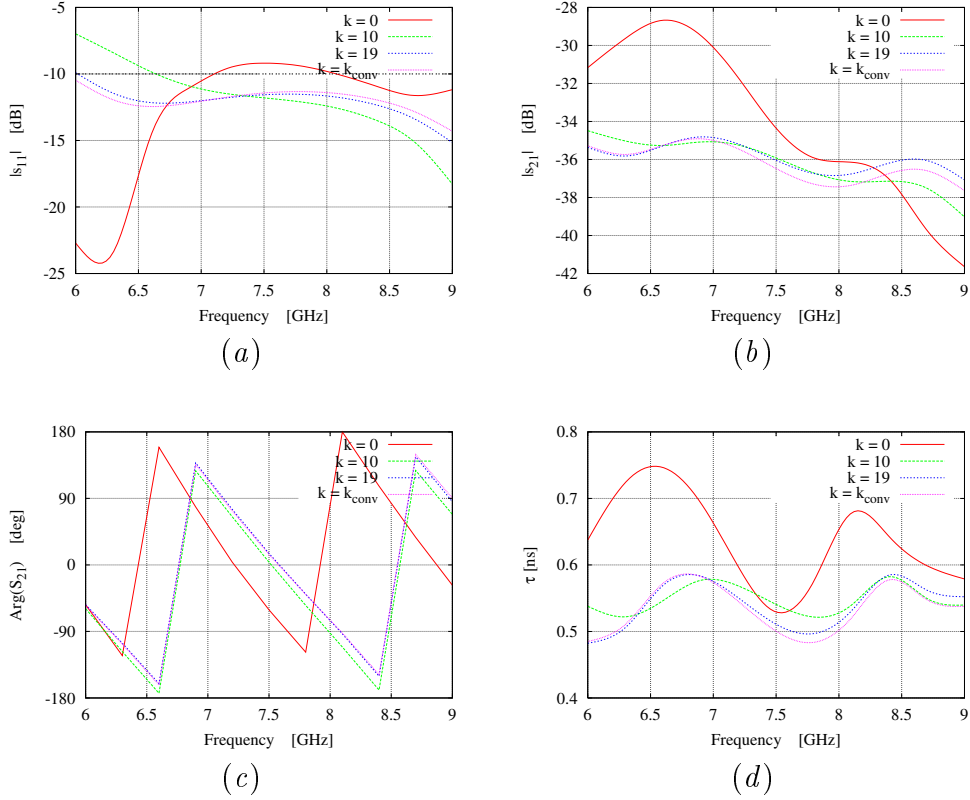


Figure 3.3: *Optimization Process Analysis* - Plot of (a) $|s_{11}|$, (b) $|s_{21}|$, (c) $\angle s_{21}$, and (d) τ versus the frequency at different iterations of the optimization process.

The second step to be faced consists in identifying a fast and reliable numerical procedure to evaluate the electric behavior of each trial shape. Because of the very large frequency band of operation of *UWB* systems and the transmission/reception of short time pulses, a natural approach would consider a time-domain description. However, from an experimental point-of-view, a frequency domain analysis could be preferable because of the higher achievable measurement accuracy [29]. Taking into account these considerations, a time domain representation is initially adopted to define the requirements of the transmitting-receiving antenna system. Then, these requirements are "translated" in the frequency domain using the scattering parameters representation to deal with physical quantities experimentally-detectable in a straightforward and accurate way. In order to have a distortionless behavior, the frequency domain transfer function H (i.e. the ratio between the voltages at the input and the output ports of the Tx/Rx antenna system) should satisfy the following constraints: (a) flat amplitude response and (b) phase response with a linear dependence on the frequency or, analogously, constant group delay.

Once an effective method to characterize a trial shape of the *UWB* antenna is available, there is the need to define an evolution strategy able to guide the synthesis process to a final design that fully satisfies the project guidelines and constraints defined by the user. To this end, let us reformulate the synthesis problem as an optimization one where a suitable cost function $\Omega(A)$ is minimized according to a *PSO*-based strategy

$$\hat{A} = \arg \min_A \{\Omega(A)\} \quad (3.7)$$

to determine the final shape $\hat{A} = AGG(\hat{\xi})$ of the *UWB* antenna.

In general, evolutionary algorithms use the concept of “fitness” to represent how well a particular solution comply with the design objective. The degree of fitness to the problem at hand of each trial solution is equal to the corresponding value of the cost function. Since the design objective is to synthesize a *UWB* system characterized by good impedance matching conditions and by distortionless properties, the cost function Ω is accordingly defined.

Let f_1 and f_2 be the lowest and highest frequency of the band of interest, respectively. As far as the impedance matching is concerned, the following constraint is imposed

$$|s_{11}(f)| \leq |s_{11}^{(d)}(f)| \quad f^{(min)} \leq f \leq f^{(max)} \quad (3.8)$$

where the superscript “ (d) ” denotes the target value of the design specification. Moreover, by assuming that (3.8) holds true and that $H \simeq s_{21}$, the conditions for a distortionless system can be reformulated in terms of: 1) a constraint on the magnitude of s_{21} [Condition (a) - Flat amplitude response]

$$\Delta |s_{21}| \leq \Delta^{(d)} |s_{21}| \quad (3.9)$$

where

$$\Delta |s_{21}| \triangleq \max_{f^{(min)} \leq f \leq f^{(max)}} \{|s_{21}(f)|\} - \min_{f^{(min)} \leq f \leq f^{(max)}} \{|s_{21}(f)|\} \quad (3.10)$$

and 2) another constraint on the group delay [Condition (b) - Constant group delay]

$$\Delta \tau \leq \Delta^{(d)} \tau \quad (3.11)$$

where

$$\Delta \tau = \max_{f^{(min)} \leq f \leq f^{(max)}} \{\tau(f)\} - \min_{f^{(min)} \leq f \leq f^{(max)}} \{\tau(f)\} \quad (3.12)$$

and

$$\tau(f) = -\frac{1}{2\pi} \frac{d}{df} \{\angle s_{21}(f)\}. \quad (3.13)$$

Starting from these conditions on the scattering parameters, the cost function, which maps the design specifications into a fitness index, is defined as follows

$$\begin{aligned}\Omega(A) &= \int_{f^{(min)}}^{f^{(max)}} \Omega_{11}(A) \mathcal{H}\{\Omega_{11}(A)\} \\ &+ \Omega_{21}(A) \mathcal{H}\{\Omega_{21}(A)\} \\ &+ \Omega_{GD}(A) \mathcal{H}\{\Omega_{GD}(A)\}\end{aligned}\quad (3.14)$$

where

$$\Omega_{11}(A) = \frac{|s_{11}(f)| - |s_{11}^{(d)}(f)|}{|s_{11}^{(d)}(f)|}\quad (3.15)$$

$$\Omega_{21}(A) = \frac{\Delta |s_{21}| - \Delta^{(d)} |s_{21}|}{\Delta^{(d)} |s_{21}|}\quad (3.16)$$

$$\Omega_{GD}(A) = \frac{\Delta\tau - \Delta^{(d)}\tau}{\Delta^{(d)}\tau}\quad (3.17)$$

\mathcal{H} being the Heaviside function

$$\mathcal{H}\{\Omega\} = \begin{cases} 1 & \Omega \geq 0 \\ 0 & \Omega < 0 \end{cases} .\quad (3.18)$$

3.2 Numerical and Experimental Validation

In this section, a selected set of numerical results from several experiments is reported to show the behavior of the synthesis method as well as to assess its reliability and efficiency in fitting the design requirements. More in detail, in Sect. 3.2.1 the optimization process is carefully analysed, while in Sects. 3.2.2 and 3.2.3 two design examples regarding an UWB antenna for wireless dongle device and an antenna compliant with the FCC released frequency range are reported, respectively. Finally, in Sect. 3.2.4, the design of an UWB antenna with rejection properties in the WLAN frequency range is reported as a preliminary assessment on the use of the proposed method for the synthesis of band-notched UWB antennas. Towards this end, the antenna geometry as well as the project requirements used in the synthesis process are accordingly modified.

For the experimental validation, several antenna prototypes have been built according to the results from the numerical simulations by means of a photolithographic printing circuit technology and considering an Arlon substrate ($\varepsilon_r = 3.38$) of thickness 0.78 mm as dielectric support. Concerning the measurements, each prototype has been fed with a coaxial line, equipped with a *SMA* connector,

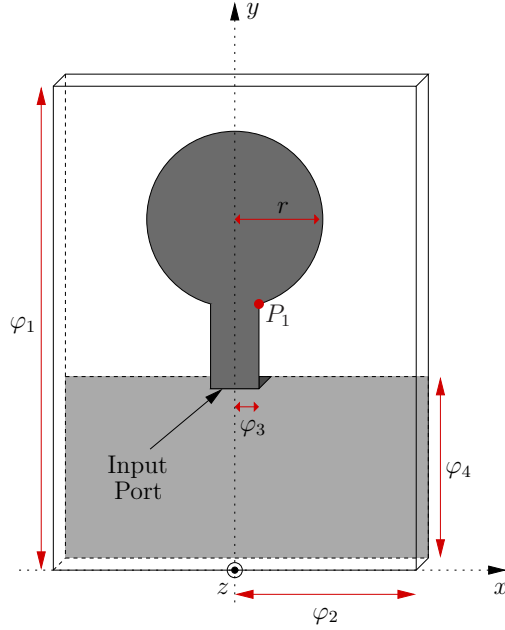


Figure 3.4: *Optimization Process Analysis - Parametric approach* - Descriptive parameters for the circular monopole reference geometry.

connected at the input port (Fig. 3.1). Moreover, a Vector Network Analyzer has been used to collect the data in a non-controlled environment and the measurements of the parameter s_{21} have been performed by considering a distance of $d = 15 \text{ cm}$ between two identical (Tx/Rx) antenna prototypes [30]. Because of the operating frequencies of UWB systems and the dimensions of the prototypes, the antennas can be reasonably considered in the far field region of each other.

Whatever the test case or experiment, if it is not specified, the project constraints have been fixed to $|s_{11}^{(d)}(f)| = -10 \text{ dB}$, $\Delta^{(d)}|s_{21}(f)| = 6 \text{ dB}$, and $\Delta^{(d)}\tau = 1 \text{ nsec}$ to guarantee suitable performances of the synthesized *UWB* antenna systems. As for the stochastic optimizer, a population of $R = 7$ particles has been used and the convergence threshold has been fixed to $\eta_{conv} = 10^{-3}$ with the maximum number of iterations equal to $K = 400$. Moreover, the values of the *PSO* control parameters have been fixed to $C_1 = C_2 = 2.0$ and $w = 0.4$. They have been selected according to the suggestions given in the reference literature where they have been found to provide good performance. For a more detailed study of convergence characteristics in correspondence with different values of these parameters, please refer to [31].

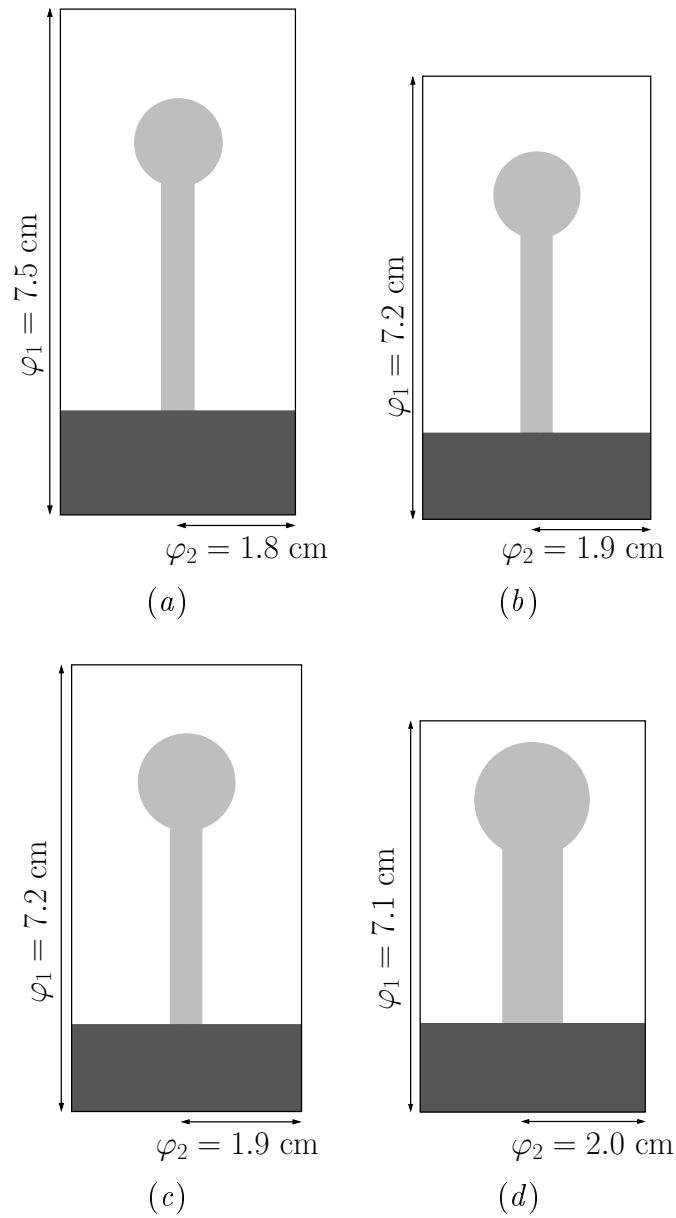


Figure 3.5: *Optimization Process Analysis - Parametric Approach* - Evolution of the antenna shape: (a) $k = 0$, (b) $k = 100$, (c) $k = 300$, and (d) $k = K = 400$.

3.2.1 Optimization Process Analysis

The first test case is about the synthesis of an *UWB* antenna operating in the range $f^{(min)} = 6\text{GHz}$ - $f^{(max)} = 9\text{GHz}$ and compliant with the guidelines of the Electronic Communications Committee (ECC) [13]. Such an experiment is aimed at analyzing the behavior of the optimization process both in terms of convergence and evolution of the antenna shape. Starting from a randomly generated perimeter [$k = 0$ - Fig. 3.2(a)] characterized by $N = 4$ control points, which does not fit at all the design objectives (Fig. 3.3) as confirmed by the value of the cost function Ω (i.e., $\Omega [AGG(\underline{\zeta}^{(0)})] \cong 5$), the trial solution improves until the convergence configuration [Fig. 3.2(d)] is found. In order to point out the main advantages of the proposed spline-based method over a parametric optimization approach, the same problem (in terms of user requirements) has been addressed by considering the reference circular geometry shown in Fig. 3.4. The same PSO algorithm has been used to modify the unknown parameters $\underline{\xi} = \{(x_1, y_1); r; \varphi_l, l = 1, \dots, 4\}$. Figure 3.5 and Figure 3.6 show the evolution of the trial geometry and the corresponding scattering values during the optimization process, respectively. As it can be noticed, although the maximum number of iterations ($k = K$) has been performed, the convergence solution does not fit the whole set of project requirements ($|\Delta |s_{21}(f)| > 6\text{dB}$). Concerning the computational issues, the plot of the cost function in correspondence with the parametric approach is compared in Fig. 3.7 with that of the proposed approach. Besides the wider set of possible solutions, the spline-based technique turns out to be more efficient in sampling the solution space since a better solution is reached in just $k_{conv} = 28$ iterations.

Let us now analyze the dependence of the iterative process on the dimension of the solution space. Since the generation of the spline geometry strictly depends on the number of control points that also defines the dimension of the solution space, some simulations have been performed by varying N . As a general rule, a small number of control points would decrease the dimension of the solution space allowing a faster search, but at the cost of a reduced capacity of representing complex contours. On the contrary, a larger number of control points would allow the description of a wider set of geometries and of more complex antenna shapes, even though with a higher computational burden and the need to enlarge the dimension of the swarm to fully exploit the additional degrees of freedom. In order to better understand the behavior of the optimization in correspondence with different values of N , let us consider the following quality indexes

$$F_{11} = \frac{1}{\Delta f} \int_{f^{(min)}}^{f^{(max)}} |\widehat{s}_{11}(f)| df \quad (3.19)$$

$$F_{21} = \frac{1}{\Delta f} \int_{f^{(min)}}^{f^{(max)}} \left\{ \frac{|\widehat{s}_{21}(f)| - |s_{21}(f)|}{|\widehat{s}_{21}(f)|} \right\} df \quad (3.20)$$

3.2. NUMERICAL AND EXPERIMENTAL VALIDATION

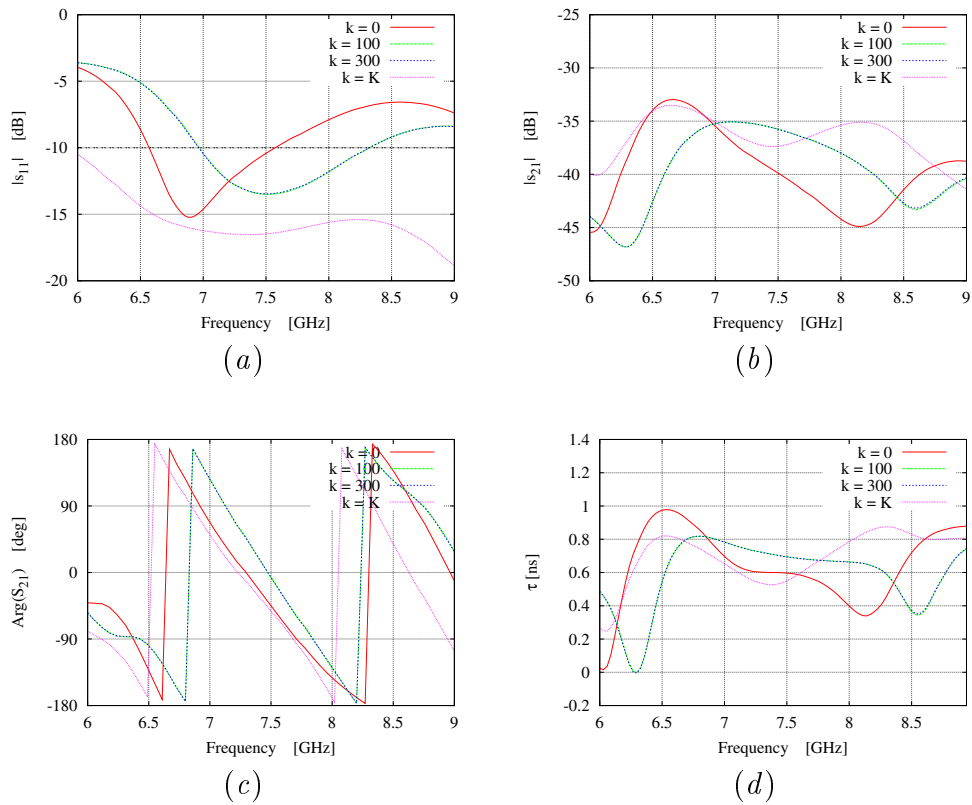


Figure 3.6: *Optimization Process Analysis - Parametric Approach* - Plot of (a) $|s_{11}|$, (b) $|s_{21}|$, (c) $\angle s_{21}$, and (d) τ versus the frequency at different iterations of the optimization process.

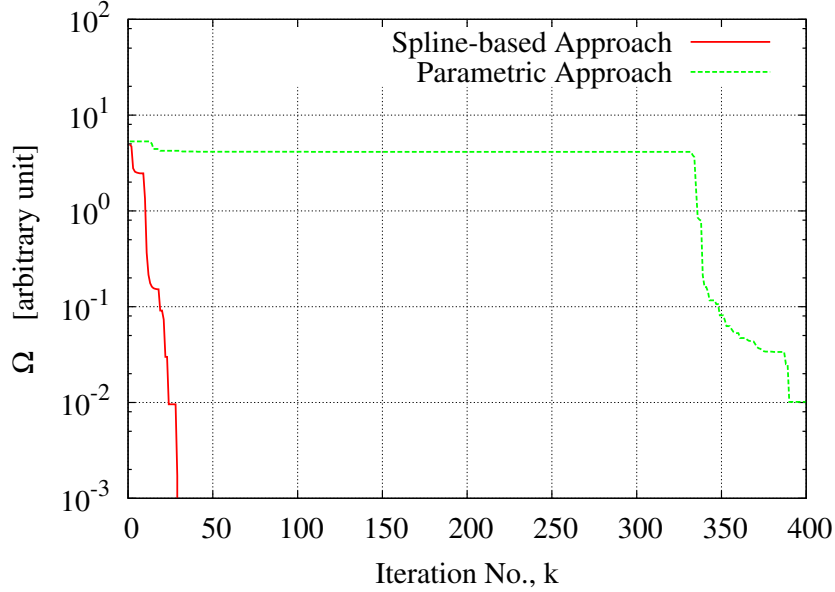


Figure 3.7: *Optimization Process Analysis* - Comparison between parametric approach and spline-based approach - Plot of the optimal value of the cost function Ω and corresponding terms versus the iteration number k .

$$F_{GD} = \frac{1}{\Delta f} \int_{f^{(min)}}^{f^{(max)}} \left\{ \frac{|\widehat{\tau}(f)| - \overline{|\tau(f)|}}{|\widehat{\tau}(f)|} \right\} df \quad (3.21)$$

where the superscript “ $\overline{}$ ” indicates the mean value, over the frequency band $\Delta f = f^{(max)} - f^{(min)}$, of the scattering parameters at the convergence [$\widehat{s}_{ij} = s_{ij}(\widehat{A})$]. Figure 3.8 shows the values of the quality indexes versus N as well as the plot of k_{conv} . As expected, the number of iterations needed to find a convergence solution increases with N since the solution space becomes larger. However, the quality indexes do not proportionally improve and the optimal trade-off between computational costs and solution efficiency turns out to be at $N = 7$ control points. In the following, this value will be assumed as reference.

3.2.2 UWB Antenna for Wireless Dongle Devices

The second test case deals with the synthesis of a planar *UWB* antenna that operates in the frequency range $3\text{GHz} \leq f \leq 5\text{GHz}$ and to be integrated in wireless USB dongle devices. The values of the antenna descriptors obtained by the *PSO*-based optimization procedure are given in Tab. 3.1 and the prototype of the antenna is shown in Fig. 3.9. The antenna has a miniaturized planar

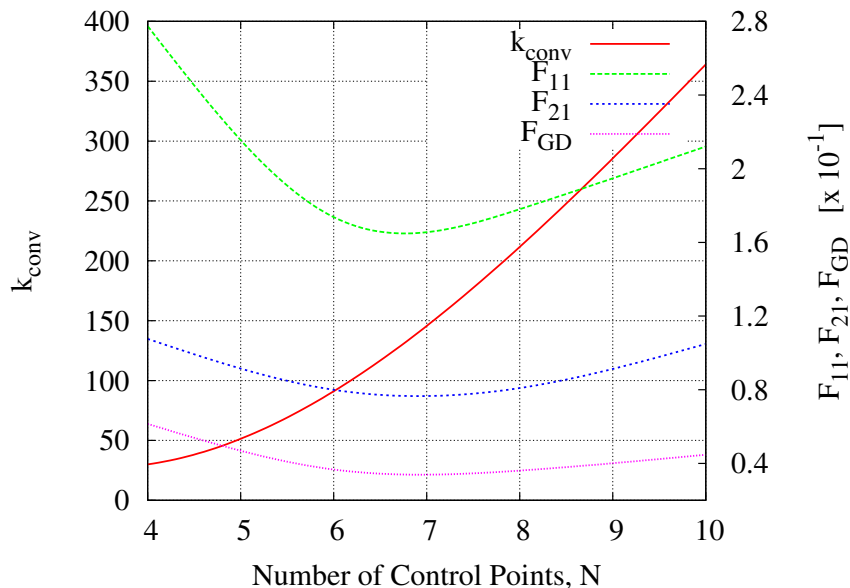


Figure 3.8: *Optimization Process Analysis* - Behavior of the quality indexes F_{11} , F_{21} , F_{GD} and of k_{conv} versus the number of control points N .

structure of maximum extension equal to $39.2 \times 19.2 \text{ mm}^2$ because of the presence of the ground plane shown in Figure 3.9(b). However, it should be noticed that such a ground plane is common to the ground plane of the dongle PCB. Therefore, the part of the dongle device only concerned with the radiator turns out to be limited to an area of $16.2 \times 19.2 \text{ mm}^2$.

In order to experimentally test the reliability and efficiency of the synthesized radiator in an UWB communication system, a pair of antenna prototypes has been built. Moreover, the receiving and transmitting antennas have been connected to 50Ω rigid coaxial cables equipped with SMA connectors. More in detail, each input coaxial cable has been placed orthogonally to the dielectric substrate (i.e., to the planar structure of the antenna) and soldered across the gap between the input section of the antenna (with width $2\varphi_3$) and the ground plane. This arrangement has been verified to be suitable to minimize the coupling effects with the antenna and also the contributions to the pattern of the cable radiation. The measurements have been performed with a vector network analyzer in a real environment (i.e., a non-controlled measurement scenario).

As shown in Fig. 3.10, both measured and simulated values of the $|s_{11}|$ parameter turn out to be compliant with the project constraints. The differences between the two plots are due to different causes: (a) the reflection contributions added by the non-controlled measurement environment, (b) the non-uniform val-

UWB Dongle Antenna							
Control Points Coordinates [mm]							
x_1	y_1	x_2	y_2	x_3	y_3	x_4	y_4
2.1	25.0	6.6	29.5	8.6	29.4	7.3	35.9
x_5		y_5	x_6	y_6	x_7	y_7	
6.9		34.9	2.2	32.4	0.0	33.8	
Geometric Variables [mm]							
φ_1		φ_2		φ_3		φ_4	
39.2		9.6		2.1		23.0	

Table 3.1: *UWB Dongle Antenna* - Geometric descriptors of the synthesized antenna.

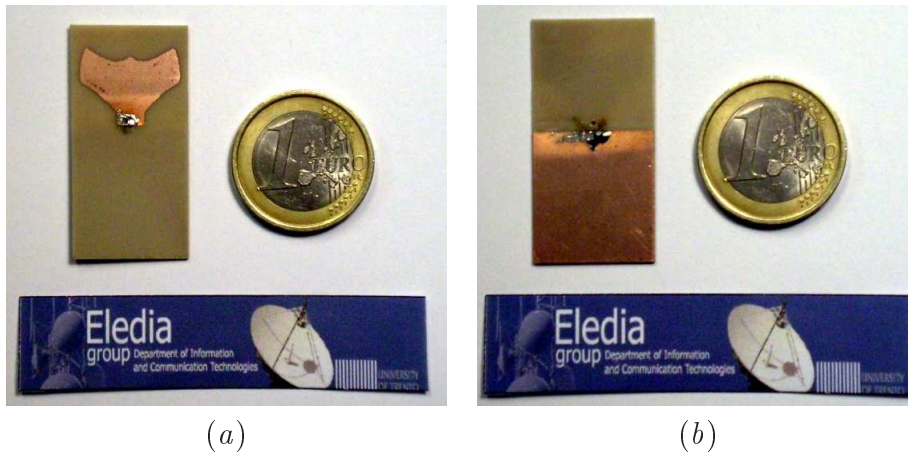


Figure 3.9: *UWB Dongle Antenna* - (a) Front view and (b) back view of the antenna prototype.

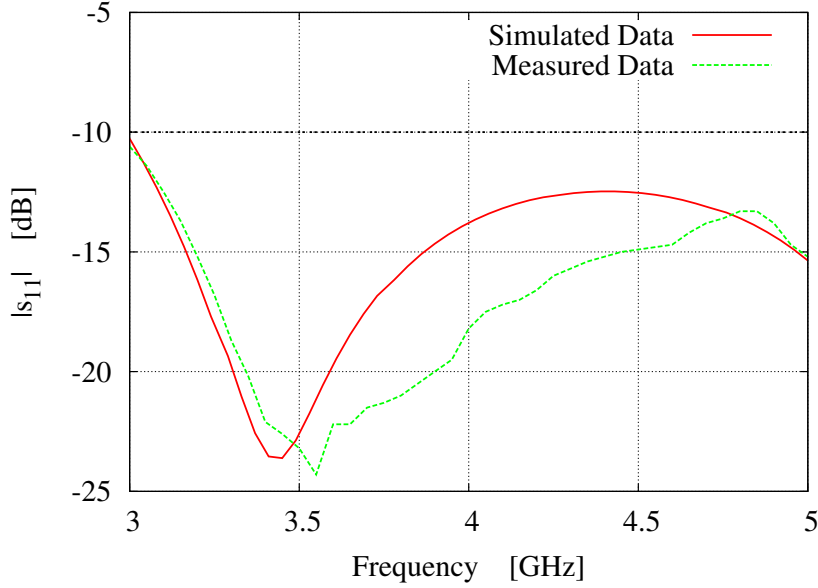


Figure 3.10: *UWB Dongle Antenna* - Amplitude of s_{11} vs. frequency.

ues of the dielectric properties of the substrate in the UWB bandwidth. Concerning the s_{21} parameter, Figure 3.11 shows the plots of experimental and numerical values of the amplitude, $|s_{21}|$. As expected, the maximum variations of the amplitudes of the mutual scattering coefficient lie within the specifications (i.e., $\Delta |s_{21}|_{sim} = 5 \text{ dB}$, $\Delta |s_{21}|_{meas} = 6 \text{ dB}$). For completeness, Figure 3.12 pictorially describes the behavior of the group delay $\tau_g(f)$ in the working band. As it can be observed, the project requirements are satisfied since $\Delta |\tau_g|_{sim} = 0.1 \text{ nsec}$ and $\Delta |\tau_g|_{meas} = 0.5 \text{ nsec}$ and there is an acceptable matching between numerical and experimental results. However, some discrepancies can be observed because of both reflection contributions in the measurement site and the dispersive behavior of the dielectric substrate.

As far as the radiation properties of the UWB antenna are concerned, Figure 3.13 shows the normalized horizontal radiation patterns in correspondence with three different representative frequency values within the band of operation ($f_1 = 3.0 \text{ GHz}$, $f_2 = 4.0 \text{ GHz}$, and $f_3 = 5.0 \text{ GHz}$). The radiation properties of the antenna have been experimentally evaluated, as well. Figure 3.14 shows the normalized measured horizontal radiation pattern. Whatever the operating frequency, the antenna presents an omnidirectional behavior. For completeness, Figures 3.15, 3.16, 3.17 and 3.18 give the normalized simulated and measured vertical patterns at two orthogonal sections (i.e., $\phi = 0^\circ$ and $\phi = 90^\circ$). From these plots, a monopole-like behavior can be inferred. Such a conclusion further confirm the reliability and suitability of the designed antenna for mobile-like

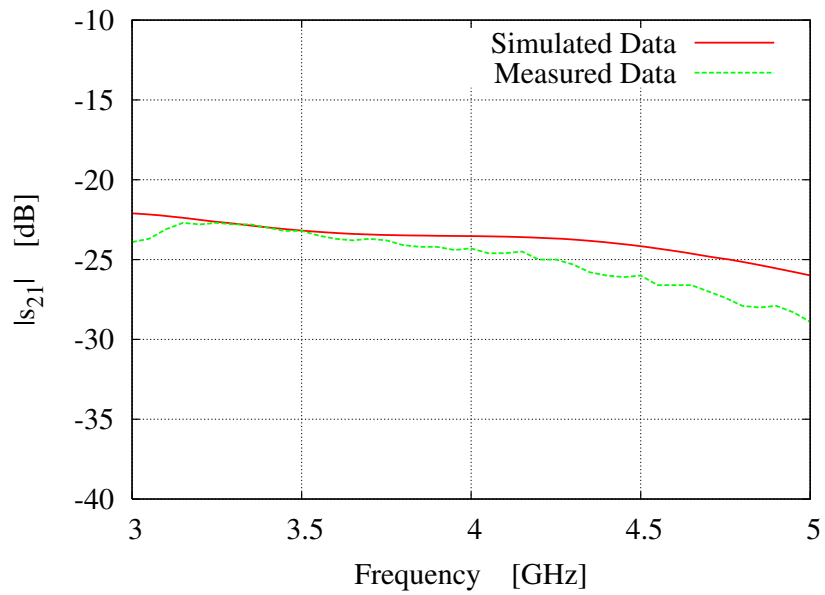


Figure 3.11: *UWB Dongle Antenna* - Amplitude of s_{21} vs. frequency.

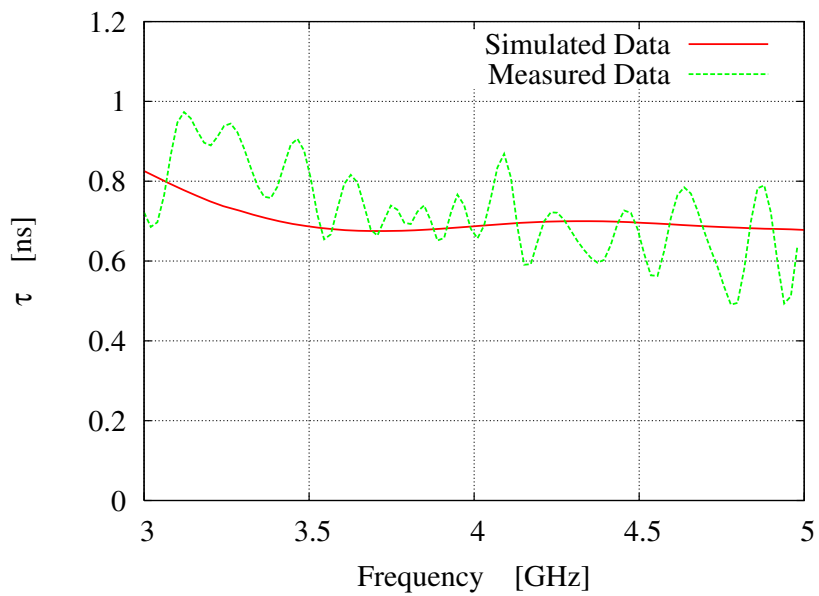


Figure 3.12: *UWB Dongle Antenna* - Group delay τ_g vs. frequency.

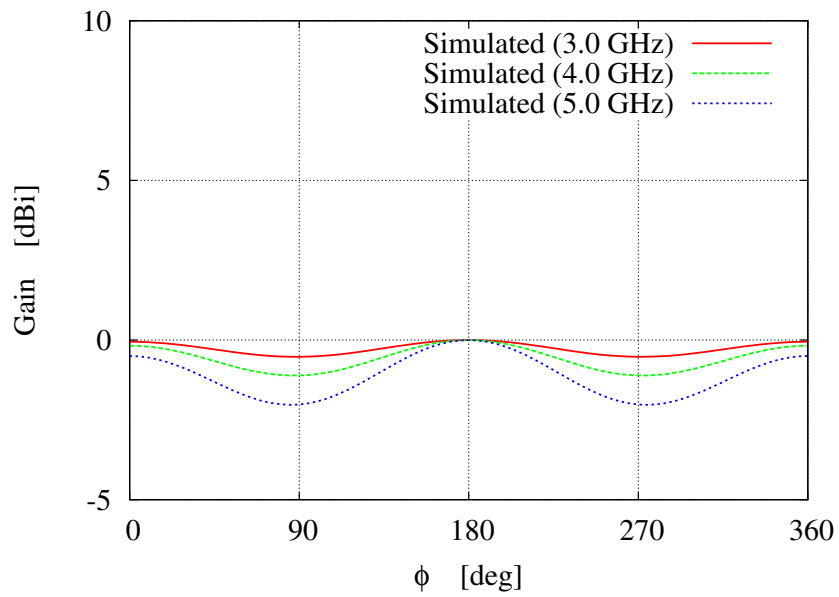


Figure 3.13: *UWB Dongle Antenna* - Simulated H-plane radiation pattern.

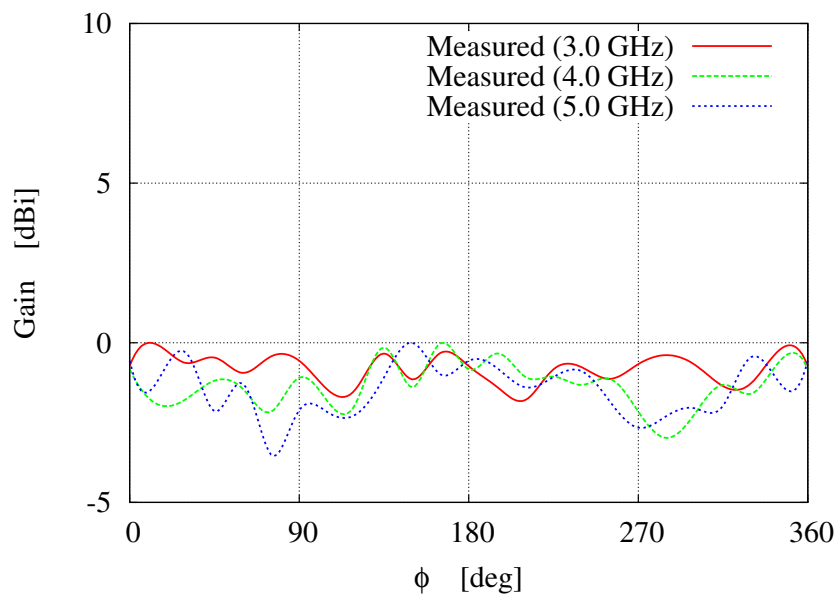


Figure 3.14: *UWB Dongle Antenna* - Measured H-plane radiation pattern.

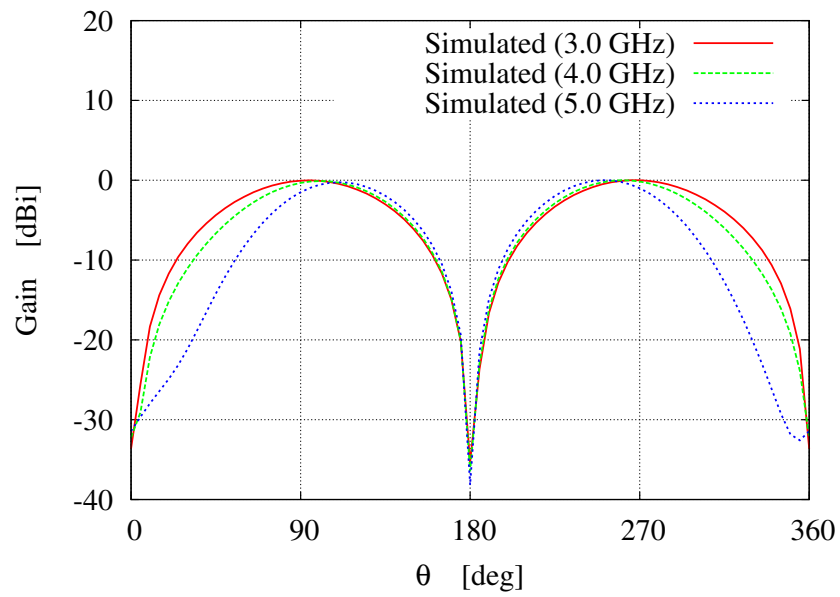


Figure 3.15: *UWB Dongle Antenna* - Simulated E-plane radiation pattern ($\phi = 0^\circ$).

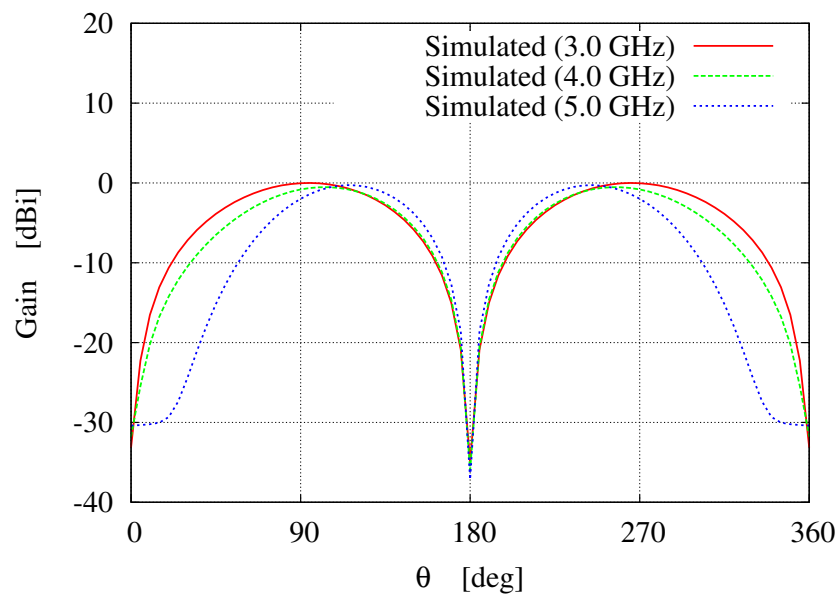


Figure 3.16: *UWB Dongle Antenna* - Simulated E-plane radiation pattern ($\phi = 90^\circ$).

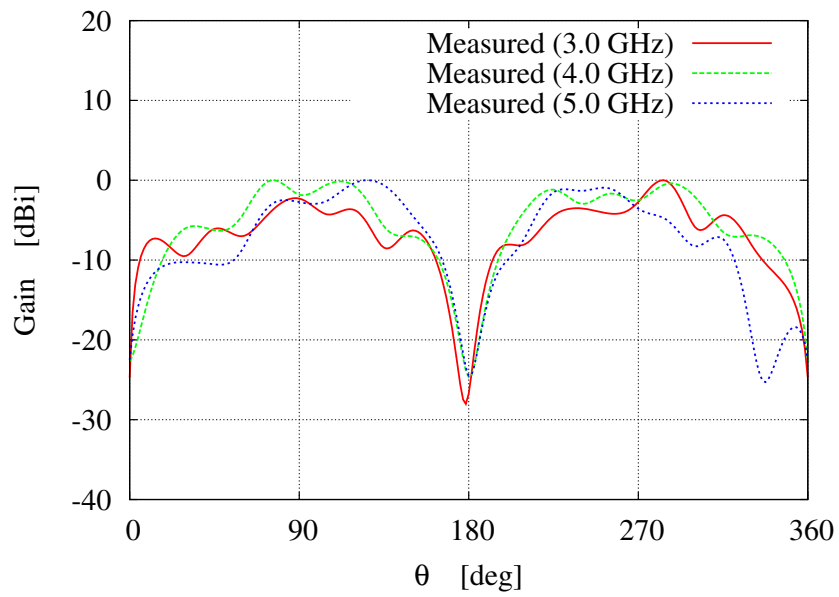


Figure 3.17: *UWB Dongle Antenna* - Measured E-plane radiation pattern ($\phi = 0^\circ$).

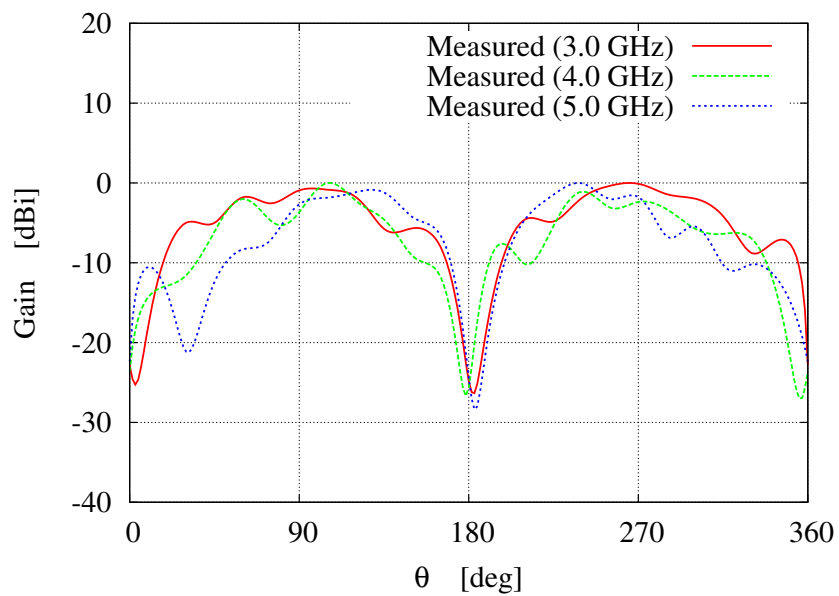


Figure 3.18: *UWB Dongle Antenna* - Measured E-plane radiation pattern ($\phi = 90^\circ$).

FCC Compliant Antenna							
Control Points Coordinates [mm]							
x_1	y_1	x_2	y_2	x_3	y_3	x_4	y_4
4.8	19.1	6.9	22.0	8.0	25.6	5.1	35.4
x_5		y_5	x_6	y_6	x_7	y_7	
5.2		26.1	4.3	23.4	0.0	23.9	
Geometric Variables [mm]							
φ_1		φ_2		φ_3		φ_4	
40.4		12.1		4.8		14.5	

Table 3.2: *FCC Compliant Antenna* - Geometric descriptors of the synthesized antenna.

wireless dongle applications.

3.2.3 FCC Compliant UWB Antenna

The next example is concerned with a more challenging problem where a wider frequency band is required (i.e., $\Delta f = 5 \text{ GHz}$, $f^{(min)} = 4 \text{ GHz}$ $f^{(max)} = 9 \text{ GHz}$). The descriptive parameters of the synthesized antenna are summarized in Tab. 3.2. The plots of numerical and measured values of the amplitude of s_{11} are reported in Figure 3.19.

As it can be noticed, besides a good agreement between measurements and simulations, the synthesized solution fits the impedance matching requirements. In Figures 3.20 and 3.21, the comparison is concerned with the s_{21} parameter. As expected (from the simulations), the range of variation in the operating frequency band does not exceed 6 dB (see Fig. 3.20). Moreover, both simulated and experimental values shown in Figure 3.21 assess the linear behavior of the phase of s_{21} . Because of the relationship between the s_{21} phase and the group delay, such a phase trend implies a maximum variation of the group delay equal to 0.18 nsec .

Finally, the compliance of the radiation properties of the synthesized antenna can be verified in Figures 3.22-3.24, where the plots of the radiation patterns in the horizontal plane (see Fig. 3.22) and along two representative vertical planes (Figs. 3.23 and 3.24) are shown.

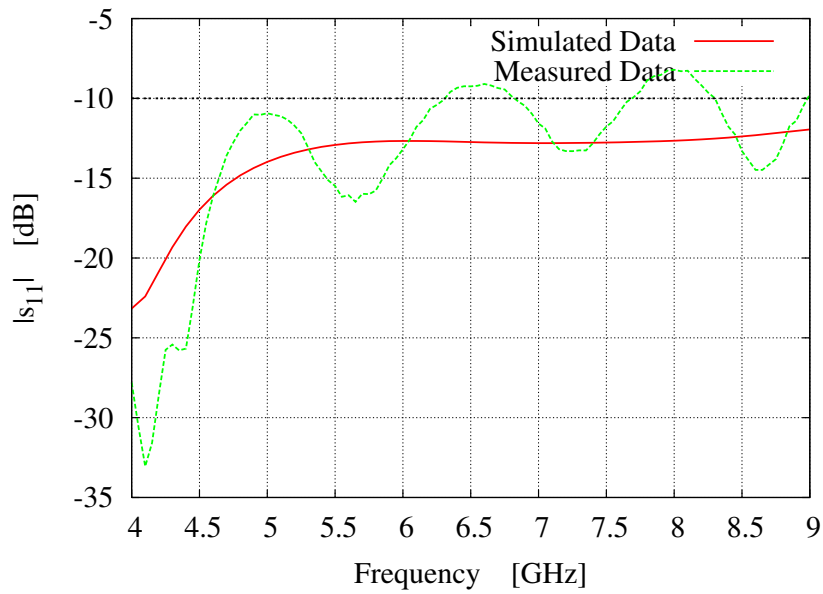


Figure 3.19: *FCC Compliant Antenna* - Comparison between simulated and measured s_{11} amplitude values.

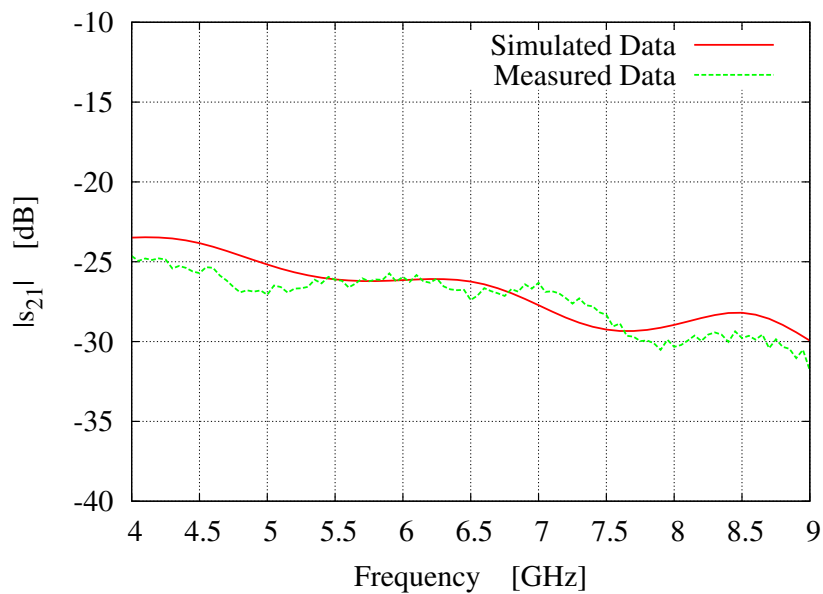


Figure 3.20: *FCC Compliant Antenna* - Comparison between simulated and measured s_{21} amplitude values.

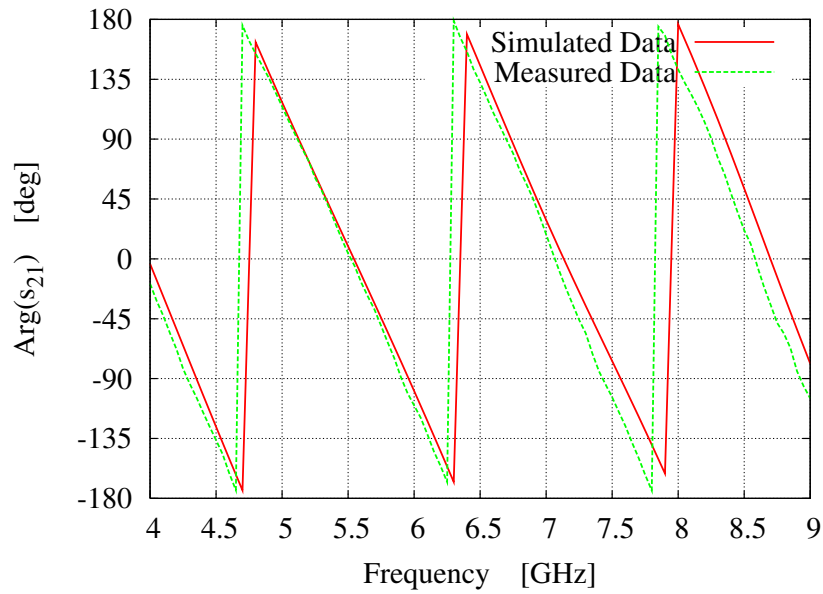


Figure 3.21: *FCC Compliant Antenna* - Comparison between simulated and measured s_{21} amplitude values.

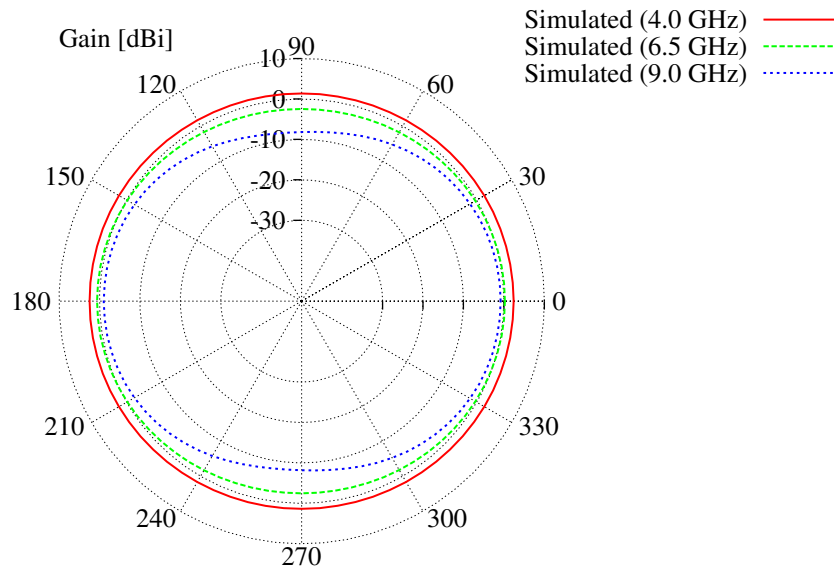


Figure 3.22: *FCC Compliant Antenna* - Radiation patterns in the horizontal plane.

3.2. NUMERICAL AND EXPERIMENTAL VALIDATION

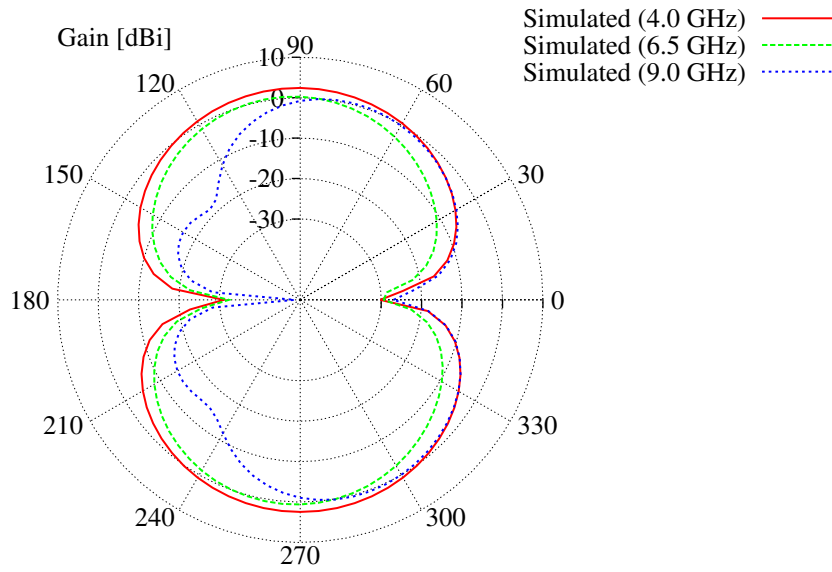


Figure 3.23: *FCC Compliant Antenna* - Radiation patterns in the $\phi = 0^\circ$ vertical plane.

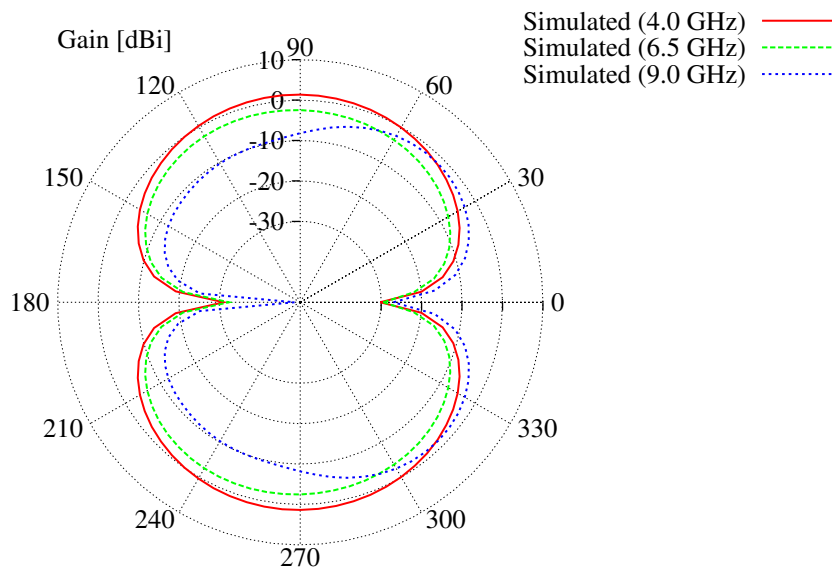


Figure 3.24: *FCC Compliant Antenna* - Radiation patterns in the $\phi = 90^\circ$ vertical plane.

3.2.4 UWB Antenna with WLAN-band Notched Characteristics

In the last years, a great attention has been paid to the topic of home networking defined as the availability of wireless links among different and heterogeneous electronic and multimedia devices (HDTVs, DVDs, cameras, personal computers, etc.) for communications, entertainment, home automation and monitoring. Such a paradigm is usually accomplished by setting Wireless Personal Area Networks (WPANs). According to the IEEE 802.15.3a recommendation aimed at defining the WPAN standards, extremely high transmission rates over very short distances are taken into account. Towards this end, a core technology is certainly the Ultra-Wideband (UWB) technology [32].

However, despite suitable regulations from the agencies of the different countries (e.g., the Federal Communication Commission - FCC [12]), there are still some concerns about the interferences among UWB systems and other devices that operate with different standards as those exploiting the range of frequencies from 5.15 up to 5.35 *GHz* [33]. Such a range of frequency is occupied by the first two sub-bands of the Unlicensed National Information Infrastructure (UNII) band. Such sub-bands, called UNII1 and UNII2, range from 5.15 to 5.25 *GHz* and from 5.25 to 5.35 *GHz*, respectively, corresponding to a portion of the so-called WLAN band.

In order to prevent/avoid such problems, UWB antennas with notched characteristics in the WLAN band are usually adopted. In [34] this task has been accomplished by introducing a fractal tuning stub in a microstrip slot antenna, while the same behavior has been obtained in [35] by printing a half-wavelength parasitic element on the back side of the antenna substrate. A more complex design approach performs a genetic algorithm optimization [36] to improve the performances of band-notched planar monopoles in terms of both impedance matching and radiation characteristics. Other solutions usually consider slot structures with different shapes within the antenna body [37][33][38][39][40][41] to realize compact systems. Such an approach is the most commonly adopted, but it usually requires two separated design steps. The first step is aimed at obtaining a reference antenna which exhibits a UWB behavior, while in the second one the slot structure is added and its geometrical parameters are tuned to obtain the notched behavior in the desired frequency range.

This last example regards the synthesis of an UWB antenna working within the FCC released frequency spectrum and showing a frequency notched behavior within the two UNII1 and UNII2 sub-bands of the WLAN band. The rejection band is yielded by means of a rectangular slot located on the front of the antenna geometry, while the UWB behavior is obtained by defining the contour of the radiating part of the antenna with a spline curve. The use of a rectangular slot allows an easier fabrication with respect to solution based on circular shapes as the one presented in [33]. Moreover, the dimensions of the antenna turn out

to be smaller than those of other radiating elements having a rejection band in the same frequency range (e.g., [34]). Finally, differently from solutions such as the one reported in [35], the proposed antenna exhibits quite stable radiation patterns.

The optimization of both the slot and the UWB antenna geometric parameters is carried out simultaneously with a non-negligible saving of the time required for the synthesis. The effectiveness of a spline-based representation has been assessed in [43] and successively profitably exploited in designing UWB antennas for wireless communication applications [44][45]. Following the scheme presented in such works, the synthesis is here performed by means of a Particle Swarm Optimization (PSO) procedure. Unlike other optimization techniques, such as Genetic Algorithms (GAs), the PSO is based on the cooperation among the trial solutions and not on their competition. In general, one of the main advantages of PSO over GA is its algorithmic simplicity. As a matter of fact, GA considers three genetic operators and the best configuration among several options of implementation needs to be chosen, while PSO considers one simple operator which is the velocity updating. Moreover, manipulating the PSO calibration parameters is easier than evaluating the optimal values of the GA parameters among various operators. In addition, there exist many studies regarding the effects of PSO parameters that makes their selection even easier [8][46]. Finally, PSO allows a more significant level of control to prevent stagnation of the optimization process [47][48][49].

Differently from [43][44][45], the antenna is now required to exhibit not only a good impedance matching over a very large bandwidth, but also a frequency notched behavior. This requirement is taken into account by adding a term in the PSO cost function [50] to maximize the impedance mismatch within the UNII1 and UNII2 bands.

3.2.4.1 Band Notched Antenna Design

Figure 3.25 shows the geometry of the antenna described by means of the the spline-based representation presented in Sect. 3.1 and now suitably integrated to realize a frequency notched behavior. More specifically, a slot structure constituted by a symmetric rectangular shape whose geometric parameters are $\{b_1, \dots, b_4\}$ has been added. The antenna structure is then univocally identified by the following set of descriptors

$$\chi = \{P_n; n = 1, \dots, 8; a_i, b_i; i = 1, \dots, 4\}. \quad (3.22)$$

In order to determine the optimal set of the antenna descriptors, an iterative procedure has been used to fit the following constraints:

$$|s_{11}(f)| \leq s_{11}^{op} \quad f \in \{[3, 4.65] \cup [5.85, 10]\} \text{ GHz} \quad (3.23)$$

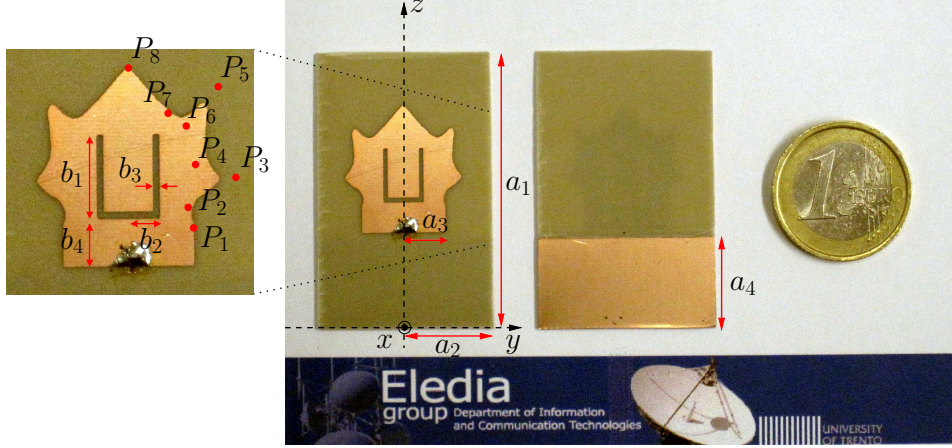


Figure 3.25: *Band Notched Antenna* - Antenna prototype and descriptive parameters.

$$|s_{11}(f)| \geq s_{11}^{fn} \quad f \in [5.15, 5.35] \text{ GHz}. \quad (3.24)$$

In (3.23) and (3.24), $s_{11}^{op} = -10 \text{ dB}$ and $s_{11}^{fn} = -5 \text{ dB}$ denote the target values at the operating frequency and within the notched bands, respectively. Moreover, the antenna is required to occupy a maximum area of $50 \times 50 \text{ mm}^2$ in order to be suitably integrated in modern communication devices.

The optimization procedure is based on the integration of a Particle Swarm Optimizer (PSO) [48][51][52][53][54], aimed at defining the strategy of evolution of the trial shapes of the antenna, and a standard electromagnetic simulator based on the Method-of-Moment (MoM) to compute the antenna electric parameters. The MoM is usually more appropriate than other methods such as the Finite Element Method (FEM) when planar geometries are considered since it is a surface discretization method [55].

More specifically, the optimization of (1) is carried out, according to the PSO logic, by minimizing a suitable cost function

$$\Psi(\chi) = \Psi_1(\chi) + \Psi_2(\chi) + \Psi_{notch}(\chi) \quad (3.25)$$

that quantifies the matching between the electric antenna performances and the project constraints. The terms $\Psi_1(\chi)$ and $\Psi_2(\chi)$ in (3.25) are related to the operating frequency ranges

$$\Psi_1(\chi) = \int_{3 \text{ GHz}}^{4.65 \text{ GHz}} \max \left\{ 0, \frac{|s_{11}(f)| - s_{11}^{op}}{s_{11}^{op}} \right\} \quad (3.26)$$

$$\Psi_2(\chi) = \int_{5.85 \text{ GHz}}^{10 \text{ GHz}} \max \left\{ 0, \frac{|s_{11}(f)| - s_{11}^{op}}{s_{11}^{op}} \right\} \quad (3.27)$$

Band Notched Antenna			
Control Point Coordinates [mm]			
P_1	P_2	P_3	P_4
(6.8, 20.3)	(6.2, 22.6)	(11.0, 25.0)	(7.2, 26.1)
P_5	P_6	P_7	P_8
(9.1, 34.9)	(6.0, 30.4)	(4.1, 32.2)	(0.0, 36.6)
Geometric Variables [mm]			
a_1	a_2	a_3	a_4
45.6	14.5	6.8	15.9
b_1	b_2	b_3	b_4
9.0	3.4	0.8	4.9

Table 3.3: *Band Notched Antenna* - Values of the geometric descriptors of the antenna prototype.

while $\Psi_{notch}(\chi)$ is concerned with the region where the stopband behavior is required

$$\Psi_{notch}(\chi) = \int_{5.15\text{ GHz}}^{5.35\text{ GHz}} \max \left\{ 0, \frac{s_{11}^{fn} - |s_{11}(f)|}{s_{11}^{fn}} \right\}. \quad (3.28)$$

As for the PSO strategy, a population of 6 particles has been used for the problem at hand and the position of each particle, which corresponds to a trial antenna configuration, has been randomly initialised within the range of physically admissible values. The positions of the particles of the swarm is iteratively updated on the basis of the corresponding values of the cost function (3.25) and the PSO control parameters: w (*inertial weight*), C_1 and C_2 (*acceleration coefficients*). In such a case-of-study, these latter have been set to $C_1 = C_2 = 2.0$ and $w = 0.4$ as suggested in [47][49]. The optimization procedure ends when a maximum number of K iterations (here $K = 500$) is reached or the value of the fitness function $\Psi(\chi)$ is smaller than a user-defined tolerance value η_Ψ (here $\eta_\Psi = 10^{-5}$).

The final outcome of the PSO-based optimization procedure when applied to the synthesis problem defined by (3.23) and (3.24) has been the shape described by the parameter set in Tab. 3.3. As it can be noticed, the synthesized antenna fits the size constraint occupying an area of $29.0 \times 45.6\text{ mm}^2$.

3.2.4.2 Antenna Performances

The performances of the synthesized antenna have been both numerically and experimentally assessed. Towards this aim, a prototype (Fig. 3.25) of the antenna has been built with an easy and low-cost photo-lithographic technology. The antenna has been printed on an Arlon dielectric substrate ($\epsilon_r = 3.38$) of 0.78 mm thickness. As for the measurements, the prototype has been fed with a

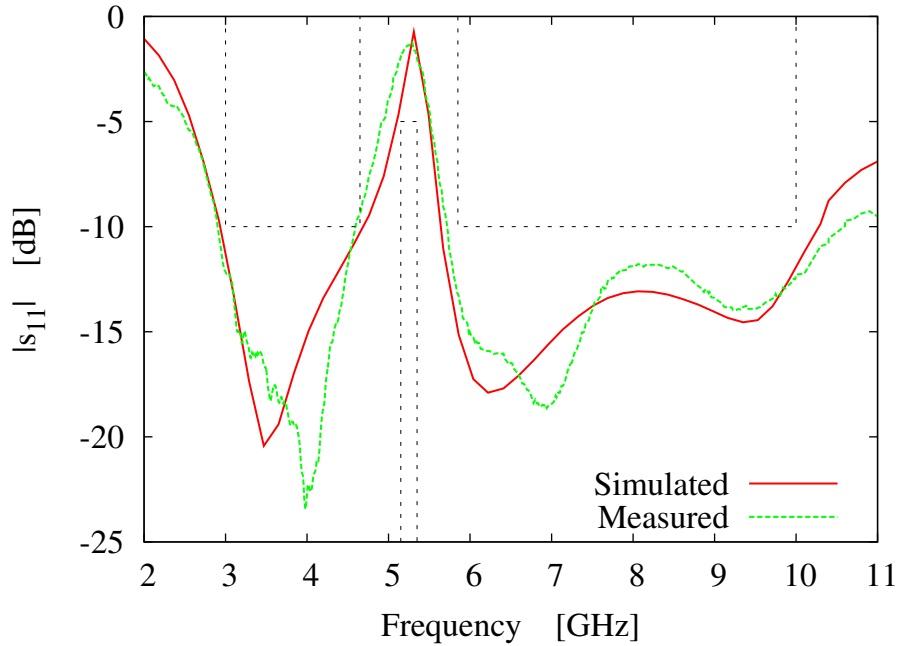


Figure 3.26: *Band Notched Antenna* - Behavior of the magnitude of s_{11} within the UWB frequency range.

coaxial cable connected to the beginning of the feedline and grounded to the edge of the metallic plane on the opposite side of the substrate. The coaxial cable has been equipped with a standard SMA connector and it has been connected to a vector network analyser to evaluate the electrical characteristics of the synthesized antenna. In order to reduce the interferences with the antenna radiating behavior, the feeding cable was connected perpendicularly to the antenna plane. The measurements have been collected in a non-controlled environment.

Concerning the impedance matching, Figure 3.26 shows a comparison between simulated and measured magnitudes of the s_{11} coefficient over the frequency range of interest. Dashed identify the mask of the requirements to be satisfied [Eqs. (3.23) and (3.24)]. As it can be observed, the antenna complies the electrical guidelines since the simulated s_{11} magnitude values turn out to be greater than -5 dB within the frequency range $5.10 - 5.50$ GHz avoiding the transmission/reception in the UNII1 and UNII2 bands. This is confirmed also by the measured rejection bandwidth going from 4.95 to 5.50 GHz. On the other hand, the prototype still provides an UWB behavior thanks to the impedance matching in the remaining part of the $3 - 10$ GHz range. As a matter of fact, the arising $|s_{11}| \leq -10$ dB bandwidths turn out to be $3.0 - 4.65$ GHz and $5.75 - 10.5$ GHz, with an adequate agreement between measured and simulated data. It is worth to notice that, while the UWB behavior is mainly due to the curvilinear shape of

3.2. NUMERICAL AND EXPERIMENTAL VALIDATION

the metallic patch on the front side of the antenna (as confirmed by the related literature, e.g. [43]), the notched characteristic is tuned by the shape and the dimension of the slot as highlighted by the behavior of the surface current distributions simulated at $f_1 = 4\text{ GHz}$, $f_{notch} = 5.25\text{ GHz}$, and $f_2 = 8\text{ GHz}$ (Fig. 3.27).

The electric currents concentrate around the slot structure in correspondence with the center frequency of the unwanted band [Fig. 3.27(c)] pointing out the effect of the slot on the antenna performance at the notched frequency. It can be also observed that the amplitude of current is greater at the top of the two vertical arms of the slot, where the slot edges are closer to the contour of the patch. On the other hand, the currents mainly move towards the edge of the metallic patch when the operating frequency is lower [Fig. 3.27(a)] or higher [Fig. 3.27(e)] than f_{notch} . Weaker current values around the slot imply that the slot does not affect the impedance matching of the antenna. On the back side of the antenna, the current distribution is almost uniform over the metallic plane at $f_1 = 4\text{ GHz}$ and $f_2 = 8\text{ GHz}$ except for the feeding point (greater values) and in the bottom region (lower values) at the rejection band.

In order to better understand the effect of the slot, a parametric study on its describing parameters has been performed. Figure 3.28 shows the behavior of the magnitude of the s_{11} parameter for different values of b_1 , b_2 , and b_3 . All the other antenna descriptors have been kept fixed to the optimized values. By varying b_1 and b_2 the overall length of the slot is modified. As expected, increasing the slot length leads to the shift towards the lower frequencies of the rejection band [Figs. 3.28(a) and 3.28(b)]. On the other hand, by enlarging the thickness of the slot, the rejection band moves towards the higher frequencies [Fig. 3.28(c)].

The radiation characteristics of the synthesized antenna have been analysed, as well. Figure 3.29 shows the three-dimensional representation of the radiation pattern at the same frequencies of the plots of the surface currents in Fig. 3.27. More specifically, the so-called “realized” (i.e., including the impedance mismatch losses) absolute gain is reported. The pattern at $f_{notch} = 5.25\text{ GHz}$ [Fig. 3.29(b)] proves that the antenna has a much lower gain in the notched band than at the other frequencies.

It can be also noticed that the antenna behaves like a classical monopole at the lower frequencies, while some distortions appear when the operating frequency increases. Such a behavior is further pointed out in Fig. 3.30 where simulated and measured absolute gains of the antenna along the horizontal ($\theta = 90^\circ$) and vertical ($\phi = 90^\circ$) planes are compared when $f_1 = 4\text{ GHz}$, $f_{notch} = 5.25\text{ GHz}$, and $f_2 = 8\text{ GHz}$. The antenna gain is almost omnidirectional in the horizontal plane whatever the frequency under analysis [Figs. 3.30(a), 3.30(c), and 3.30(e)], while two nulls are visible along the vertical plane at $\theta = 0^\circ$ and $\theta = 180^\circ$ [Figs.

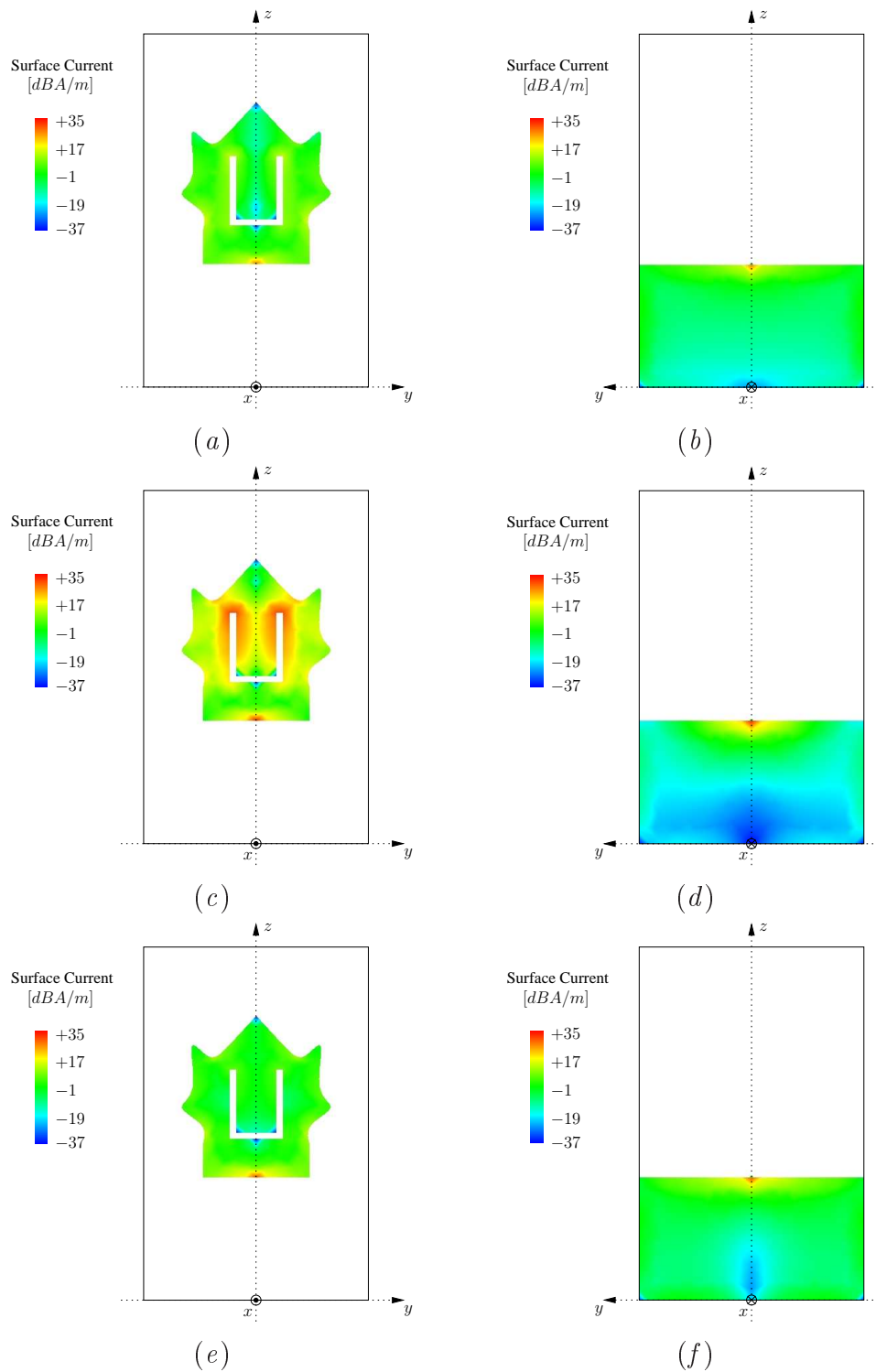
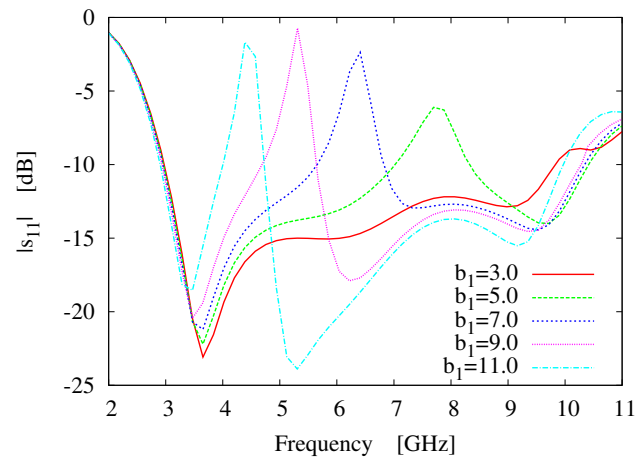
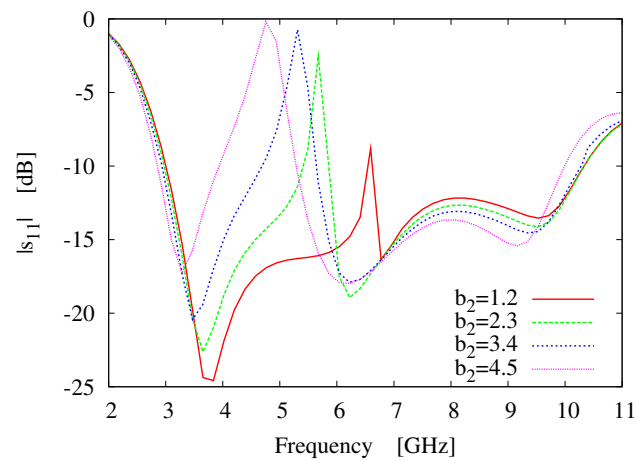


Figure 3.27: *Band Notched Antenna* - Plots of the surface currents at $f_1 = 4 \text{ GHz}$ [(a) Front side and (b) back side], $f_{notch} = 5.25 \text{ GHz}$ [(c) Front side and (d) back side], and $f_2 = 8 \text{ GHz}$ [(e) Front side and (f) back side].

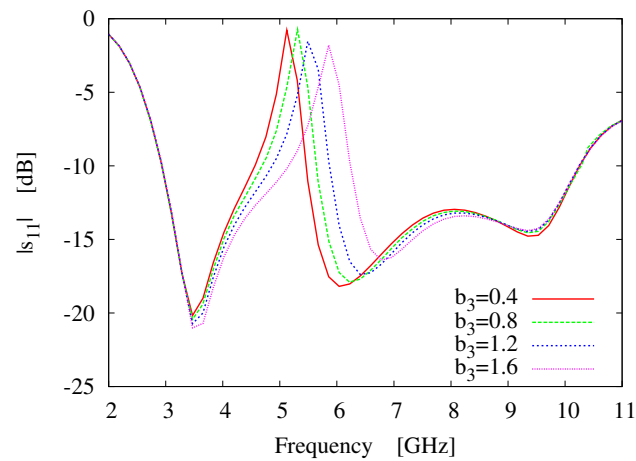
3.2. NUMERICAL AND EXPERIMENTAL VALIDATION



(a)



(b)



(c)

Figure 3.28: *Band Notched Antenna* - Behavior of the magnitude of s_{11} varying the parameters (a) b_1 , (b) b_2 , and (c) b_3 describing the slot.

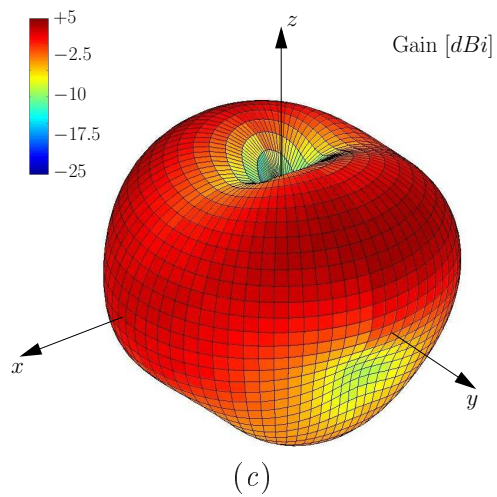
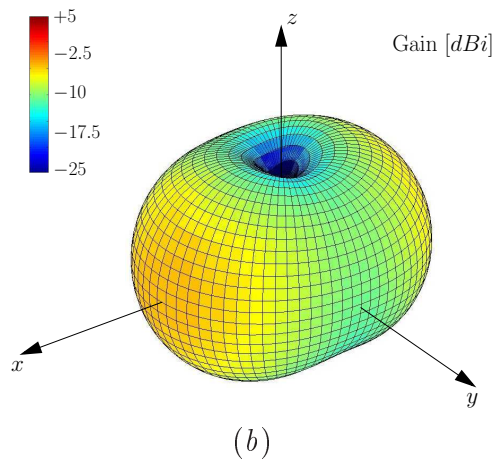
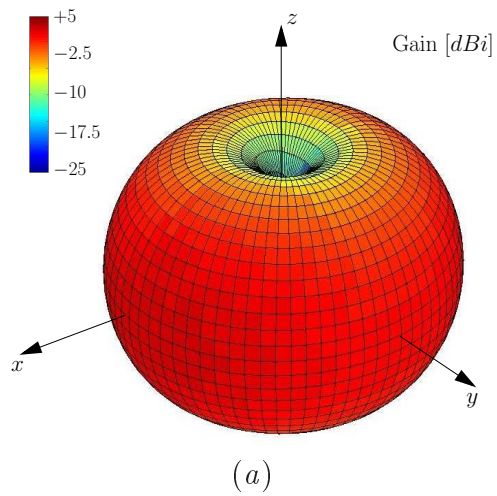


Figure 3.29: *Band Notched Antenna* - Three-dimensional representation of the absolute gain pattern at (a) $f_1 = 4 \text{ GHz}$, (b) $f_{notch} = 5.25 \text{ GHz}$, and (c) $f_2 = 8 \text{ GHz}$.

3.30(b), 3.30(d), and 3.30(f)]. As expected and already shown in Fig. 3.29, the gain at the notched frequencies is almost 10 dB lower than the one exhibited around $f_1 = 4\text{ GHz}$.

For completeness, Figure 3.31(a) and 3.31(b) show the behavior of the cross-polar gain components in the horizontal and vertical planes, respectively. It can be noticed that in the horizontal plane, the cross-polar component is very small at $f_1 = 4\text{ GHz}$ and $f_{notch} = 5.25\text{ GHz}$, while it increases just at $f_2 = 8\text{ GHz}$. On the other hand, it turns out to be always lower than -20 dB whatever the considered frequency in the vertical plane. For the sake of comparison, the behavior of the co-polar components are also reported in Fig. 3.31(c) and 3.31(d).

Since the antenna is intended for UWB applications, the distortion of the transmitted waveform has been finally evaluated. Towards this end, a UWB communication system has been simulated. Two identical copies of the antenna prototype have been placed face-to-face and separated by a distance of 25 cm [56]. Moreover, two Gaussian pulses (one with spectral content in the lower UWB band from 3 to 5 GHz [Fig. 3.32(a)] and the other extended over the higher UWB band from 6 to 10 GHz [Fig. 3.32(c)]) have been separately used as input signals of one antenna used as transmitter. Figures 3.32(b) and 3.32(d) show the received waveforms at the other antenna. Despite the low amplitudes, the shapes of the received signals are very close to the transmitted ones. The arising distortion can be quantified by means of the *system fidelity*

$$F = \max_{\tau} \int_{-\infty}^{+\infty} \tilde{v}(t - \tau) \tilde{u}(t) dt \quad (3.29)$$

defined as the maximum value of the cross-correlation between the transmitted signal and the received one [57]. In (3.29), both waveforms are normalized to their energy so that

$$\tilde{u}(t) \triangleq u(t) / \sqrt{\int_{-\infty}^{+\infty} |u(t)|^2 dt} \quad (3.30)$$

and

$$\tilde{v}(t) \triangleq v(t) / \sqrt{\int_{-\infty}^{+\infty} |v(t)|^2 dt}. \quad (3.31)$$

As an example, let us consider that $F = 100\%$ in correspondence with an ideal transmission without distortions. As for the case at hand, the fidelity indexes are $F = 98.11\%$ and $F = 92.46\%$ for Figs. 3.32(a)-3.32(b) and Figs. 3.32(c)-3.32(d), respectively. Such results assess the non-distortion features of the system in both UWB bands.

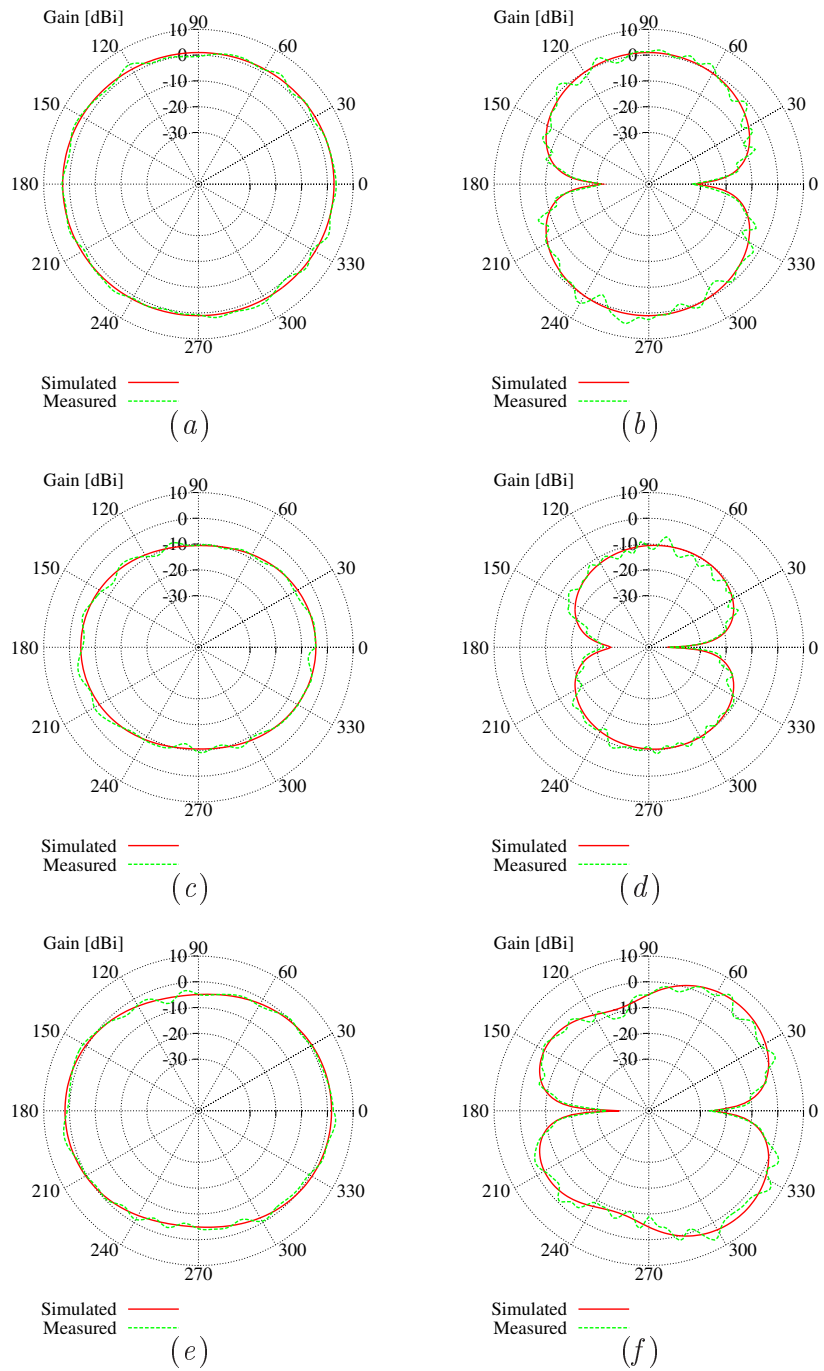


Figure 3.30: *Band Notched Antenna* - Behavior of the absolute gain at (a)-(b) $f_1 = 4 \text{ GHz}$, (c)-(d) $f_{\text{notch}} = 5.25 \text{ GHz}$, and (e)-(f) $f_2 = 8 \text{ GHz}$ along (a)(c)(e) the horizontal ($\theta = 90^\circ$) and (b)(d)(f) the vertical plane ($\phi = 90^\circ$).

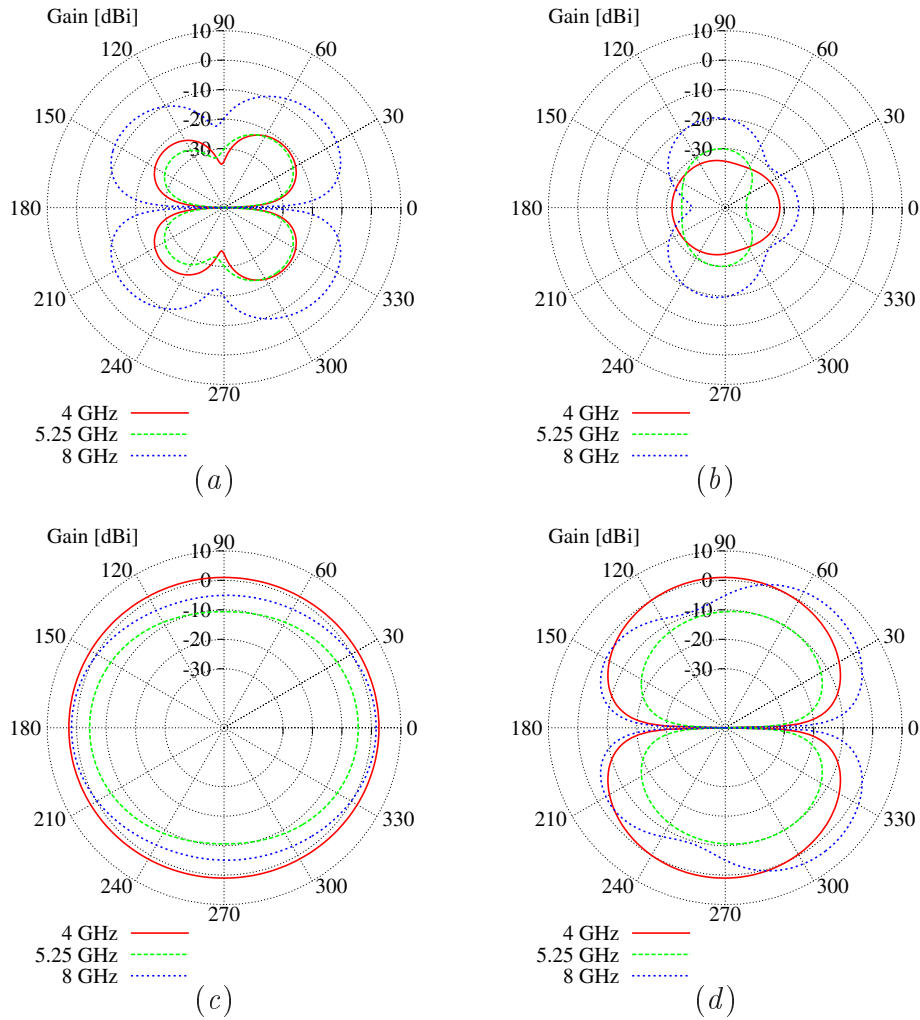


Figure 3.31: *Band Notched Antenna* - Behavior of the (a)-(b) cross-polar and (c)-(d) co-polar gain components along (a)-(c) the horizontal ($\theta = 90^\circ$) and (b)-(d) the vertical plane ($\phi = 90^\circ$) at $f_1 = 4\text{ GHz}$, $f_{notch} = 5.25\text{ GHz}$, and $f_2 = 8\text{ GHz}$.

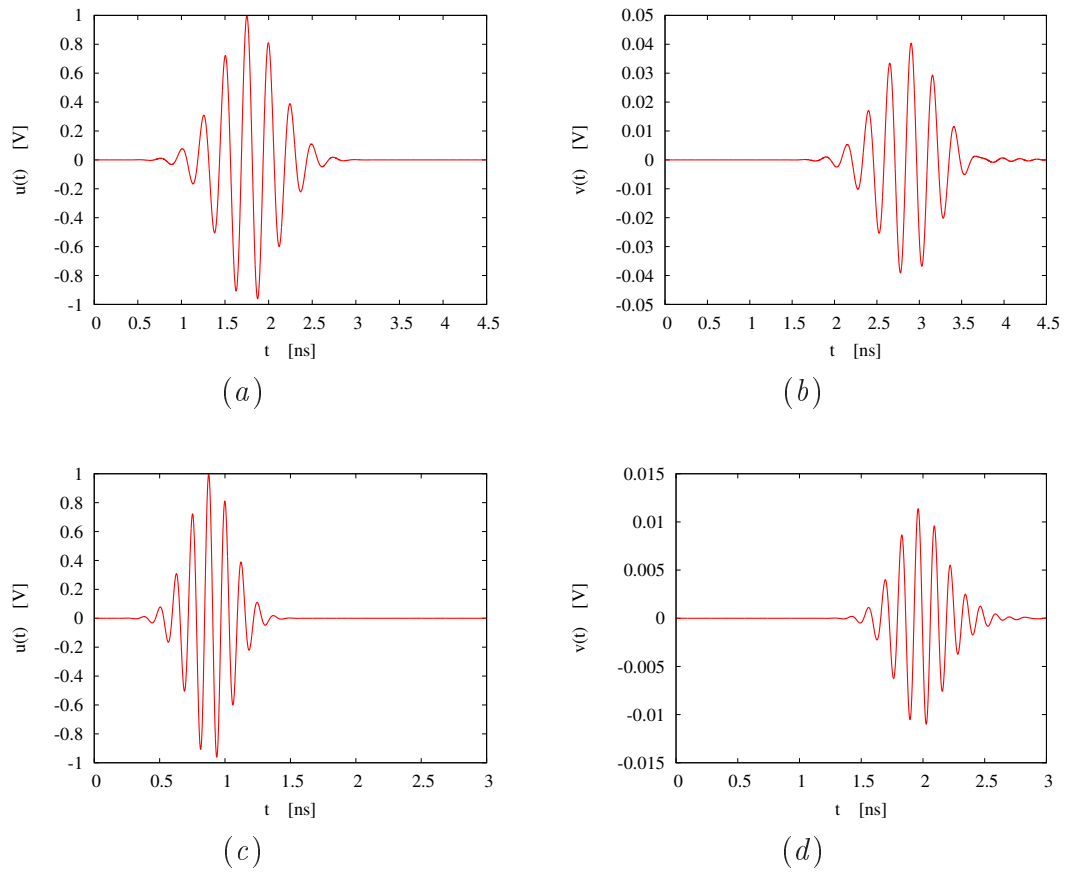


Figure 3.32: *Band Notched Antenna* - Transmitted (a)(c) and received (b)(d) pulses at the frequency bands (a)(b) 3–5 GHz and (c)(d) 6–10 GHz of the UWB system composed of two identical face-to-face copies of the proposed antenna.

3.3 Conclusion

In this section, an innovative synthesis approach based on the use of a spline-based representation for *UWB* antennas has been presented. The final shape of the antenna is determined by means of a *PSO*-based optimization procedure that exploits a suitable and computationally efficient electromagnetic representation of the whole Tx/Rx *UWB* system.

The assessment has been conducted on different test cases. Firstly, the proposed technique has been tested by considering numerical examples to show the features and the behavior of the iterative procedure. In order to point out some of the main advantages of the proposed method, the same test case has been addressed with a parametric approach, as well. Secondly, the dependence of the synthesis method on the descriptors of the antenna shape has been analyzed. Finally, the synthesis results have been verified with some comparisons with the experimental data measured from the antenna prototypes. These results regarded the design of an *UWB* antenna for wireless dongle device, an antenna compliant with the FCC released frequency spectrum, and an *UWB* antenna with WLAN-band notched characteristics.

The conclusion, which is derived from all the numerical and experimental results obtained, is that the proposed approach represents a very promising methodology for *UWB* antenna design because of its flexibility in dealing with different user-defined requirements as well as its computational efficiency.

Chapter 4

Time Domain Synthesis of UWB Antennas

In general, antenna systems are analysed in the frequency domain and their electrical properties are characterized by means of parameters such as efficiency, input impedance, gain, effective area, polarization properties and radiation patterns [2]. All these terms depend strongly on frequency [58]. For narrowband applications, they can be analysed at the center frequency, providing a comprehensive description of the system. For wider bandwidths, antenna parameters are usually expressed as a function of frequency.

Several approaches for the design of UWB antennas based on the analysis of frequency domains parameters have been proposed in the last years. As an example, in [59] the design is carried out by performing a parametric analysis aimed at obtaining an antenna exhibiting a good impedance matching in the required UWB band. Similarly, a synthesis approach for semi-elliptical UWB antennas is presented in [60]. Such an approach is based on the exploitation of some simple design equations and it is aimed at minimizing the antenna return loss in a very large bandwidth. Finally, a method for the synthesis of UWB spline-shaped antennas showing good impedance matching and distortionless characteristics has been proposed in [43]. Such a method is based on a Particle Swarm Optimizer (PSO) and an analysis of the antenna performances in terms of scattering parameters.

However, when the antenna parameters are expressed as a function of frequency, they will lose their usefulness as compact descriptions of the antenna's behavior [6]. Moreover, since the very short duration of UWB pulses means, in the frequency domain, a very large bandwidth, a frequency-by-frequency analysis can be particularly inefficient.

Therefore, it seems to be more natural to analyse UWB systems in the time domain, where all the frequencies are treated simultaneously [61]. Several time domain definitions of the classical antenna parameters can be found in [6, 57, 62, 63].

An example of design procedure partially carried out in the time domain can be found in [64], where Telzhensky *et al.* proposed a method for the optimization of a simplified version of the volcano smoke antenna based on a genetic algorithm. Such an optimization procedure is aimed at minimizing the antenna return loss (a frequency-domain parameter), while maximizing the correlation factor (a time-domain parameter). The same design approach has been successfully exploited by the same authors to design also a planar differential elliptical UWB antenna [65].

In this chapter, an approach for the synthesis of UWB antennas is presented, in which the analysis of the antenna performance is completely carried out in the time domain. Towards this end, the requirements needed to obtain antennas suitable for UWB communications are conveniently translated into the time domain. As in the case of narrowband systems, the antenna should be able to radiate as much energy as possible. However, for UWB systems, this requirement results to be more important because of the very low energy characterizing the UWB pulses. Accordingly, a constraint on the *antenna efficiency*, defined as the complementary of the ratio between the reflected energy and the total input energy, is considered. Ideally, in order to fully exploit the advantages given by UWB the received signal should be a faithful replica of the transmitted waveform. This is taken into account by the *system fidelity* parameter that gives a measure of the distortion occurred during the transmission. Finally, also the radiation pattern is optimized in order to have an omnidirectional behavior over all the frequencies. This is usually required for antennas for communication applications and it is addressed by means of the so-called *similarity factor*. Such a parameter describes the changes in the signal waveform towards different directions. On the basis of this time domain analysis, then an approach for the synthesis of antennas for UWB communications is proposed. Following the guidelines of the approach presented [43], the synthesis technique is based on a PSO [8] and on a spline representation [66] of the radiating structure. However, in [43] the analysis was based completely in the frequency domain, and the requirement on the radiation properties was not considered.

4.1 Time Domain Analysis

Let us consider a UWB communication system composed by a pair of two identical antennas placed at distance d from each other (Fig. 4.1). When the UWB waveform $u(t)$ is transmitted, the non-ideal behavior of the antennas and the channel can lead to the incorrect reception of the output signal $v(t)$. In order to avoid such an issue, the system, and in particular the antennas, must be properly designed to fit a set of requirements. First, the transmitting antenna must be able to radiate as much energy as possible of the input signal. A measurement of the radiated energy with respect to the total input energy can be performed by defining the *antenna efficiency* E as

$$E = 1 - \frac{\int_{-\infty}^{+\infty} |w(t)|^2 dt}{\int_{-\infty}^{+\infty} |u(t)|^2 dt} \quad (4.1)$$

where $w(t)$ is the reflected component of the input signal at the first antenna. Clearly, $0 \leq E \leq 1$ and it tends to the unit when the energy content of the reflected signal $w(t)$ tends to zero. In other words, higher values of the E parameter means that the communication will be possible for higher distances. As an example, Fig. 4.2 shows two pairs of input and reflected signals giving an high and a low antenna efficiency value respectively.

However, UWB systems require not only a good antenna efficiency, but also the non-distorted reception of the transmitted signal must be guaranteed. Towards this end, a useful measure of the distortion between the transmitted and the received signals is represented by the *system fidelity* F

$$F = \max_{\tau} \int_{-\infty}^{+\infty} \hat{v}(t - \tau) \hat{u}(t) dt \quad (4.2)$$

defined as the maximum of the cross-correlation function [57]. In this relation the signals have been normalized in order to have unit energy, so that $\hat{u}(t) = u(t) / \sqrt{\int_{-\infty}^{+\infty} |u(t)|^2 dt}$ and $\hat{v}(t) = v(t) / \sqrt{\int_{-\infty}^{+\infty} |v(t)|^2 dt}$, respectively. Again, the parameter F is constrained to be in the range $[0, 1]$ and it tends to be equal to zero when the two signal are completely different, while it assumes the unit value when the received waveform is only an attenuated and delayed version of the transmitted signal. As an example, Fig. 4.3 shows two pairs of signals providing high and low fidelity values respectively.

Finally, for communication applications, antennas are usually required to have omnidirectional radiation patterns. In UWB systems, such a behavior must be guaranteed for a very large frequency bandwidth. In the time domain, the change of the waveform shape of the radiated pulse as the observation direction (θ, ϕ) is varied can be described by the *similarity factor* $S(\theta, \phi)$

$$S(\theta, \phi) = 1 - \frac{\int_{-\infty}^{+\infty} |\mathbf{e}_{rad}(r, \theta_0, \phi_0, t) - \mathbf{e}_{rad}(r, \theta, \phi, t)|^2 dt}{\int_{-\infty}^{+\infty} |\mathbf{e}_{rad}(r, \theta_0, \phi_0, t)|^2 dt} \quad (4.3)$$

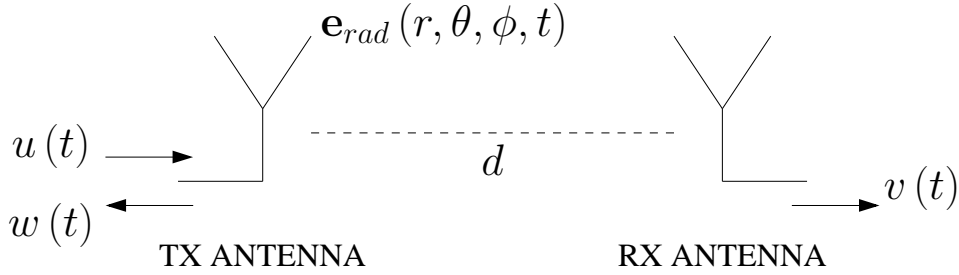


Figure 4.1: UWB communication system composed by a pair of two identical antennas.

where $\mathbf{e}_{rad}(r, \theta, \phi, t)$ is the radiated electric field and (θ_0, ϕ_0) is the direction of maximum radiation [62]. From (4.3) it results that $0 \leq S(\theta, \phi) \leq 1$, where equality is attained for the direction (θ_0, ϕ_0) . Two examples of radiated electric fields towards different directions and the corresponding similarity factor values are shown in Fig. 4.4. In this case only the ϕ direction is considered.

4.2 Antenna Synthesis

The discussion in the previous section points out that the time domain analysis based on these parameters should carefully taken into account in the antenna synthesis process in order to obtain solutions suitable for UWB communications. Towards this end, the synthesis process is recast as an optimization problem aimed at minimising a customized cost function ξ based on the time domain UWB requirements just shown. Each trial solution of the optimization problem is given by a particular antenna configuration \mathbf{a} , univocally described by a set of N parameters $\mathbf{a} = \{a_n; n = 1, \dots, N\}$ that represents the geometrical variables of the antenna structure.

Let us now refer to the antenna geometry shown in Fig. 4.5 based on the work presented in the previous section. The antenna is modeled as a microstrip structure constituted by a radiating part based on a spline representation and a metallic ground plane printed on a dielectric substrate. More in detail, α_1 and α_2 are the length and one half of the width of the substrate respectively, α_3 is one half of the feedline width, and α_4 is the length of the ground plane on the back side of the substrate. Moreover, the spline curve defining the contour of the radiating part of the antenna is controlled by a set of I control points $\{P_i = (y_{pi}, z_{pi}); i = 1, \dots, I\}$.

In the present work also the ground plane is modeled by a spline curve as shown in Fig. 4.5(b). The J control points governing the shape of the ground

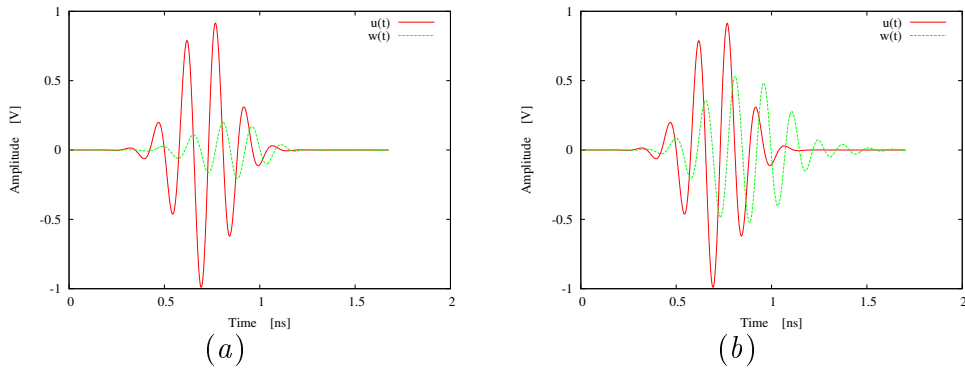


Figure 4.2: *Antenna Efficiency* - Examples of transmitted and reflected signals giving (a) $E = 0.9$ and (b) $E = 0.5$.

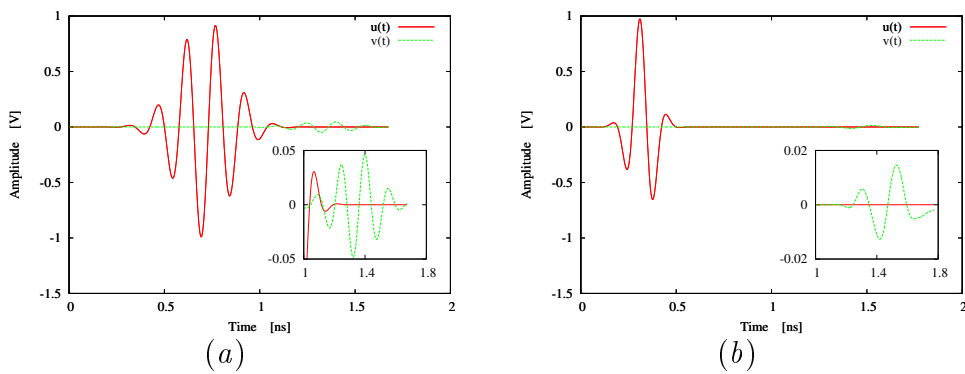


Figure 4.3: *System Fidelity* - Examples of transmitted and received signals giving (a) $F = 0.9$ and (b) $F = 0.5$.

4.2. ANTENNA SYNTHESIS

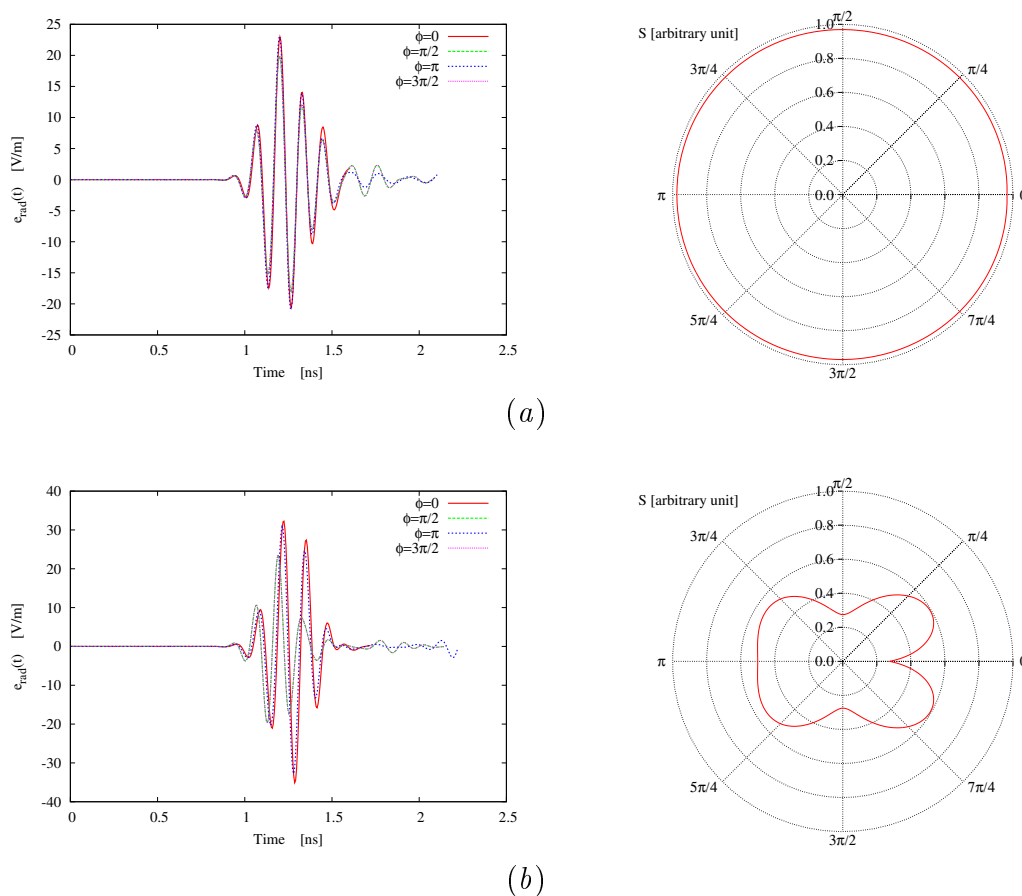


Figure 4.4: *Similarity Factor* - Examples of radiated electric field towards different directions and the corresponding similarity factor values. (a) $0.9 < S(\theta, \phi) < 1$ and (b) $0.2 < S(\theta, \phi) < 0.6$.

plane are denoted by $\{Q_j = (y_{qj}, z_{qj}); j = 1, \dots, J\}$. This allows the control of the radiation pattern in order to obtain antennas characterized by a good similarity factor.

Accordingly, the parameter vector \mathbf{a} results to be the collection of the geometric variables $\{\alpha_1, \dots, \alpha_4\}$ and of the coordinates of the control points of both the spline curves

$$\mathbf{a} = \{\alpha_1, \dots, \alpha_4; (y_{pi}, z_{pi}); i = 1, \dots, I; (y_{qj}, z_{qj}); j = 1, \dots, J\}. \quad (4.4)$$

The total number of variables to be optimized is therefore given by $N = 4 + 2(I + J)$.

The optimization is carried out by means of a PSO. According to the PSO logic, the final solution \mathbf{a}_{opt} will be the solution that minimizes the cost function

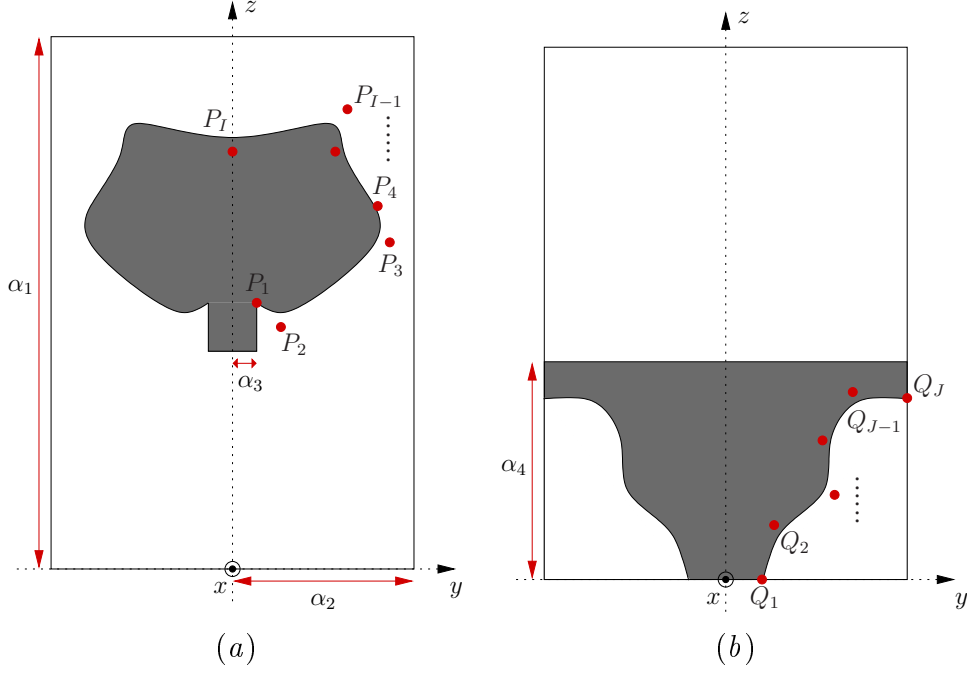


Figure 4.5: Antenna geometry.

 ξ

$$\mathbf{a}_{opt} = \arg \min_{\mathbf{a}} [\xi(\mathbf{a})]. \quad (4.5)$$

The cost function ξ is a metric for the wellness of the solution. In other words, the value $\xi(\mathbf{a})$ represents how well the trial solution \mathbf{a} complies with the design objectives. Following the guidelines given in the previous section, ξ is defined as the sum of three components

$$\xi(\mathbf{a}) = \xi_E(\mathbf{a}) + \xi_F(\mathbf{a}) + \xi_S(\mathbf{a}) \quad (4.6)$$

that take into account for the different UWB requirements. More in detail $\xi_E(\mathbf{a})$ and $\xi_F(\mathbf{a})$ refer to the constraints on the radiated energy and on the fidelity of the system respectively and they are given by

$$\xi_E(\mathbf{a}) = \max \left\{ 0, \frac{E^T - E}{E^T} \right\} \quad (4.7)$$

$$\xi_F(\mathbf{a}) = \max \left\{ 0, \frac{F^T - F}{F^T} \right\} \quad (4.8)$$

where the superscript T indicates the target values of the design specifics. $\xi_S(\mathbf{a})$ deals with the similarity factor and, in order to consider all the possible radiation directions, it is defined as

$$\xi_S(\mathbf{a}) = \text{mean}_{\theta, \phi} \left\{ \xi_S^{(\theta, \phi)}(\mathbf{a}) \right\} \quad (4.9)$$

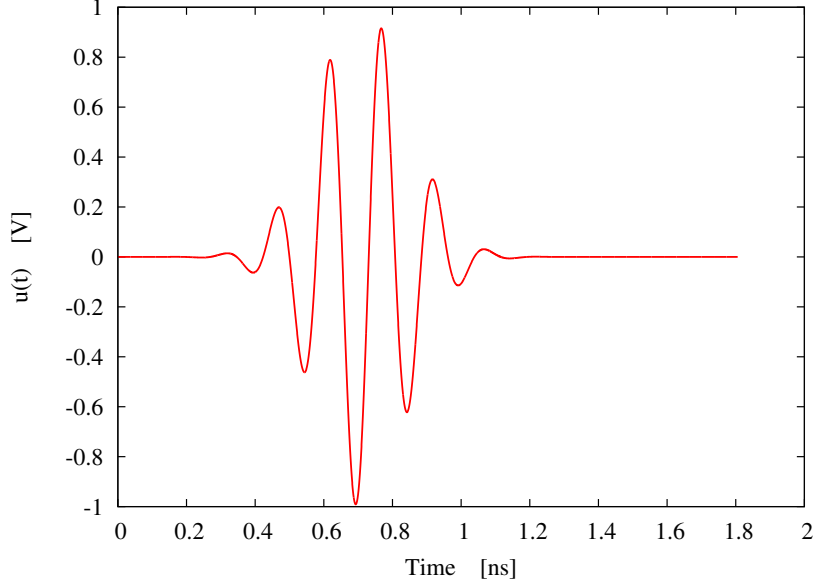


Figure 4.6: *Test Case A* - Time domain behavior of the input signal $u(t)$.

where

$$\xi_S^{(\theta, \phi)}(\mathbf{a}) = \max \left\{ 0, \frac{S^T(\theta, \phi) - S(\theta, \phi)}{S^T(\theta, \phi)} \right\}. \quad (4.10)$$

The research for the optimal solution in the solution space is carried out by means of the PSO research strategy. Towards this end, a swarm of R particles $\mathbf{a}_r^{(k)}$; $r = 1, \dots, R$ is randomly initialized at the first iteration $k = 0$. At each iteration k the positions of the particles in the solution space are updated until a maximum number of iteration K is reached (i.e., $k = K$) or until the value of the cost function falls below a user-defined threshold η (i.e., $\xi(\mathbf{a}_r^{(k)}) < \eta$).

4.3 Numerical and Experimental Validation

This section is aimed at presenting a set of numerical and experimental results in order to show the reliability as well as the effectiveness of the synthesis approach. More in detail, two different test cases (Test Case A and Test Case B), will be discussed as representative results of the proposed method.

The first test case (Test Case A) deals with the synthesis of an UWB antenna system constituted by a pair of two identical antennas placed at a distance of $d = 15 \text{ cm}$. Such a system must be designed in order to correctly transmit/receive the UWB input waveform shown in Fig. 4.6. The duration of the pulse in the time domain is equal to about 1 ns , thus resulting in a 5 GHz bandwidth going from 4 to 9 GHz . As far as the project constraints are concerned, both the antenna

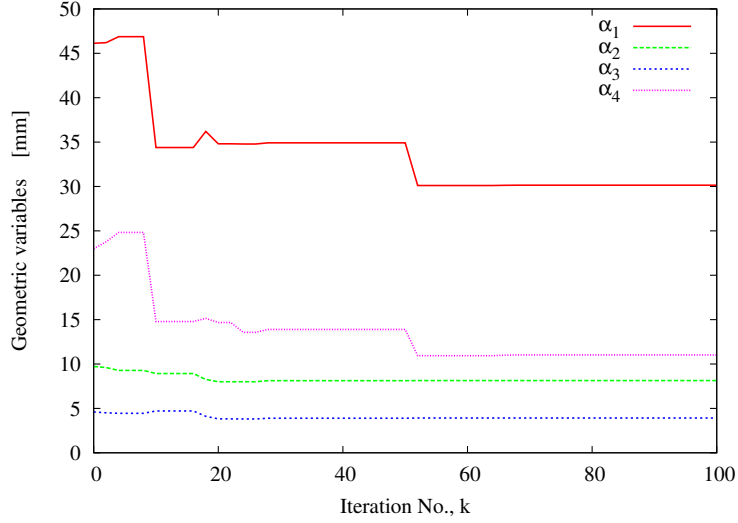


Figure 4.7: *Test Case A* - Evolution of the geometric variables $\{\alpha_1, \dots, \alpha_4\}$ over the iterations.

efficiency and the system fidelity target values have been set to $E^T = F^T = 0.95$, while the similarity factor is required to be greater than $S^T(\theta, \phi) = 0.95$ only in the $x - y$ plane ($\theta = 90^\circ$) in order to guarantee an omnidirectional behavior in the horizontal plane. Concerning the antenna geometry, the number of control point governing the spline curves on the front and on the back of the antenna has been selected equal to $I = J = 7$. Consequently, each trial antenna results to be univocally described by a set of $N = 32$ variables. Moreover, the antenna is required to have a maximum overall dimension equal to $50 \times 50 \text{ mm}^2$. Finally, for the optimization process, a population of $R = 5$ particles has been used, while the maximum number of iterations and the convergence threshold have been fixed to $K = 100$ and $\eta = 10^{-5}$, respectively.

Let us now analyse the optimization process in terms of the evolution of both the antenna geometry and the antenna performance. Starting from an antenna configuration randomly generated, the optimization procedure iteratively modifies the values of the antenna parameters in order to find the best solution in term of UWB requirements. The evolution of the geometric variables $\{\alpha_1, \dots, \alpha_4\}$ over the iterations is reported in Fig. 4.7 while the behaviors of the coordinates of the control points governing the shapes of the radiating part and of the ground plane of the antenna are shown in Fig. 4.8. As expected, the variations of the parameters are greater at the first iterations while they decrease when the optimization process reaches the convergence. Concerning the evolution of the antenna performance, Fig. 4.9 shows the performance given by the trial solution

4.3. NUMERICAL AND EXPERIMENTAL VALIDATION

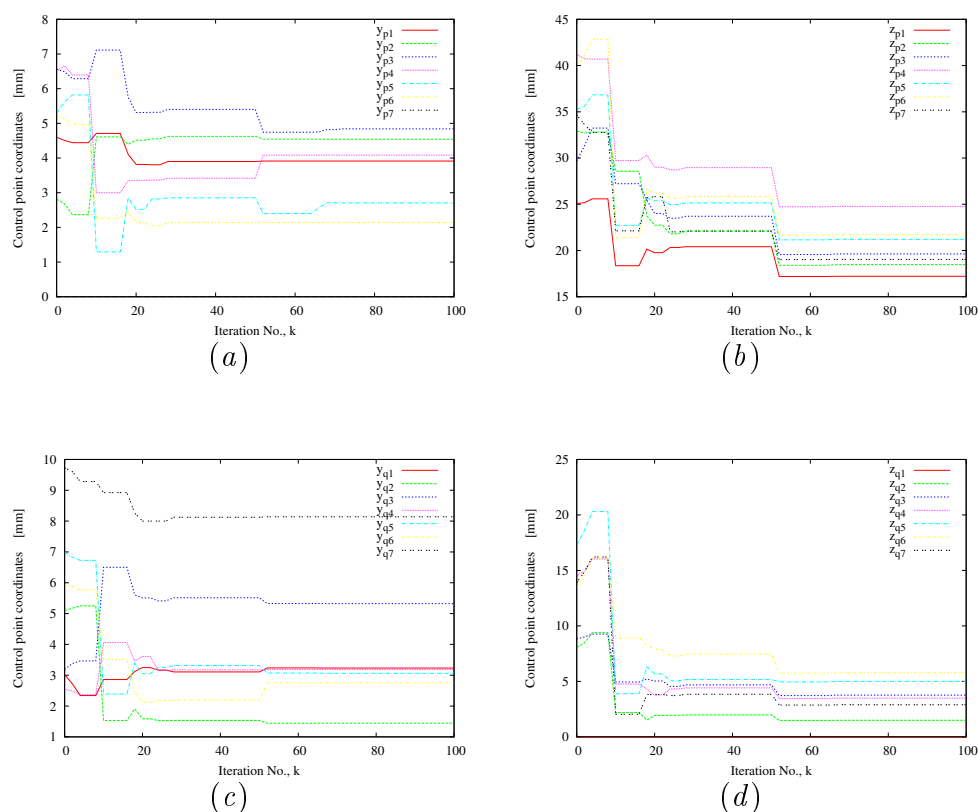


Figure 4.8: *Test Case A* - Evolution of the coordinates of the control points of the splines modeling (a) the radiating part and (b) the ground plane of the antenna over the iterations.

at each iteration together with the corresponding cost function values. More in detail, the solid line and the dashed line represent the antenna efficiency E and the system fidelity F respectively, as defined in (4.1) and (4.2). The dot line describes the behavior of the mean value S_m of the similarity factor over all the possible directions. This is given by $S_m = \text{mean}_{\theta, \phi} \{S(\theta, \phi)\}$. As it can be seen, all the values of the antenna performance parameters improve during the optimization process until they fit the design objectives. Finally, the cost function line (dot-dashed line) shows how the PSO reaches the maximum number of iterations $K = 100$ providing a final cost function value equal to $1.2 \cdot 10^{-5}$.

The synthesized antenna results to be characterized by very small dimensions ($30.1 \times 16.2 \text{ mm}$) as shown in Tab. 4.1 where the values of the optimized antenna descriptive parameters are reported. Concerning its performance, Fig. 4.10 shows the comparison between the input signal $u(t)$ and the reflected signal $w(t)$. As it can be noticed, the amplitude values of $w(t)$ are very low if compared to those of the input waveform. This means that the synthesized antenna is able

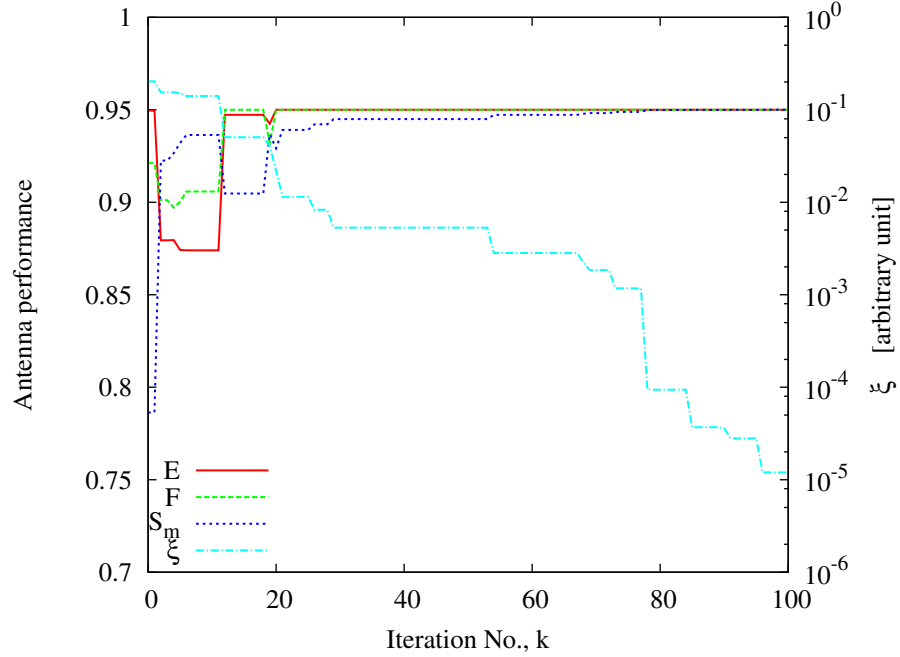


Figure 4.9: *Test Case A* - Evolution of the antenna performance (antenna efficiency E , system fidelity F , and similarity factor S) over the iterations compared with the cost function ξ .

to radiate the main part of the signal energy, as confirmed by the resulting antenna efficiency value equal to $E = 0.98$. Moreover, also the resulting system fidelity parameter is very high ($F = 0.97$) as confirmed by Fig. 4.11 where the energy-normalized version of the received signal $\hat{v}(t)$ has been superimposed to the energy-normalized version of $\hat{u}(t)$. As a matter of fact, the shape of $\hat{v}(t)$ is very similar to that of $\hat{u}(t)$. Finally, Fig. 4.12 shows the radiated electric field toward different ϕ directions and the resulting similarity factor. As required, the antenna presents an omnidirectional behavior in the horizontal plane, exhibiting $S(\theta = 90^\circ, \phi) \geq 0.95$ whatever the considered direction.

For completeness, the performance of the resulting antenna have been analyzed in the frequency domain. The system constituted by the transmitting and the receiving antennas can be seen as an equivalent two-port network, allowing the description of the antennas' behavior in terms of scattering parameters. The simulated and measured s_{11} and s_{21} parameters for the synthesized antenna system are shown in Fig. 4.13. For the experimental validation, the synthesized antenna has been built by means of a photolithographic printing circuit technology on an Arlon dielectric substrate ($\epsilon_r = 3.38$) of thickness 0.78 mm . The prototype

4.3. NUMERICAL AND EXPERIMENTAL VALIDATION

Geometric Variables [mm]						
α_1	α_2	α_3	α_4			
30.1	8.1	3.9	11.0			
Control Points Coordinates [mm]						
P_1	P_2	P_3	P_4	P_5	P_6	P_7
(3.9, 17.2)	(4.5, 18.5)	(4.8, 19.6)	(4.1, 24.8)	(2.7, 21.2)	(2.1, 21.7)	(0.0, 19.0)
Q_1	Q_2	Q_3	Q_4	Q_5	Q_6	Q_7
(3.2, 0.0)	(1.4, 1.5)	(5.3, 3.8)	(3.2, 3.5)	(3.1, 5.0)	(2.8, 5.8)	(8.1, 2.9)

Table 4.1: *Test Case A* - Descriptive parameters of the synthesized antenna.

(Fig. 4.14) has been equipped with a SMA connector and fed with a coaxial cable at the point ($y_{feed} = 0.0, z_{feed} = \alpha_4$). The measurements, which have been performed in an anechoic chamber using a Vector Network Analyzer, reasonably fit the simulated data.

As it can be observed, the values of the magnitude of the s_{11} parameter are less than -10 dB in almost the entire band apart from a small portion of the spectrum going from 4 to 4.5 GHz [Fig. 4.13(a)]. This indicates a good impedance matching of the antenna and it confirms the obtained antenna efficiency value of $E = 0.98$ and the low amplitude of the reflected signal $w(t)$. Moreover, the almost flat behavior of the magnitude of the s_{21} parameter [Fig. 4.13(b)], characterized by a variation less than 7 dB , guarantees the non-distorted reception of the transmitted UWB pulse, as previously shown in Fig. 4.11 and suggested by the value of the system fidelity parameter of $F = 0.97$.

Finally, the radiation characteristics of the synthesized antenna have been analyzed. Fig. 4.15 shows the simulated three-dimensional radiation patterns of the antenna total gain at the frequencies of 4, 6.5, and 9 GHz. The antenna works as an omnidirectional radiator in the horizontal plane ($x - y$ plane) confirming the result obtained in term of similarity factor (Fig. 4.12). Moreover, similarly to a conventional dipole antenna, two nulls are visible in the radiation patterns along the z -axis. Such a behavior is visible also in Fig. 4.16, where the comparisons between numerical and experimental values of the total gain in the horizontal and vertical planes are reported. As it can be seen, there is a good agreement between simulations and measurements.

The second test case (Test Case B) deals with the synthesis of a UWB antenna

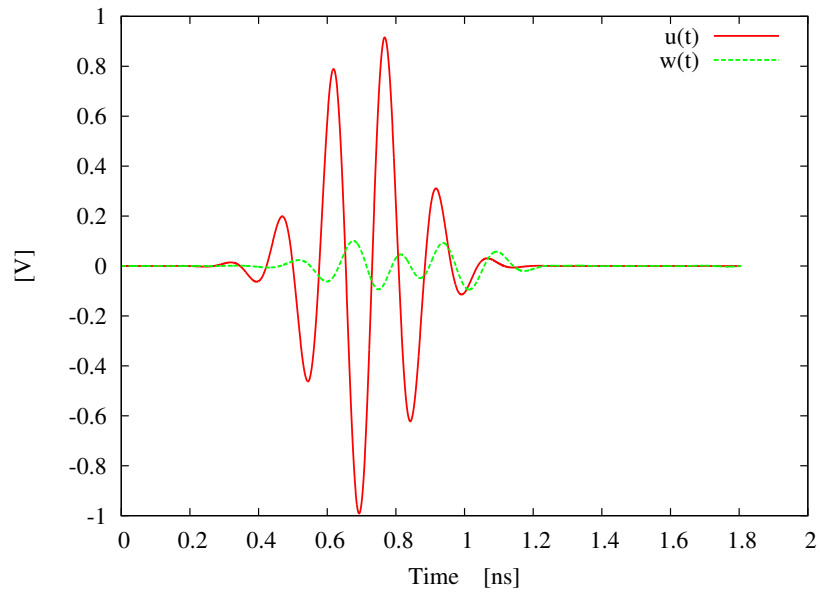


Figure 4.10: *Test Case A* - Comparison between the input signal $u(t)$ and the reflected signal $w(t)$.

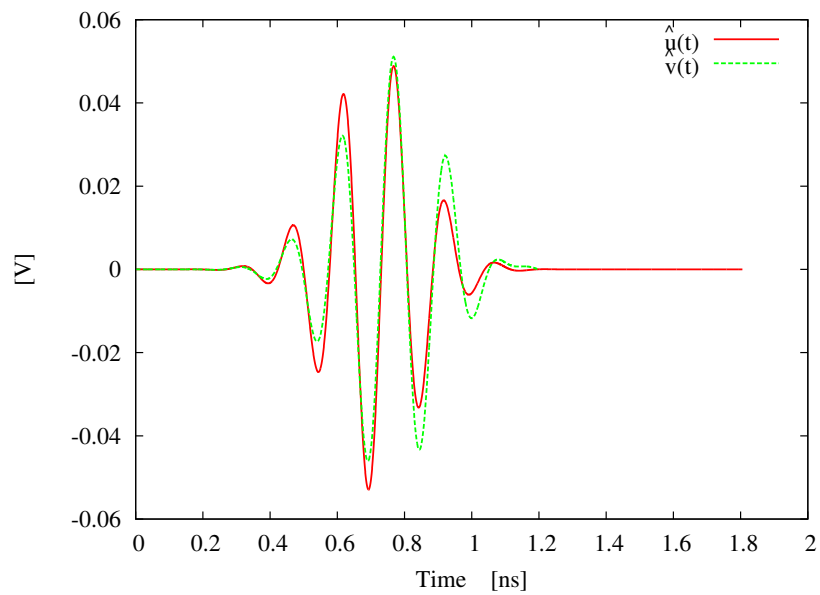


Figure 4.11: *Test Case A* - Comparison between the energy-normalized input signal $\hat{u}(t)$ and the energy normalized received signal $\hat{v}(t)$.

4.3. NUMERICAL AND EXPERIMENTAL VALIDATION

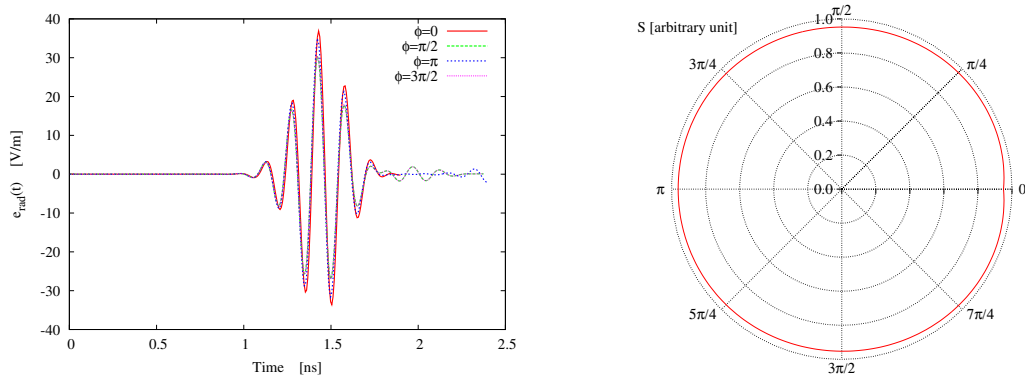


Figure 4.12: *Test Case A* - Radiated electric field towards different directions and corresponding similarity factor values.

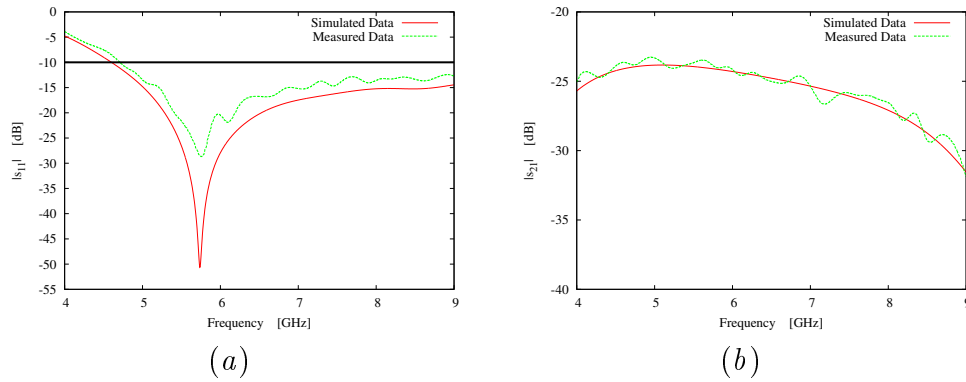


Figure 4.13: *Test Case A* - Magnitude of (a) s_{11} and (b) s_{21} parameters.

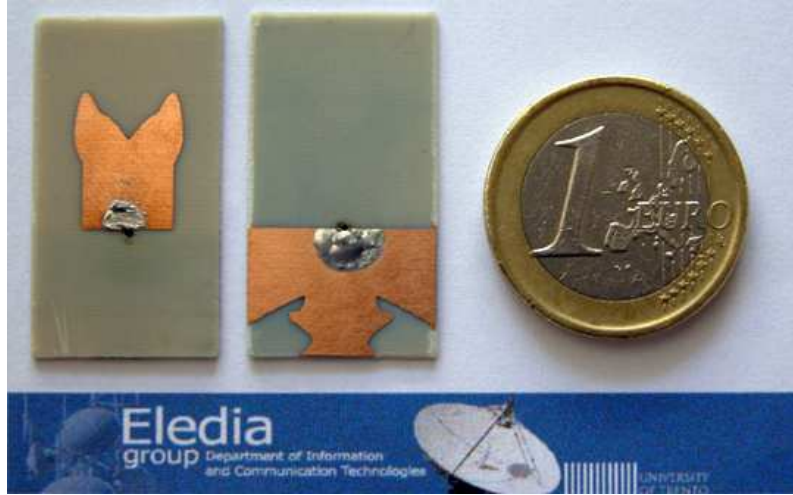


Figure 4.14: *Test Case A* - Antenna prototype.

system operating in a lower band going from 2.5 to 5.5 GHz . The antennas are placed at a distance of $d = 30\text{ cm}$. Regarding the project constraints, the target values for the design process have been set to $E^T = F^T = 0.92$ and $S^T(\theta, \phi) = 0.95$ only in the $x - y$ plane ($\theta = 90^\circ$), while the antenna size must be not larger than $80 \times 60\text{ mm}^2$. The optimization has been carried out by considering the same number of PSO particles, the same maximum number of iterations, and the same convergence threshold of the previous test case. Concerning the antenna geometry the number of control points governing the spline curves has been varied to $I = 8$ and $J = 5$, so that each trial antenna is univocally described by $N = 30$ variables.

At the end of the optimization process, the antenna turns out to be described by the values reported in Tab. 4.2, occupying an overall area of $68.7 \times 38.8\text{ mm}^2$. A prototype of the optimized antenna (Fig. 4.17) has been built on an Arlon substrate having the same characteristics of the first test case.

As far as the antenna performances are concerned, the efficiency value turns out to be equal to $E = 0.97$ fitting the project requirement. Such a value is confirmed by Fig. 4.18 showing the reflected signal $w(t)$ in comparison with the input waveform $u(t)$. As it can be observed, the amplitude of $w(t)$ is very small if compared to that of $u(t)$. Figure 4.19 shows the energy-normalized versions of the input and the received waveforms. It can be observed that the agreement between the two curves is slightly worse than the previous test case, resulting in a lower fidelity value equal to $F = 0.95$, but that still fits the project requirements.

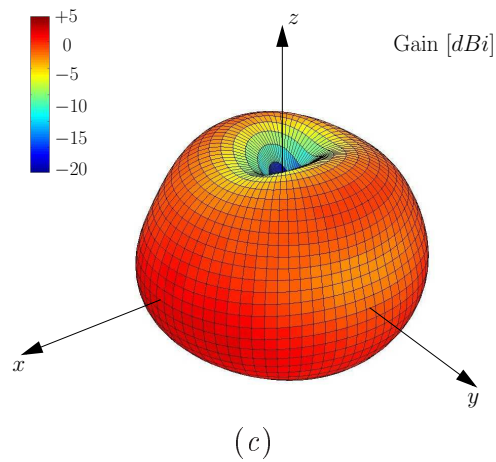
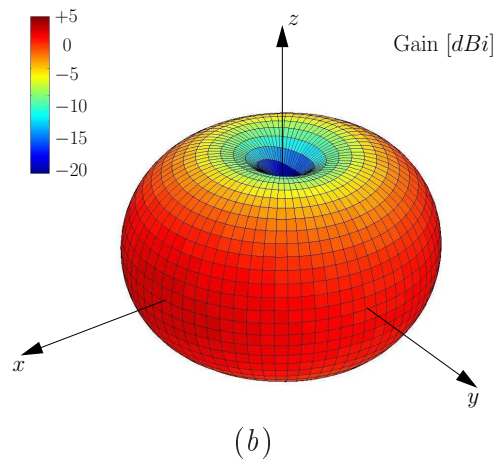
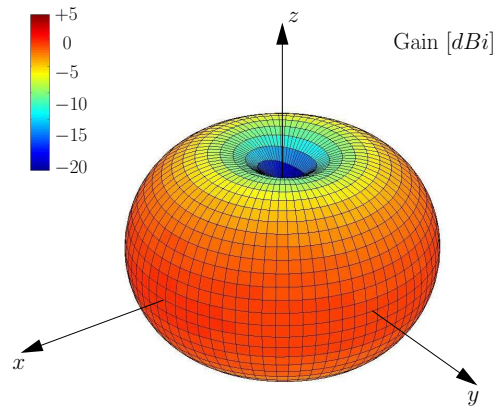


Figure 4.15: *Test Case A* - Simulated total gain radiation patterns at (a) 4 GHz, (b) 6.5 GHz, and (c) 9 GHz.

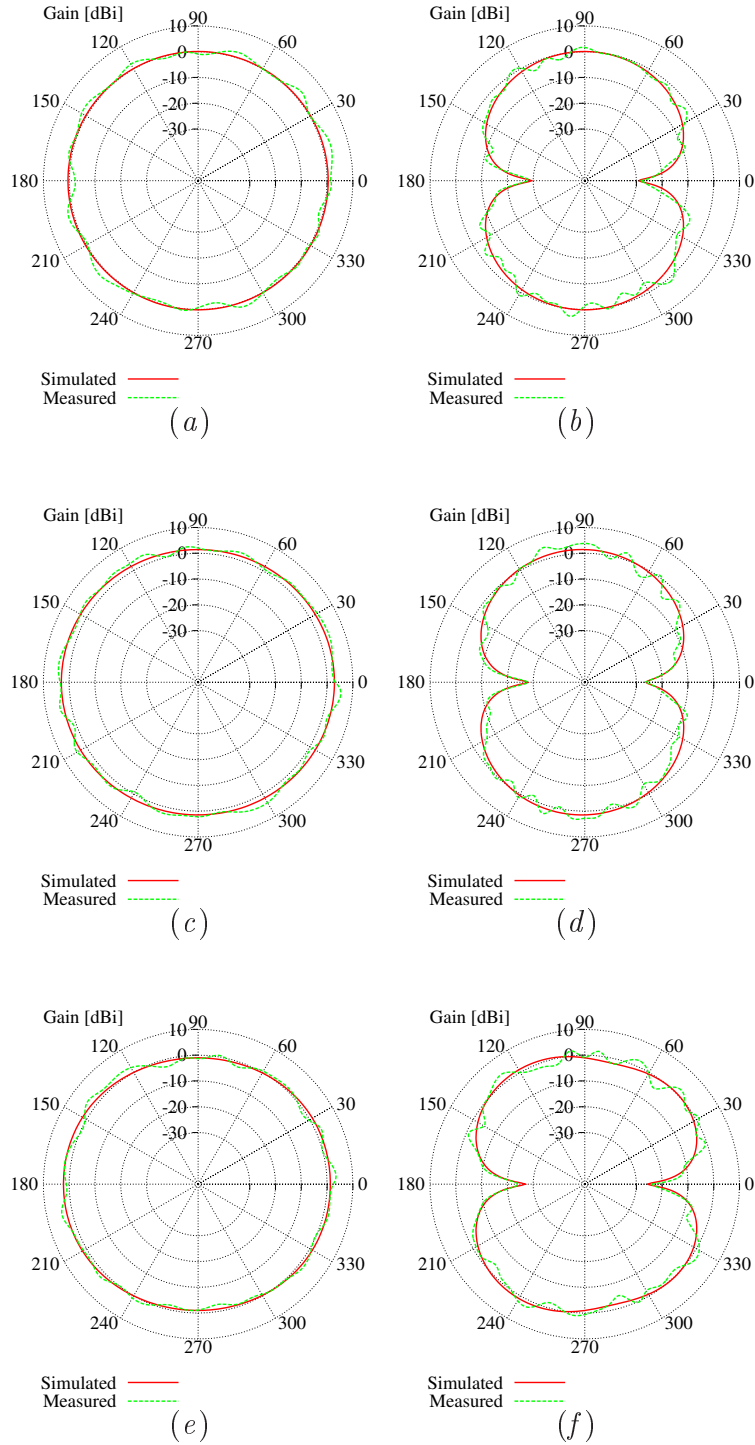


Figure 4.16: *Test Case A* - Comparison between simulated and measured values of total gain at (a)-(b) 4 GHz, (c)-(d) 6.5 GHz, and (e)-(f) 9 GHz in the (a)-(c)-(e) horizontal ($\theta = 90^\circ$) and (b)-(d)-(f) vertical plane ($\phi = 90^\circ$).

4.3. NUMERICAL AND EXPERIMENTAL VALIDATION



Figure 4.17: *Test Case B* - Antenna prototype.

Geometric Variables [mm]							
α_1		α_2		α_3		α_4	
68.7		19.4		2.1		16.8	
Control Points Coordinates [mm]							
P_1	P_2	P_3	P_4	P_5	P_6	P_7	P_8
(2.1, 18.3)	(7.2, 18.8)	(13.4, 19.2)	(5.5, 22.4)	(6.7, 24.4)	(16.4, 28.5)	(9.7, 31.8)	(0.0, 42.6)
Q_1		Q_2		Q_3		Q_5	
(16.6, 0.0)		(12.7, 9.0)		(13.4, 12.6)		(8.0, 13.7)	
						(19.4, 14.2)	

Table 4.2: *Test Case B* - Descriptive parameters of the synthesized antenna.

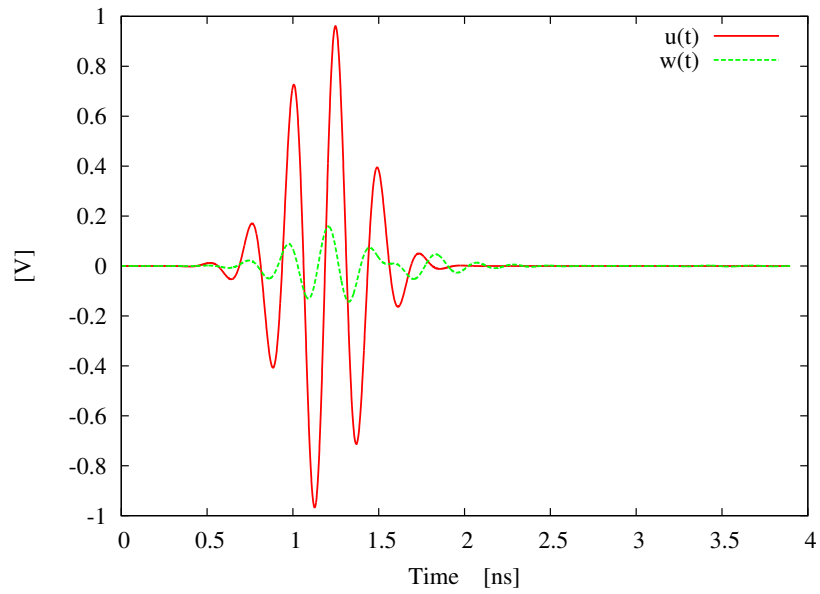


Figure 4.18: *Test Case B* - Comparison between the input signal $u(t)$ and the reflected signal $w(t)$.

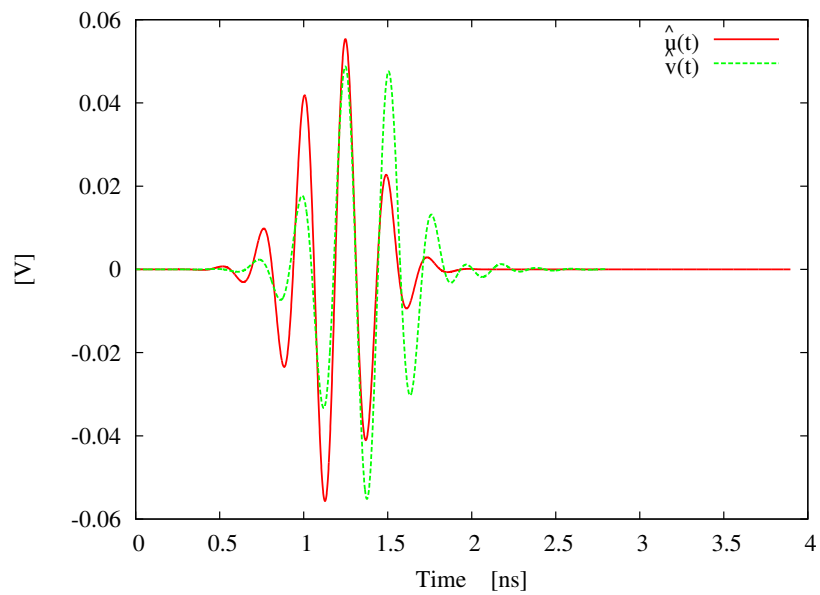


Figure 4.19: *Test Case B* - Comparison between the energy-normalized input signal $\hat{u}(t)$ and the energy normalized received signal $\hat{v}(t)$.

4.3. NUMERICAL AND EXPERIMENTAL VALIDATION

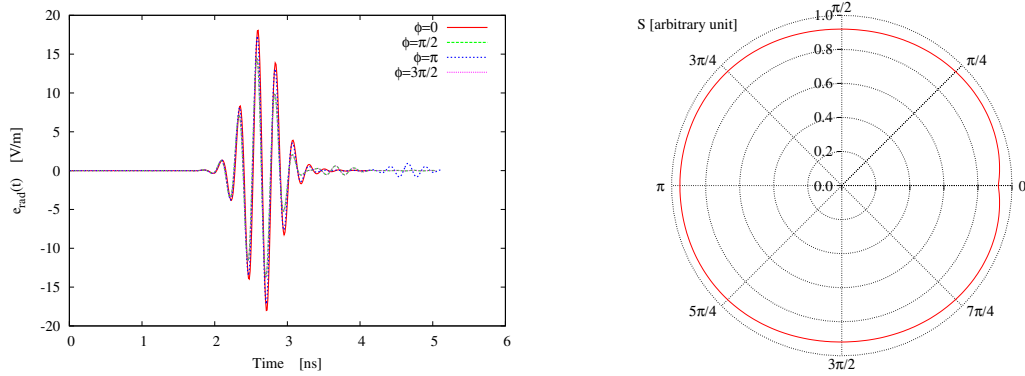


Figure 4.20: *Test Case B* - Radiated electric field towards different directions and corresponding similarity factor values.

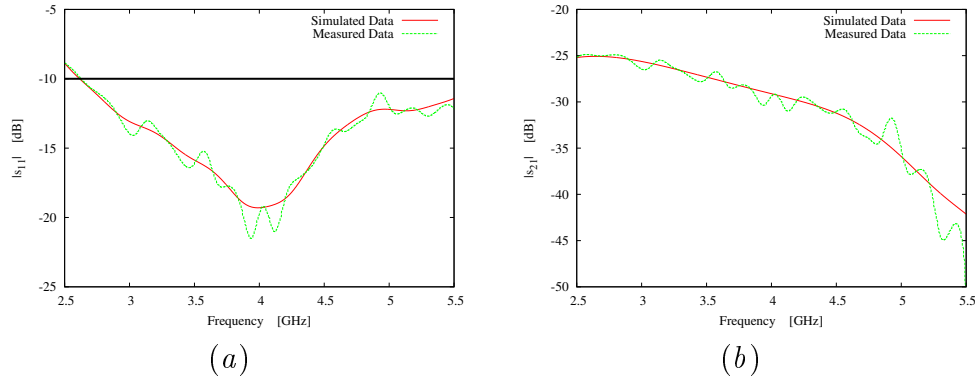
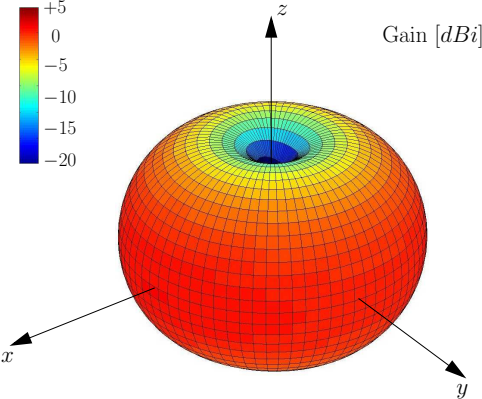


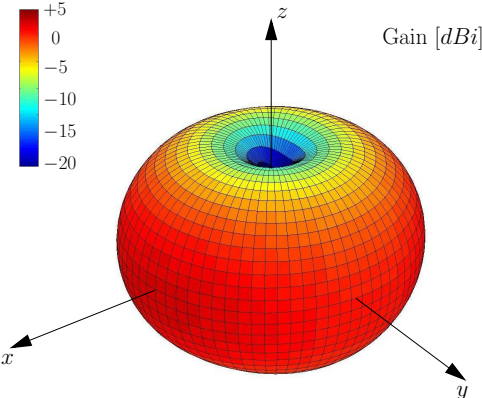
Figure 4.21: *Test Case B* - Magnitude of (a) s_{11} and (b) s_{21} parameters.

Finally, the radiated electric field toward different ϕ directions and the resulting similarity factor are shown in Fig. 4.20. As for the first test case, the antenna exhibits an omnidirectional behavior in the horizontal plane with $S(\theta = 90^\circ, \phi)$ always greater than 0.92.

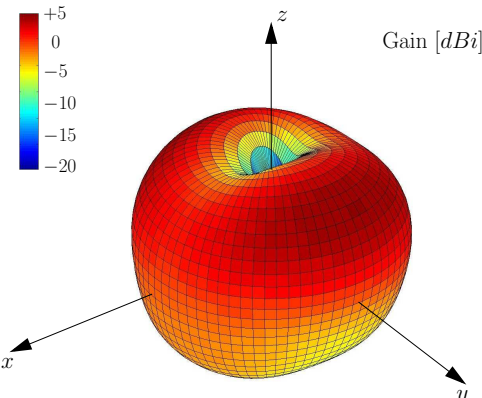
The performances of the antenna system in the frequency domain are shown in Fig. 4.21 in terms of scattering parameters. From Fig. 4.21(a) it is possible to notice that the antenna exhibits a good impedance matching, showing s_{11} magnitude values lower than -10 dB in almost the entire $2.5 - 5.5$ GHz band and confirming the obtained efficiency value of $E = 0.97$. Concerning the s_{21} parameter, its variation is larger than that exhibited by the first test case, reflecting



(a)



(b)



(c)

Figure 4.22: *Test Case B* - Simulated total gain radiation patterns at (a) 2.5 GHz, (b) 4 GHz, and (c) 5.5 GHz.

4.3. NUMERICAL AND EXPERIMENTAL VALIDATION

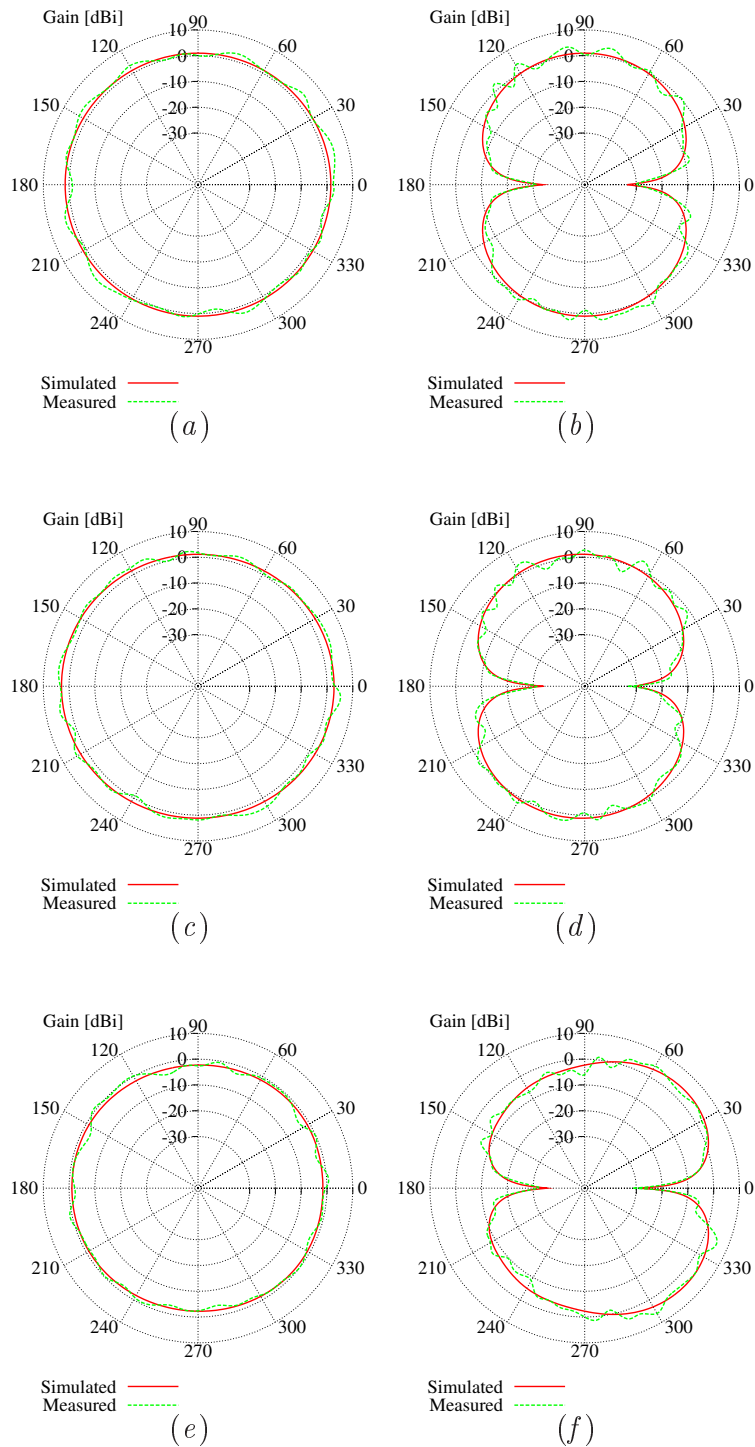


Figure 4.23: *Test Case B* - Comparison between simulated and measured values of total gain at (a)-(b) 2.5 GHz, (c)-(d) 4 GHz, and (e)-(f) 5.5 GHz in the (a)-(c)-(e) horizontal ($\theta = 90^\circ$) and (b)-(d)-(f) vertical plane ($\phi = 90^\circ$).

the slightly lower value of $F = 0.95$. Moreover, simulated and experimental data are again in good agreement.

Finally, Fig. 4.22 shows the three-dimensional total gain radiation patterns of the synthesized antenna at 2.5, 4, and 5.5 GHz. The antenna acts like a standard dipole antenna, showing an almost omnidirectional behavior in the horizontal plane, confirming the obtained similarity values shown in Fig. 4.20. For completeness, the comparisons with the experimental data in the horizontal and vertical planes are reported in Fig. 4.23. As it can be observed, there is a good agreement between simulation and measurements.

4.4 Conclusion

In this chapter, a fully time domain approach for the synthesis of UWB antenna systems has been presented. The final antenna configuration is determined by means of an integrated strategy based on a spline representation of the antenna geometry, an analysis of the antenna performance completely carried out in the time domain, and a PSO procedure. In order to point out the effectiveness of the proposed technique, both numerical and experimental results have been shown. Firstly, the optimization process has been analyzed by studying the evolution over the iterations of both the antenna geometry and performance. Secondly, the behavior of the synthesized antenna in the time domain has been analyzed by means of numerical simulations. Finally, the obtained results have been translated into the frequency domain and compared with measurements performed in an anechoic chamber. The agreement between simulated and measured data indicates the proposed technique as an efficient methodology for the synthesis of UWB antenna systems.

4.4. CONCLUSION

Chapter 5

Synthesis of Multiband Antennas

Today's competitive market requires multimode capabilities for each wireless device because of the rising demand for new higher-speed mobile broadband and multifunction applications. On the other hand, mobile handsets are characterized by smaller and smaller sizes and reduced weights thanks to the progress of modern integrating circuit technology and following the users' needs. To this end, the design of suitable RF front-ends plays a very important and critical role. As a matter of fact, it is usually necessary to integrate the RF-part (i.e., the whole set of wireless interfaces) in only one antenna. Such a requirement becomes even more challenging when also a high degree of miniaturization is required. Moreover, to satisfy a standard constraint of today's communication devices, the antennas must be easily manufactured and integrated into system boards.

Concerning the dimension requirement, the use of conventional monopole-like antennas is generally avoided because of their relatively large sizes when compared to that of the device itself [67]. A more effective solution considers microstrip planar radiators, which are more easily adaptable to the shape of the handset at hand. Moreover, they present other advantages such as low profile, cheap cost, light weight, robustness, and suitability for mass production. However, standard half-wavelength microstrip antennas at the operating frequencies of modern mobile applications (e.g., DVBH) turn out to be still too large for an efficient integration into a miniaturized mobile device.

As regards to the multiband operation [68], new strategies are under development for integrating multiple functionalities and reducing, at the same time, both costs and complexity. Such a task is usually addressed by using duplexers along with band-pass filters in the receiving and transmitting paths. Unfortunately, such a solution needs Surface Acoustic Wave (SAW) filters and Low Noise Amplifiers (LNAs) with a non-negligible increase of the costs and of the dimensions. Some attempts to minimize the occupied space have been done by integrating on-chip the LNA. Nevertheless, further efforts are devoted to avoid the use of external filters in order to reduce the number of components and to simplify the board layout. Towards this end, a possible solution consists in moving the frequency selectivity functions "closer" to the antenna. In other words, this means

that the radiating system must show an adequate impedance matching within each band of operation without external components.

This is often obtained by properly modifying the reference geometry of a suitable radiation element. Examples of such a design procedure can be found in [69]-[74], where several multiband solutions based on the reference planar inverted-F antenna (PIFA) are described. However, it should be pointed out that excessive modifications and complex designs might strongly modify the original antenna impedance matching parameters (e.g., the $VSWR$ or the S_{11} scattering parameter) as well as the corresponding radiations indexes (e.g., the efficiency, the radiation patterns, and the polarization). Moreover, the architectural complexity of the radiator certainly causes an increase in the manufacturing costs [75].

Another promising approach to synthesize miniaturized and multiband radiators exploits the positive features of fractal shapes [76][77]. As a matter of fact, the self-similarity property of the fractal shapes is suitable to obtain a multi-frequency resonances. In literature, many fractal antennas have been discussed. The Sierpinski Gasket fractal monopole antenna has been widely studied as a solution for multi-frequency systems. It was introduced in [78] by Puente *et al.* who showed that the self-similarity properties of the fractal shape are directly translated into the electromagnetic behavior of the antenna. Further investigations and a comparison with the well-known bow-tie antenna are provided in [79]. Concerning the design of electrically small antennas, the Koch monopole antenna is often used. Its behavior has been numerically and experimentally analysed in [80], while the relation between its multiple resonant frequencies and the fractal dimension has been discussed in [81]. Finally, a comparison with other wire monopole antennas is reported in [82]. A review of some other fractal geometries useful in antenna engineering such as the Hilbert curve or the fractal tree is reported in [83].

Unfortunately, standard fractal antennas present an harmonic behavior rather than a real multiband behavior. This is, for example, the case of the standard Koch monopole antenna presented in [80]. A possible solution consists in perturbing the fractal geometry. This adds some degrees of freedom in the antenna synthesis process in order to customize the antenna performance to different applications. The effectiveness of such a solution has been demonstrated in several published papers. In [81] it has been shown that the variation of the indentation angle of the Koch geometry affects the primary resonant frequency, the input resistance at this resonance, and the ratio of the first two resonant frequencies of dipole antennas using this geometry. In [84], a dual-band antenna based on a perturbed Koch geometry is proposed for GPS applications. In order to obtain the multiband behavior, the parameters of the fractal shape are optimized without the need to insert any lumped element. Finally, the performances in terms of $VSWR$ values and gain functions of a pre-fractal Koch-like antenna operating in the Wi-Max band are compared with those of a standard resonant quarter wave

monopole in [85]. Regarding the Sierpinski geometry, Puente *et al.* presented in [86] that the spacing between the bands of a Sierpinski antenna can be controlled by modifying the characteristic scale factor of the fractal structure. However, a worsening of the input impedance of the first resonance was visible [87]. Towards this end, further investigations have been performed in [87] in order to add flexibility in the design process. As a matter of fact, the fundamental frequency match was improved as well as the band allocation, where a dual scaling factor was achieved. Variations of the Sierpinski geometry have been analysed also in [88] in order to obtain a physically small monopole antenna with high efficiency operating in the ISM bands. Finally, a three-band antenna based on a perturbed Sierpinski fractal geometry has been presented in [89].

5.1 Fractal-shaped Antennas

In this section, starting from the preliminary analysis reported in [90], the idea of perturbing the fractal geometry is further investigated to develop an automatic approach for the synthesis of multiband antennas, whose working frequencies are fully tunable. Towards this end, the effects caused by the variation of the geometrical parameters of fractal antennas are carefully analysed to define some *a-priori* rules for the synthesis of efficient antennas. In particular, the Sierpinski and the Koch fractal antenna will be considered. However, such an analysis can be easily extended to any fractal antenna structure. In order to define some analytic relations for the behavior of the resonant frequencies, a set of descriptive parameters of the antenna geometry is firstly defined. Successively, the performances of the antenna structure varying its descriptors are studied by means of numerical simulations. However, since only an exhaustive analysis of all the parameters would provide an analytic synthesis tool, the obtained relations are exploited to provide a suitable initialization for a global optimization procedure. Such an optimization procedure is based on a Particle Swarm Optimizer (PSO) [8] and it is aimed at identifying an antenna structure fitting a set of requirements in terms of impedance matching and size reduction.

5.1.1 Fractals

As originally intended by Mandelbrot [4], fractals are complex shapes characterized by an inherent self-similarity in their geometrical structure. They are the result of the study of the biological structures that nature has optimized during millions of years of evolution. As a matter of fact, unlike classical Euclidean shapes, fractals can be profitably used to model the geometries of complex natural objects such as coastlines, clouds, snowflakes, galaxies, etc [83][91]. However, thanks to their unique characteristics, fractal geometries have recently been introduced in the field of the antenna design in order to obtain a new class of radiating structures.

In general, there is not a strict definition of fractal geometries [92]. They are generated by iteratively applying a geometric *generator* to a starting Euclidean geometry, called *initiator*. Such a procedure can continue for an infinite number of times, resulting in a final curve, whose structure is infinitely intricate and not differentiable at any point [92][77]. However, there are several geometric characteristics that can be used to describe fractals [76]. Among them, the *self-similarity* and the *space-filling* capability are the more interesting properties from an antenna design point of view. The first one indicates that small regions of the geometry have the same shape of the whole structure, but on a reduced scale. Objects owning such a property can be expected to show a similar electromagnetic behavior at different frequencies. Consequently, they can be profitably used in order to design multiband antennas [93]. The second one is instead related to the fact that fractal geometries usually fall between the classi-

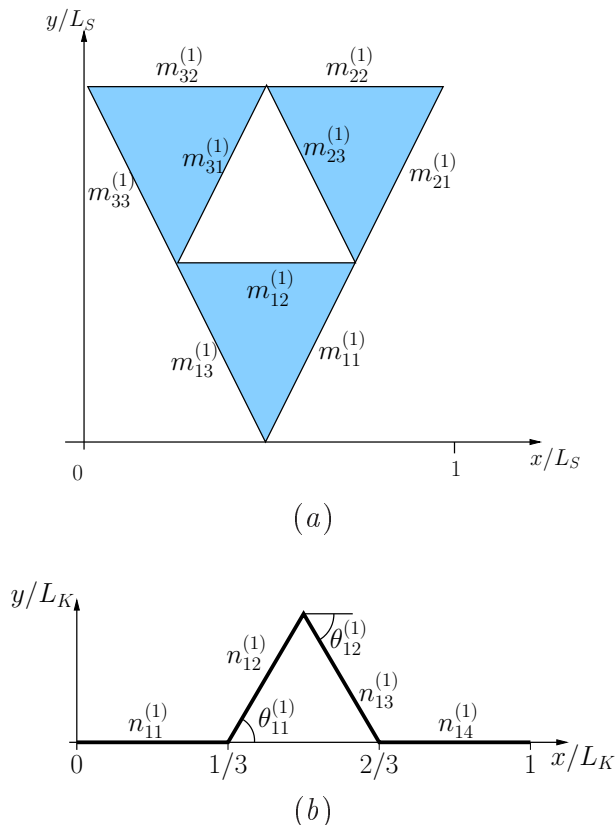


Figure 5.1: Fractal antenna geometries considered in the perturbation analysis. (a) Sierpinski antenna and (b) Koch antenna.

cal definitions of lines, planes or volumes. For example, a line can grow in such a way that it effectively almost fill the entire plane. In this sense, a fractal can be a line that approaches a plane [77]. Such an ability of fractal curves to be very long occupying a compact physical space can be exploited to design electrically small antennas [92].

Mathematically, a fractal geometry can be defined by means of the *fractal dimension* parameter given by

$$D = \frac{\ln(N)}{-\ln(\gamma)} \quad (5.1)$$

where N is the number of copies of the whole geometry, and γ is the scale factor of each copy. Such a parameter gives an indication about the complexity and the space-filling capacity of the fractal shape. For instance, at each fractal iteration the Koch curve [80] is constituted by $N = 4$ copies of the curve at the previous iteration scaled by a factor $\gamma = \frac{1}{3}$. Consequently, the fractal dimension of a Koch curve is approximately $D = 1.26$, meaning that it occupies more space than a

monodimensional segment, but less than a filled two-dimensional area.

Fractals are abstract objects that cannot be physically implemented. Therefore, when applied to antenna synthesis problems, some related geometries have to be considered. These geometries, usually called “pre-fractals” [94], can be used to approach an ideal fractal and to extract some of the advantages that can theoretically be obtained by the mathematical abstractions. In general, pre-fractals decrease the complexity of the fractal geometry, by eliminating the intricacies that are not distinguishable in a particular applications. As regards antenna synthesis, this means that the geometric structures whose lengths are much smaller than a wavelength in the band of interest, and that usually appear for high fractal iterations, can be avoided [95]. In the following, the term fractal antenna will be used to intend antennas whose geometries are based on pre-fractals.

5.1.2 Fractal Perturbation

Two different kind of fractal antennas have been considered in the perturbation analysis: the Sierpinski antenna and the Koch antenna. The Sierpinski antenna is characterized by a planar geometry, that can be univocally described at each fractal iteration k by the following vector of geometric parameters

$$\mathbf{w}_k = \left\{ m_{ij}^{(k)}; i = 1, \dots, 3^k; j = 1, 2, 3 \right\} \quad (5.2)$$

where $m_{ij}^{(k)}$ is the j -th side of the i -th triangle constituting the antenna structure at the k -th fractal iteration. On the other hand, the linear geometry of the Koch antenna can be described by

$$\mathbf{z}_k = \left\{ n_{ij}^{(k)}, \theta_{il}^{(k)}; i = 1, \dots, 4^{k-1}; j = 1, \dots, 4; l = 1, 2 \right\} \quad (5.3)$$

where $n_{ij}^{(k)}$ and $\theta_{il}^{(k)}$ indicate the j -th segment and the l -th angle characterizing the shape of the i -th Koch generator at the k -th fractal iteration, respectively. The effects of the variations of the geometric parameters at the iteration k have been evaluated in terms of the shift of the first two resonant frequencies $f_1^{(k)}$ and $f_2^{(k)}$.

Let us first consider the Sierpinski antenna at the first fractal iteration ($k = 1$), whose geometry (normalized with respect to the antenna length L_S) is reported in Fig. 5.1(a). In order to have the equilateral outside border, the following constraints are imposed on the antenna structure: $m_{21}^{(1)} = 1 - m_{11}^{(1)}$, $m_{32}^{(1)} = 1 - m_{22}^{(1)}$, and $m_{13}^{(1)} = 1 - m_{33}^{(1)}$. Moreover, to avoid any reliance on the working frequency, the resonant frequencies have been normalized such that

$$\tilde{f}_i^{(1)} = \frac{f_i^{(1)} - f_i^{(SS)}}{f_i^{(SS)}}; \quad i = 1, 2 \quad (5.4)$$

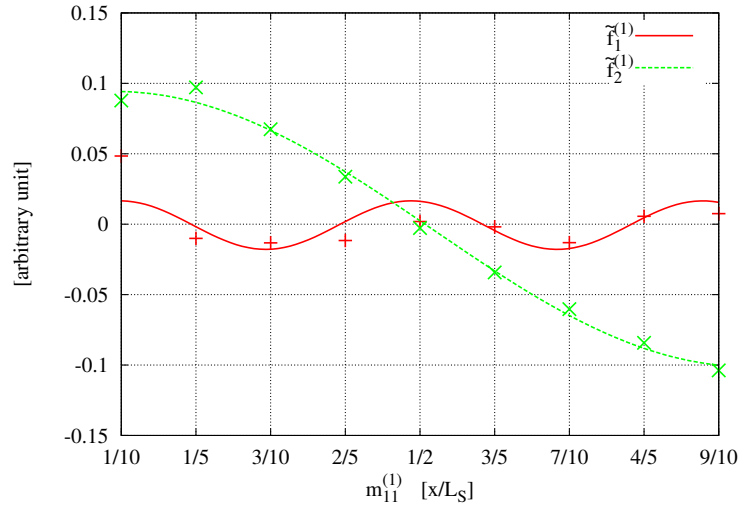


Figure 5.2: *Perturbation analysis*. Behavior of the normalized resonant frequencies of the Sierpinski antenna varying the $m_{11}^{(1)}$ parameter.

where $f_i^{(SS)}$ indicates the i -th resonance of the standard Sierpinski monopole antenna ($m_{11}^{(1)} = m_{22}^{(1)} = m_{33}^{(1)} = 0.5$).

To illustrate some representative results from the analysis, two different test cases are reported in the following. The first one is aimed at verifying the effects of varying $m_{11}^{(1)}$ while keeping the other set to $m_{22}^{(1)} = m_{33}^{(1)} = 0.5$. The normalized first and second resonant frequencies are shown in Fig. 5.2. A sinusoidal behavior characterized by the following relations

$$\begin{aligned} \tilde{f}_1^{(1)} &= 0.02 \cos \left(16.1m_{11}^{(1)} - 1.6 \right) \\ \tilde{f}_2^{(1)} &= 0.1 \cos \left(3.7m_{11}^{(1)} - 0.3 \right) \end{aligned} \quad (5.5)$$

is obtained for both the resonant frequencies. However, the entity of the shift is completely different. As a matter of fact, the maximum shift of the first resonance is about $\pm 2\%$ with respect to standard Sierpinski antenna, while that of the second one reaches $\pm 10\%$. Such a behavior suggests that the second resonant frequency is mainly driven by the length of $m_{11}^{(1)}$ (or equivalently, by the length of $m_{21}^{(1)}$), while the position of the first one is mainly due to the length of the side of the outside triangle, i.e. $(m_{11}^{(1)} + m_{21}^{(1)})$.

In the second test case, $m_{22}^{(1)}$ is varied in the range $[\frac{1}{10}, \frac{9}{10}]$ while $m_{11}^{(1)} = m_{33}^{(1)} = 0.5$. The obtained frequency shifts are shown in Fig. 5.3. The position of both

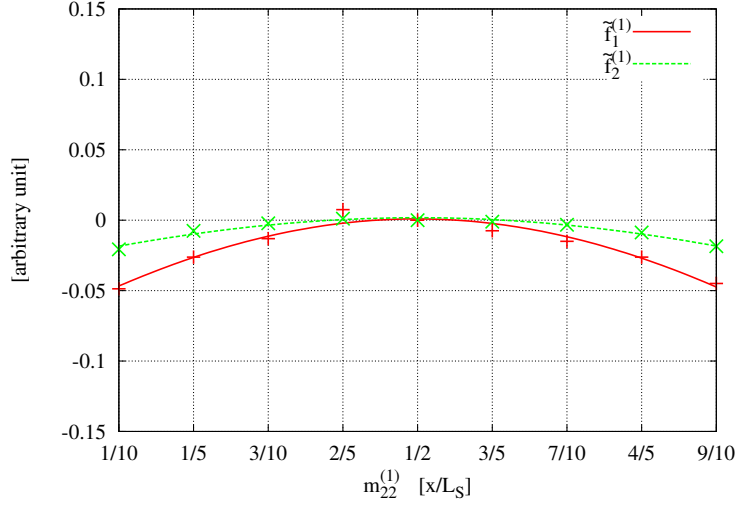


Figure 5.3: *Perturbation analysis*. Behavior of the normalized resonant frequencies of the Sierpinski antenna varying the $m_{22}^{(1)}$ parameter.

the resonances varies following a quadratic trend, described by

$$\begin{aligned} \tilde{f}_1^{(1)} &= -0.07 + 0.3 - 0.3 \left(m_{22}^{(1)}\right)^2 \\ \tilde{f}_2^{(1)} &= -0.03 + 0.13 - 0.13 \left(m_{22}^{(1)}\right)^2. \end{aligned} \quad (5.6)$$

The variation is symmetrical with respect to the position with $m_{22}^{(1)} = 0.5$ and its magnitude is not larger than 5% and 2% for the first and the second resonance, respectively. Such a result confirms that the position of the first resonant frequency is mainly controlled by the dimensions of the outside triangle, but it also shows that the perturbation of the top side of the antenna geometry nearly does not affect the position of the second resonance. This is due to the fact the current flows from the bottom to the top of the antenna on the tilted sides. As a matter of fact, the analysis of the perturbation of the $m_{33}^{(1)}$ parameter (here not reported) provides the same results obtained with the first test case.

Similar test cases have been analysed for the Koch monopole antenna at the first fractal iteration, whose normalized geometry with respect to the antenna size L_K is shown in Fig. 5.1(b). In the following some representative results are reported. The following constraints are imposed on the antenna structure: $n_{13}^{(1)} = n_{12}^{(1)}$, $\theta_{21}^{(1)} = \theta_{11}^{(1)}$, and $n_{14}^{(1)} = 1 - n_{11}^{(1)} - 2n_{12}^{(1)} \cos(\theta_{11}^{(1)})$. The last requirement forces the antenna to always occupy the same area. Moreover, as in the case of the Sierpinski antenna, the resonant frequencies have been normalized with respect to the resonant frequencies $f_i^{(KS)}$ of a standard Koch monopole antenna

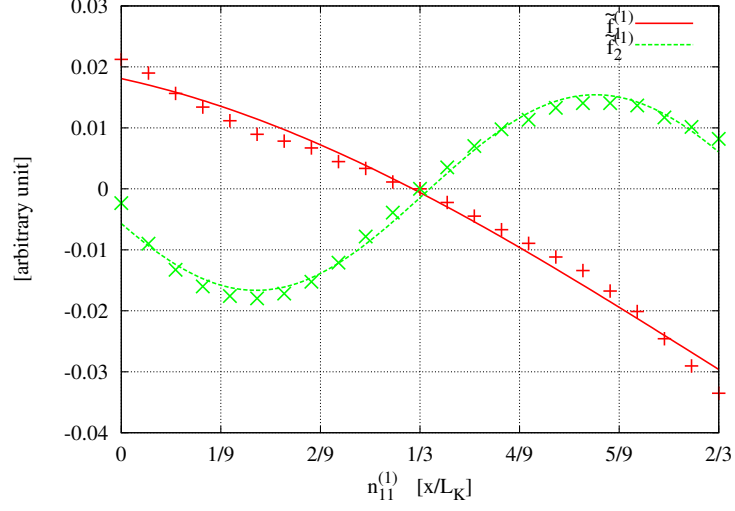


Figure 5.4: *Perturbation analysis*. Behavior of the normalized resonant frequencies of the Koch antenna varying the $n_{11}^{(1)}$ parameter.

characterized by $n_{11}^{(1)} = n_{12}^{(1)} = \frac{1}{3}$ and $\theta_{11}^{(1)} = \frac{\pi}{3}$, i.e.,

$$\tilde{f}_i^{(1)} = \frac{f_i^{(1)} - f_i^{(KS)}}{f_i^{(KS)}}; \quad i = 1, 2. \quad (5.7)$$

The first test case deals with the variation of the $n_{11}^{(1)}$ parameter in the range $[0, \frac{2}{3}]$ while $n_{12}^{(1)} = \frac{1}{3}$ and $\theta_{11}^{(1)} = \frac{\pi}{3}$. It turns out that both the first and the second resonant frequencies present a sinusoidal behavior (Fig. 5.4) described by

$$\begin{aligned} \tilde{f}_1^{(1)} &= -0.03 + 0.05 \cos(1.87n_{11}^{(1)} + 0.36) \\ \tilde{f}_2^{(1)} &= 0.02 \cos(8.38n_{11}^{(1)} + 1.9). \end{aligned} \quad (5.8)$$

As it can be observed, the variation is not larger than $\pm 3\%$ for both the resonances. This is essentially due to the fact that the perturbation of $n_{11}^{(1)}$ does not change the overall length of the antenna. However, since the second resonant frequency is higher than the first one, it moves faster than the first one, as demonstrated by the different periods of the two sinusoids.

The effects of the perturbation of $n_{12}^{(1)}$ are analysed in the second test case. Figure 5.5 shows the behavior of the resonant frequencies when $n_{12}^{(1)}$ is varied in the range $[0, \frac{2}{3}]$ while $n_{11}^{(1)} = \frac{1}{3}$ and $\theta_{11}^{(1)} = \frac{\pi}{3}$. The positions of the resonances change with linear trends described by

$$\begin{aligned} \tilde{f}_1^{(1)} &= 0.23 - 0.65n_{12}^{(1)} \\ \tilde{f}_2^{(1)} &= 0.28 - 0.74n_{12}^{(1)} \end{aligned} \quad (5.9)$$

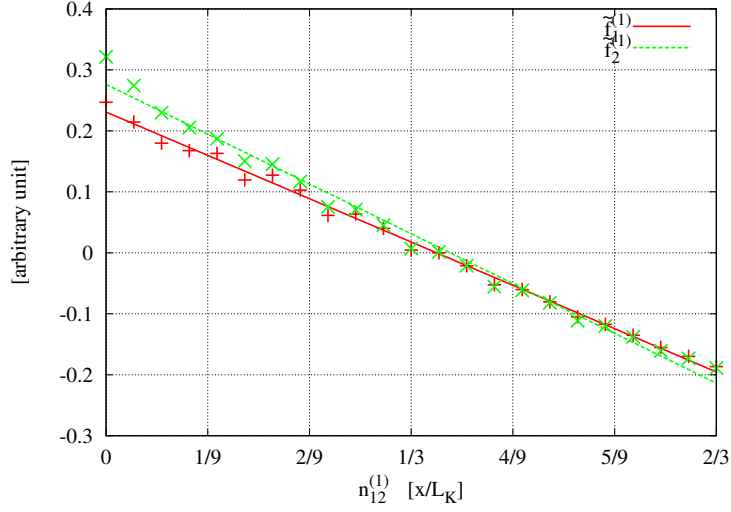


Figure 5.5: *Perturbation analysis*. Behavior of the normalized resonant frequencies of the Koch antenna varying the $n_{12}^{(1)}$ parameter.

and characterized by a variation that is almost from -20% to 20% . As expected, since the perturbation of such a parameter varies the physical length of the antenna, the effects on the resonant frequencies are much more evident.

Finally, let us consider the Koch monopole antenna at the second fractal iteration ($k = 2$) and analyse the effects of perturbing $n_{11}^{(2)}$ with the constraint that $n_{21}^{(2)} = n_{31}^{(2)} = n_{31}^{(2)} = n_{11}^{(2)}$. The obtained results are shown in Fig. 5.6. As it can be noticed, both the first and the second resonant frequencies vary according to a linear behavior, whose describing relations are

$$\begin{aligned} \tilde{f}_1^{(2)} &= -0.1 - 0.03n_{11}^{(2)} \\ \tilde{f}_2^{(2)} &= -0.1 - 0.04n_{11}^{(2)}. \end{aligned} \quad (5.10)$$

Moreover, the maximum variation is less than 2% for the first resonance and less than 3% for the second one, thus reflecting the results obtained in the first test case, i.e. varying $n_{11}^{(1)}$ when $k = 1$. However, both the resonant frequencies are shifted towards the lower frequencies of about 10% with respect to those of the Koch antenna at the first fractal iteration. Clearly, this is due to the increment of the overall antenna length caused by the second fractal iteration.

5.1.3 Antenna Synthesis

From the few examples shown in the previous section, it is evident that the perturbation analysis can provide very useful information about what are the

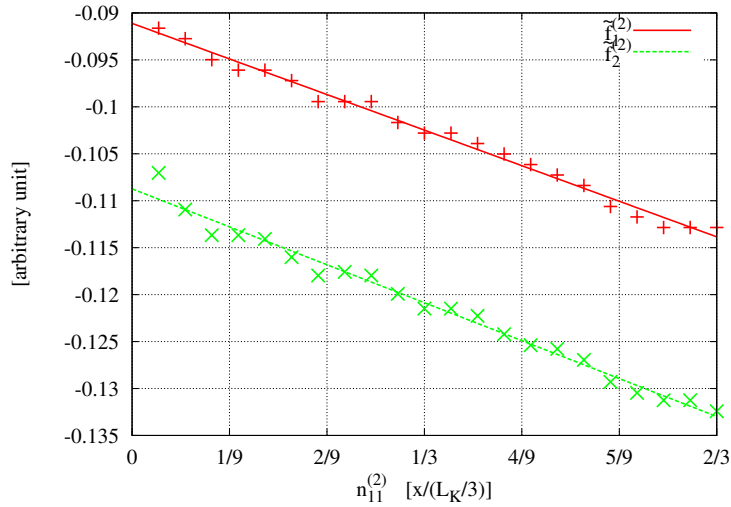


Figure 5.6: *Perturbation analysis*. Behavior of the normalized resonant frequencies of the Koch antenna varying the $n_{11}^{(2)}$ parameter.

geometric parameters affecting more the resonant behavior of the antenna. However, an exhaustive analysis is not possible, since the number of these parameters increases with the fractal iteration. Moreover, also the effects of the combined perturbation of several parameters should be studied. For these reasons, the identification of a unique formula that allows the prediction of the positions of the resonant frequencies of the antenna on the basis of its geometrical parameters is not feasible task.

From an engineering perspective, the relations obtained varying the different antenna descriptors, give a set of *a-priori* information that can be exploited as a suitable initialization for a successive optimization process aimed at identifying the best solution, i.e., the optimal antenna parameters. As a matter of fact, a good initialization usually results in an efficient method for minimizing the time as well as the computational required resources.

The optimization process is aimed at fitting a set of requirements in terms of impedance matching at the input port in the bands of interest, and in terms of size reduction compared to a standard quarter-wave monopole antenna. More specifically, let us denote with f_{bL} and f_{bH} the lowest and the highest frequency of the b -th band where the antenna is required to operate, respectively. The impedance matching requirement can be defined by means of the VSWR parameter Ω as

$$\Omega(f) \leq VSWR_{\max} \quad f \in [f_{bL}, f_{bH}]; \quad b = 1, \dots, B \quad (5.11)$$

where $VSWR_{\max}$ is a user-defined threshold and B is the number of bands of interest. Concerning the geometrical constraints, the antenna should respect $L \leq L_{\max}$ where $L = \{L_S, L_K\}$ and L_{\max} indicates the maximum admissible

antenna size.

In order to satisfy the project guidelines, the following cost function Ψ , defined as the least-square difference between requirements and estimated specifications,

$$\Psi(\xi) = \sum_{b=1}^B \sum_{i=0}^{I-1} \left\{ \max \left[0, \frac{\Omega(f_{bL} + i\Delta f_b) - VSWR_{\max}}{VSWR_{\max}} \right] \right\} \quad (5.12)$$

is optimized. In (5.12) $\xi \in \{\mathbf{w}_k, \mathbf{z}_k\}$ is the array describing the antenna structure, $i\Delta f_b$ is the sampling frequency interval in the b -th band, and $\Omega(f_{bL} + i\Delta f_b)$ is the VSWR value at the frequency $f_{bL} + i\Delta f_b$ when ξ_k is considered.

The minimization of the cost function in (5.12) is carried out by means of an automatic process whose main building blocks are a PSO and a Method-of-Moment (MoM) [26] electromagnetic simulator. More in detail, an initial set of T trial solutions ξ_t^q is randomly generated at the first step ($q = 0$) of the optimization process. For each array ξ_t^q , the corresponding antenna structure is generated, and its performance are evaluated by means of the MoM simulator. Starting from the calculated VSWR values, the fitness value $\Psi_t^q = \Psi(\xi_t^q)$ of the trial antenna is computed through the cost function (5.12). On the basis of the fitness values and according to the PSO logic, the antenna descriptors in ξ_t^q are iteratively updated until $q = Q$ (Q being the maximum number of iterations) or

$$\Psi_{opt}^{q=q_{conv}} = \Psi(\xi_{opt}^{q=q_{conv}}) \leq \eta \quad (5.13)$$

where η is the convergence threshold and $\Psi_{opt}^{q=q_{conv}} = \min_t \{\Psi_t^{q=q_{conv}}\}$.

5.1.4 Numerical and Experimental Validation

This section is aimed at presenting a representative test cases demonstrating the effectiveness of the proposed synthesis approach. More specifically, numerical and experimental results regarding the design of a Sierpinski fractal antenna will be discussed. The optimized planar antenna works in three different frequency bands and it is suitable to be integrated in multimode wireless devices. It is fed by a single RF port without any matching circuit and it operates in a DVBH channel and at GSM and UMTS frequency bands.

The geometry of the antenna is shown in Fig. 5.7. As it can be observed, the reference shape is a planar Sierpinski pre-fractal where three iteration stages ($s = 0, 1, 2$) have been considered to set three different resonances [79]. From a geometric point of view, the antenna structure is uniquely defined by the following descriptors

$$\chi = \{U, W, P_i = (X_i, Y_i); i = 1, \dots, 15\} \quad (5.14)$$

where U and W are the length and the width of the input section, respectively. Moreover, (X_i, Y_i) $i = 1, \dots, 15$ are the coordinates of the vertexes of the void triangles in Fig. 5.7 descriptive of the antenna geometry.

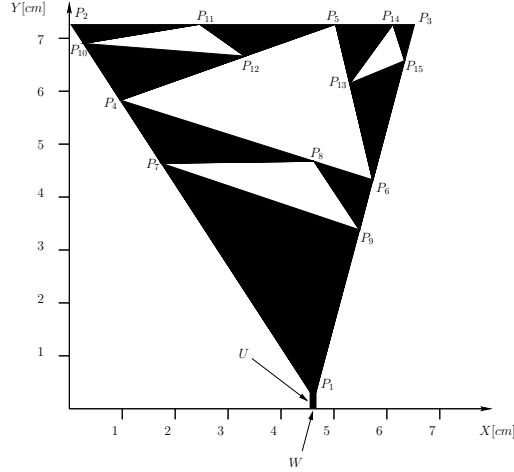


Figure 5.7: Geometry of the multimode three-band antenna.

Since the antenna is required to be compact (maximum size 8×8 [cm²]) and to simultaneously operate at three different frequency bands, the user-defined constraints require *VSWR* values lower than 2.5 at the center of each frequency band and smaller than 3.0 along the whole bandwidths, respectively. As regards to the synthesis process, a swarm of $R = 5$ particles has been randomly initialized and iteratively updated according to the *PSO* logic until a solution fitting the user-defined requirements has been found. In Fig. 5.8, the behavior of the cost function Φ over the iterations ($k_{conv} = 50$) is given. For completeness, the cost function mean value μ_{Φ} as well as the standard deviation σ_{Φ} are reported. As regards to the optimization results, Figure 5.9 shows a scatter plot of the *VSWR* values at k_{conv} . Each point of the plot indicates the simulated *VSWR* value at the center of a frequency band in correspondence with a swarm solution. As it can be observed, all the trial solutions at the convergence meet the performance requirements in the *GSM* and *UMTS* bands, but only one representative point (i.e., only one trial solution) falls below *VSWR* = 2.5 in the *DVBH* band.

Taking into account the constraints on the shape and electric behavior of the device at hand, the following values of the antenna descriptors have been identified at the end of the *PSO*-based optimization process. The dimensions of the input section turns out to be $U = 0.28$ mm and $W = 0.12$ mm. Moreover, the coordinates of the control points (in [cm]) result: $P_1 = (4.5, 0.1)$, $P_2 = (0.0, 7.4)$, $P_3 = (6.6, 7.4)$, $P_4 = (1.0, 5.8)$, $P_5 = (5.2, 7.4)$, $P_6 = (5.8, 4.3)$, $P_7 = (1.8, 4.7)$, $P_8 = (4.7, 4.7)$, $P_9 = (5.5, 3.4)$, $P_{10} = (0.3, 7.0)$, $P_{11} = (2.5, 7.4)$, $P_{12} = (3.3, 6.7)$, $P_{13} = (5.4, 6.2)$, $P_{14} = (6.2, 7.4)$, and $P_{15} = (6.4, 6.7)$. As a macroscopic result, the antenna prototype covers an area of 6.6×7.4 cm². More specifically, the maximum linear dimension of the antenna at the highest wavelength of operation is equal to 0.15λ with a reduction of more than 40% with respect to the corresponding quarter-wave resonant monopole.

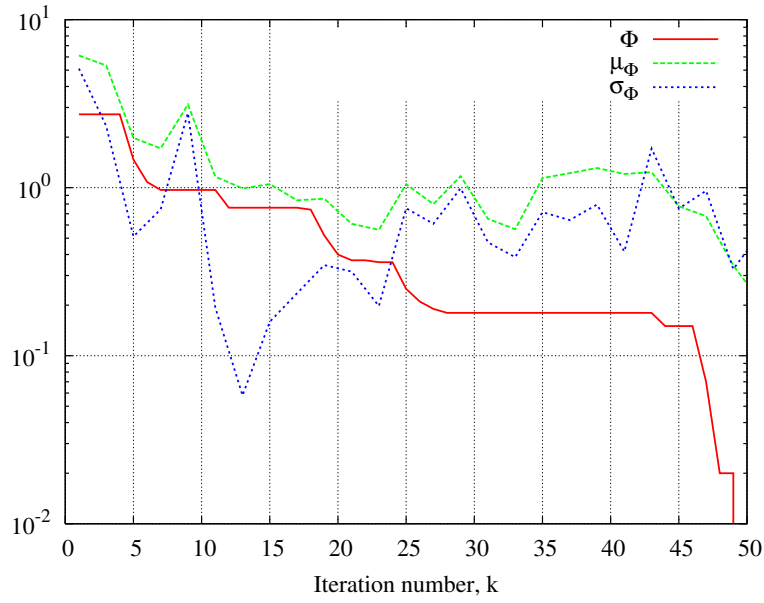


Figure 5.8: Behaviors of the cost function statistics during the iterative *PSO* optimization.

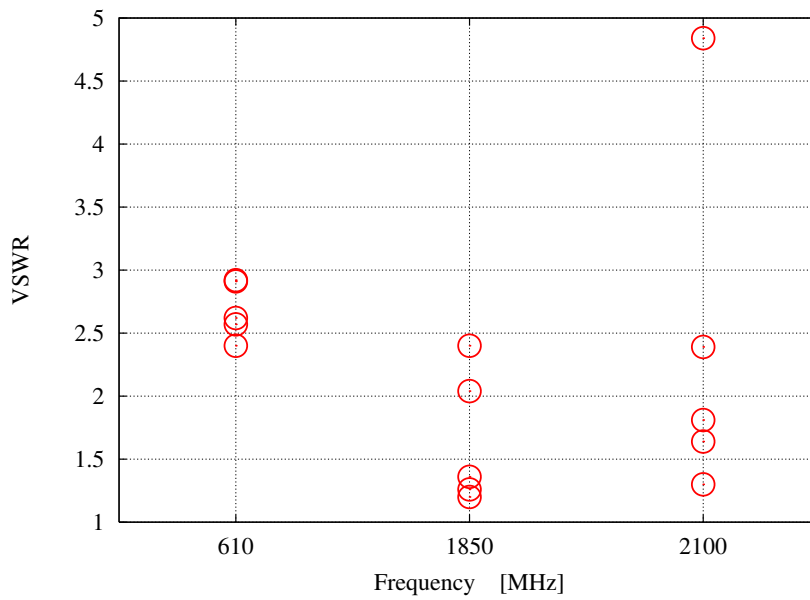


Figure 5.9: Simulated VSWR values, at the center of each frequency band, for the trial solutions at the convergence.

Wireless Service	Frequency Band [MHz]	VSWR Centerband	VSWR on Band
DVBH	606 ÷ 614	2.4	2.5
GSM	1800 ÷ 1900	1.2	1.8
UMTS	2000 ÷ 2200	1.3	1.9

Table 5.1: Simulated performances.



Figure 5.10: Three-band Antenna Prototype.

In order to validate the efficiency and reliability of the proposed antenna some numerical and experimental results are reported. To perform the experimental measurements, a prototype of the antenna has been built (Fig. 5.10) on a planar dielectric substrate (Arlon: thickness $h = 0.8\text{ mm}$, relative permittivity $\epsilon_r = 3.38$, $\tan \delta = 0.002$ at $f = 10\text{ GHz}$). The prototype, fed by a single $50\ \Omega$ RF port connected to the antenna structure in P_1 and mounted on a metallic ground plane, has been used to collect both VSWR and radiation patterns measurements in an anechoic chamber.

The electric performances of the synthesized antenna are summarized in Tab. 5.1. As far as the impedance matching is concerned, Figure 5.11 shows a comparison between measured and simulated VSWR values. As expected, the antenna resonances are located at the center of a DVBH channel ($f_0^{DVBH} = 610\text{ MHz}$), in the higher GSM band ($f_0^{GSM1800} = 1850\text{ MHz}$), and in correspondence with the UMTS band ($f_0^{UMTS} = 2100\text{ MHz}$). Besides the good agreement between the two plots (i.e., numerical and measured values), the antenna shows a good

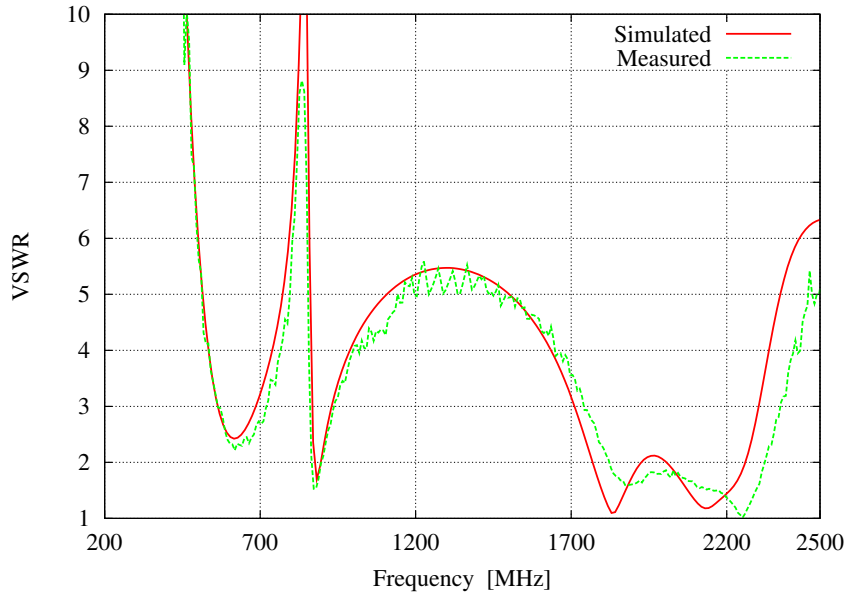
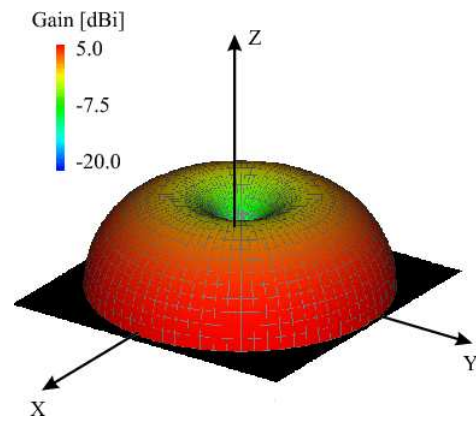


Figure 5.11: Simulated and measured VSWR values.

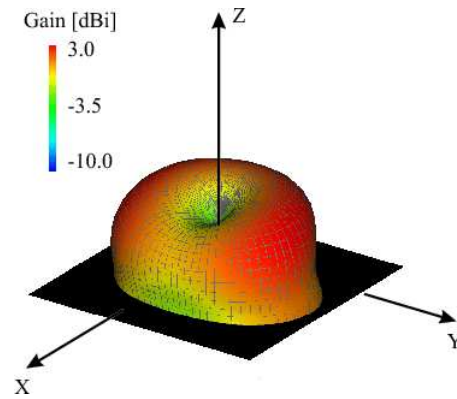
impedance matching in the GSM band ($1.2 \leq VSWR_{simulated}^{GSM1800} \leq 1.8$, $1.6 \leq VSWR_{measured}^{GSM1800} \leq 2.1$) and in the UMTS band ($1.3 \leq VSWR_{simulated}^{UMTS} \leq 1.9$, $1.3 \leq VSWR_{measured}^{UMTS} \leq 1.8$). On the other hand, an acceptable matching has been also obtained at the lowest working frequency devoted to the reception of a DVBH channel ($2.4 \leq VSWR_{simulated}^{DVBH} \leq 2.5$, $2.2 \leq VSWR_{measured}^{DVBH} \leq 2.3$). Higher VSWR values in this latter band are mainly caused by the constraint on the antenna size. As a matter of fact, a VSWR value below 2 : 1 can be easily reached by relaxing the miniaturization requirement (e.g., from $8 \times 8 [cm^2]$ to $9.5 \times 9.5 [cm^2]$).

As regards to the radiation properties, Figure 5.12 shows the simulated three-dimensional gain patterns computed at the center of each frequency band. As it can be observed, the radiation pattern is monopole-like at the lowest frequency [Fig. 5.12(a)], while some variations occur when the working frequency increases [Fig. 5.12(b)-(c)]. As a matter of fact, the antenna tends to work like a half-wave monopole in the highest frequency bands. Such a behavior is further pointed out by the appearance of additional lobes in the radiation diagram. Nevertheless, the omnidirectional behavior along the horizontal plane makes the antenna suitable for mobile wireless devices.

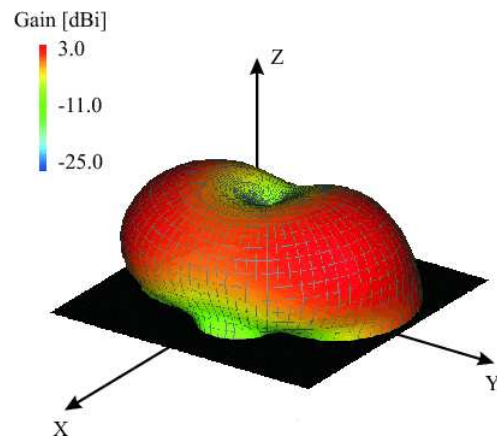
For completeness, the numerical values are compared with the measurements at the horizontal plane ($\theta = 90^\circ$) and at the vertical one ($\phi = 90^\circ$) (Fig. 5.13). Once again, measurements and simulations turn out to be in good agreement



(a)



(b)



(c)

Figure 5.12: Simulated 3D radiation patterns - (a) Total gain at $f_0^{DVBH} = 610 \text{ MHz}$; (b) Total gain at $f_0^{GSM1800} = 1850 \text{ MHz}$; (c) Total gain at $f_0^{UMTS} = 2100 \text{ MHz}$.

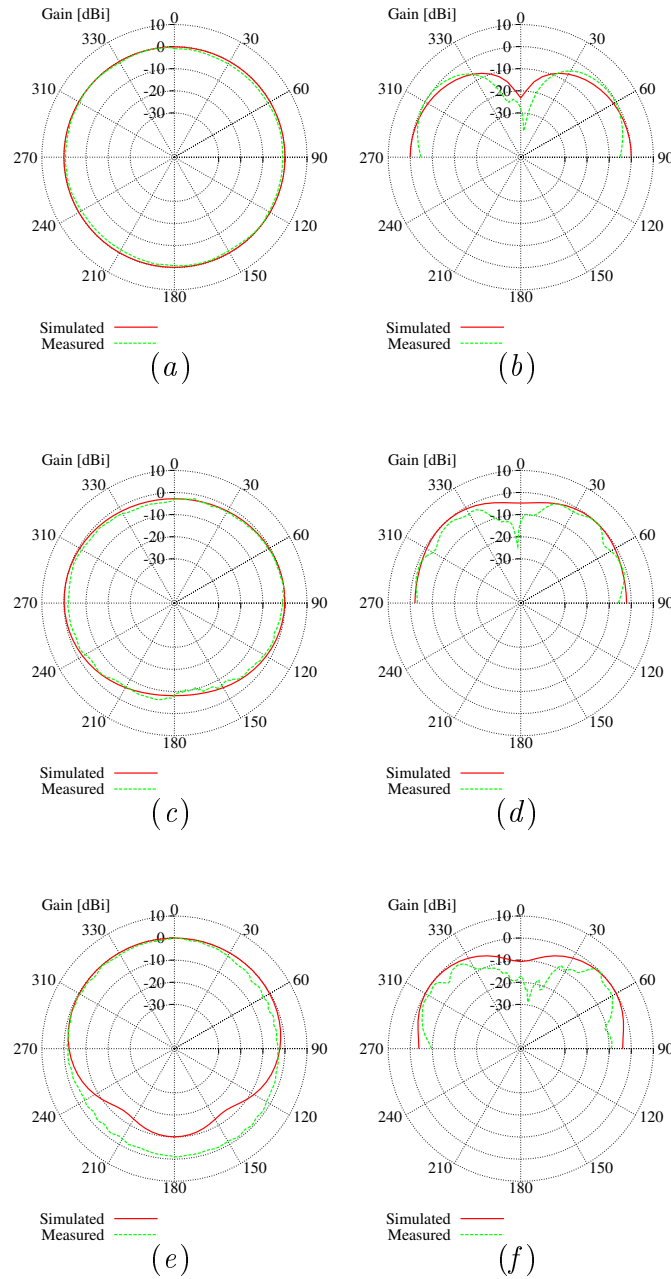
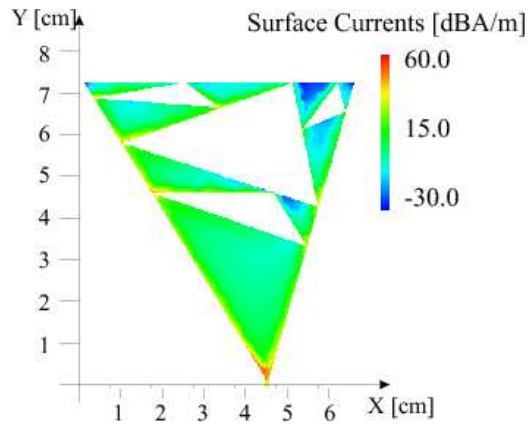
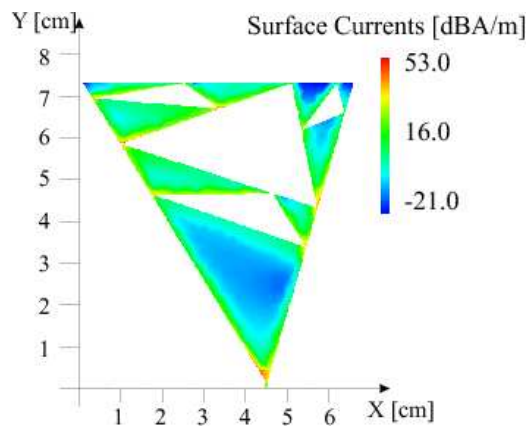


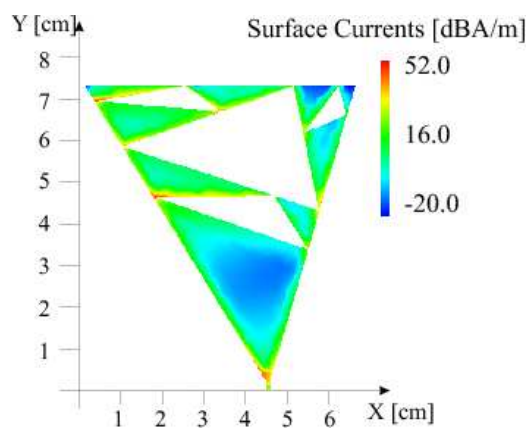
Figure 5.13: Simulated and measured radiation patterns - (a) Horizontal plane ($\theta = 90^\circ$) at $f_0^{DV BH} = 610 \text{ MHz}$; (b) Vertical plane ($\phi = 90^\circ$) at $f_0^{DV BH} = 610 \text{ MHz}$; (c) Horizontal plane ($\theta = 90^\circ$) at $f_0^{GSM1800} = 1850 \text{ MHz}$; (d) Vertical plane ($\phi = 90^\circ$) at $f_0^{GSM1800} = 1850 \text{ MHz}$; (e) Horizontal plane ($\theta = 90^\circ$) at $f_0^{UMTS} = 2100 \text{ MHz}$; (f) Vertical plane ($\phi = 90^\circ$) at $f_0^{UMTS} = 2100 \text{ MHz}$.



(a)



(b)



(c)

Figure 5.14: Simulated surface currents at (a) $f_0^{DVBH} = 610 \text{ MHz}$, (b) $f_0^{GSM1800} = 1850 \text{ MHz}$, and (c) $f_0^{UMTS} = 2100 \text{ MHz}$.

although some difference are present in the UMTS band [Fig. 5.13(*e*)-(*f*)]. They can be ascribed to the non-ideal behavior of the measurement environment at higher frequencies.

Finally, the simulated behaviors of the surface currents are shown in Fig. 5.14. As expected and because of the multi-band operation, the plots at the different frequencies significantly differ. Moreover, the variations of the surface current along the longitudinal direction show a trend similar to that of a quarter-wave monopole in the DVBH band [Fig. 5.14(*a*)], while they turn out to be close to that of a half-wave monopole at the higher working frequencies [Fig. 5.14(*b*)-(*c*)].

5.1.5 Conclusion

In this section, the perturbation of the geometry of different fractal antennas has been carefully analysed. Such an analysis has been carried out by studying the variations of the resonant frequencies of the antenna caused by the modification of its geometric descriptors. The result is a set of analytic relations that can be exploited in the design phase of the antenna. Unfortunately, only an exhaustive analysis of all the possible perturbations of the geometry and their combinations would provide an analytic tool able to correctly predict the resonant behavior of the antenna. This kind of solution is clearly computationally too expensive and it becomes completely unfeasible when high fractal iterations are considered. Consequently, the obtained relations have been used as a suitable initialization of an optimization procedure aimed at identifying the set of antenna parameters fitting all the project requirements. As a matter of fact, a good initialization can reduce both the time and the computational resources required by the optimization procedure. The effectiveness of the synthesis approach has been demonstrated by reporting a representative result concerning the synthesis of a three-band Sierpinski fractal antenna. Further investigations will be aimed at analysing other antenna characteristics such as the gain, the radiation patterns, or the bandwidth.

5.2 Spline-shaped Antennas

In this section, a preliminary assessment of an approach based on spline shapes for multi-band systems is presented. Unlike other methods, the multi-band behavior is obtained by modifying a spline curve, which describes the antenna geometry. Such a simple description allows one to generate in an easy fashion several candidate configurations aimed at satisfying both dimensional and electrical user-defined requirements. The results are cheap and low profile PCB antennas suitable for integration and mass production, as well.

5.2.1 Antenna Design

Let us consider a microstrip structure printed on a planar dielectric substrate. The geometry of the proposed antenna (Fig. 5.15) model is based on the Spline representation discussed in Sect. 3.1. Hence, the antenna geometry turns out to be uniquely identified by the values of the descriptive vector

$$\mathbf{s} = \{(y_i, z_i); i = 1, \dots, N; a_j; j = 1, \dots, 4\} \quad (5.15)$$

which includes the coordinates of the control points $\{P_i = (y_i, z_i); i = 1, \dots, N\}$ governing the spline curve that identifies the radiating part of the antenna, and a set of geometrical variables $\{a_j; j = 1, \dots, 4\}$ that describes the remaining part of the antenna structure.

As far as project constraints are concerned, the antenna must be able to operate over B frequency bands whose lower and higher limits are denoted by $f_{L_i}^\Psi$ and $f_{H_i}^\Psi$, respectively, with $i = 1, \dots, B$. Towards this end, the good impedance match is ensured by requiring the antenna to exhibit $VSWR$ values lower than a fixed threshold value $VSWR_{th}$ over the operating bands. Moreover, in order to avoid the reception of unwanted signals, a minimum threshold value $VSWR_{Rej}$ is imposed on the antenna impedance match behavior in the frequency ranges from $f_{L_j}^\Upsilon$ to $f_{H_j}^\Upsilon$, $j = 1, \dots, B - 1$, separating the operating bands. Concerning the geometrical constraints, the size of the antenna support must be limited to an area of $y_{max} \times z_{max} \text{ mm}^2$.

The optimal shape of the antenna (i.e., \mathbf{s}^{opt}) is determined by fitting the set of user-defined constraints and considering an iterative procedure [42] whose main blocks are an electromagnetic simulator based on the method-of-moment (MoM) [26] and a Particle Swarm Optimizer (PSO) [8]. Towards this end, the following cost function $\Psi(\mathbf{s})$ is adopted

$$\Psi(\mathbf{s}) = \sum_{i=1}^B \Psi_i(\mathbf{s}) + \sum_{j=1}^{B-1} \Upsilon_j(\mathbf{s}) \quad (5.16)$$

where

$$\Psi_i(\mathbf{s}) = \int_{f_{L_i}^\Psi}^{f_{H_i}^\Psi} \max \left\{ 0, \frac{VSWR(f) - VSWR_{th}}{VSWR_{th}} \right\} df \quad i = 1, \dots, B \quad (5.17)$$

are the terms concerned with the B operating bands, while

$$\Upsilon_j(\mathbf{s}) = \int_{f_{L_j}^\Upsilon}^{f_{H_j}^\Upsilon} \max \left\{ 0, \frac{VSWR_{Rej} - VSWR(f)}{VSWR_{Rej}} \right\} df \quad j = 1, \dots, B - 1 \quad (5.18)$$

are the terms related to the rejection bands.

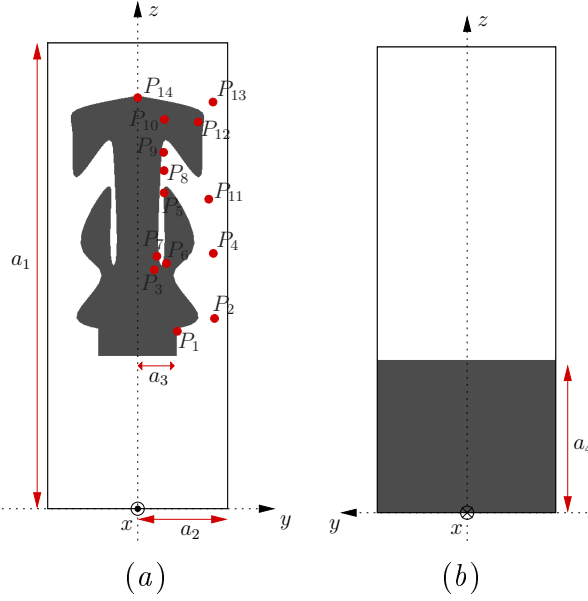


Figure 5.15: Antenna geometry - (a) Front view and (b) back view.

5.2.2 Numerical and Experimental Validation

In recent years, there has been a significant development of wireless communication systems for local area networks (WLANs). This has facilitated the connection and the data exchange between wireless devices, such as laptops, routers, PCs, and other portable wireless devices. For these applications, the Wi-Fi standard (IEEE 802.11 a/b/g/n) operating at 2.4 and 5 GHz is one of the most commonly used [96][97]. Therefore, there is a growing demand of radiating devices suitable for Wi-Fi applications.

In order to assess the effectiveness of the proposed synthesis approach, a representative result regarding the design of a dual-band PCB antenna suitable for Wi-Fi applications is described. The proposed antenna is suitable for Wi-Fi bands and it guarantees good impedance matching conditions at the working frequencies centered at 2.448 GHz and 5.512 GHz . More in detail, an antenna structure characterized by $N = 14$ control points has been optimized in order to operate from $f_{L1}^{\Psi} = 2.412\text{ GHz}$ up to $f_{H1}^{\Psi} = 2.484\text{ GHz}$ and from $f_{L2}^{\Psi} = 5.150\text{ GHz}$ up to $f_{H2}^{\Psi} = 5.875\text{ GHz}$ with $VSWR$ values lower than $VSWR_{th} = 2$. Moreover, in order to force a true dual-band behavior the antenna is required to exhibit a rejection band with $VSWR$ values greater than $VSWR_{Rej} = 10$ from $f_{L1}^{\Upsilon} = 3.5\text{ GHz}$ to $f_{H1}^{\Upsilon} = 4.0\text{ GHz}$. Concerning the geometrical constraints, the maximum antenna dimensions have been set to $y_{max} = z_{max} = 70\text{ mm}$.

After the optimization process, the geometric parameters of the prototype

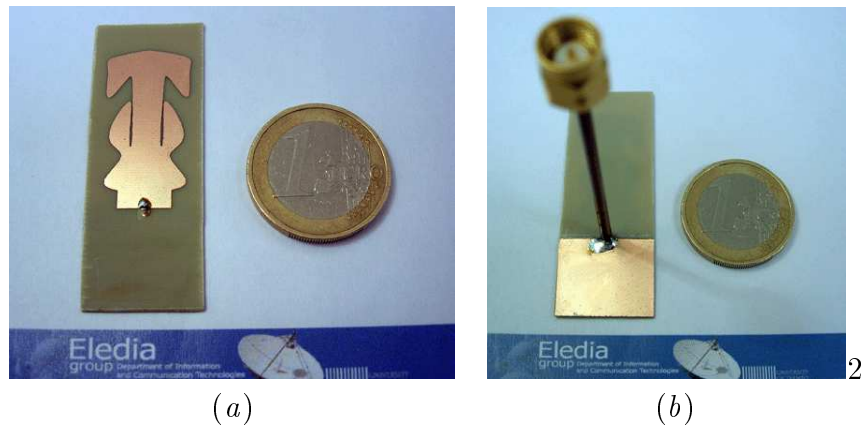


Figure 5.16: Antenna Prototype - (a) Front view and (b) back view.

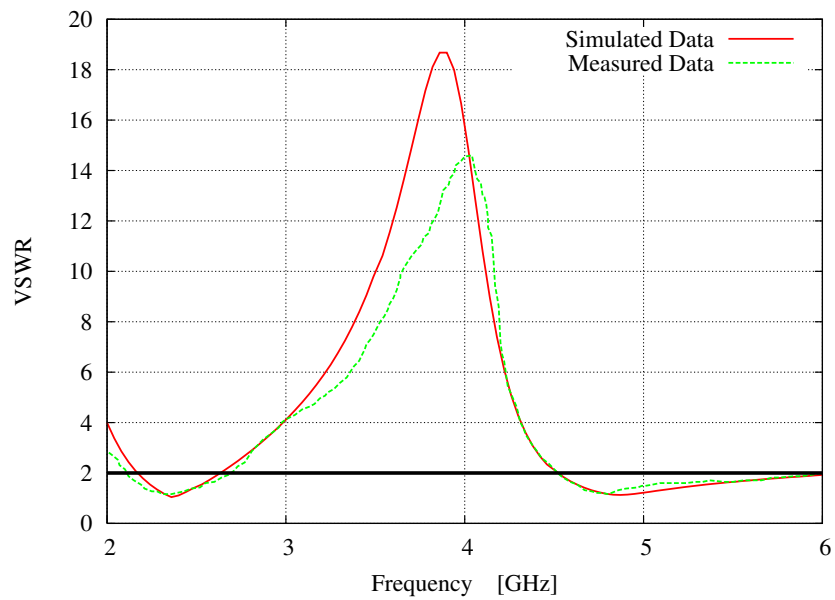


Figure 5.17: Simulated and measured VSWR values.

turned out to be: $a_1 = 50.1\text{ mm}$, $a_2 = 9.6\text{ mm}$, $a_3 = 4.2\text{ mm}$, and $a_4 = 16.4\text{ mm}$. Moreover, the coordinates of the spline control points resulted to be: $y_1 = 4.2\text{ mm}$, $z_1 = 19.3\text{ mm}$, $y_2 = 8.1\text{ mm}$, $z_2 = 20.2\text{ mm}$, $y_3 = 1.7\text{ mm}$, $z_3 = 25.7\text{ mm}$, $y_4 = 8.0\text{ mm}$, $z_4 = 27.2\text{ mm}$, $y_5 = 2.7\text{ mm}$, $z_5 = 36.0\text{ mm}$, $y_6 = 2.8\text{ mm}$, $z_6 = 33.6\text{ mm}$, $y_7 = 3.0\text{ mm}$, $z_7 = 25.7\text{ mm}$, $y_8 = 1.9\text{ mm}$, $z_8 = 25.7\text{ mm}$, $y_9 = 2.6\text{ mm}$, $z_9 = 37.8\text{ mm}$, $y_{10} = 2.6\text{ mm}$, $z_{10} = 41.3\text{ mm}$, $y_{11} = 7.5\text{ mm}$, $z_{11} = 32.7\text{ mm}$, $y_{12} = 6.4\text{ mm}$, $z_{12} = 41.2\text{ mm}$, $y_{13} = 8.1\text{ mm}$, $z_{13} = 43.0\text{ mm}$, $y_{14} = 0.0\text{ mm}$, and $z_{14} = 44.3\text{ mm}$. As it can be verified, the synthesized solution fits the size requirement being characterized by an overall dimension of $50.2 \times 19.2\text{ mm}^2$.

The performances of the dual-band spline-shaped antenna have been numerically and experimentally evaluated. Towards this end, a prototype of the synthesized antenna (Fig. 5.16) has been printed with a photo-lithographic process on an Arlon dielectric substrate ($\epsilon_r = 3.38$) of 0.78 mm thickness. The prototype has been equipped with a SMA connector and fed by a coaxial cable in order to measure its electrical parameters.

As far as the impedance matching is concerned, Figure 5.17 shows a comparison between simulated and measured VSWR values. As it can be noticed, there is a good agreement between measured and simulated values over the entire frequency range. Moreover, the obtained results confirm that the antenna design as well as the corresponding prototype fit the project guidelines showing a VSWR lower than 2 in both the Wi-Fi operating bands. The measured bandwidths turn out to be quite large. The former is equal to 500 MHz , from 2.1 up to 2.6 GHz , and a fractional bandwidth equal to 21%. The second one is equal to 1.5 GHz , from 4.5 up to 6 GHz , with a fractional bandwidth of 29%. Such a wideband behavior is due to the spline shape that already demonstrated, as other planar monopole shapes, its effectiveness and reliability in designing wideband and ultra-wideband antennas [42].

As regards to the radiation properties of the prototype, the three-dimensional radiation patterns of the device under test are displayed in Fig. 5.18. Each diagram refers to the central frequency of a *Wi-Fi* working band (i.e., $f_1 = 2.448\text{ GHz}$ and $f_2 = 5.512\text{ GHz}$). As expected, the antenna behaves as a dipolar radiator at both the working frequencies [Figs. 5.18(a)-(b)], showing an omnidirectional radiation pattern on the horizontal plane. Moreover, it can be observed that no additional lobes appear in the radiation patterns at the higher frequency band confirming the multi-band behavior of the antenna. As a matter of fact, the presence of additional lobes would indicate that the current mode at the 5 GHz band is a simple overtone of the fundamental mode in the 2.4 GHz band, analogous to what occurs at higher frequencies with a wire monopole or a dipole antenna. For completeness, the co-polar components [Figs. 5.18(c)-5.18(d)] and

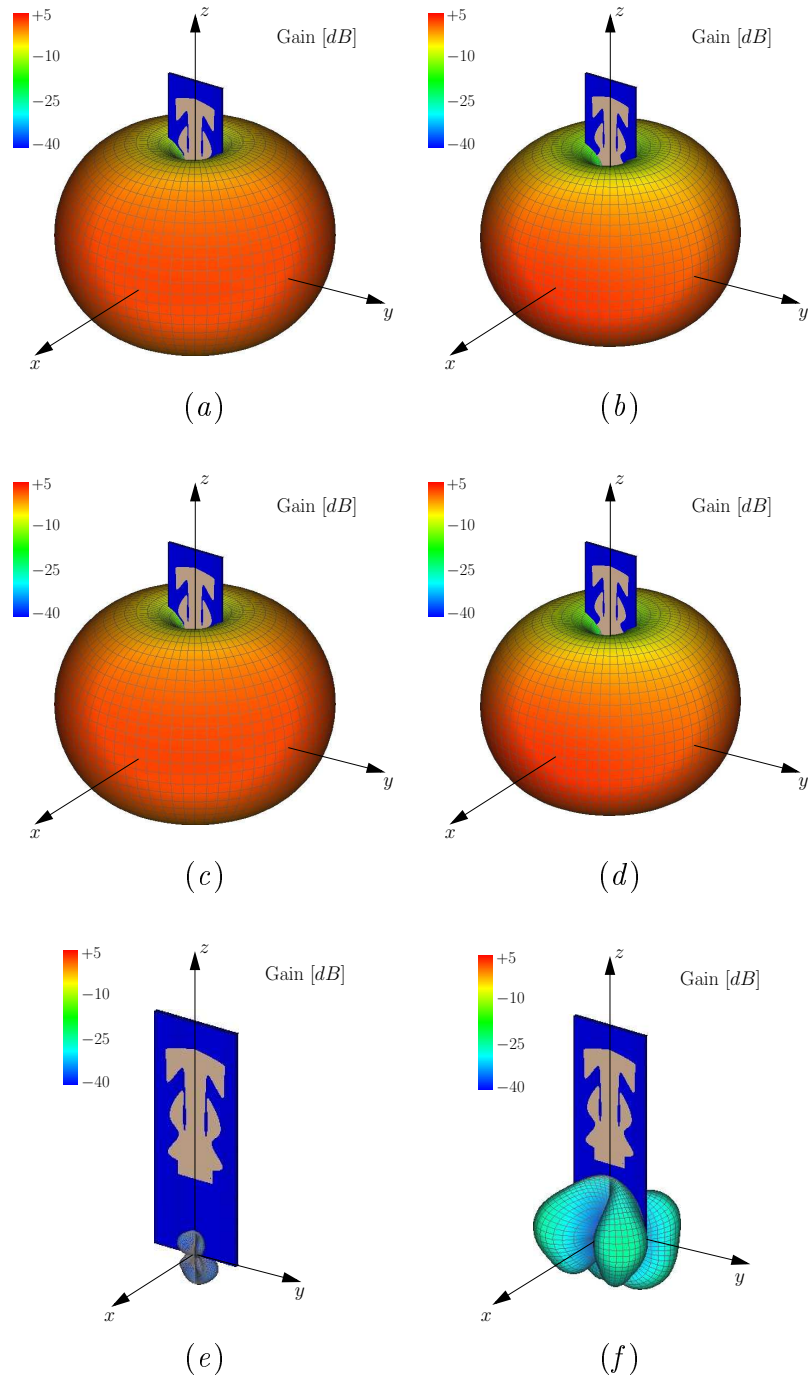


Figure 5.18: Simulated 3D radiation patterns - Total gain at (a) $f_1 = 2.448 \text{ GHz}$ and (b) $f_2 = 5.512 \text{ GHz}$. Co-polar component at (c) $f_1 = 2.448 \text{ GHz}$ and (d) $f_2 = 5.512 \text{ GHz}$. Cross-polar component at (e) $f_1 = 2.448 \text{ GHz}$ and (f) $f_2 = 5.512 \text{ GHz}$.

5.2. SPLINE-SHAPED ANTENNAS

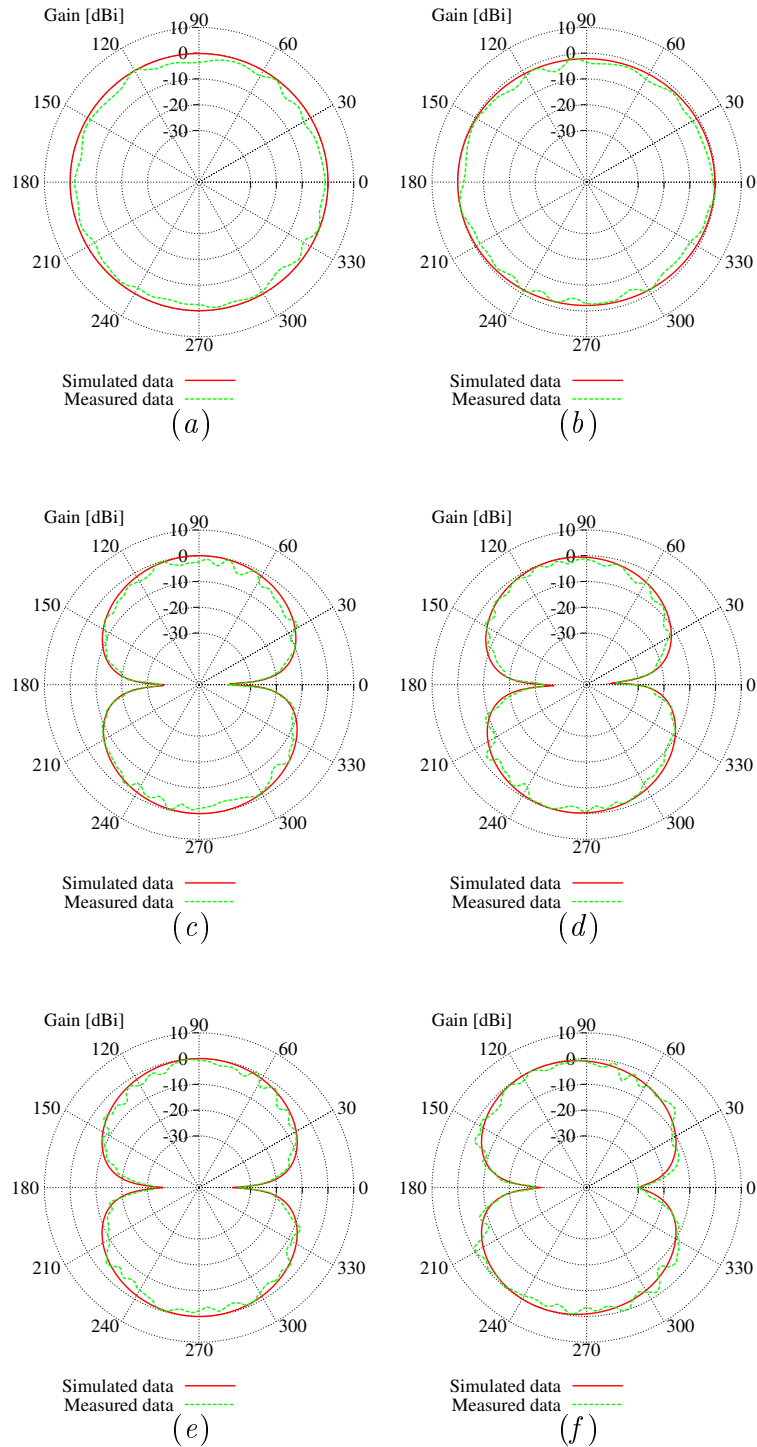


Figure 5.19: Simulated and measured radiation patterns - Horizontal plane ($\theta = 90^\circ$) at (a) $f_1 = 2.448 \text{ GHz}$ and (b) $f_2 = 5.512 \text{ GHz}$. Vertical plane ($\phi = 0^\circ$) at (c) $f_1 = 2.448 \text{ GHz}$ and (d) $f_2 = 5.512 \text{ GHz}$. Vertical plane ($\phi = 90^\circ$) at (e) $f_1 = 2.448 \text{ GHz}$ and (f) $f_2 = 5.512 \text{ GHz}$.

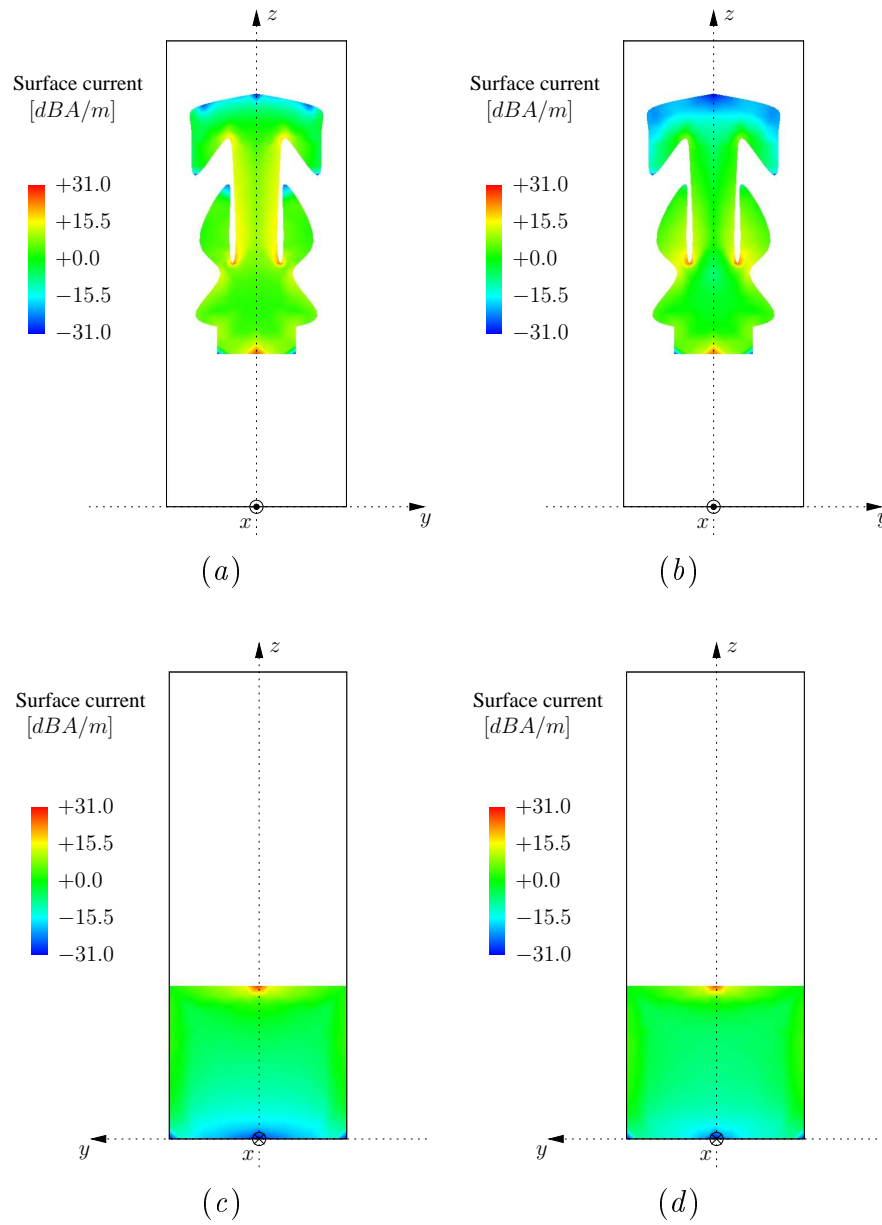


Figure 5.20: Simulated surface current - Front view at (a) $f_1 = 2.448 GHz$ and (b) $f_2 = 5.512 GHz$. Back view at (c) $f_1 = 2.448 GHz$ and (d) $f_2 = 5.512 GHz$.

the cross-polar ones [Figs. 5.18(e)-5.18(f)] are shown, as well. As it can be observed, the cross-polar components turn out to be smaller than the co-polar ones and the corresponding maximum gain values are equal to -34 dB (vs. 2 dB) and -24 dB (vs. 3 dB) at 2.4 GHz and 5 GHz , respectively. In order to further assess and experimentally validate these indications on the radiation features of the antenna model, a set of measurements has been carried out by probing the synthesized prototype in a controlled measurement environment. The obtained results are shown in Fig. 5.19. Once again, there is a good agreement between simulated and measured values. The measured patterns confirm the omnidirectional behavior of the antenna in the horizontal plane [$\theta = 90^\circ$ - Figs. 5.19(a)-5.19(b)] as well as the presence of the nulls of the radiation diagrams along the z -direction [$\phi = 0^\circ$ - Figs. 5.19(c)-5.19(d); $\phi = 90^\circ$ - Figs. 5.19(e)-5.19(f)].

Finally, for completeness, Figure 5.20 gives a pictorial representation of the currents flowing on the metallic surfaces of the antenna geometry. More specifically, the amplitudes of the surface currents computed at f_1 and f_2 are displayed. As expected, the concentration of the current shifts to different portions of the antennas in the two different operating bands further confirming the true dual-band behavior of the antenna.

5.2.3 Conclusion

In this section, an approach for the synthesis of multiband spline-shaped antennas has been described. A representative result regarding the synthesis of a dual-band PCB antenna suitable for Wi-Fi applications has been reported in order to preliminarily assess the effectiveness of the proposed approach. The antenna has been synthesized to achieve a good impedance matching in both the 2.4 and 5 GHz Wi-Fi bands. A prototype of the synthesized antenna has been built on a dielectric substrate. The reliability of the antenna model as well as the corresponding prototype has been assessed by means of numerical simulations and experimental measurements of both electrical and radiation parameters.

Chapter 6

Synthesis of UWB Aperiodic Linear Arrays

In recent years, much research has been invested in finding new techniques for the design of array layouts that are able to operate over ultra-wide bandwidths. In order to be considered “ultra-wideband” (UWB), an array must exhibit no grating lobes and low sidelobe levels when the operating frequency is increased greatly, or equivalently, when the electrical distance between the elements becomes large. Such properties are usually obtained by designing array layouts with nonuniform element spacing. Among nonuniform arrays, the so-called random arrays have been the first examples studied in the 1960s [98][99]. The locations of their elements are chosen randomly and independently from a probability density distribution. Once the element positions have been defined, the array represents a particular realization from the set of all the possible arrays determined by the given probability distribution [100][101]. One advantage of random arrays is that they can be probabilistically analyzed [102] and their patterns can be predicted [103]. Random arrays are usually void of grating lobes, however, they typically exhibit only moderate sidelobe level suppression, making them less than ideal for many applications [104]. Additionally, there is no minimum element spacing restriction in random arrays, potentially creating issues with antenna overlap or strong mutual coupling when the array is physically realized.

In order to avoid the issues of random arrays, various forms of optimized aperiodic arrays have been developed. One early example derives an aperiodic linear array layout from a periodic structure by using a Genetic Algorithm (GA) to turn specific elements on or off [105]. Another technique uses the GA to perturb the element locations in a periodic array to obtain reduced sidelobes and grating lobes during scanning (analogous to an increase in array bandwidth) [106]. These techniques are usually limited to small array sizes due to the rapidly increasing scope of the optimization problem as the array grows larger.

More recently, new methodologies have arisen that aim to define a relatively large array layout using a small set of parameters. Polyfractal arrays

[107][108][104] incorporate the ordered and disordered properties of fractal-random arrays [109], with the use of connection factors and a limited set of GA-defined generators to fully determine array layout. The recursive nature of polyfractal arrays allows the description of the array layout by using only a few parameters and additionally, the iterated function systems employed to build the structure are also useful for rapid beamforming calculations. Another method used to describe complex array layouts introduced in [103] requires fewer parameters for moderate sized arrays (100 to 1000 elements) by using raised power series (RPS) representations. These techniques allow the synthesis of aperiodic arrays that operate over ultra-wide bandwidths with excellent sidelobe suppression and no grating lobes. Most recently, a powerful optimization technique known as the Covariance Matrix Adaption Evolutionary Strategy (CMA-ES) has been applied to directly optimize the element spacings in a linear array to meet a targeted UWB performance goal [110]. This approach offers the main advantage of being able to successfully handle problems characterized by a large number of variables and is typically useful for optimizing arrays up to 100 elements.

The analysis and the optimization of the aforementioned arrays is usually carried out by considering isotropic radiating elements. However, when the array is employed in practical applications, the presence of realistic antenna elements must be taken into account. The element must be carefully designed in order to meet certain design requirements. It must primarily be able to operate with acceptable input impedance over a very large frequency range. Several antennas showing a good impedance matching over an ultra-wide bandwidth have been proposed over the past decade. Their designs are usually based on the optimization of the geometrical descriptors of reference shapes, such as triangles [111], rectangles [112], circles [59], bow-tie structures [113], and ellipses [60][114]. These techniques allow the description of the geometrical characteristics of the antenna in a simple and effective way, however, they lack flexibility in generating the variety of different antenna configurations which are usually required to fulfill difficult design requirements.

An alternative and much more flexible approach is to represent the antenna geometry with spline curves. The spline representation allows the definition of complex curvilinear shapes which are described by a small set of control points. In [115] a broadband planar dipole antenna whose contour is modeled with a spline curve was presented. The design begins with a standard flared dipole antenna with a circular and a rectangular section; the final antenna geometry is obtained by way of a GA optimization procedure that determines the positions of a set of control points which define the circular shape. Similarly, John *et al.* proposed in [116] the use of a spline curve to describe the contour of a printed monopole antenna. The optimization is also carried out by means of a GA, however, the positions of the control points are not varied starting from a reference curve as in [115]. The same authors then extended the spline representation technique to include the groundplane in [117]. The effectiveness of a

spline-based representation integrated with a PSO has been assessed in [43]. The use of the PSO is preferable over the binary GA when real-valued optimization problems are to be handled. Moreover, it offers several advantages over the GA such as simplicity of implementation and calibration, and a more significant level of control to prevent stagnation of the optimization process [47]. The synthesis approach presented in [43] has been successfully exploited by the same authors to design UWB antennas for communication applications [44][45].

As previously mentioned, a good impedance match over an extended bandwidth is a necessary requirement for antennas that must be used as elements of an UWB array, however, maintaining low cross-polarized radiation over the operating bandwidth is also an important factor deserving of consideration. Indeed, it is not uncommon for UWB antennas to develop several lobes in the radiation pattern and possess increased cross-polarized radiation at their upper range of operating frequencies. This behavior must be avoided since it will degrade the performances of the entire UWB array.

In this chapter, a methodology for the design of UWB aperiodic arrays populated by realistic radiating elements is proposed. The synthesis of the single array element is carried out by means of an integrated strategy that combines a PSO together with a spline-based representation of the antenna geometry. Unlike [43], however, proper attention is paid to the cross-polarization of the antenna during the synthesis process in order to produce UWB elements that minimize all the aforementioned undesirable characteristics. Towards this end, a new term of the PSO cost function is included for optimizing the antenna element. The linear UWB antenna array layout is optimized through use of the Covariance Matrix Adaptation Evolutionary Strategy (CMA-ES) as in [118]. Consequently, the operating frequency range of the synthesized element is carefully taken into account during the optimization of the array layout. The final result is a linear array of practical antenna elements capable of efficiently operating with very low sidelobe levels and no grating lobes over an ultra-wide bandwidth.

6.1 Design Approach

The first step in the proposed design approach is the synthesis of a suitable radiating element. Towards this end, let us consider the spline-based antenna geometry discussed in Sect. 3.1. The antenna structure is based on two copper layers printed on opposite sides of a dielectric substrate of thickness s_t characterized by relative permittivity ε_r and loss tangent δ_t and it is fully identified by the parameters shown in Fig. 6.1. Moreover, the following geometric constraints are imposed: $f_w = 2y_1$, $f_l = z_1$, $y_N = 0.0$, and $g_w = s_w$.

The antenna performance requirements are taken into consideration during optimization. Before determining a cost function, the requirements must be formulated. The first one is that the antenna must exhibit acceptable input impedance over a large bandwidth. Therefore, the constraint

$$|s_{11}(f)| \leq \eta_1 \quad f_1 \leq f \leq f_2 \quad (6.1)$$

is imposed on the antenna return loss, where η_1 indicates the maximum value permissible for the magnitude of the s_{11} parameter, while f_1 and f_2 are the respective lowest and highest frequencies of the band of interest. The second requirement is that the antenna must exhibit low cross-polarized radiation over the prescribed operating bandwidth. Since the elements will be placed side-by-side in parallel to form the array, the requirement can be limited to the xy -plane. Consequently the following constraint

$$\hat{g}_\phi(f) \leq \eta_2 \quad f_1 \leq f \leq f_2 \quad (6.2)$$

is imposed, where η_2 is the target value of cross-polarized gain and

$$\hat{g}_\phi(f) = \frac{1}{M} \sum_{m=1}^M g_\phi \left(\theta = \frac{\pi}{2}, \phi = -\frac{\phi_0}{2} + m \frac{\phi_0}{M-1} \right) \quad m = 0, \dots, M-1 \quad (6.3)$$

is the spatially averaged cross-polarized gain (the cross-polarized gain is indicated with g_ϕ) in the xy -plane calculated over M points in the range $-\frac{\phi_0}{2} \leq \phi \leq \frac{\phi_0}{2}$.

Lastly, the antenna is required to be compact. Rather than incorporate this characteristic into the optimization cost function, it is implemented by fixing certain input parameters. Consequently, the respective width and the length of the substrate are limited to $s_w \leq W_{max}$ and $s_l \leq L_{max}$, where W_{max} and L_{max} are the maximum allowable antenna dimensions.

The search for the optimal antenna geometry is carried out by means of the particle swarm optimization technique [8][119]. For integration into PSO, all the parameters to be optimized are collected into a single vector

$$\alpha = \{s_w, s_l, g_l, (y_n, z_n), n = 1, \dots, N-1, z_N\} \quad (6.4)$$

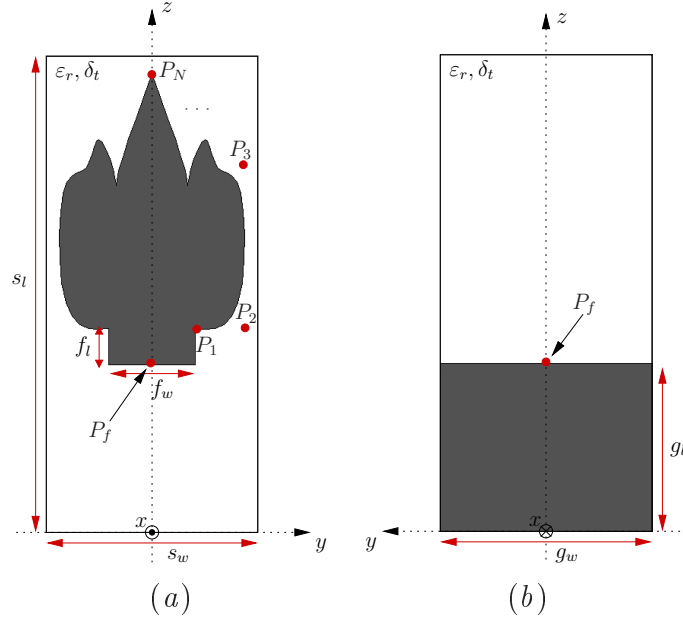


Figure 6.1: Array element geometry. (a) Front view and (b) back view.

. The parameters which are not optimized are those that are subject to constraints, i.e. $\{g_w, f_w, f_l, y_N\}$, or that are related to the adopted dielectric substrate, i.e. $\{s_t, \epsilon_r, \delta_t\}$. When the values of α are chosen, then α fully identifies a particular antenna configuration, or equivalently, a particular position of the PSO particle in the solution space. At the beginning of the particle swarm optimization technique (i.e. iteration $k = 0$), a swarm of R particles is randomly positioned in the solution space, corresponding to R trial antenna configurations $\alpha_{r,k}$; $r = 1, \dots, R$. With successive iterations, the positions of each particle are iteratively modified according to the knowledge of the “best” location encountered by itself and by the other particles. The quality of a location (i.e. acceptability of an antenna configuration) is evaluated by means of a suitable cost function Ω that takes into account the different performance requirements. By integrating (6.1) and (6.2), the cost function is defined as

$$\Omega(\alpha) = \int_{f_1}^{f_2} [\omega_1(f) + \omega_2(f)] df \quad (6.5)$$

where

$$\omega_1(f) = \begin{cases} \frac{|s_{11}(f)| - \eta_1}{\eta_1} & \text{if } |s_{11}(f)| > \eta_1 \\ 0 & \text{if } |s_{11}(f)| \leq \eta_1 \end{cases} \quad (6.6)$$

$$\omega_2(f) = \begin{cases} \frac{\hat{g}_\phi(f) - \eta_2}{\eta_2} & \text{if } \hat{g}_\phi(f) > \eta_2 \\ 0 & \text{if } \hat{g}_\phi(f) \leq \eta_2 \end{cases} \quad (6.7)$$

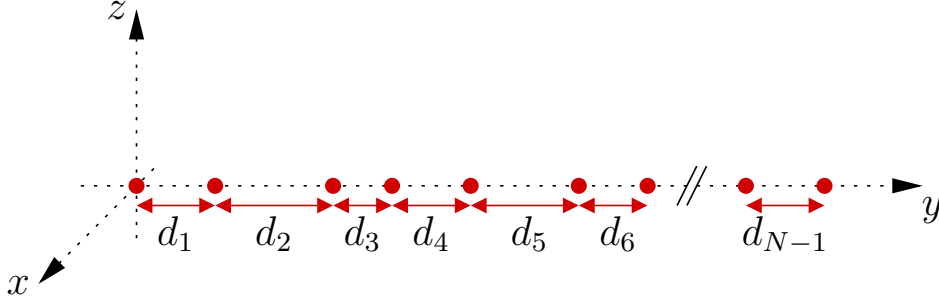


Figure 6.2: Array parametrization.

It is easily seen from (6.5)-(6.7) that the cost function $\Omega(\alpha)$ assumes a value equal to zero only when the trial antenna configuration α fulfills all of the design requirements. The optimization procedure ends when the maximum number of K iterations has been reached or when the value of the cost function Ω falls below a user-defined threshold γ .

After the single element has been synthesized, a suitable UWB array layout of Q elements is generated by directly optimizing each element position (spacing) in the linear array. For such a challenging optimization task where there can be a very large number of parameters, a very powerful evolutionary strategy must be employed. The recently developed CMA-ES is applied for this task [120][118]. The optimization technique is based on the movement of a multivariate normal distribution about the solution space to search for the global optimum. The parameters optimized by the CMA-ES are the $Q - 1$ distances d_q ; $q = 1, \dots, Q - 1$ between two consecutive elements of the array (Fig. 6.2). These parameters are collected in the vector $\beta = \{d_q; q = 1, \dots, Q - 1\}$ which identifies a trial array layout. The performance of the trial array is evaluated based solely on the peak sidelobe level (SLL) at a single value for the minimum element spacing d_{min} at the highest intended operating frequency f_2 . Consequently the simple cost function Φ is used for the optimization of the array, where

$$\Phi(\beta) = -SLL^{dB}(d_{min}). \quad (6.8)$$

In order to control the minimum element spacing of the array, the constraint

$$d_q \geq c\lambda_1 \quad q = 1, \dots, Q - 1 \quad (6.9)$$

is imposed during the optimization. In (6.9), $c \in \mathbb{R}$ is a user-defined coefficient and λ_1 is the wavelength corresponding to the lowest operating frequency f_1 .

<i>Spline Control Point Coordinates [mm]</i>			
P_1	P_2	P_3	P_4
(6.20, 29.22)	(13.51, 28.71)	(13.39, 53.32)	(8.78, 50.06)
P_5	P_6	P_7	P_8
(8.03, 59.74)	(4.38, 49.11)	(5.99, 49.18)	(0.00, 65.75)

Table 6.1: Coordinates of the spline control points describing the patch geometry of the synthesized antenna element.

6.2 Optimized Antenna System

6.2.1 Element Geometry and Array Layout

The design procedure described in the previous section is used to synthesize an UWB antenna array operating from $f_1 = 2\text{ GHz}$ to $f_2 = 6\text{ GHz}$, i.e. having a fractional bandwidth of 100%. The radiating element is accordingly optimized for the same frequency range. The element is designed on an Arlon dielectric substrate characterized by $\epsilon_r = 3.38$ and $\delta_t = 0.0025$ and having a thickness of $s_t = 0.8\text{ mm}$. Moreover, its dimensions must be smaller than $W_{max} = L_{max} = 80\text{ mm}$. Finally, $N = 8$ control points are considered for the spline representation of the antenna geometry.

For antenna performance, a return loss greater than ($\eta_1 = -10\text{ dB}$) is desired over the entire operating bandwidth, as is typical for communications applications. Concerning the goal in (6.2), the averaged cross-polarized gain is calculated over $M = 5$ points in an angular range of $\phi_0 = 120^\circ$ and must be lower than $\eta_2 = -30\text{ dB}$.

The antenna element optimization is carried out via PSO with a swarm size of $R = 6$ particles, a convergence threshold equal to $\gamma = 10^{-5}$ and a maximum number of iterations $K = 200$. The optimized upper-patch spline control points are shown in Tab. 6.1 with the remaining antenna descriptors given by $s_w = 68.27\text{ mm}$, $s_l = 30.20\text{ mm}$, and $g_l = 24.10\text{ mm}$.

The CMA-ES technique is then used to obtain the layout of an array of $Q = 50$ copies of the optimized element arranged in parallel along the y -axis. The array is optimized for best performance at minimum element spacing $d_{min} = 4\lambda_2$, λ_2 being the wavelength corresponding to the highest operating frequency f_2 . In order to reduce the coupling among the elements, the spacing coefficient c is set to 1. The locations of the antenna elements obtained after the optimization are shown in Fig. 6.3. The minimum, average and maximum element spacings are $1.00\lambda_1$, $1.96\lambda_1$ and $3.60\lambda_1$, respectively.

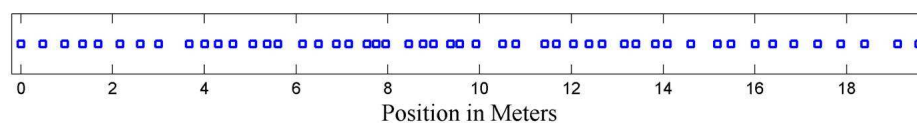


Figure 6.3: Positions (in meters) in the elements of the optimized array layout.

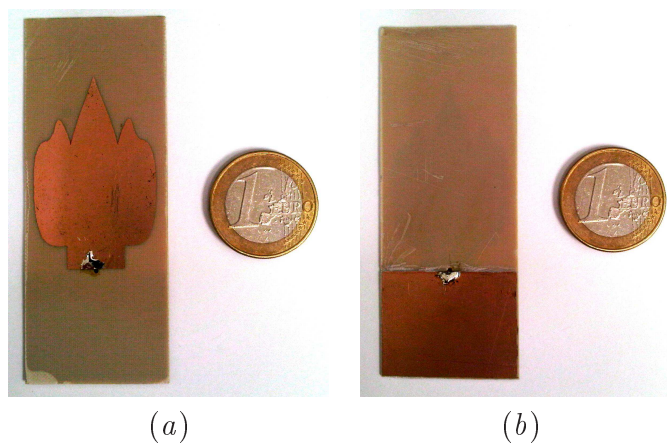


Figure 6.4: Prototype of the synthesized array element. (a) Front view and (b) back view.

6.2.2 Element Performances

This section is aimed at presenting the performance of the optimized single array element. In order to experimentally validate the numerical simulations, a prototype of the antenna has been constructed by means of a photolithographic technology (Fig. 6.4). The prototype has been equipped with a standard SMA connector and analyzed via a vector network analyzer. The measurements have been collected in a non-controlled environment.

Fig. 6.5 gives a comparison between simulated and measured return loss values for the optimized antenna. The optimized antenna exhibits a ultra-wide bandwidth with simulated $|s_{11}(f)| \leq -10 \text{ dB}$ covering the entire band from 2.0 to 6.0 GHz , corresponding to a fractional bandwidth of 100%. As can be seen, the measured antenna s -parameters are in good agreement with the prediction of the simulation.

Several radiation patterns of the optimized antenna are shown in Fig. 6.6. Three-dimensional total gain plots are given for operating frequencies of 2, 4, and 6 GHz . It is observed that the antenna presents a classical monopolar-like behavior at the lowest frequency [Fig. 6.6(a)], while some distortions appear as the operating frequency is increased [Figs. 6.6(b) and 6.6(c)].

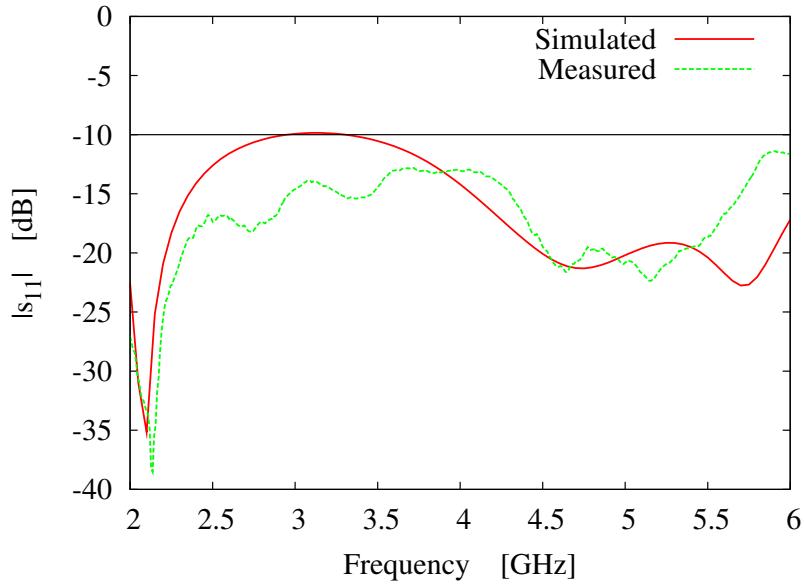
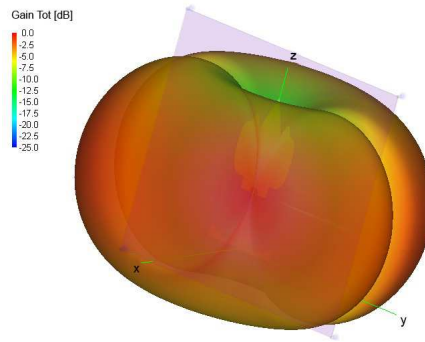


Figure 6.5: Simulated and measured s_{11} magnitude values exhibited by the synthesized array element.

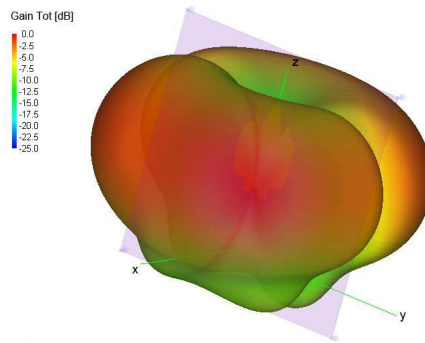
In addition to total gain, the cross-polarized radiation of the antenna is also evaluated as it pertains to the goal assigned in (6.2). Fig. 6.7 shows the co-polarized and cross-polarized gain in the plane of $\theta = \frac{\pi}{2}$ for the three previously mentioned operating frequencies. Co-polarized gain remains nearly flat in the range $-\frac{\pi}{2} \leq \phi \leq \frac{\pi}{2}$ with a variation less than 5 dB . As desired, cross-polarized gain falls below -30 dB at 4 and 6 GHz [Fig. 6.7(a) and 6.7(b)], however, an increase is observed at the upper limit of the operating frequency band [6 GHz - Fig. 6.7(c)].

6.2.3 Array Performances

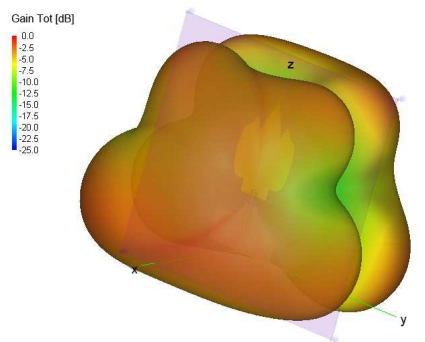
The layout of an array of $Q = 50$ elements was determined for the synthesized element by means of the direct CMA-ES optimization technique. The result is an array exhibiting a maximum peak sidelobe level of -12.9 dB at an element spacing of up to 4λ when the main beam is steered to broadside. The performance of the array has also been evaluated over an extended bandwidth (up to 10λ) with the results shown in Fig. 6.8. Even though the array was optimized for use up to a minimum element spacing of 4λ (for a 4 : 1 frequency bandwidth when the array is used with a minimum element spacing of λ at the lowest operating frequency), the array is characterized by a usable peak sidelobe level lower than -6 dB at up to 10λ (for a 10 : 1 frequency bandwidth under the same condition).



(a)

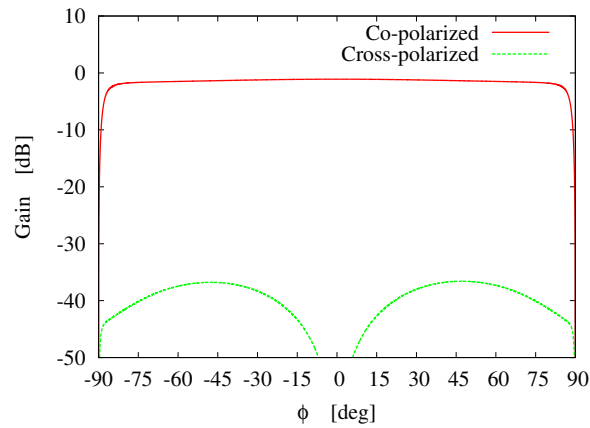


(b)

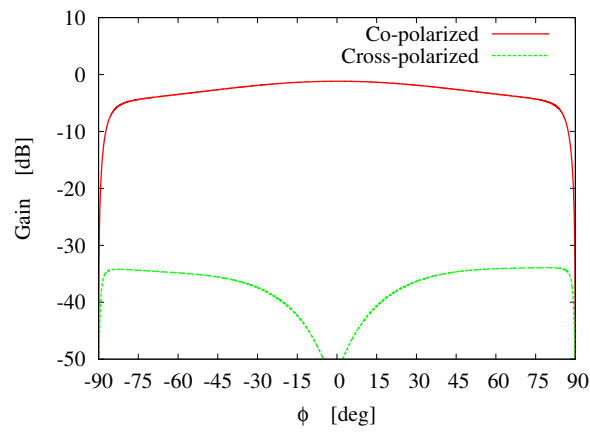


(c)

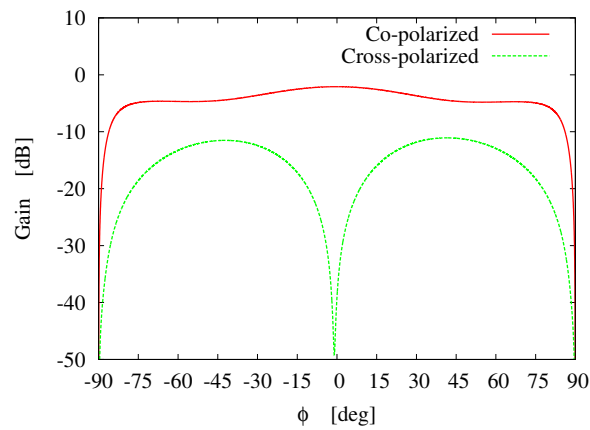
Figure 6.6: Three-dimensional representation of the total gain pattern at (a) 2, (b) 4 and (c) 6 GHz.



(a)



(b)



(c)

Figure 6.7: Behavior of the co-polarized and cross-polarized gain components in the plane of $\theta = \frac{\pi}{2}$ at (a) 2, (b) 4 and (c) 6 GHz.

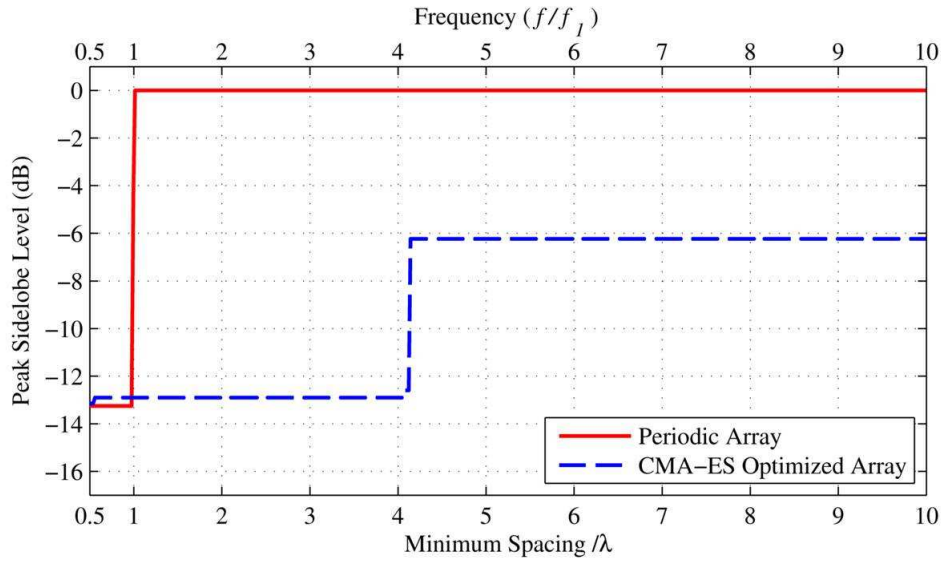


Figure 6.8: Peak sidelobe level performances over an extended bandwidth of the optimized array and of a periodic array populated by the same number of elements.

Fig. 6.8 also shows the performance of a periodic array populated by the same number of elements, which exhibits grating lobes at a minimum element spacing beyond 1λ .

Since the array is simulated in its entirety, the effects of mutual coupling between the elements can be observed. Fig. 6.9 gives the $VSWR$ values of all the array elements computed at 2, 4, and 6 GHz. The synthesized antenna element is shown to exhibit a good impedance match even when integrated into the array layout. For the three simulated frequencies, element $VSWR$ remains lower than or equal to 2, corresponding to a s_{11} magnitude lower than -10 dB. The irregularity of the array layout together with the minimum element spacing constraint serves to mitigate mutual coupling between the elements, even at the lower operating frequencies where coupling is typically highest.

Lastly, the radiation pattern of the entire UWB array has been simulated and compared to the array factor computed for the array layout shown in Fig. 6.3. The two results are shown plotted alongside each other in Fig. 6.10, where excellent agreement is observed between the isotropic predictions and the patterns obtained via full-wave simulations. The effects of the element patterns can be observed near $\pm 90^\circ$ and with the tapering of the sidelobes as the operating

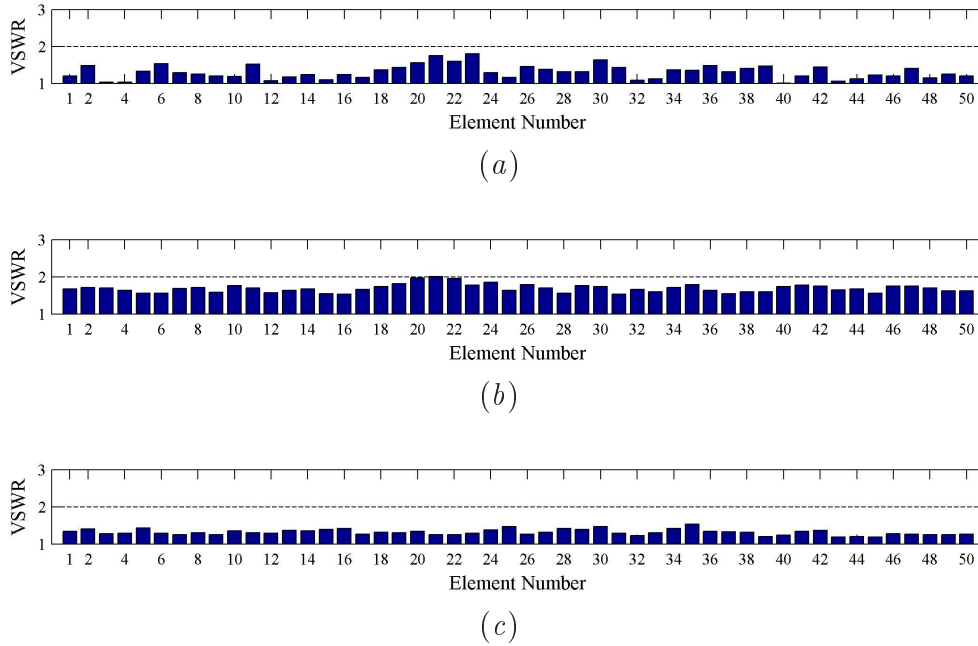


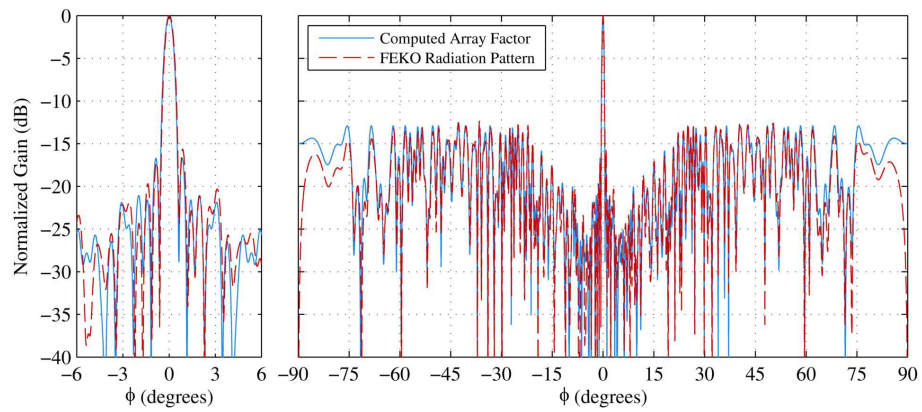
Figure 6.9: $VSWR$ values for all the elements of the array at (a) 2, (b) 4 and (c) 6 GHz.

frequency is increased. The pattern agreement again confirms that the sparse element locations of the optimized array layout provides low mutual coupling among the elements. The array maintains a high gain 15.8 dB at both 2 and 4 GHz, while it slightly decreases at 6 GHz to 14.9 dB due to the changes in the element pattern shown in Fig. 6.7(c).

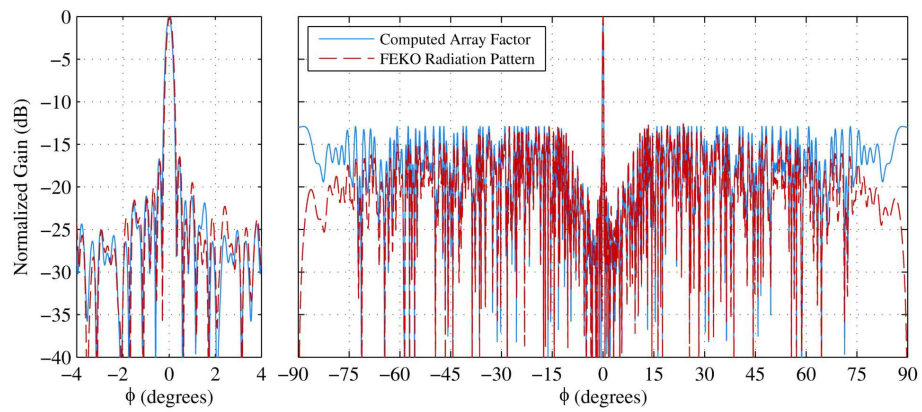
6.3 Conclusion

In this chapter, an approach for integrating UWB elements with aperiodic array topologies has been presented. The approach is based on a two-step process. The first is the design via optimization of a UWB antenna element suitable for integration into an aperiodic array. The element is not only designed for an acceptable impedance match over a prescribed ultra-wide bandwidth, but also low cross-polarized radiation in order to maintain polarization purity over the full operating bandwidth. Antenna element design is carried out by means of a synthesis approach that integrates a spline-based representation of the antenna shape together with a particle swarm optimization procedure which accounts for all of the performance requirements. The second step is the optimization of a nonuniform array layout suitable for the synthesized element, which is accomplished by employing CMA-ES to determine the optimal spacing between each element in the array. The effectiveness of the proposed approach has been

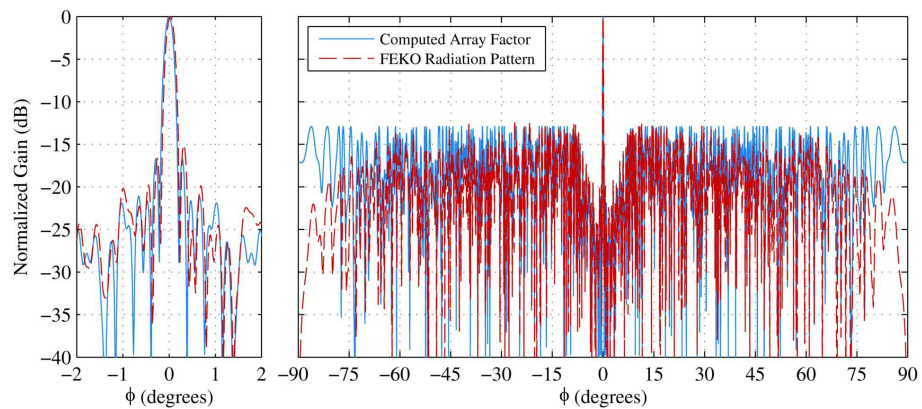
6.3. CONCLUSION



(a)



(b)



(c)

Figure 6.10: Comparison between the normalized power pattern and the array factor of the array at (a) 2, (b) 4 and (c) 6 GHz.

demonstrated through synthesis of an UWB array designed to operate over a frequency range of 2 to 6 GHz . The performances of both the single element and the full array have been assessed by means of rigorous full-wave simulations and measurements. The array is shown to efficiently operate over the intended bandwidth while exhibiting a radiation pattern that maintains a low sidelobe level and no grating lobes.

6.3. CONCLUSION

Chapter 7

Synthesis of an Array of UWB Antennas for Imaging Applications

In the last years, great effort has been made in the study and development of different inverse scattering techniques. Thanks to the electromagnetics waves' capability of penetrating materials, most of them are able to retrieve information about the objects' characteristics on the base of measurements of the scattered field caused by a known incident field [121]. Such techniques have been successfully applied in a number of different fields including mine detection [122][123], nondestructive testing or evaluation [124][125][126], and medical imaging [127]. In particular, the use of microwave imaging for the detection of tumors represents a promising solution since it gives a number of possible advantages such as low-cost system implementation, patient comfort [128], and the use of non-ionizing low power radiation [129][130]. Moreover, successful initial clinical investigations [131] suggest that such a technique has the potential to make the transition from the laboratory to the real medical environment.

Theoretical analysis and numerical simulation results have been widely provided, but the practical fabrication of a microwave imaging system requires to face several issues [128]. In this framework, the optimal design of the antenna array used to collect the data is one of the more challenging task [133][134]. In [135] a planar array constituted by several copies of the wideband patch antenna presented in [136] has been proposed for breast imaging application. Starting from such a design, a conformal version of the array has been proposed by the same authors in [137]. More in detail, 16 stacked-patch antennas were fabricated on separated substrates and located on a section of a hemisphere. In order to shield the antenna from the surrounding environment, a cavity lined with a broadband absorbing material was added at the back of each antenna, while a metallic screen was included on the front face of the antenna to reduce mutual coupling effects. An array of 32 tapered patch antenna working at the single frequency of 2.7 GHz has been presented in [134]. Such an array is constituted by 4 subarray of 8 antennas printed on the same substrate and joined together to

form a cubic chamber. The same authors redesigned the array into a bra-shaped semi-conformal chamber that can be directly attached to the patient's breast [138]. The elements of both the arrays exhibit a good impedance matching at the working frequency but no information about the transmission coefficients among the different antennas have been reported. Finally, Yu *et al.* presented in [133] an array of 36 half oval patch antennas printed on the sides of a dielectric cube. The array element operates in a wider frequency band from 2.7 to 5 GHz, allowing the possibility of detecting tumors over a large range of sizes [133].

In this chapter, an array of 24 UWB printed rectangular monopole antennas for imaging applications is presented. The array elements are printed on a cubic dielectric chamber. However, differently from [133] and [134], the monopole antennas are printed not only on the 4 vertical sides of the chamber but also on the bottom side, increasing the collected information. The chamber can contain a breast with or without a matching liquid and consequently can be used for tumor detection applications. On the other hand, also small objects (for an example see [139]) can be inserted into the chamber to perform nondestructive testing or evaluation. Both the array layout and the single antenna geometry are very simple, making the realization of a prototype easy. Moreover, the use of simple geometrical shapes allows the numerical simulation of the imaging system without the need of large computational resources. As a matter of fact, the discretization of the geometry in a large number of computational cells is usually required to correctly approximate the contours of complicated shapes.

The synthesis of the array is carried out by means of a two-steps procedure. First, a printed rectangular UWB monopole antenna is designed taking into consideration that it must not be used as a single radiator but as the element of an array for imaging applications. For this purpose, appropriate constraints have been imposed on both the physical and the electric properties of the antenna. Successively, multiple copies of the synthesised element are properly arranged to form an array that fulfill the requirements needed by this kind of application.

7.1 Single Radiating Element

7.1.1 Element Design

Concerning the geometry of the single radiating element, in general, it should be selected to be as simple as possible. As a matter of fact, the use of simple antenna geometries provide several advantages. First of all, simple shapes can be correctly approximated with a minor number of computational cells by electromagnetic simulators. This means the reduction of time and memory requirements which results to be particularly important when dealing with the simulation of large antenna arrays. Secondly, the realization of the antenna prototype turns out to be easier, resulting in less fabrication imperfections and consequently in a better match between numerical and experimental data. Finally, simple antenna geometries can be usually described by a minor number of parameters. From the synthesis point of view, a small number of antenna descriptors corresponds to a smaller solution space, which can be more rapidly explored by an optimization procedure.

On the basis of such an idea, the printed rectangular monopole antenna shown in Fig. 7.1 has been considered as the array element. As a support for the antenna, a dielectric substrate of thickness $s_t = 1.27 \text{ mm}$ characterized by a permittivity $\varepsilon_r^s = 10.2$ and a conductivity $\sigma_s = 0.0026$ has been adopted. On the front side of the substrate, a metallic rectangle of dimensions $p_w \times p_l$ constituting the radiating part of the antenna is placed above the feedline whose width and length are denoted by f_w and f_l , respectively. On the back side, a partial metallic plane of size $g_w \times g_l$ acts as a groundplane.

Since the antenna is supposed to be small, the coaxial connector has to be considered in the simulations. Assuming that the connector adopted is a standard SMA junction, it is modeled by means of a rectangular cuboid of dimensions $r_w = 16.0 \text{ mm}$, $r_l = 5.7 \text{ mm}$ and $r_t = 1.7 \text{ mm}$, and some concentric cylinders whose maximum length is $r_d = 9.5 \text{ mm}$. The radius of the inner conductor of the connector is $r_{in} = 0.635 \text{ mm}$, while the thickness of the metallic shell is $r_{sh} = 0.795 \text{ mm}$. The dielectric insulator is modeled as a hollow cylinder of thickness $r_{te} = 1.42 \text{ mm}$ and made of Teflon ($\varepsilon_r = 2.08$). The connector is placed so that the feed point is located at the coordinates $(x_p = 0, y_p = 0)$. In order to guarantee that the whole connector was placed on the metallic plane, the distance between the lower borders of the groundplane and the feedline on the opposite side is set to $g_s = 3.0 \text{ mm}$ while the groundplane length is required to be $g_l \geq r_l = 5.7 \text{ mm}$.

Finally, in order to reduce the coupling between the feedline and the groundplane, a slit of dimensions $s_l = 6.18 \text{ mm}$ and $s_w = 4.0 \text{ mm}$ is cut on the groundplane just under the feedline. This solution allows also the reduction of the currents on the connection cable that flow to the opposite direction with respect to the feed point.

7.1. SINGLE RADIATING ELEMENT

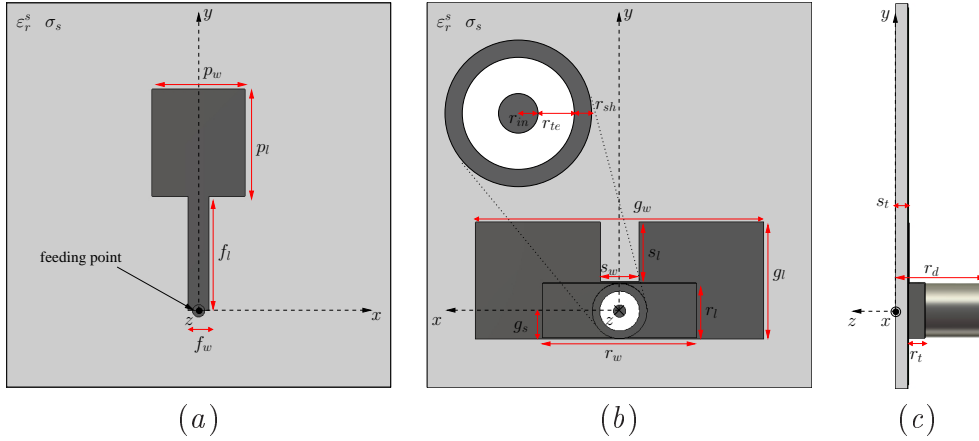


Figure 7.1: Geometry of the printed rectangular monopole antenna. (a) Front view, (b) back view and (c) side view.

Since the antenna is intended for imaging applications, it is required to fulfill the following project constraints. First of all, the antenna must be able to operate from $f_1 = 2.5$ to $f_2 = 5.5 \text{ GHz}$. The use of a higher center frequency such as $f_c = 4 \text{ GHz}$ allows for obtaining higher resolution images of smaller objects [132], while the wide bandwidth is preferable to increase the possibility of detecting objects over a large range of sizes [133]. Antennas for communication applications are usually required to exhibit $|s_{1,1}(f)| \leq s_{1,1}^T = -10 \text{ dB}$ over the interested range of frequencies to guarantee the radiation of the most part of the energy. However, when dealing with imaging applications, the distances between transmitting and receiving antennas or between the antennas and the objects are so small that a loss in the radiated energy can be accepted. Accordingly, the constraint $|s_{1,1}(f)| \leq s_{1,1}^T = -5 \text{ dB}; f_1 \leq f \leq f_2$ is considered. In addition, the antenna must be small enough so that multiple copies of it can be printed on the different sides of the dielectric chamber. In order to allow the displacement of a maximum number of 5 antennas on the same side of the chamber, the single element is required to occupy an area smaller than $30 \times 30 \text{ mm}^2$.

The search of an antenna fulfilling all the projects requirements is carried out by means of a Particle Swarm Optimization (PSO) procedure. PSO is a multiple-agents optimization algorithm which imitates the social behavior of groups of animals such as the swarms of bees. Differently from other optimization methods as the Genetic Algorithm (GA), PSO is based on the cooperation among the agents rather than their competition [48]. During the optimization, each trial solution is identified by a vector $\mathbf{a} = \{p_w, p_l, f_w, f_l, g_w, g_l\}$ defined as the collection of the antenna geometric descriptors. In order to take into account the effects given by the presence of the dielectric chamber, the optimization process is carried out by considering the trial antenna at hand as located at the center of one of the vertical sides of the same dielectric chamber that will be used for the array.

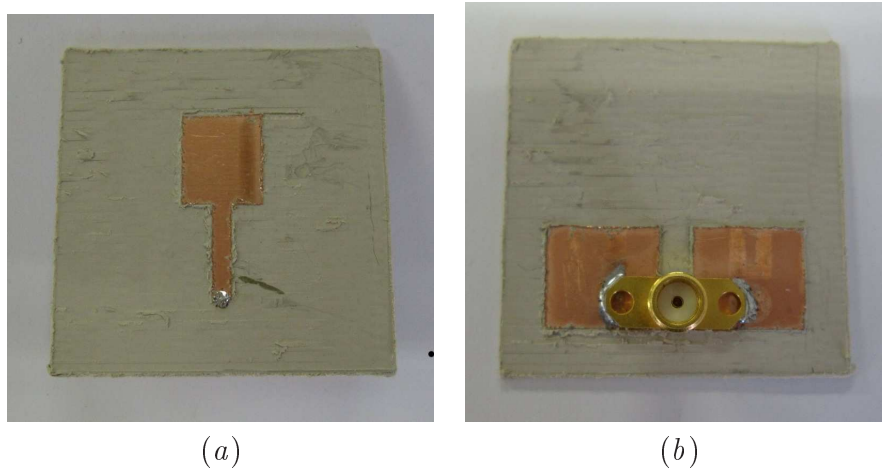


Figure 7.2: Prototype of the synthesized antenna element. (a) Front view and (b) back view.

According to the PSO research strategy, $R = 6$ particles (or agents) are initially placed into the multidimensional solution space identified by \mathbf{a} in a random manner. The particles, then, iteratively change their positions on the base of the knowledge of the best locations encountered by themselves and by the others. The optimization procedure iterates until a maximum number of $K = 100$ iterations is reached or until an antenna fulfilling all the project requirements is found. At the end of the optimization process, the values of the antenna descriptors turn out to be [in mm]: $p_w = 9.68$, $p_l = 11.11$, $f_w = 2.22$, $f_l = 11.89$, $g_w = 30$, and $g_l = 12.18$. As it can be noticed, the optimized element fits the size constraint occupying an area of $30 \times 26 \text{ mm}^2$.

7.1.2 Element Performances

The performances of the synthesized element have been first evaluated in isolation without the presence of the dielectric chamber. Towards this end, the antenna has been simulated as printed on a dielectric substrate of dimensions $40 \times 40 \text{ mm}^2$. For the experimental validation, a prototype of the synthesized antenna (Fig. 7.2) has been built and equipped with the SMA connector modeled in the simulations. The measurements have been performed using a vector network analyzer which was connected to the antenna with a coaxial cable.

Figure 7.3 shows the comparison between simulated and measured $s_{1,1}$ magnitude values exhibited by the synthesized antenna. As it can be observed, the simulated operating bandwidth (with $|s_{1,1}| \leq -5 \text{ dB}$) of the antenna is from 2.45 to more than 6 GHz . The experimental data well agree with the numerical ones, with values lower than $s_{1,1}^T = -5 \text{ dB}$ from 2.23 to 6 GHz , corresponding to a

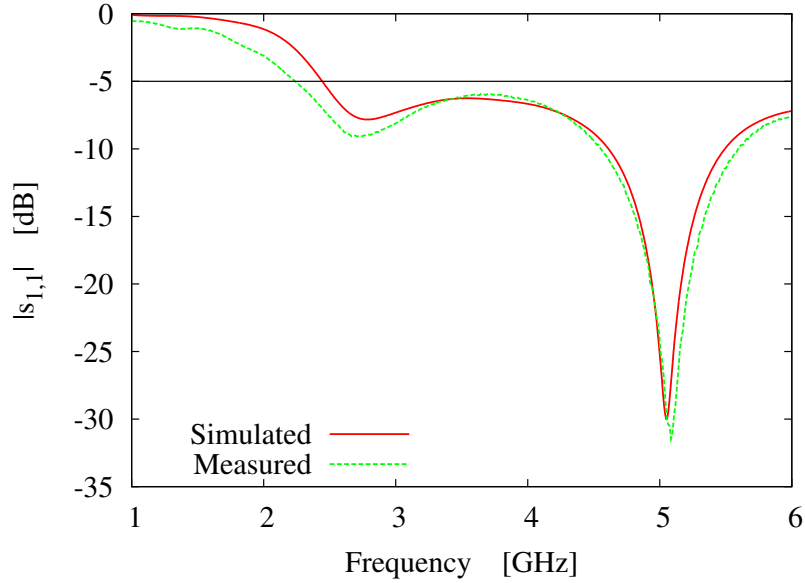


Figure 7.3: Simulated and measured $s_{1,1}$ magnitude values exhibited by the synthesized antenna element.

fractional bandwidth of 91.6%.

The use of a slit on the groundplane of the antenna has been fundamental in order to obtain the good match between simulated and measured return loss values. As a matter of fact, this solution reduces the coupling between the microstrip line and the groundplane and decreases the electric currents on the connection cable which flow in the opposite direction with respect to the feed point. This effect can be clearly seen in the surface current distributions which are plotted at 2.5, 4.0, and 5.5 GHz in Figs. 7.4 and 7.5. More in detail, the currents flowing on the front and back sides of the metallic part constituted by the feedline and the patch are shown in Fig. 7.4, while those relative to the two sides of the groundplane on the back of the substrate are shown in Fig. 7.5. In general, on the front side of the substrate the currents flow on the feedline towards the edges of the patch, while they concentrate around the slit and the top edge of the groundplane on the back of the substrate. In this sense, the slit avoid the flowing of the currents just behind the feedline, thus reducing the coupling effects. For the sake of comparison, Figures 7.6 and 7.7 reports the current distribution plots at the same frequencies on a modified version of the antenna, in which the slit has been removed. As it can be observed, the general behavior is the same. However, the absence of the slit allows the flowing of the currents behind the feedline on the groundplane [Figs. 7.7(a), 7.7(c), and 7.7(e)]. The stronger values are visible on the back side of the feedline and on the front side of

the groundplane at the lowest frequency [Figs. 7.6(b) and 7.7(a)], meaning that there is a strong coupling between the two surfaces. This is confirmed by the comparison of the simulated and measured $s_{1,1}$ magnitude values of the modified antenna reported in Fig. 7.8. Even though a good match between the data is still visible, the largest difference is obtained in correspondence with the minimum close to 2.5 GHz , i.e. the frequency where the surface currents show stronger values.

Since the slit avoids the flowing of the current behind the feedline, larger slits should be preferable since they will reduce more the coupling effect. However, as it can be seen by comparing Figs. 7.3 and 7.8, the presence of the slit also changes the behavior of the antenna return loss. Consequently, the slit width should be chosen in order to be the largest one which does not compromise the antenna impedance matching. In order to clarify this point, Figure 7.9 shows the behavior of the simulated $|s_{1,1}|$ of the antenna for different values of the slit width s_w . The obtained results show that when $s_w > 4.0\text{ mm}$ the antenna shows a return loss very close to the threshold value $s_{1,1}^T = -5\text{ dB}$ in some parts of the frequency spectrum. Consequently, a slit whose width is equal to $s_w = 4.0\text{ mm}$ has been adopted.

Finally, the radiation behavior of the single array element has been analysed. Since the antenna is intended for imaging application, the interest is in the near field radiation properties. Towards this end, Figure 7.10 shows the electric field radiated by the antenna at 2.5 , 4.0 , and 5.5 GHz . More in detail, Fig. 7.10(a), 7.10(c) and 7.10(e) show the electric field on the vertical plane passing by the center of the rectangular patch as seen from the right side of the antenna, while Fig. 7.10(b), 7.10(d) and 7.10(f) report the electric field on the horizontal plane passing by the center of the patch as seen from above the antenna. It can be noticed that in the vertical plane the antenna mostly radiates in the z -direction while less energy is radiated towards the top and the bottom of the antenna. In the horizontal plane, the largest part of the energy is still radiated in the z -direction only at 2.5 GHz [Fig. 7.10(b)], while a more uniform behavior is visible at the two higher frequencies [Fig. 7.10(d) and 7.10(f)]. Consequently, it can be expected that when the antenna will be used as element of the array, the effects produced by the mutual coupling on the array performances should be limited.

7.1. SINGLE RADIATING ELEMENT

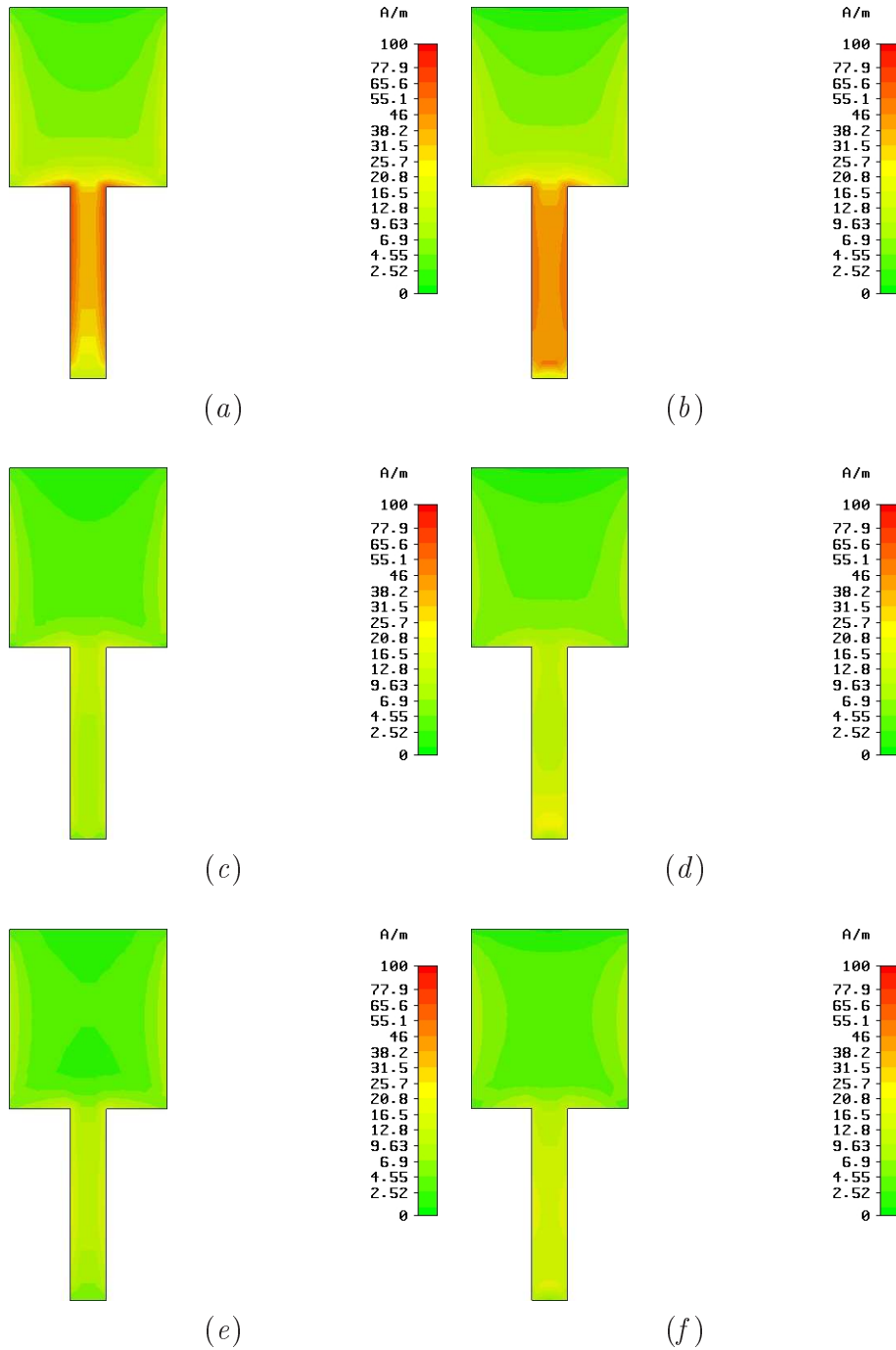


Figure 7.4: Surface currents flowing on the feedline and the patch of the synthesized antenna element. (a)(c)(e) Front and (b)(d)(f) back side at (a)(b) 2.5, (c)(d) 4.0, and (e)(f) 5.5 GHz.

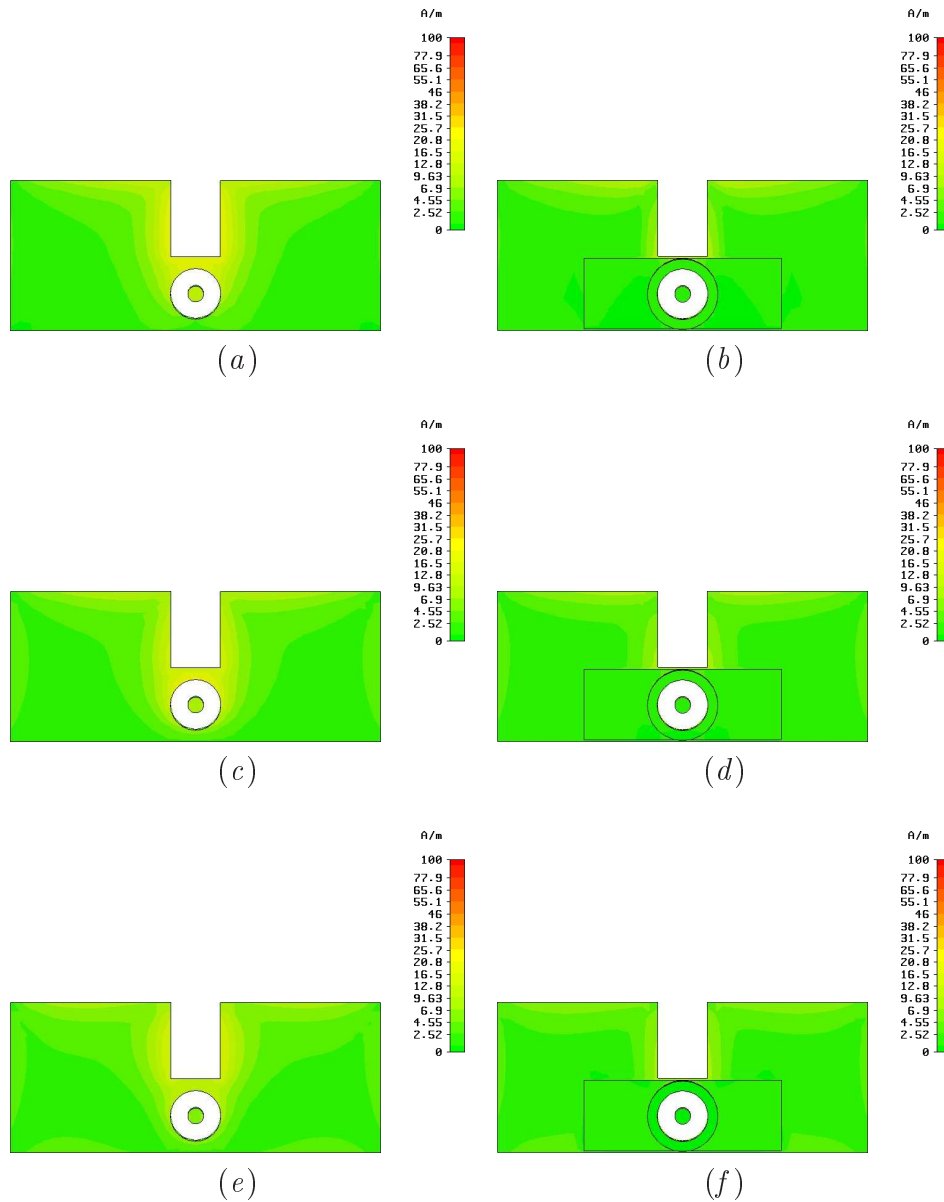


Figure 7.5: Surface currents flowing on the groundplane of the synthesized antenna element. (a)(c)(e) Front and (b)(d)(f) back side at (a)(b) 2.5, (c)(d) 4.0, and (e)(f) 5.5 GHz.

7.1. SINGLE RADIATING ELEMENT

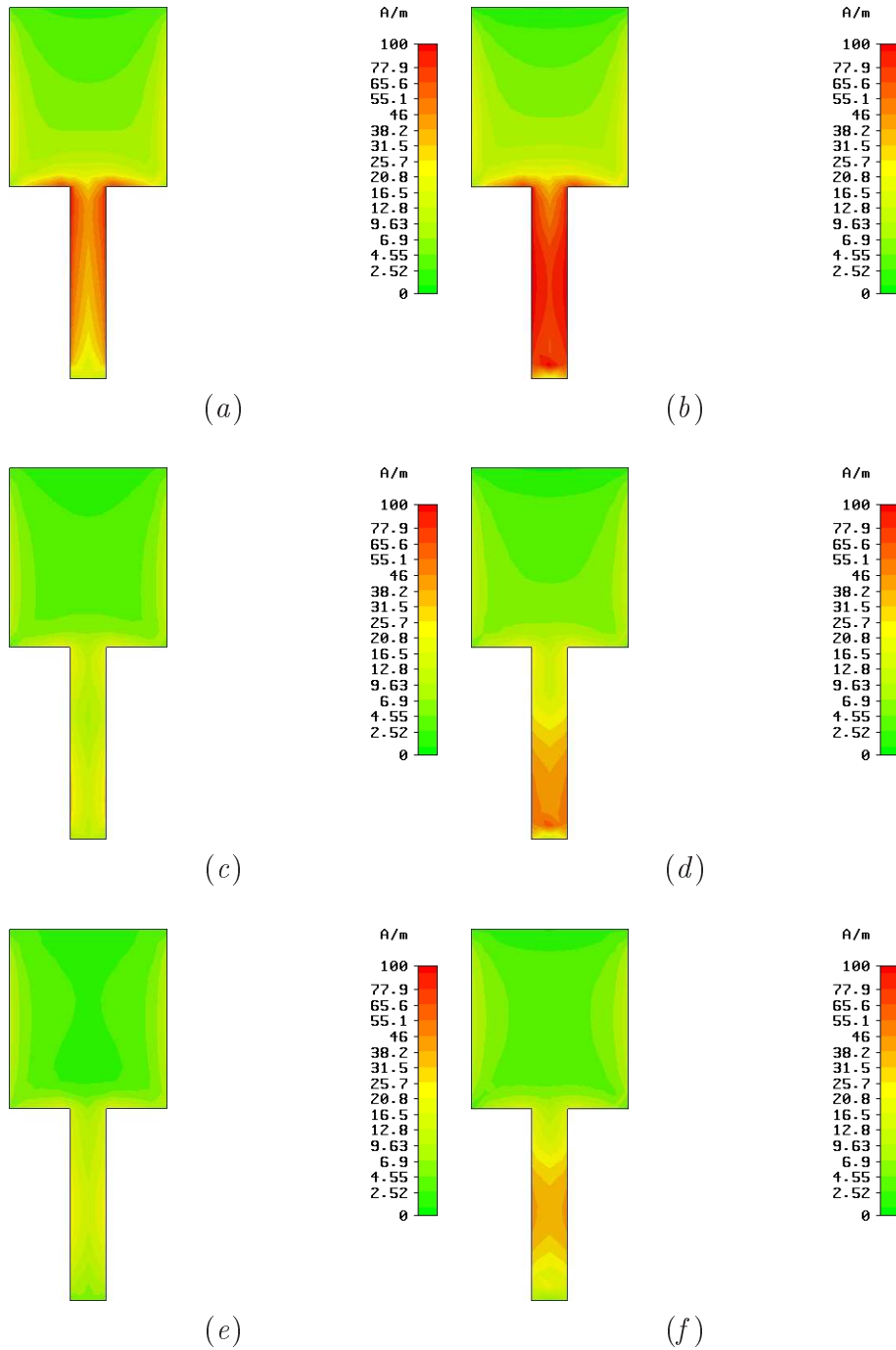


Figure 7.6: Surface currents flowing on the feedline and the patch of the modified antenna element (without the slit). (a)(c)(e) Front and (b)(d)(f) back side at (a)(b) 2.5, (c)(d) 4.0, and (e)(f) 5.5 GHz.

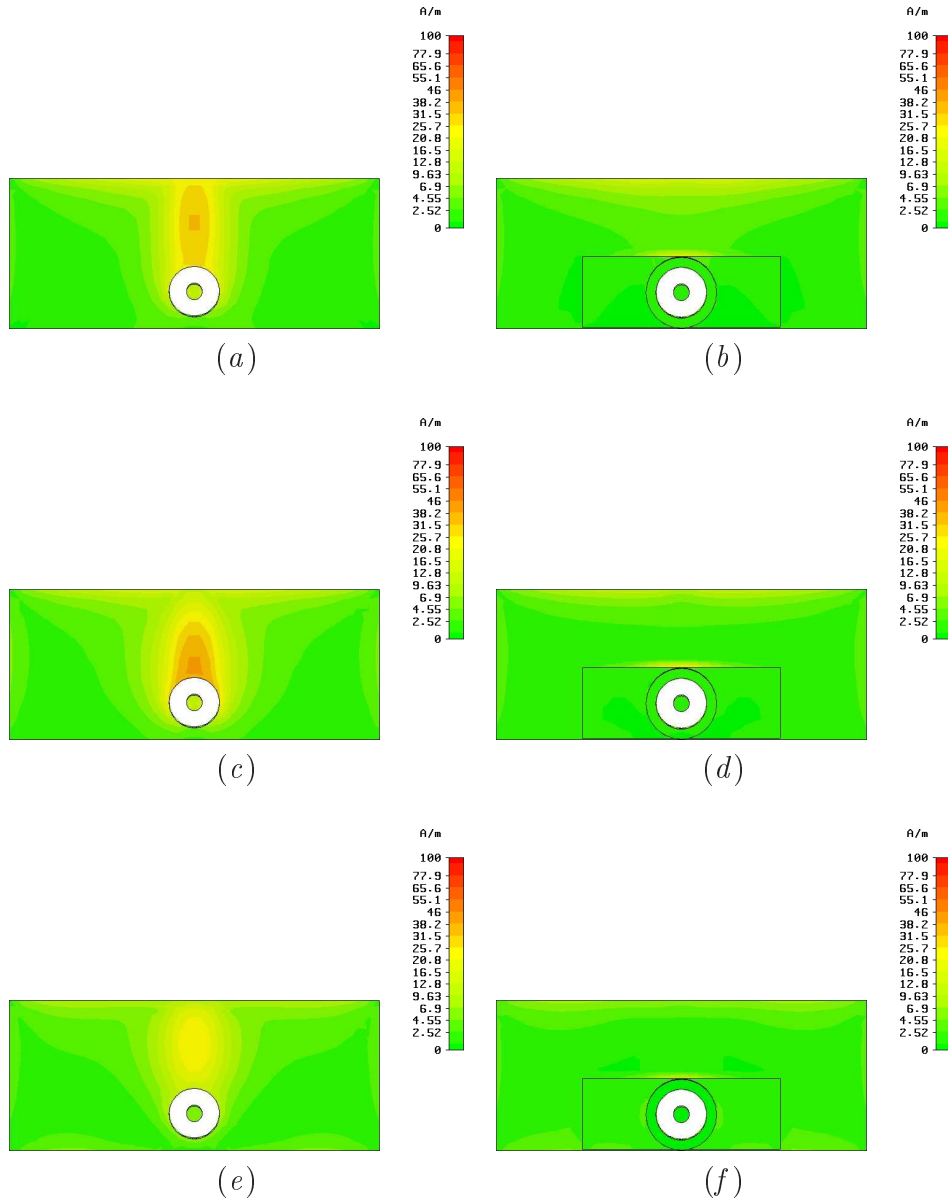


Figure 7.7: Surface currents flowing on the groundplane of the modified antenna element (without the slit). (a)(c)(e) Front and (b)(d)(f) back side at (a)(b) 2.5, (c)(d) 4.0, and (e)(f) 5.5 GHz.

7.1. SINGLE RADIATING ELEMENT

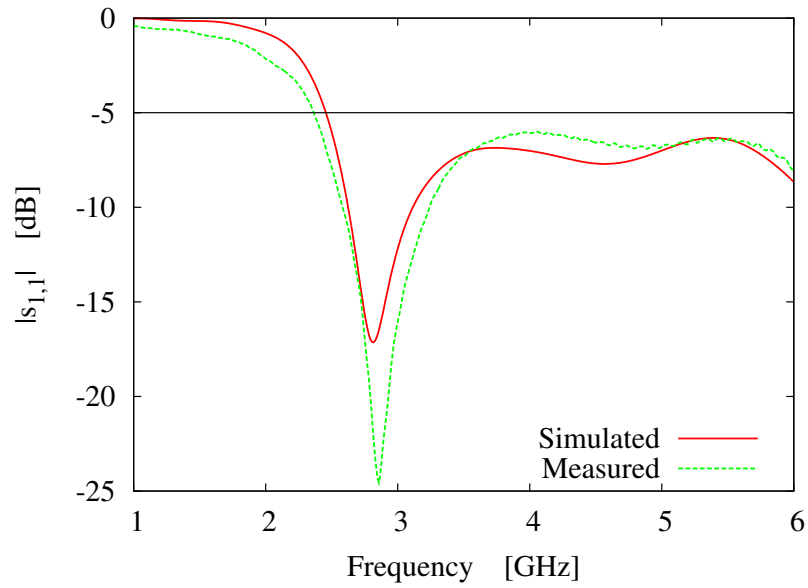


Figure 7.8: Simulated and measured $s_{1,1}$ magnitude values exhibited by the modified antenna element (without the slit).

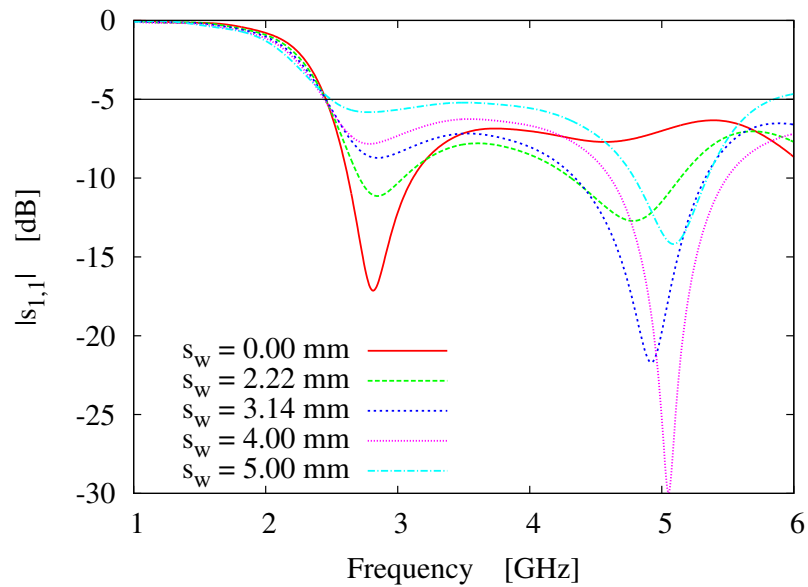


Figure 7.9: Simulated $s_{1,1}$ magnitude values exhibited by the antenna for different values of the slit width s_w .

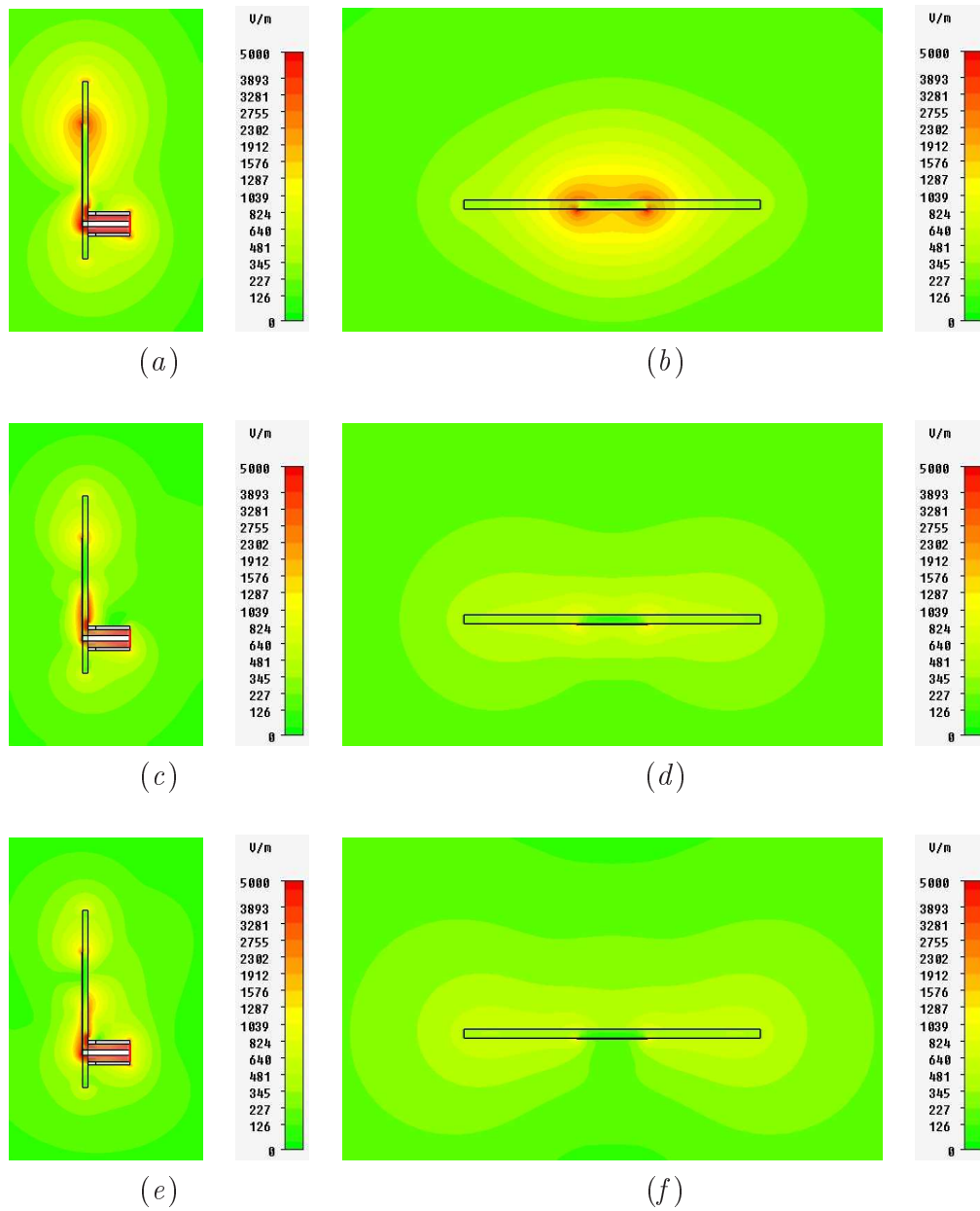


Figure 7.10: Electric near field radiated by the synthesized antenna. (a)(c)(e) Vertical and (b)(d)(f) horizontal plane passing by the center of the rectangular patch at (a)(b) 2.5, (c)(d) 4.0, and (e)(f) 5.5 GHz.

7.2 Array Design and Performances

The synthesised rectangular monopole antenna has been then employed as the element of an array for imaging applications. For this purpose, multiple copies of it have been arranged following the scheme reported in Fig. 7.11. The antennas are printed on the four vertical sides and on the bottom of a cubic dielectric chamber open at the top. The dielectric chamber has dimensions of $c_l = c_w = c_t = 100\text{ mm}$. $N_1 = 5$ antennas are printed on each vertical side of the chamber, while only $N_2 = 4$ antennas are printed on the bottom. Consequently, the total number of the array elements turns out to be $N = 4N_1 + N_2 = 24$.

The performances of the array composed by 24 copies of the optimized element have been numerically and experimentally evaluated. Towards this end, the prototype shown in Fig. 7.12 has been built. This configuration is aimed at reducing the mutual coupling effects among the antennas. As for the single element, each antenna of the array has been equipped with a coaxial SMA connector placed on the outer face of the chamber.

Figure 7.13 shows the comparison between simulated and measured return loss values for 6 array elements placed on different positions on the chamber. As representative results, two elements placed on the first vertical wall (antenna #1 - Fig. [7.13(a)] and antenna #3 - Fig. [7.13(b)]), two on the third vertical wall (antenna #11 - Fig. [7.13(c)] and antenna #14 - Fig. [7.13(d)]), one on the fourth vertical wall (antenna #18 - Fig. [7.13(e)]), and one on the bottom (antenna #22 - Fig. [7.13(f)]) have been selected. As it can be observed, the antennas printed on the dielectric chamber still show a good impedance matching whatever is their location. As a matter of fact, the simulated return loss values are lower or equal to $s_{1,1}^T = -5\text{ dB}$ in the frequency range $2.5 - 5.5\text{ GHz}$, thus fitting the project requirements. The variations of the return loss values are faster with respect to single element case shown in Fig. 7.3. This behavior is caused by the reflections occurring inside the chamber. Nevertheless, there is still a good agreement between numerical and experimental data, unless for a slight frequency shift at the higher frequencies.

When dealing with an antenna system for imaging application, it is important to analyse not only the impedance matching of the array elements but also the quality of the links among them. Towards this end, the simulated and measured transmission coefficients relative to a subset of all the possible antenna pairs are compared in Fig. 7.14. Usually, imaging algorithms use this kind of information

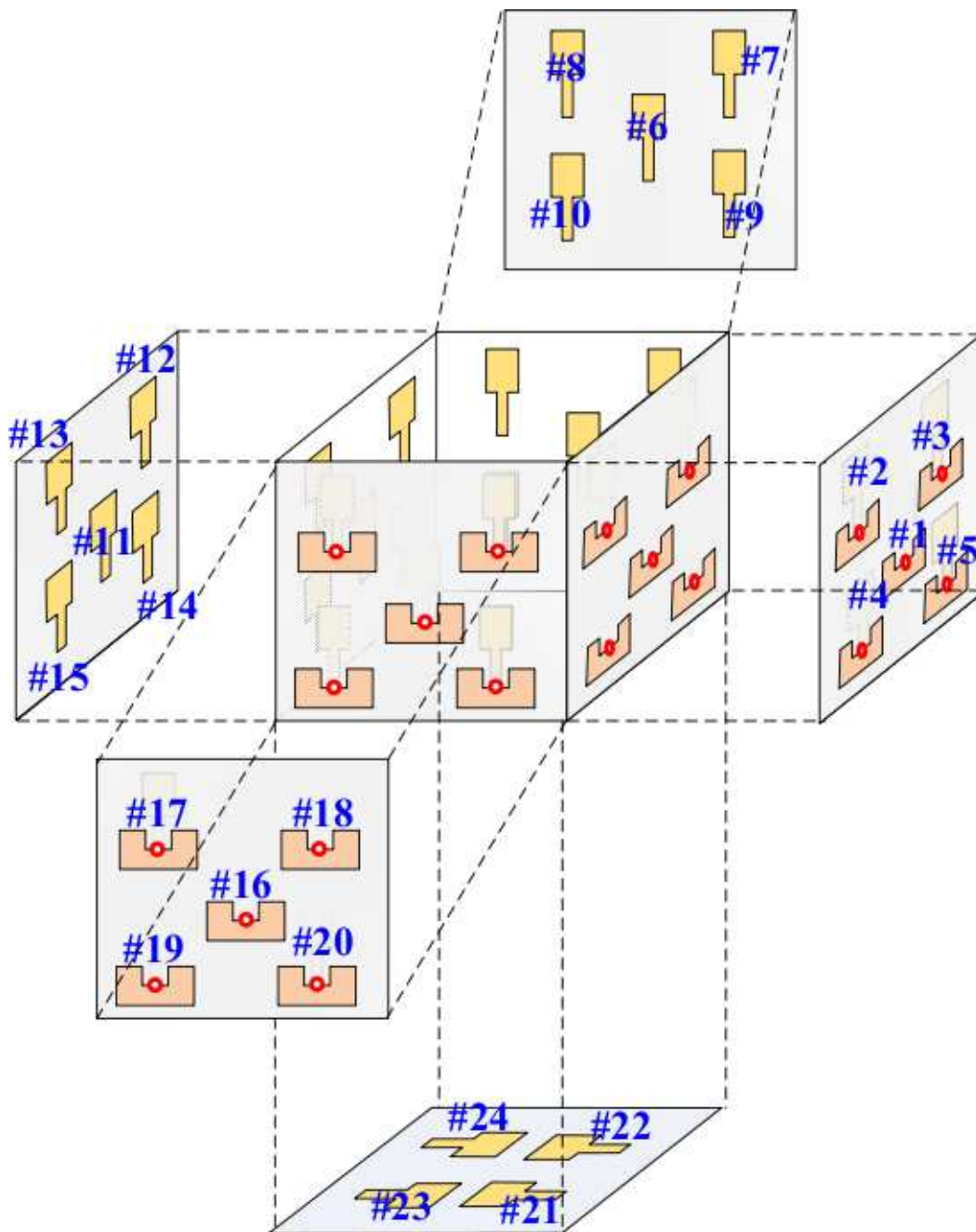


Figure 7.11: Layout of the 24-element array.

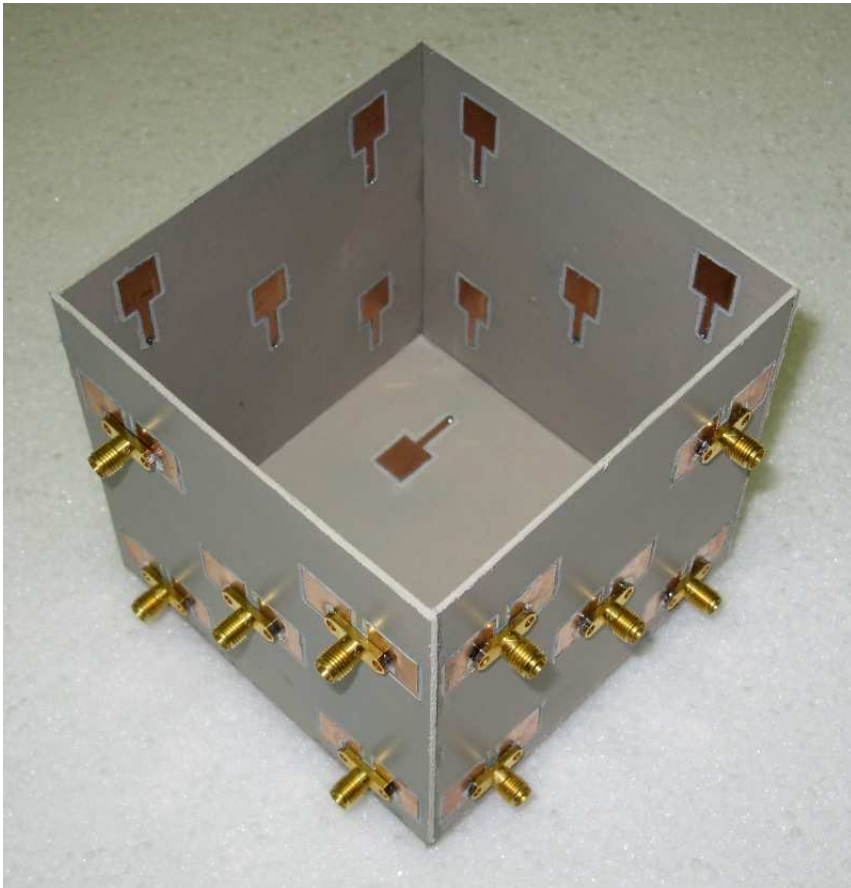


Figure 7.12: Prototype of the 24-element array.

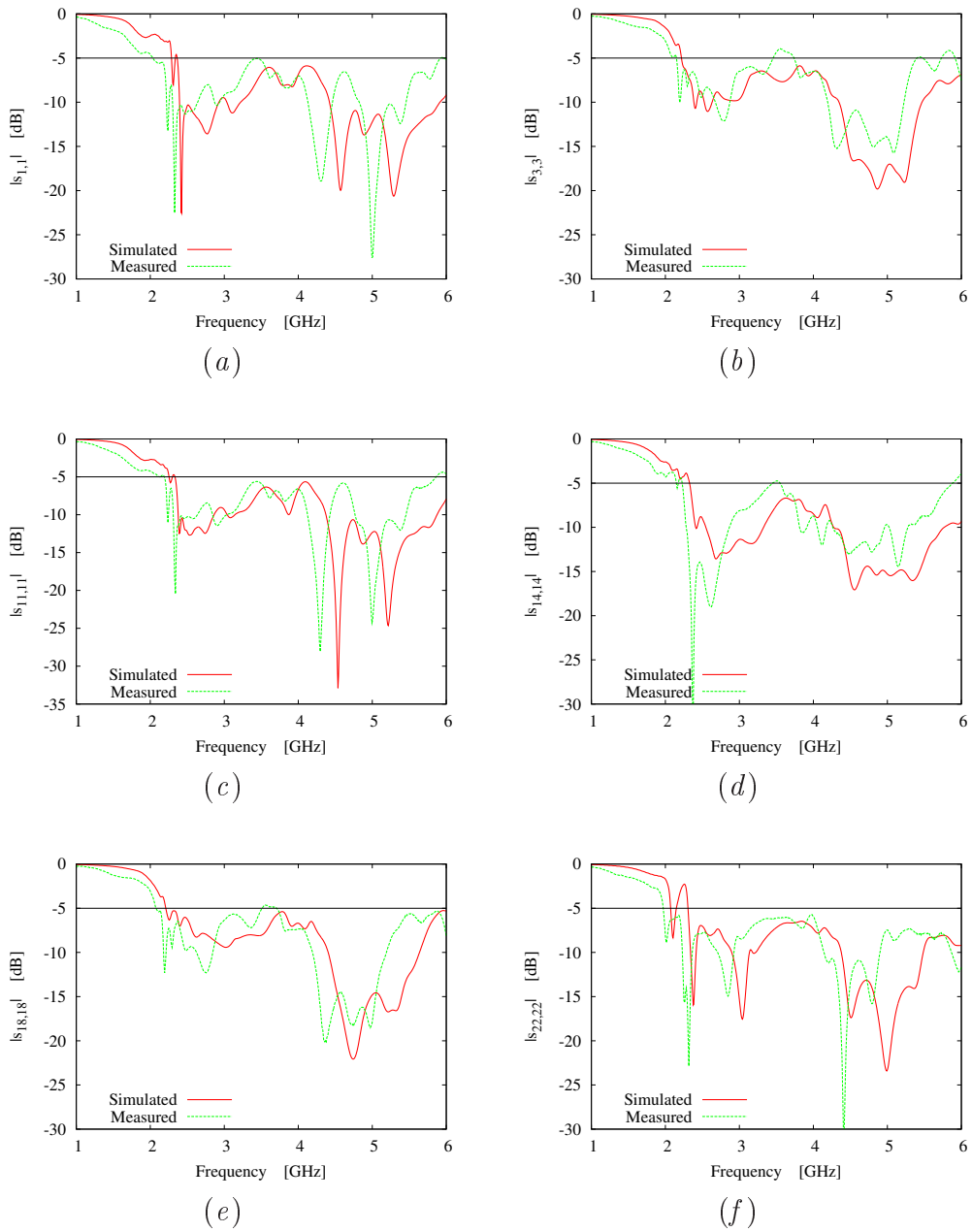


Figure 7.13: Simulated and measured return loss values exhibited by the array elements. (a) $|s_{1,1}|$, (b) $|s_{3,3}|$, (c) $|s_{11,11}|$, (d) $|s_{14,14}|$, (e) $|s_{18,18}|$, and (f) $|s_{22,22}|$.

7.2. ARRAY DESIGN AND PERFORMANCES

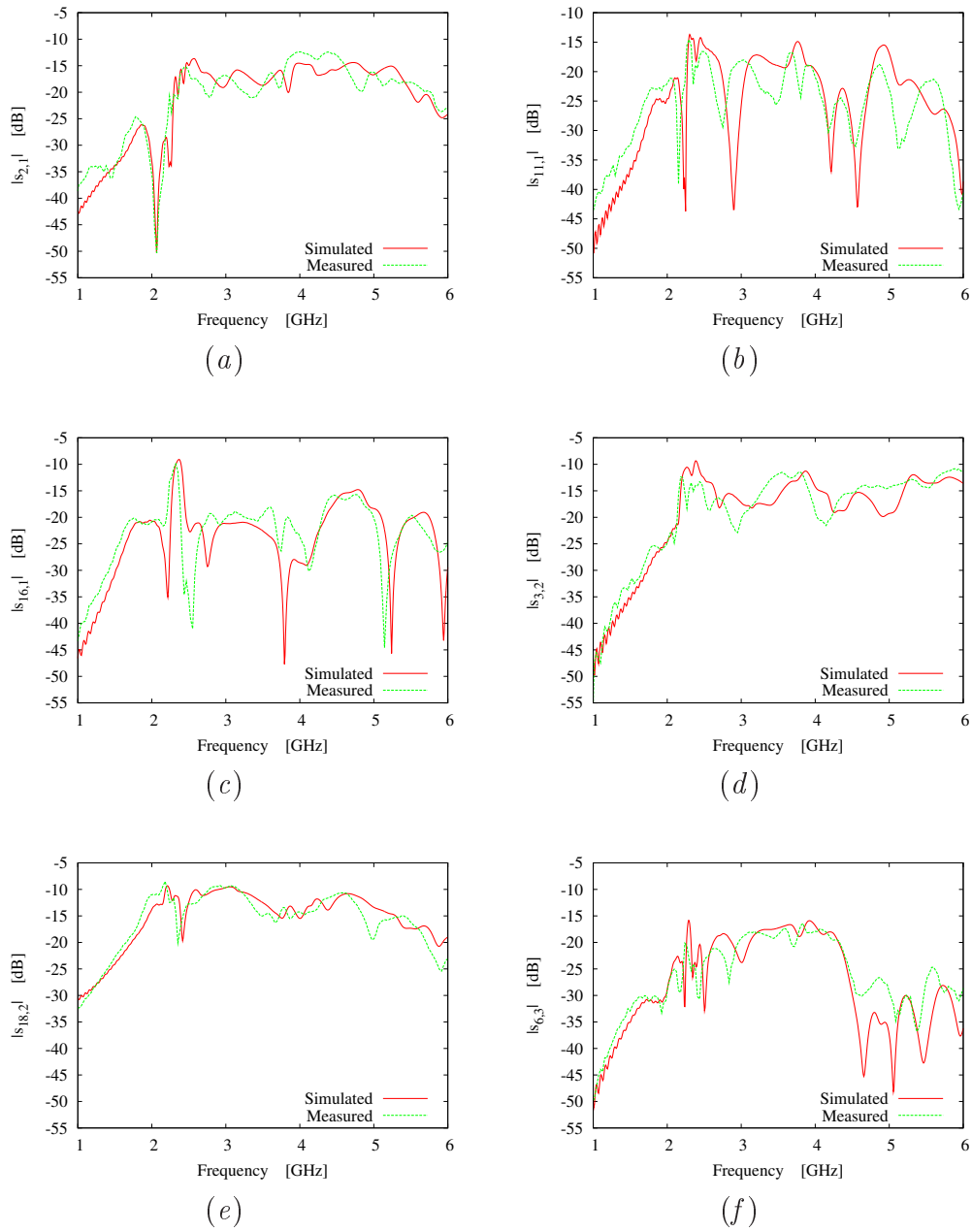
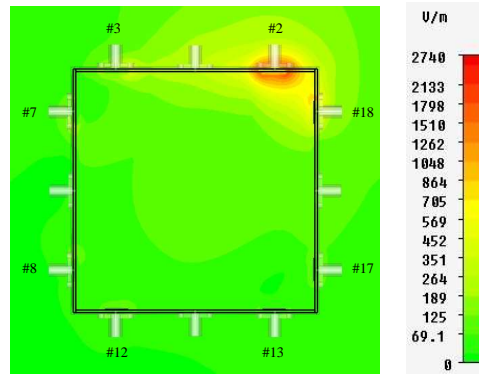
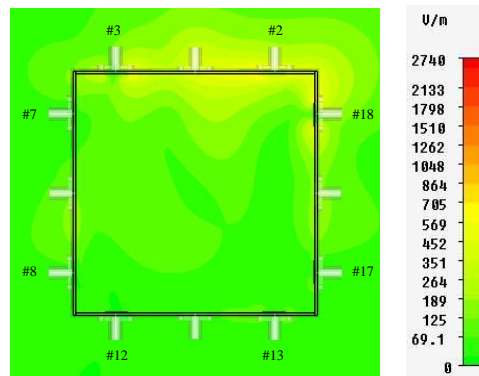


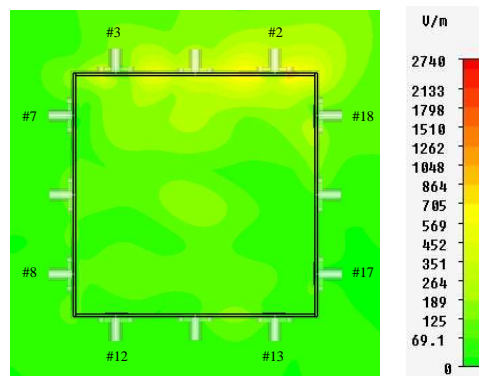
Figure 7.14: Simulated and measured transmission coefficient values exhibited by the array elements. (a) $|s_{2,1}|$, (b) $|s_{11,1}|$, (c) $|s_{16,1}|$, (d) $|s_{3,2}|$, (e) $|s_{18,2}|$, and (f) $|s_{6,3}|$.



(a)

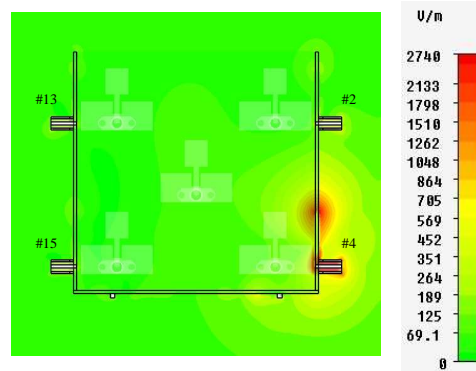


(b)

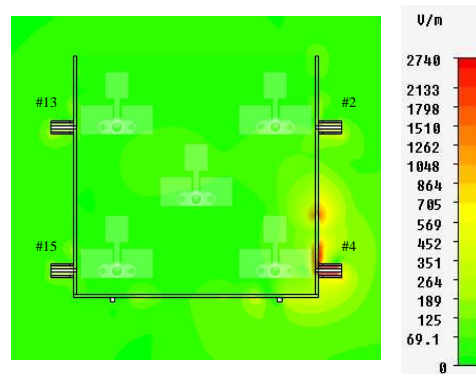


(c)

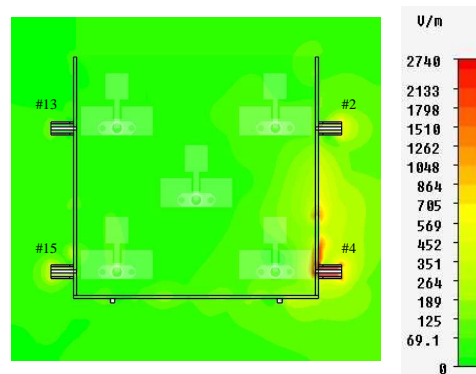
Figure 7.15: Electric near field radiated by the array antenna #4 on the horizontal plane passing by the center of the rectangular patch at (a) 2.5, (b) 4.0, and (c) 5.5 GHz.



(a)

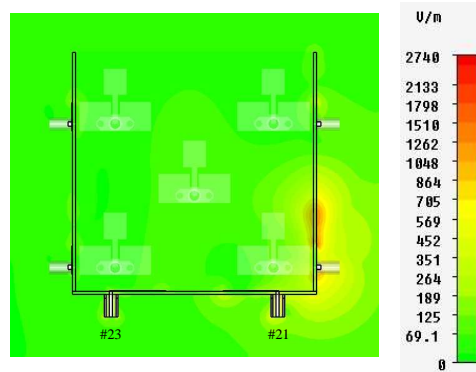


(b)

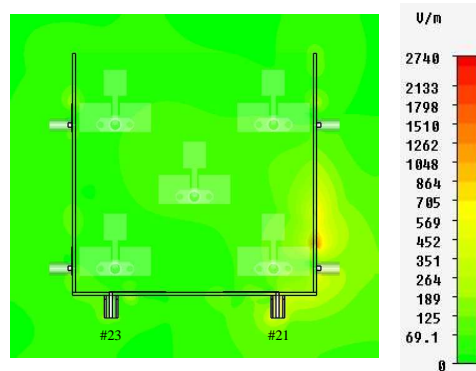


(c)

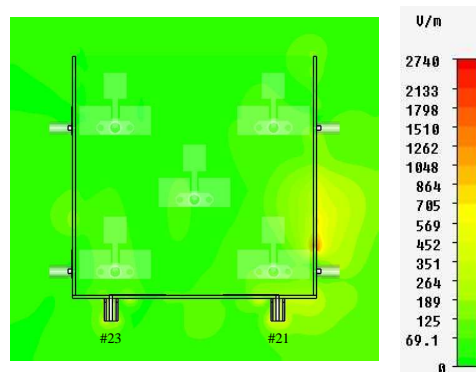
Figure 7.16: Electric near field radiated by the array antenna #4 on the vertical plane passing by the center of the rectangular patch at (a) 2.5, (b) 4.0, and (c) 5.5 GHz.



(a)



(b)



(c)

Figure 7.17: Electric near field radiated by the array antenna #4 on the vertical plane passing by the center of the antenna #21 rectangular patch at (a) 2.5, (b) 4.0, and (c) 5.5 GHz.

7.3. CONCLUSION

to perform the reconstruction of the object under analysis. However, if the attenuation among the antennas is too strong, it will become very difficult to separate the information about the target from the noise. The representative results here reported refer to configurations in which the two considered antennas are located on the same side of the chamber [Figs. 7.14(a) and 7.14(d)] or on different faces [Figs. 7.14(b), 7.14(c), 7.14(e) and 7.14(f)]. Whatever pair is considered, it can be noticed that the measured values of the transmission coefficients are around -20 dB in the most part of the operating band, indicating a good quality of the link between the antennas. It is worth noting also that there is a good agreement between numerical and experimental data.

Finally, the mutual coupling occurring among the antennas of the array is evaluated. The worst case in terms of mutual coupling effects occurs when the antennas located near the bottom vertexes of the chamber transmit since they are close to antennas on the same side, the contiguous side, and also on the bottom side of the chamber. Consequently, the behavior of the near electric field radiated by the antenna #4 is here reported. Figure 7.15 show the field radiated by the antenna on the horizontal plane passing by the center of the square patch (the view is from the top of the chamber) at 2.5, 4.0, and 5.5 GHz. As it can be noticed, the amplitude of the field around the closest antennas in the same plane (i.e., antennas #5 and #20) is very low. Moreover, the field is stronger around antenna #4 at the lower frequency [Fig. 7.15(a)] with respect to the other two analysed frequencies [Figs. 7.15(b) and 7.15(c)]. The behavior of the electric field on the vertical plane passing by the center of the patch is reported in Fig 7.16. It can be observed that also in this case the amplitude of the field sensed by the antenna #2 is very low at the first two frequencies [Figs. 7.16(a) and 7.16(b)] and slightly increases just at 5.5 GHz [Fig. 7.16(c)]. Finally, Figure 7.17 shows the behavior of the field radiated by antenna #4 in the vertical plane passing by the center of the patch of the closest antenna located on the bottom of the chamber (antenna #21). As for the two previous cases, the field amplitude sensed by antenna #21 is very low whatever the frequency. Such results demonstrate that the proposed array layout (Fig. 7.11) allows reduced mutual coupling effects among the antennas.

7.3 Conclusion

In this chapter, an antenna array for imaging applications has been presented. The array is constituted by 24 rectangular UWB monopole antennas printed on the sides and on the bottom of a cubic dielectric chamber. The synthesis of the single element has been carried out by means of a PSO-based optimization procedure aimed at identifying an antenna design fulfilling the project requirements in terms of both impedance matching and occupancy. The performances of both the single antenna and the 24-element array have been assessed with numerical simulations and experimentally validated by measurements performed

on the corresponding prototype.

From the numerical and experimental results, it is derived that the designed antenna array is suitable for imaging applications. As a matter of fact, the return loss of each array element indicates that the antenna array is able to operate in a wide frequency bandwidth from 2.5 to 5.5 GHz , while the high values of the forward transmission coefficients indicate a good quality of the links among the different elements. Moreover, thanks to the radiation characteristics of the single radiators, the effects of the mutual coupling among the elements on the array performances are limited.

Two different issues will be the objectives of the future research work. The first one will be the use of measurements performed with the designed array within reconstruction algorithms for NDT/NDE applications. On the other hand, the optimization procedure presented in this paper will be exploited to design an antenna array for breast imaging applications working on a different frequency band and taking into account the presence of a matching liquid.

7.3. CONCLUSION

Chapter 8

Conclusions and Future Developments

In this thesis, innovative techniques for the synthesis of radiating systems able to fit the tight requirements needed by modern wireless communication applications have been presented. In order to design small UWB and multi-band antennas, such techniques profitably exploit the characteristics of spline curves and fractal geometries.

The synthesis of UWB antennas has been carried out by means of an optimization strategy in which the description of the antenna geometry is based on the spline representation. Such an approach is aimed at obtaining antennas fulfilling all the UWB specifications including a good impedance match over a large bandwidth and the un-distorted reception of the transmitted waveform. The characterization of the antenna has been carried out both in the frequency and the time domain.

Concerning multi-band antennas, a synthesis approach based on the perturbation of fractal geometries has been proposed. The effects of geometrical variations on the performance of the Koch and the Sierpinski fractal antennas have been deeply analysed. Such analysis has been devoted to define some a-priori rules for the synthesis process. More in detail, some analytic relationships for the behavior of the resonant frequencies have been defined and used to obtain a suitable initialization for global optimization procedures. The result has been an automatic approach for the synthesis of multi-band fractal antennas requiring reduced time and computational resources. A preliminary assessment of a different multi-band antenna synthesis approach which exploits the spline geometries used in dealing with UWB antennas has been also proposed.

Finally, the integration of UWB antennas into array layout has been investigated. More specifically, first a design methodology for aperiodic linear arrays populated with spline-shaped radiating elements has been proposed. Successively, the realization of an array of UWB antennas for imaging applications has been described.

The effectiveness as well as the reliability of all the proposed design techniques have been assessed by means of both numerical and experimental results.

As for the novelties of this work, the main contribution is concerned with the following issues:

- the exploitation of spline-based geometries in the synthesis of UWB antennas which allow the description of the antenna with a limited set of parameters but also the generation of widely different complex and widely different shapes suitable to meet the tight requirements of UWB systems;
- the exploitation of the effects given by perturbing the fractal geometries in order to break the fixed relationships among resonances typical of standard fractal antennas allowing the realization of multi-band antennas suitable for practical applications;
- the flexibility demonstrated by the proposed approaches in dealing with the synthesis of antennas suitable for various applications characterized by different project requirements.

Future works will be devoted to:

- the identification of effective solutions for the miniaturization of spline-shaped antennas in order to obtain more compact UWB antennas;
- the analysis of the fractal perturbation in terms of other antenna properties such as radiation characteristics or operating bandwidth;
- the customization of the proposed synthesis approaches in order to obtain antennas suitable for integration in MIMO systems;
- the identification of alternative designs to obtain antennas exhibiting more directive radiation patterns.

References

- [1] P. L. Carro and J. de Mingo, "Ultrawide-band antenna distortion characterization using Hermite-Gauss signal subspace," *IEEE Antennas Wireless Propag. Lett.*, vol. 7, pp. 267-270, 2008.
- [2] C. A. Balanis, *Antenna Theory: Analysis and Design*. New York: Wiley, 1996.
- [3] W. Soergel and W. Wiesbeck, "Influence of the antennas on the ultrawideband transmission," *EURASIP J. Appl. Signal Process.*, no. 3, pp. 296-305, 2005.
- [4] B. B. Mandelbrot, *The Fractal Geometry of Nature*. New York: W. H. Freeman, 1983.
- [5] H. O. Peitgen, H. Jurgens, and D. Saupe, *Chaos and Fractals, New Frontiers of Science*. New York: Springer-Verlag, 1990.
- [6] G. Farr and C. E. Baum, "Extending the definitions of antenna gain and radiation pattern into the time domain," *Sensor Sim. Notes*, note 350, 1992.
- [7] D. H. Wolpert and W. G. Macready, "No free lunch theorems for optimization," *IEEE Trans. Evol. Comput.*, vol. 1, no. 1, pp. 67-82, 1997.
- [8] J. Robinson and Y. Rahmat-Samii, "Particle swarm optimization in electromagnetics," *IEEE Trans. Antennas Propag.*, vol. 52, no. 2, pp. 397-407, Feb. 2004.
- [9] J. Kennedy, R. C. Eberhart, and Y. Shi, *Swarm Intelligence*. San Francisco: Morgan Kaufmann Publishers, 2001.
- [10] H. Arslan, Z. N. Chen, and M. Di Benedetto, *Ultra Wideband Wireless Communication*. Hoboken, NJ: Wiley, 2006.
- [11] L. Yang and G. B. Giannakis, "Ultra-wideband communications," *IEEE Signal Processing Mag.*, pp. 26-94, Nov. 2004.

REFERENCES

- [12] Federal Communication Commission, First Report and Order, "Revision of part 15 of the commission's rules regarding ultra-wideband transmission systems," *FCC 02-48*, 2002. Available: http://hraunfoss.fcc.gov/edocs_public/attachmatch/FCC-02-48A1.pdf
- [13] Electronic Communications Committee, Draft ECC/DEC/(06)AA, "On the harmonised conditions for devices using UWB technology in bands below 10.6 GHz," *ECC/DEC/(06)AA*, 2006.
- [14] Z. N. Chen, X. H. Wu, H. F. Li, N. Yang, and M. Y. W. Chia, "Consideration for source pulses and antennas in UWB radio system," *IEEE Trans. Antennas Propag.*, vol. 52, no. 7, pp. 1739-1748, Jul. 2004.
- [15] X. Qing, Z. N. Chen and M. Y. W. Chia, "Characterization of ultrawideband antennas using transfer functions," *Radio Sci.*, vol. 41, RS1002, pp. 1-10, 2006.
- [16] C. C. Lin, Y. C. Kan, L. C. Kuo, and H. R. Chuang, "A planar triangular monopole antenna for UWB communication," *IEEE Microwave Wireless Compon. Lett.*, vol. 15, no. 10, pp. 624-626, Oct. 2005.
- [17] J. Liang, C. C. Chiau, X. Chen and C. G. Parini, "Study of a printed circular disc monopole antenna for UWB systems," *IEEE Trans. Antennas Propag.*, vol. 53, no. 11, pp. 3500-3504, Nov. 2005.
- [18] Y. Ren and K. Chang, "An annular ring antenna for UWB communications," *IEEE Antennas Wireless Propag. Lett.*, vol. 5, pp. 275-276, 2006.
- [19] J. Jung, W. Choi, and J. Choi, "A small wideband microstrip-fed monopole antenna," *IEEE Microwave Wireless Compon. Lett.*, vol. 15, no. 10, pp. 703-705, Oct. 2005.
- [20] G. Lu, S. von der Mark, I. Korisch, L. J. Greenstein, and P. Spasojevic, "Diamond and rounded diamond antennas for ultrawide-band communications," *IEEE Antennas Wireless Propag. Lett.*, vol. 3, pp. 249-252, 2004.
- [21] X. H. Wu and Z. N. Chen, "Design and optimization of UWB antennas by a powerfull CAD tool: PULSE KIT," *Proc. IEEE Antennas Propag. Int. Symp.*, vol. 2, pp. 1756-1759, Jun. 2004.
- [22] K. Kiminami, A. Hirata, and T. Shiozawa, "Double-sided printed bow-tie antenna for UWB communications," *IEEE Antennas Wireless Propag. Lett.*, vol. 3, pp. 152-153, 2004.
- [23] J. M. Johnson and Y. Rahmat-Samii, "Genetic algorithms and method of moments (GA/MOM) for the design of integrated antennas," *IEEE Trans. Antennas Propag.*, vol. 47, no. 10, pp. 1606-1614, Oct. 1999.

-
- [24] F. J. Villegas, T. Cwik, Y. Rahmat-samii, and M. Manteghi, "A parallel electromagnetic genetic-algorithm optimization (EGO) application for patch antenna design," *IEEE Trans. Antennas Propag.*, vol. 52, no. 9, pp. 2424-2435, Sep. 2004.
- [25] C. De Boor, *A Practical Guide to Spline*. Springer, New York, 2001.
- [26] R. F. Harrington, *Field Computation by Moment Methods*. Malabar, FL: Robert E. Krieger, 1987.
- [27] C. A. Balanis, *Advanced Engineering Electromagnetics*. New York, NY: John Wiley & Sons, 1989.
- [28] S. Rao, D. Wilton, and A. Glisson, "Electromagnetic scattering by surfaces of arbitrary shape," *IEEE Trans. Antennas Propag.*, vol. 30, pp. 409-418, May 1982.
- [29] C. A. Balanis, *Antenna Theory: Analysis and Design*. New York: Wiley, 1982.
- [30] S. H. Lee, J. K. Park, and J. N. Lee, "A novel CPW-fed ultra-wideband antenna design," *Microw. Opt. Technol. Lett.*, vol. 44, no. 5, pp. 393-396, Mar. 2005.
- [31] F. van den Bergh, "An analysis of particle swarm optimizers," Ph. D. dissertation, Dept. Comput. Sci., Univ. Pretoria, Pretoria, South Africa, 2002.
- [32] T. Ma and S. Wu, "Ultrawideband band-notched folded strip monopole antenna," *IEEE Trans. Antennas Propag.*, vol. 55, no. 9, pp. 2473-2479, 2007.
- [33] J. Kim, C. S. Cho, and J. W. Lee, "5.2 GHz notched ultra-wideband antenna using slot-type SRR," *Electron. Lett.*, vol. 42, no. 6, pp. 315-316, 2006.
- [34] W. J. Lui, C. H. Cheng, Y. Cheng, and H. Zhu, "Frequency notched ultra-wideband microstrip slot antenna with fractal tuning stub," *Electron. Lett.*, vol. 41, no. 6, pp. 294-295, 2005.
- [35] N. Choi, C. Jung, J. Byun, F. J. Harackiewicz, M. Park, Y. Chung, T. Kim, and B. Lee, "Compact UWB antenna with I-shaped band-notch parasitic element for laptop applications," *IEEE Antennas Wireless Propag. Lett.*, no. 8, pp. 580-582, 2009.
- [36] A. J. Kerkhoff and H. Ling, "Design of a band-notched planar monopole antenna using genetic algorithm optimization," *IEEE Trans. Antennas Propag.*, vol. 55, no. 3, pp. 604-610, 2007.

REFERENCES

- [37] T. Dissanayake and K. P. Esselle, "Prediction of the notch frequency of slot loaded printed UWB antennas," *IEEE Trans. Antennas Propag.*, vol. 55, no. 11, pp. 3320-3325, 2007.
- [38] J. Martinez-Fernandez, V. de la Rubia, J. M. Gil, and J. Zapata, "Frequency notched UWB planar monopole antenna optimization using a finite element method-based approach," *IEEE Trans. Antennas Propag.*, vol. 56, no. 9, pp. 2884-2893, 2008.
- [39] H. J. Zhou, B. H. Sun, Q. Z. Liu, and J. Y. Deng, "Implementation and investigation of U-shaped aperture UWB antenna with dual band-notched characteristics," *Electron. Lett.*, vol. 44, no. 24, pp. 1387-1388, 2008.
- [40] Q. Chu and Y. Yang, "A compact ultrawideband antenna with 3.4/5.5 GHz dual band-notched characteristics," *IEEE Trans. Antennas Propag.*, vol. 56, no. 12, pp. 3637-3644, 2008.
- [41] H. Liu, C. Ku, and C. Yang, "Novel CPW-Fed planar monopole antenna for WiMAX/WLAN applications," *IEEE Antennas Wireless Propag. Lett.*, no. 9, pp. 240-243, 2010.
- [42] L. Lizzi, F. Viani, R. Azaro, and A. Massa, "Optimization of a spline-shaped UWB antenna by PSO," *IEEE Antennas Wireless Propag. Lett.*, vol. 6, pp. 182-185, 2007.
- [43] L. Lizzi, F. Viani, R. Azaro, and A. Massa, "A PSO-driven spline-based shaping approach for ultrawideband (UWB) antenna synthesis," *IEEE Trans. Antennas Propag.*, vol. 56, no. 8, pp. 2613-2621, 2008.
- [44] F. Viani, L. Lizzi, R. Azaro, and A. Massa, "Spline-shaped ultra-wideband antenna operating in ECC released frequency spectrum," *Electron. Lett.*, vol. 44, no. 1, pp. 7-8, 2008.
- [45] F. Viani, L. Lizzi, R. Azaro, and A. Massa, "A miniaturized UWB antenna for wireless dongle devices," *IEEE Antennas Wireless Propag. Lett.*, vol. 7, pp. 714-717, 2008.
- [46] R. C. Eberhart and Y. Shi, "Particle swarm optimization: developments, applications and resources," in *Proc. Congress on Evolutionary Computation*, Seoul, Korea, 2001, pp. 81-86.
- [47] M. Donelli and A. Massa, "Computational approach based on a particle swarm optimizer for microwave imaging of two-dimensional dielectric scatterers," *IEEE Trans. Microwave Theory Tech.*, vol. 53, pp. 1761-1776, 2005.
- [48] M. Donelli, R. Azaro, F. G. B. De Natale, and A. Massa, "An innovative computational approach based on a particle swarm strategy for adaptive

-
- phased-arrays control,” *IEEE Trans. Antennas Propag.*, vol. 54, no. 4, pp. 888-898, 2006.
- [49] P. Rocca, M. Benedetti, M. Donelli, D. Franceschini, and A. Massa, “Evolutionary optimization as applied to inverse problems,” *Inverse Problems*, vol. 25, doi: 10.1088/0266-5611/25/12/123003, Dec. 2009.
- [50] L. Lizzi, F. Viani, and A. Massa, “Dual-band spline-shaped PCB antenna for Wi-Fi Applications,” *IEEE Antennas Wireless Propag. Lett.*, vol. 8, pp. 616-619, 2009.
- [51] A. Martini, M. Donelli, M. Franceschetti, and A. Massa, “Particle density retrieval in random media using a percolation model and a particle swarm optimizer,” *IEEE Antennas Wireless Propag. Lett.*, vol. 7, pp. 213-216, 2007.
- [52] M. Donelli, D. Franceschini, P. Rocca, and A. Massa, “Three-dimensional microwave imaging problems solved through an efficient multi-scaling particle swarm optimization,” *IEEE Trans. Geosci. Remote Sens.*, vol. 47, no. 5, pp. 1467-1481, May 2009.
- [53] M. Donelli, A. Martini, and A. Massa, “A hybrid approach based on PSO and Hadamard difference sets for the synthesis of square thinned arrays,” *IEEE Trans. Antennas Propag.*, vol. 57, no. 8, pp. 2491-2495, Aug. 2009.
- [54] L. Poli, P. Rocca, L. Manica, and A. Massa, “Handling sideband radiations in time-modulated arrays through particle swarm optimization,” *IEEE Trans. Antennas Propag.*, vol. 58, no. 4, pp. 1408-1411, Apr. 2010.
- [55] T. Weiland, M. Timm, and I. Munteanu, “A practical guide to 3-D simulation,” *IEEE Microw. Magazine*, vol. 9, no. 6, pp. 62-75, Dec. 2008.
- [56] C. R. Medeiros, J. R. Costa, C. A. Fernandes, “Compact tapered slot UWB antenna with WLAN band rejection,” *IEEE Antennas Wireless Propag. Lett.*, vol. 8, pp. 661-664, 2009.
- [57] D. Lamensdorf and L. Susman, “Baseband-pulse-antenna techniques,” *IEEE Antennas Propag. Magazine*, vol. 36, pp. 20-30, 1994.
- [58] W. Soergel and W. Wiesbeck, “Influence of the antennas on the ultra-wideband transmission,” *EURASIP J. Appl. Signal Process.*, no. 3, pp. 296-305, 2005.
- [59] M. E. Bialkowski and A. M. Abbosh, “Design of UWB planar antenna with improved cut-off at the out-of-band frequencies,” *IEEE Antennas Wireless Propag. Lett.*, vol. 7, pp. 408-410, 2008.

REFERENCES

- [60] M. Gopikrishna, D. Das Krishna, C. K. Anandan, P. Mohanan, and K. Vasudevan, "Design of a compact semi-elliptic monopole slot antenna for UWB systems," *IEEE Trans. Antennas Propag.*, vol. 57, no. 6, pp. 1834-1837, 2009.
- [61] A. Karousos and C. Tzaras, "Multiple time-domain diffraction for UWB signals," *IEEE Trans. Antennas Propag.*, vol. 56, no. 5, pp. 1420-1427, 2008.
- [62] G. Franceschetti, J. Tatoian, and G. Gibbs, "Timed arrays in a nutshell," *IEEE Trans. Antennas Propag.*, vol. 53, no. 12, pp. 4073-4082, 2005.
- [63] A. Shlivinski, E. Heyman, and R. Kastner, "Antenna characterization in the time domain," *IEEE Trans. Antennas Propag.*, vol. 45, no. 7, pp. 1140-1149, 1997.
- [64] N. Telzhensky and Y. Leviatan, "Novel method of UWB antenna optimization for specified input signal forms by means of genetic algorithm," *IEEE Trans. Antennas Propag.*, vol. 54, no. 8, pp. 2216-2225, 2006.
- [65] N. Telzhensky and Y. Leviatan, "Planar differential elliptical UWB antenna optimization," *IEEE Trans. Antennas Propag.*, vol. 54, no. 11, pp. 3400-3406, 2006.
- [66] C. De Boor, *A Practical Guide to Spline*. New York: Springer, 2001.
- [67] Y.-X. Guo, M. Y. W. Chia, and Z. Nn. Chen, "Miniature built-in multiband antennas for mobile handsets," *IEEE Trans. Antennas Propag.*, vol. 52, no. 8, pp. 1936-1944, 2004.
- [68] M. Martinez-Vazquez, O. Litschke, M. Geissler, D. Heberling, A. M. Martinez-Gonzalez, and D. Sanchez-Hernandez, "Integrated planar multi-band antennas for personal communication handsets," *IEEE Trans. Antennas Propag.*, vol. 54, no. 2, pp. 384-391, 2006.
- [69] O. Saraereh, M. Jayawardene, P. McEvoy, and J. C. Vardaxoglou, "Quad-band handset antenna operation for GSM900/DCS1800/PCS1900/UMTS," in *IEE Wideband Multi-band Antennas Arrays*, 2005, pp. 129-133.
- [70] C. Di Nallo and A. Faraone, "Multiband internal antenna for mobile phones," *Electron. Lett.*, vol. 41, no. 9, pp. 514-515, Apr. 2005.
- [71] Y. X. Guo, M. Y. W. Chia, and Z. N. Chen, "Miniature built-in quad-band antennas for mobile handsets," *IEEE Antennas Wireless Propagat. Lett.*, vol. 2, pp. 30-32, 2003.

-
- [72] F.-R. Hsiao and K.-L. Wong, "Compact planar inverted-F patch antenna for triple-frequency operation," *Microw. Opt. Techn. Lett.*, vol. 33, no. 6, pp. 459-462, 2002.
- [73] Y.-S. Wang, M.-C. Lee, and S.-J. Chung, "Two PIFA-related miniaturized dual-band antennas," *IEEE Trans. Antennas Propagat.*, vol. 55, no. 3, pp. 805-811, 2007.
- [74] D.-Y. Kim, J. W. Lee, C. S. Cho, and T. K. Lee, "Design of a compact tri-band PIFA based on independent control of the resonant frequencies," *IEEE Trans. Antennas Propagat.*, vol. 56, no. 5, pp. 1428-1436, 2008.
- [75] J. S. Lee, H. Rhyu, and B. Lee, "Design concept of multi-band antenna with resonant circuit on PCB," *Electron. Lett.*, vol. 43, no. 6, pp. 5-6, Mar. 2007.
- [76] D. H. Werner and R. Mittra, *Frontiers in Electromagnetics*. Piscataway, NJ: IEEE Press, 2000.
- [77] J. Gianvittorio and Y. Rahmat-Samii, "Fractal antennas: a novel antenna miniaturization technique, and applications," *IEEE Antennas Propagat. Mag.*, vol. 44, no. 1, pp. 20-36, Feb. 2002.
- [78] C. Puente, J. Romeu, R. Pous, X. Garcia, and F. Benitez, "Fractal multi-band antenna based on the Sierpinski gasket," *Electron. Lett.*, vol. 32, no. 1, pp. 1-2, 1996.
- [79] C. Puente, J. Romeu, R. Pous, and A. Cardama, "On the behavior of the Sierpinski multiband fractal antenna," *IEEE Trans. Antennas Propag.*, vol. 46, no. 4, pp. 517-524, Apr. 1998.
- [80] C. Puente, J. Romeu, and A. Cardama, "The Koch monopole: a small fractal antenna," *IEEE Trans. Antennas Propag.*, vol. 48, no. 11, pp. 1773-1781, Nov. 2000.
- [81] K. J. Vinoy, J. K. Abraham, and V. K. Varadan, "On the relationship between fractal dimension and the performance of multi-resonant dipole antennas using Koch curves," *IEEE Trans. Antennas Propag.*, vol. 51, no. 9, pp. 2296-2303, Sep. 2003.
- [82] S. R. Best, "On the resonant properties of the Koch fractal and other wire monopole antennas," *IEEE Antennas Wireless Propagat. Lett.*, vol. 1, pp. 74-76, 2002.
- [83] D. H. Werner and S. Ganguly, "An overview of fractal antenna engineering research," *IEEE Antennas Propag. Mag.*, vol. 45, no. 1, pp. 38-57, Feb. 2003.

REFERENCES

- [84] R. Azaro, F. De Natale, M. Donelli, E. Zeni, and A. Massa, "Synthesis of a prefactal dual-band monopolar antenna for GPS applications," *IEEE Antennas Wireless Propagat. Lett.*, vol. 5, pp. 361-364, 2006.
- [85] R. Azaro, G. Boato, M. Donelli, A. Massa, and E. Zeni, "Design of a prefractal monopolar antenna for 3.4-3.6 GHz Wi-Max band portable devices," *IEEE Antennas Wireless Propagat. Lett.*, vol. 5 pp. 116-119, 2006.
- [86] C. Puente, J. Romeu, R. Bartolomé, and R. Pous, "Perturbation of the Sierpinski antenna to allocate operating bands," *Electron. Lett.*, vol. 32, no. 24, pp. 2186-2188, Nov. 1996.
- [87] C. T. P. Song, P. S. Hall, H. Ghafouri-Shiraz, and D. Wake, "Sierpinski monopole antenna with controlled band spacing and input impedance," *Electron. Lett.*, vol. 35, no. 13, pp. 1036-1037, Jun. 1999.
- [88] G. F. Tsachtsiris, C. F. Soras, M. P. Karaboikis, and V. T. Makios, "Analysis of a modified Sierpinski gasket monopole antenna printed on dual band wireless devices," *IEEE Trans. Antennas Propag.*, vol. 52, no. 10, pp. 2571-2579, Oct. 2004.
- [89] L. Lizzi, F. Viani, E. Zeni, and A. Massa, "A DVBH/GSM/UMTS planar antenna for multimode wireless devices," *IEEE Antennas Wireless Propagat. Lett.*, vol. 8, pp. 568-571, 2009.
- [90] L. Lizzi and A. Massa, "Analysis of perturbed fractals for antenna synthesis," *Proc. 2009 IEEE AP-S Int. Symp.*, Charleston, SC (USA), June 1-5, 2009, 4 pp.
- [91] W. J. Krzysztofik, "Modified Sierpinski fractal monopole for ISM-bands handset applications," *IEEE Trans. Antennas Propag.*, vol. 57, no. 3, pp. 606-615, 2009.
- [92] S. R. Best, "A discussion on the significance of geometry in determining the resonant behavior of fractal and other non-euclidean wire antennas," *IEEE Antennas Propag. Mag.*, vol. 45, no. 3, pp. 9-28, Jun. 2003.
- [93] C. Puente, J. Romeu, R. Bartolome, and R. Pocus, "Perturbation of the Sierpinski antenna to allocate operating bands," *Electron. Lett.*, vol. 32, no. 24, pp. 1-2, Nov. 1996.
- [94] J. Gouyet, *Physics and Fractal Structures*. New York: Springer, 1996.
- [95] S. R. Best and J. D. Morrow, "The effectiveness of space-filling fractal geometry in lowering resonant frequency," *IEEE Antennas Wireless Propagat. Lett.*, vol. 1, pp. 112-115, 2002.

-
- [96] X. N. Low, W. K. Toh, and Z. N. Chen, "Broadband suspended plate antenna for WiFi/WiMAX applications," in *6th Int. Conf. Commun. Signal Process.*, 2007, pp. 1-5.
- [97] Y. Shen, Y. Wang, and S. Chung, "A printed triple-band antenna for WiFi and WiMAX applications," in *Asia Pacific Microwave Conf.*, 2006, pp. 1715-1717.
- [98] D. D. King, R. F. Packard, and R. K. Thomas, "Unequally-spaced, broadband antenna arrays," *IRE Trans. Antennas Propag.*, vol. AP-8, no. 4, pp. 382-384, 1960.
- [99] Y. T. Lo, "A mathematical theory of antenna arrays with randomly spaced elements," *IEEE Trans. Antennas Propag.*, vol. 12, pp. 257-268, 1964.
- [100] B. D. Steinberg, "Comparison between the peak sidelobe of the random array and algorithmically designed aperiodic arrays," *IEEE Trans. Antennas Propag.*, vol. 21, pp. 366-370, 1973.
- [101] M. B. Donvito and S. Al. Kassam, "Characterization of the random array peak sidelobe," *IEEE Trans. Antennas Propag.*, vol. 27, pp. 379-385, 1979.
- [102] K. C. Kerby and J. T. Bernhard, "Sidelobe level and wideband behavior of arrays of random subarrays," *IEEE Trans. Antennas Propag.*, vol. 54, no. 8, pp. 2253-2262, 2006.
- [103] M. D. Gregory and D. H. Werner, "Ultrawideband aperiodic antenna arrays based on optimized raised power series representations," *IEEE Trans. Antennas Propag.*, vol. 58, no. 3, pp. 756-764, 2010.
- [104] J. S. Petko and D. H. Werner, "The pareto optimization of ultrawideband polyfractal arrays," *IEEE Trans. Antennas Propag.*, vol. 56, no. 1, pp. 97-107, 2008.
- [105] R. L. Haupt, "Thinned arrays using genetic algorithms," *IEEE Trans. Antennas Propag.*, vol. 42, no. 7, pp. 993-999, 1994.
- [106] M. G. Bray, D. H. Werner, D. W. Boeringer, and D. W. Machuga, "Optimization of thinned aperiodic linear phased arrays using genetic algorithms to reduce grating lobes during scanning," *IEEE Trans. Antennas Propag.*, vol. 50, no. 12, pp. 1732-1742, 2002.
- [107] J. S. Petko and D. H. Werner, "The evolution of optimal linear polyfractal arrays using genetic algorithms," *IEEE Trans. Antennas Propag.*, vol. 53, no. 11, pp. 3604-3615, 2005.

REFERENCES

- [108] J. S. Petko and D. H. Werner, "An autopolyploidy-based genetic algorithm for enhanced evolution of linear polyfractal arrays," *IEEE Trans. Antennas Propag.*, vol. 55, no. 3, pp. 583-593, 2007.
- [109] Y. Kim and D. L. Jaggard, "The fractal random array," *Proceedings of the IEEE*, vol. 74, no. 9, pp. 1278-1280, 1986.
- [110] M. D. Gregory and D. H. Werner, "Design of high performance compact linear ultra-wideband arrays with the CMA evolutionary strategy," *Proc. IEEE Antennas Propag. Int. Symp.*, Toronto, ON, Canada, Jul. 2010, pp. 1-4.
- [111] M. Naser-Moghadasi, H. Rousta, and B. S. Virdee, "Compact UWB planar monopole antenna," *IEEE Antennas Wireless Propag. Lett.*, vol. 8, pp. 1382-1385, 2009.
- [112] Q. Wu, R. Jin, J. Geng, and M. Ding, "Printed omni-directional UWB antenna with very compact size," *IEEE Trans. Antennas Propag.*, vol. 56, no. 3, pp. 896-899, 2008.
- [113] T. Karacolak and E. Topsakal, "A double-sided rounded bow-tie antenna (DSRBA) for UWB communication," *IEEE Antennas Wireless Propag. Lett.*, vol. 5, pp. 446-449, 2006.
- [114] H. Nazh, E. Bicak, B. Turetken, and M. Sezgin, "An improved design of planar elliptical dipole antenna for UWB applications," *IEEE Antennas Wireless Propag. Lett.*, vol. 9, pp. 264-267, 2010.
- [115] S. Koulouridis and J. L. Volakis, "A novel planar conformal antenna designed with splines," *IEEE Antennas Wireless Propag. Lett.*, vol. 8, pp. 34-36, 2009.
- [116] M. John and M. J. Ammann, "Spline-based geometry for printed monopole antennas," *Electron. Lett.*, vol. 43, no. 6, pp. 7-8, 2007.
- [117] M. John and M. J. Ammann, "Antenna optimization with a computationally efficient multiobjective evolutionary algorithm," *IEEE Trans. Antennas Propag.*, vol. 57, no. 1, pp. 260-263, 2009.
- [118] M. D. Gregory, Z. Bayraktar, and D. H. Werner, "Fast optimization of electromagnetic design problems using the covariance matrix adaption evolutionary strategy," *IEEE Trans. Antennas Propag.*, in press.
- [119] D. W. Boeringer and D. H. Werner, "Particle swarm optimization versus genetic algorithms for phased array synthesis," *IEEE Trans. Antennas Propag.*, vol. 52, no. 3, pp. 771-779, 2004.

-
- [120] A. Ostermeier, A. Gawelczyk, and H. Hansen, "A derandomized approach to self adaptation of evolution strategies," *Evolutionary Computation*, vol. 2, no. 4, pp. 369-380, 1994.
- [121] D. Colton and R. Krees, *Inverse Acoustic and Electromagnetic Scattering Theory*. Berlin, Germany: Springer-Verlag, 1992.
- [122] A. Massa, A. Boni, and M. Donelli, "A classification approach based on SVM for electromagnetic subsurface sensing," *IEEE Trans. Geosci. Remote Sens.*, vol. 43, no. 9, pp. 2084-2093, 2005.
- [123] I. Catapano, L. Crocco, and T. Isernia, "Improved sampling methods for shape reconstruction of 3-D buried targets," *IEEE Trans. Geosci. Remote Sens.*, vol. 46, no. 10, pp. 3265-3273, 2008.
- [124] S. Kharkovsky and R. Zoughi, "Microwave and millimeter wave nondestructive testing and evaluation - Overview and recent advances," *IEEE Instrum. and Measur. Mag.*, vol. 10, 2007.
- [125] M. Benedetti, M. Donelli, D. Lesselier, and A. Massa, "A two-step inverse scattering procedure for the qualitative imaging of homogeneous cracks in known host media - Preliminary results," *IEEE Antennas Wireless Propag. Lett.*, vol. 6, pp. 592-595, 2007.
- [126] O. Mudanyali, S. Yildiz, O. Semerci, A. Yapar, and I. Akduman, "A microwave tomographic approach for nondestructive testing of dielectric coated metallic surfaces," *IEEE Geosci. Remote Sens. Lett.*, vol. 5, no. 2, pp. 180-184, 2008.
- [127] S. Caorsi, A. Massa, M. Pastorino, and A. Rosani, "Microwave medical imaging: potentialities and limitations of a stochastic optimization technique," *IEEE Trans. Microwave Th. Techn.*, vol. 52, no. 8, pp. 1909-1916, 2004.
- [128] P. M. Meaney, M. W. Fanning, D. Li, S. Poplack, and K. D. Paulsen, "A clinical prototype for active microwave imaging of the breast," *IEEE Trans. Microwave Th. Techn.*, vol. 48, no. 11, pp. 1841-1853, 2000.
- [129] J. Johnson and T. Takenaka, "Preliminary assessment of electromagnetic absorption in the breast for cylindrical microwave breast cancer detection systems," in *Proc. Progress Electromagn. Res. Symp.*, Tokyo, Japan, 2006, pp. 256-260.
- [130] E. Zastrow, S. Davis, and S. Hagness, "Safety assessment of breast cancer detection via ultrawideband microwave radar operating in pulsed-radiation mode," *Microw. Opt. Technol. Lett.*, vol. 49, no. 1, pp. 224-225, 2007.

REFERENCES

- [131] P. M. Meaney, M. W. Fanning, T. Reynolds, C. J. Fox, Q. Fang, C. A. Kogel, S. P. Poplack, and K. Paulsen, "Initial clinical experience with microwave breast imaging in women with normal mammography," *Acad. Radiol.*, vol. 14, no. 2, pp. 207-218, 2007.
- [132] J. E. Johnson, T. Takenaka, and T. Tanaka, "Two-dimensional time-domain inverse scattering for quantitative analysis of breast composition," *IEEE Trans. Biomed. Eng.*, vol. 55, no. 8, pp. 1941-1945, 2008.
- [133] J. Yu, M. Yuan, and Q. H. Liu, "A wideband half oval patch antenna for breast imaging," *Progress In Electromagnetics Research*, PIER 98, pp. 1-13, 2009.
- [134] J. P. Stang and W. T. Joines, "A tapered microstrip patch antenna array for microwave breast imaging," in *Proc. IEEE MTT-S Int. Microw. Symp.*, Atlanta, GA, USA, 2008, pp. 1313-1316.
- [135] I. J. Craddock, R. Nilavalan, A. Preece, J. Leendertz, and R. Benjamin, "Experimental investigation of real aperture synthetically organized radar for breast cancer detection," in *Proc. IEEE Antennas Propag. Society Int. Symp.*, Washington, DC, USA, 2005, pp. 179-182.
- [136] R. Nilavalan, I. J. Craddock, A. Preece, J. Lendertz, and R. Benjamin, "Wideband microstrip patch antenna design for breast cancer tumor detection," *IET Microw. Antennas Propag.*, vol. 1, no. 2, pp. 277-281, 2007.
- [137] M. Klemm, I. J. Craddock, J. A. Leendertz, A. Preece, and R. Benjamin, "Radar-based breast cancer detection using a hemispherical antenna array - Experimental results," *IEEE Trans. Antennas Propag.*, vol. 57, no. 6, pp. 1692-1704, 2009.
- [138] J. P. Stang, W. T. Joines, Q. H. Liu, G. A. Ybarra, R. T. George, M. Yuan, and I. Leonhardt, "A tapered microstrip patch antenna array for use in breast cancer screening via 3D active microwave imaging," in *Proc. IEEE Antennas Propag. Society Int. Symp.*, Charleston, SC, USA, 2009, pp. 1-4.
- [139] T. Moriyama, Y. Yamaguchi, K. A. Hong Ping, T. Tanaka, and T. Takenaka, "Parallel processing of forward-backward time-stepping method for time domain inverse scattering," in *Proc. Progress Electromagn. Res. Symp.*, Cambridge, USA, 2008, pp. 551-556.